RMIT
UNIVERSITY

INVESTIGATION OF ADDITIVELY MANUFACTURED SUBSTRATES

IN HETEROGENEOUS CATALYSIS

A thesis submitted in fulfilment of the requirements for the degree of Master of Engineering

Christopher William Hurt

Bachelor of Engineering UNSW

School of Engineering

College of Science, Engineering and Health

RMIT University

JULY, 2017

ABSTRACT

Selective Laser Melting (SLM) is an additive manufacturing technology for alloys capable of producing complex, miniature geometries and as such the pursuit of functionalising catalysts effectively onto these SLM-printed materials, like catalysts for dimethyl ether (DME) synthesis processes, presents an opportunity to open the research space into miniature catalytic reaction vessels, termed by some as 'reactionware' [1]. However, there is precious little evidence in the literature of a thorough attempt to catalytically functionalise SLM substrates and demonstrate activity in chemical reactions. This is a little-explored field due to the difficulty of properly immobilising the catalyst materials on the metallic alloys that SLM is capable of printing. It follows that the major aim of this project was to develop, produce and test miniature, functionalised reactor components made by SLM, both in liquid and gaseous phase catalytic reactions. Methods to coat catalysts on SLM substrates were explored for several catalytic applications:

- Dry reforming of methane (DRM), a step towards DME synthesis
- 4-Nitrophenol reduction, a reaction applicable to water purification.
- Glycerol acetalisation, this synthesis provides a bio-diesel fuel additive.

Flat, planar substrates printed by SLM with Ti6Al4V and 17-4 PH were coated with the relevant catalysts to explore the chemical activity of these systems in batch or continuous setups of these reactions.

Scanning electron microscopy (SEM), energy-dispersive X-ray spectroscopy (EDX), X-ray diffraction (XRD) and x-ray photoelectron spectroscopy (XPS) were used to assess the structure, composition, and topography of the catalytic coatings applied to the various substrates used in this research project. Online and offline gas chromatography (GC) as well as uv-vis spectroscopy were used to determine conversion and/or selectivity of the reactions undertaken by the various catalytic systems. For some reactions, more complex structures were SLM-printed and functionalised with the relevant catalyst and exposed to continuous flow of the reactants.

In the process of testing SLM substrates for catalytic activity, it was found that some catalysts were active but would not remain immobilised during the reaction and some remained immobilised but failed to demonstrate suitably high activity. Au nanoparticles anchored effectively on Ti6Al4V substrates but demonstrated low or inconsistent conversion in 4-nitrophenol (4-NP) reduction. Conversely $FeCl_3$ coats &

Pd nanoparticles on Ti6Al4V substrates gave higher conversions (53% & ~100%) for these reactions but were immediately stripped off the substrates during the glycerol acetalisation & 4-NP reduction reactions.

The best catalyst for DRM was metallic supported by magnesium alumina on 17-4 PH steel with a 5 wt.% Ni loading, a small conversion of both CH_4 and CO_2 at ~1.5% and ~4% was achieved respectively. The most active catalyst for Glycerol Acetalisation was a $FeCl_3$ catalyst on a Ti6Al4V titanium alloy; this gave a glycerol conversion of 53.55%. For 4-Nitrophenol Reduction, the best catalyst was dip-coated Pd on Ti6Al4V titanium alloy which reduced 4-Nitrophenol to 4-Aminophenol at near 100% conversion in 20 minutes or less for the calcined and untreated conditions alike.

This early work demonstrates that catalytic functionalisation of SLM substrates is viable and worth further investigation.

ACKNOWLEDGEMENTS

DECLARATION

I certify that except where due acknowledgement has been made, the work is that of the author alone; the work has not been submitted previously, in whole or in part, to qualify for any other academic award; the content of the thesis is the result of work which has been carried out since the official commencement date of the approved research program; any editorial work, paid or unpaid, carried out by a third party is acknowledged; and, ethics procedures and guidelines have been followed.

I acknowledge the support I have received for my research through the provision of an Australian Government Research Training Program Scholarship.

04/07/17

Christopher W. Hurt

School of Engineering

RMIT University

TABLE OF CONTENTS

LIST OF FIGURES

LIST OF TABLES

LIST OF SYMBOLS

'R_a'	-	Surface roughness of a line	-	Eq. 1	-	Eq. 2	-	Eq. 3
'L'	-	Layer thickness at given location	-	Eq. 1				
'L_t'	-	Printed layer thickness	-	Eq. 1				
'α'	-	Inclination angle	-	Eq. 1				
'S_a'	-	Surface roughness of a plane	-	Eq. 4				
$\dot{V}$	-	Build up rate	-	Eq. 5				
Δy_s	-	Hatch distance	-	Eq. 5				
D_s	-	Layer thickness	-	Eq. 5				
Δy_s	-	Hatch distance	-	Eq. 5				
V_{scan}	-	Scan Speed	-	Eq. 5				
'k'	-	A constant	-	Eq. 6				
'Re'	-	Reynolds number	-	Eq. 6				
'A'	-	Outlet width	-	Eq. 6				
'B'	-	Inlet width	-	Eq. 6				
'C'	-	Channel height	-	Eq. 6				
'D_H'	-	Hydraulic diameter	-	Eq. 6	-	Eq. 8	-	Eq. 9
'Bo'	-	Bond number	-	Eq. 7				
'ρ_L'	-	Liquid phase density	-	Eq. 7	-	Eq. 8		
'ρ_G'	-	Gas phase density	-	Eq. 7	-	Eq. 8	-	Eq. 9
'g'	-	Gravitational Acceleration	-	Eq. 7	-	Eq. 10		
'σ'	-	Surface Tension Force	-	Eq. 7	-	Eq. 9		
'$Bo_{critical}$'	-	Critical Bonds number	-	Eq. 8				
'We_G'	-	Vapour phase Weber Number	-	Eq. 9				
'U_g'	-	Superficial gas velocity	-	Eq. 9				
'H'	-	Coating thickness	-	Eq. 10				
'μ'	-	Fluid Viscosity	-	Eq. 10				

'v'	-	Withdrawal speed	-	Eq. 10
'γ'	-	Liquid-air surface tension	-	Eq. 10
'ρ'	-	Fluid density	-	Eq. 10
'M'	-	Metal	-	Eq. 11
'z'	-	Metal reduction state	-	Eq. 11
'Q*'	-	Dimensionless Heat Transfer Rate	-	Fig. 33

LIST OF EQUATIONS

$$Glycerol\ remaining\ (\%) = Glycerol\ moles(Solketal + glycerol)\ Moles * 100 \qquad \text{Eq. 21 Glycerol remaining}$$ **Error! Bookmark not defined.**

CHAPTER ONE - INTRODUCTION

1.1 INTRODUCTION

Whilst 3D printing technology is used foremost in the field of rapid prototyping there is an increasing interest in the manufacturing of end-use products. This is primarily because 3D printing has the unique ability to produce complex geometries not possible through other methods without the need for part-specific tooling [2].

3D printing is a popular term for processes which utilise Additive Manufacturing (AM) technologies. Whilst there are many varieties of 3D printing, most operate on the same principles. Most 3D Printers work by using layer-by-layer AM, whereby material is deposited within one layer before subsequent layers are deposited on top of it in succession to form a 3D part.

AM has been applied to biomaterial implants, prosthetics, and rapid prototyping to quite an extent but there has been little application of this technology to chemical industries. There is significant potential for AM to develop chemical plants beyond their traditional standards.

To this end, efforts are currently being made to develop new equipment and techniques that could transform the current chemical plants into compact, safe, energy-efficient, sustainable, and environmentally friendly processes. A common strategy is to place process intensification as the focus of research and development [2]. Process intensification of current large-scale processes may involve reducing the scale of the plant by a significant extent without compromising its' productivity. This is achievable by scaling down the current equipment volume and by replacing or removing equipment from the process entirely. It is generally agreed that "process intensification" requires a substantial reduction or improvement of some character of the chemical plant. Changes which achieve this may include:

- A marked improvement in the productivity capacity to equipment volume ratio
- Significantly reduced energy consumption or waste output
- Drastically improved reaction efficiency

To achieve process intensification, it's necessary to develop new equipment and techniques that bring dramatic improvements compared to those commonly used today in manufacturing and processing. Any chemical engineering development that leads to a substantially smaller, cleaner and more energy efficient technology is process intensification.

Recently considered process-intensifying equipment includes micro-structured reactors, intensive mixers, separation devices and heat/mass transfer devices. Micro-structured reactors usually consist of a several straight narrow channels [3-19] with defined uniform cross-sections in the sub-millimetre size range [20, 21]. The beauty of micro-structured reactors is that they can perform multiple functions; mixing or separation and heat exchange may all happen simultaneously [22, 23]. Mixing and separation are controlled by varying channel geometry and heat removal is achieved by dispersion through the channel walls, making the primary heat transport mechanism conduction. As such, micro-structured reactors present improved mass and heat transfer performances compared to traditional reactors and heat exchangers, leading to process intensification. If process intensification for chemical reactor design is to be achieved, a micro-structured reactor housing catalysts is an appropriate path to consider. In this context, 3D printing offers large scope in making process-intensification possible.

1.2 RATIONALE FOR THIS INVESTIGATION

There are numerous chemical and industrial processes which can be process-intensified using AM technologies. For example, consider the possibility of developing process-intensified DME Reactors or the value-adding potential of converting the biodiesel by-product glucose into the biodiesel additive solketal.

It is worth investigating how AM can help us process intensify reactors such as this. In most cases 3D printed fluidic devices have been implemented with plastic printing technologies; this reduces the upper limits of temperature and pressure. Metallic 3D printing is a less-used technology in fluidic devices and reactor design but has considerable potential in lifting the upper limits on temperature and pressure. The preference for plastic printing is largely due to the better resolutions and smoother surface qualities these technologies offer. However, given that increased surface area improves the catalyst interfacial area and thereby the

catalytic activity [24, 25], the rough surface qualities of metallic 3D printing can prove beneficial rather than a hindrance in the context of heterogeneous catalysis.

SLM is an AM technology that is capable of producing layers down to 15 microns thick [26]. It is a flexible AM technology which can produce complex structures in short periods of time. This makes it suitable for producing a micro-structured reactor of sub-millimetre dimensions.

Unfortunately, SLM produces surfaces which are quite rough compared to subtractive manufacturing methods. This is disadvantageous in most contexts because it decreases the surface quality, however it is commonly known that an increased interfacial area like this between catalyst and reactants will lead to more rapid reaction conditions.

To activate reactor channels with a catalyst there are two common approaches: Washcoat may be applied to create a support for subsequent wall coating of the catalytically active species or the catalyst may be loaded directly as a packed bed.

There is found to be a trade-off between using a packed bed or a wall coated catalyst. Packed beds have higher loadings and cause high pressure drops [27]. Wall coatings apply lower loadings of and don't introduce high pressure drops. Wall coatings are often preferred to catalyst packed bed reactor because of their low pressure drop and economical use of catalyst material. Overall, a wall-coating approach would be appropriate to pursue when loading catalysts onto SLM-based micro-structured reactor designs. This is advantageous because as the wall coating is deposited on a rougher surface, the surface area of the catalyst is increased. This means that the surface defects of SLM can potentially be used to enhance catalytic reactions.

One challenge of functionalising substrates produced by SLM is developing a method that homogenously coats/functionalises the entire surface despite its inherent roughness. Ideally the coats will be evenly-dispersed, either preserving or enhancing the roughness of their SLM-printed substrate underneath. In addition, the coating fluid must not be too viscous otherwise it will be unable to infiltrate the micro reactor channels due to excessive surface tension.

The significance of this research lies in the unique advantage of SLM in its potential ability to combine the surface morphology and manufacturing of complex three-dimensional

structures to efficiently produce monoliths with surfaces that are superior for catalytic functionality. Traditional methods often involve having to produce a three-dimensional structure through multiple subtractive manufacturing and joining processes [28]. Any desired surface modification must be done as a secondary processing adding to the production time and complicating the design process. If SLM can combine multiple manufacturing needs into one process it would provide a significant advantage to the design and implementation of micro-structured reactors by reducing cost and increasing functionality. It may well be possible to achieve process intensification with improvements made by this technique alone.

Whilst in the literature there are articles that consider microfluidics produced by SLM or articles that consider catalytically functionalised SLM substrates, there are few studies on micro-structured reactors functionalised for catalytic reactions which have been demonstrated using SLM. To this end, the aim of the project was to investigate the applicability of SLM in producing substrates which may be suitably coated for multiple different catalytic reactions.

1.3 RESEARCH QUESTIONS FOR THIS INVESTIGATION

My primary research question was what observable distinctions are there between active and inactive catalysts? Consider catalyst deposition method, chemical composition, phase, crystal structure and surface topography. Which factors appear to be most crucial in determining the catalysts activity?

My secondary research questions were:

1. What observable distinctions are there between anchored and loose catalyst systems? Consider substrate and support properties: chemical composition, phase, crystal structure and surface topography. Which factors appear to most crucial in anchoring the catalysts?
2. Do the SLM substrates influence the catalyst conversion and selectivity?
3. Do the SLM substrates successfully demonstrate both anchoring and support of catalysts for liquid and gaseous phase reactions?

1.4 AIMS AND OBJECTIVES OF THIS INVESTIGATION

The major aim is to develop, produce and test miniature, functionalised reactor components made by SLM, both in liquid and gaseous phase catalytic reactions.

Research Objectives

1. Design/Print geometries for batch reactions without removable internal support structures.

2. Design/Print geometries for continuous reactions with high Surface Area to Volume Ratios & without removable internal support structures.

3. Develop & Implement a deposition method for catalysts of known gaseous phase reactions, including: Catalytic Partial Oxidation (CPOX), the Dry Reforming of Methane (DRM) & Methanol Synthesis (MS).

4. Develop & Implement a deposition method for catalysts of known liquid phase reactions, including: 4-NP reduction & glycerol acetalisation.

5. Test catalysts under batch reaction conditions
   a. Measure conversion and selectivity by GC-FID/MS &/or UV-Vis
   b. Perform these methods for further data – XRD, XPS & SEM/EDX

6. Test the best catalysts under continuous reaction conditions
   a. Measure conversion and selectivity by GC-FID/MS &/or UV-Vis
   b. Perform these methods for further data – XRD, XPS & SEM/EDX

1.5 THESIS LAYOUT

To explore this project's potential a Literature Review on related research follows the Introduction, after which the Experimental Method is described before the Results are discussed.

Chapter 2, the Literature Review identifies the gap present in the literature followed by covering the types of AM found applied to Heterogeneous catalysis with a focus on SLM. Examples of catalyst immobilisation in the literature are discussed, with observations about probable future developments. Following on, micro-reactors are reviewed as well as the impact of their geometries and typical coating methods applied in this context before looking at the vapour phase and liquid phase reactions which were examined during this thesis project.

Chapter 3, the Experimental Method, describes the methods used to explore the viability of SLM-based catalytic systems, including the development of methods for reactions, for sampling reactant conversion and product selectivity by GC-FID/MS &/or UV-Visible Spectroscopy as well as analysis of the substrates by XRD, XPS & SEM/EDX.

Chapter 4, Vapour Phase Reactions, focuses on the implementation of functionalised SLM substrates to vapour phase heterogeneous catalysis, i.e. dry reforming of methane (DRM), a reaction relating to DME synthesis.

Chapter 5, Liquid Phase Reactions, focuses on the implementation of functionalised SLM substrates to liquid phase heterogeneous catalysis, i.e. 4-NP reduction & glycerol acetalisation.

Chapter 6, Conclusions and Future Research, summarises all conclusions made in the chapters whilst providing recommendations for future research directions.

CHAPTER TWO – LITERATURE REVIEW

2.1 RESEARCH GAP

Many fields in the chemical sciences have utilized AM technologies in recent times and their scope is ever increasing. The topics of greatest interest are tissue engineering and bioprinting [29-39] followed by microfluidics [30, 31, 34, 39-41]. Other articles have been published on reactionware [29, 31, 42-44], drug synthesis and delivery [29, 31-33], biological studies [35, 36, 40], electrochemistry [39, 41, 42], electronics [30, 31, 39, 42] and education/communication [31, 36]. Further reviews were published on food synthesis [45], analytical chemistry [41] and robotics [46].

However, the application of this emerging technology in the field of chemical sciences is still in its infancy. This is particularly true for heterogeneous catalysis; an important technology by which several chemical processes are carried out in manufacturing industries.

The main driving force to implementing AM in heterogeneous catalysis is based on two facts. Firstly, heterogeneous catalysis is an integral part of our large-scale energy, fuel, chemical and pharmaceutical industries and implementing alternative small-scale AM technologies will create a major change in existing technology and have an enormous and immediate impact. As early work can demonstrate [47], high conversion is possible with miniature AM printed geometries.

Secondly, these traditional large-scale chemical manufacturing units are difficult to adapt once built as the cost of change at this stage is quite high [48]. If there is any poor resource management, hazardous processing practices or poor environmental sustainability in the final design, implementing the necessary changes is costly. However, the societal demands of energy, fuels, medicines, polymers and food stuffs are fulfilled only by these industries. Therefore, introducing AM in heterogeneous catalysis will potentially improve the ease of adapting reactor designs by enabling reduced sizes for chemical plants and through the facilitation of modular design also reduce the costs of design and manufacturing. In addition, the relative cost efficiency of AM technologies for short production runs make them ideal for late-term

adjustments to chemical plants either due to unknowns in the process, or just the need for new process functionality [2].

AM technology, has a unique and significant advantage in its ability to address multiple design issues simultaneously. The technologies can produce complex three-dimensional structures of smaller dimensions and, in some cases, high surface roughness [49]. These unique characteristics enable AM technologies to efficiently produce micro-structured reactors with surfaces that are superior for catalytic functionality. There is a variety of chemical and industrial processes which can be process-intensified using AM technologies; as such this is a promising area of research.

However, heterogeneous catalysis is a complex multidisciplinary science and introducing AM technologies without compromising the effectiveness of heterogeneous catalysts is difficult. There are numerous technical challenges in introducing AM structures towards conventional catalytic processes. Technical challenges include the limited materials palette & the restrictions of catalysts this implies, and the chemical interfacing of catalysts with build materials.

In comparison to the large number of catalytic processes, the choice of materials that are used in AM is limited by what is 'printable' [50]. This makes it difficult to cater towards the specific needs of chemical processes such as temperature and solvent compatibilities [49]. The limited materials choice is also exacerbated by the preference of some AM technology providers to lock their user into using only their proprietary materials. This increases the expense and hides knowledge of the specifics of the material compositions. Furthermore, this results in a reduced palate of materials capable of addressing requirements of some petrochemical, pharmaceutical, fine chemical and polymer industries that use specific catalysts. It's clear that further materials development and less proprietary material restrictions are required to best enable catalyst exploration.

Chemically bonding catalysts to their supports usually requires calcination. This treatment must be applied without compromising the stability of the SLM substrate or the catalyst activity.

On the topic of AM and catalysis, whilst some review articles refer to catalysis briefly [42, 43], and some review articles even look at the design of chemical reactors more comprehensively [29, 31, 42-44], there is no review article addressing the application of AM in heterogeneous catalysis or the chemical interfacing of catalysts to AM structures. It is the intent of this chapter to explore AM as it is applied to heterogeneous catalysis.

2.2 AM TECHNOLOGIES

2.2.1 Common Steps in AM

All AM technologies use the following steps or a close variant thereof as the basis for manufacturing a part:

- **Acquire** a 3D model
- **Convert** the 3D model file to the STL format
- **Slice** the file (Create printer instructions)
- **Build** the part

A more detailed overview of the common steps involved in AM has been given by Stephanie Crawford [51].

The printing process proceeds through the placement of material(s) in 2D patterns that directly correlate to sections or 'slices' through the objects' final 3D geometry. When each layers' section is printed, successive layers are printed upon the previous layer and so on until a 3D part has been fully printed. The AM technology can be classified as metal-based or polymer-based depending on the feedstock material. In the metal-based systems a laser or electron beam is used to melt and fuse the metal alloy powder layer-by-layer while in the polymer-based systems UV light or thermal energy are used to fuse the layers together.

2.2.2 AM Technology for Heterogeneous Catalysis

There are many different AM technologies available. Only those relevant to heterogeneous catalysis are considered in this review. Table 1 and Table 2 include

reported material properties and printing properties from AM technologies applied to heterogeneous catalysis.

Table 1 Printing properties and material properties for AM technologies part 1 of 2

AM Technology	Materials Applied	Thermal Stability Upper Limit Examples	Engineering & Design Limitations	Best Recorded Resolution (XY/Z) (μm)
FDM	Thermoplastics such as ABS, PLA, PC, PP [43, 49, 52, 53].	Material Specific, not over 260°C. ABS: ~220°C, PC: ~147°C [49].	External support easily removed [49]. Internal removal difficult for complex geometries.	250/50 [31].
SL (or SLA)	UV curable photopolymers [49], such as Polyethylene Glycol Diacrylate (PEGDA) hydrogel [54]. Most proprietary.	Accura Bluestone: ~83°C Accura 60: ~58°C [49].	Compressed air easily removes internal un-cured resin [49]. 2nd UV cure necessary afterwards.	70-250/1-10 [31]. Two-Photon-Polymerisation -/<1
SLM	Alloys, such as titanium alloys, steels, aluminium, inconel and other alloys [49, 55].	High Melting points: Al ~660°C Ti ~1660°C Oxidation occurs at lower temperature [49].	External supports difficult to remove. Rough surface quality often requires polishing for smoothness [49].	80/20 [56]
Modified Office Inkjet Printer	Mixed Metal Oxides [57-65]	High; corresponds to metal oxide properties.	Post-printing calcination needed [57-65]. Applies mostly thin sheets [62], rah although rather than bulk printing of 3D objects [50].	Matches office inkjet print resolution/Layers are nm's thick.
Robocasting	Mixed Metal Oxides, Alloys, Polymers, Supported Metal [1, 47, 66-70]	Material Specific, varies greatly. $BaMn_2Al_{10}O_{19-\alpha}$ ~1300°C [67].	Post-printing calcination needed [68]. Huge material libraries due to ease of compositional variation.	Rod Diameters: 410 μm [47, 66]. Spacing: 450 μm [69]. Layer Heights: 287 μm [71].

Table 2 Printing properties and material properties for AM technologies part 2 of 2

AM Technology	Chemical Stability	Multi-Material Fabrication
FDM	Polymers are susceptible to degradation by organic solvents or acidic/basic conditions [43].	Many filament materials & dual-head FDM extruders are available.
SL (or SLA)	Poor stability. Easily degraded by solvents, sometimes swells [49]	No known multi-material building setups found.
SLM	Metal Oxide layers are quite stable. Resistant to many chemical reagents [49].	No known multi-material building setups found.
Modified Office Inkjet Printer	Ethanol most often used as an ink solvent [57-65]. Printed materials vulnerable to dissolution in deposition solvents.	Combinatorial materials extensively demonstrated [1, 47, 66-70].
Robocasting	Varies widely, many materials are available [1, 47, 66-70].	Two-component mixing & dispensing unit for graded compositions demonstrated by Kokkinis et al. [72].

Capel et. al.'s article on AM of microfluidics is a useful supplementary resource for these tables [49]. The distinctions of each AM technology have significant impacts on what materials the technology is suited to printing and what geometries it can produce. The remainder of this section explores the distinctions of each AM technology as it applies to heterogeneous catalysis.

2.2.2.1 Robocasting

In the literature this AM technology is known under several names: Robotic Deposition [31], Robocasting [42, 44, 68], Direct Writing [31], Direct Ink Writing (DIW) [42], Syringe Extrusion Printing [43] and even as 3D Fibre Deposition (3DFD) [68]. There are subtle nuances in the use of these terns, like 'Syringe Extrusion Printers' being a name for robocasting printers that extrude discontinuously using a syringe pump mechanism. Since "Robocasting" appears to be the most widely used name, it is appropriate for this name to be used and it will be used henceforth in this thesis.

Robocasting dispenses concentrated colloidal suspensions called 'inks' through a nozzle or syringe that are self-supporting during assembly due to rapid setting mechanisms [73]. Aside from room temperature printing, the feedstock material is the

critical distinction between this method and Fused Deposition Modelling (FDM). A typical setup for Robocasting is shown in Figure 1.

Printing proceeds through the deposition of these inks in 2D patterns that directly correlate to sections or 'slices' through the objects final 3D geometry. When each layers' section is printed the print head moves upwards and prints upon the previous layer and so on until a 3D part has been printed.

The xyz print-head mobility for robocasting is the most commonly observed setup and the extrusion may be continuous or discontinuous. Discontinuous extrusion is better for design freedom, as it affords more flexibility to the process [74].

Robocasting has relatively larger layer thickness, especially compared to Stereolithography [75]. It is predominantly intended for printing ceramics, having been designed for that in the first place [76]. Although almost anything that can be made into a powder can be printed by robocasting, provided the fluid properties are readjusted after adding this powder.

Catalysts, supports and substrates printed with Robocasting in this review include:

- o Mixed Metal Oxide [67]
- o Metal Alloys [68, 69]
- o Polymers [1, 70]
- o Supported Metal [1, 47, 66]
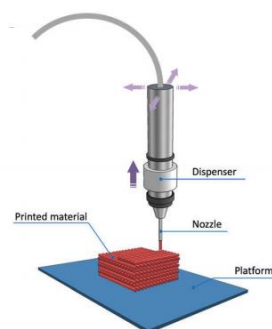
Figure 1 Schematic diagram of robocasting. A material dispenser connected to a computer-controlled robot scans across the build platform depositing 'ink' layer-by-layer [42].

2.2.2.2 FDM – Fused Deposition Modelling

FDM is an AM process that utilises filament-based feedstocks [42]. The layer-by-layer printing requires a heated nozzle to locally melt the plastic to allow filament extrusion to a thinner diameter and to enable adhesion by solidification of the extrudate during contact with the already-built material. Some FDM machines are like Figure 2 in that a separate support material and structural material may be printed layer-by-layer to produce a 3D object.

In many other setups, it's normal to print support material using thin, mechanically removable sheets of the structural material instead. FDM is the most readily available AM technology. It's inexpensive and many printers are available for private and professional use.

Build volumes as large as 914 x 610 x 914 mm^3 have been reported [77]. And layer thicknesses as small as 20 µm [78] for some professional printers and speeds up to 300mm/s. Typical materials are polymers such as PLA, ABS, PVA, CPE, Nylon, PA, PBT, PEEK, PMMA, PEI and PP [77, 78].

In the scope of this review, FDM was used to print:

- o Polymers [43, 52]
- o Polymers with small metal oxide loadings [79]

This method is limited to polymers shaped as a filament with minimal powder loadings [79] because increased loadings inhibit printability.
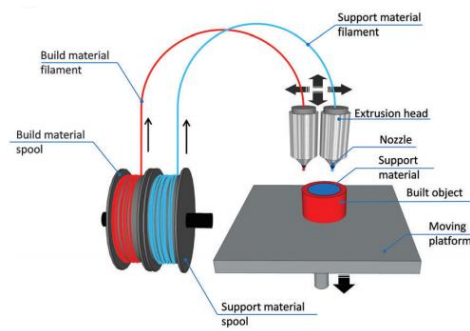
Figure 2 Schematic diagram of Fused Deposition Modelling (FDM). A nozzle fed with a thermoplastic wire moves in two dimensions across a vertically-mobile build platform onto which molten polymer is deposited [42].

2.2.2.3 Inkjet Printing

Inkjet printing (IJP) originated from adaptations made to ink on paper printers that facilitate thicker layers of 'ink' that are printable in a layer-by-layer fashion. Liu, X., et al. [50] report the property requirements of inks used in InkJet printing as being dependent on the print mode.

The specific ink properties of interest are the viscosity, surface tension, density and particle size, the specific limits thereof are reported in Table 3. Continuous IJP pumps ink through a nozzle to form a liquid jet [80, 81]. Droplets are controlled through periodic perturbations of the jet that overcome the liquid surface tension. Drop on Demand (DOD) printing is less stringent for ink requirements. Acoustic pulses thermally or piezo-electrically eject ink droplets from a reservoir through the nozzle, see Figure 3.

Table 3 Fluid properties requirements for InkJet Printers, reported by Liu, X., et al. [50]

		Particle size (μm)	Viscosity (cP)	Surface tension (dynes/cm)	Density (g/cm^3)
Continuous inkjet ink		<1	1–10	25–70	~1
DOD inkjet ink	Thermal	<1	5–30	35–70	~1
	Piezoelectric	<1	1–20	35–70	~1

AM technologies that use inkjet technology mostly fall into 3 broad categories that are commercially available: Poly Jetting, Binder Jetting & Material Jetting [82].
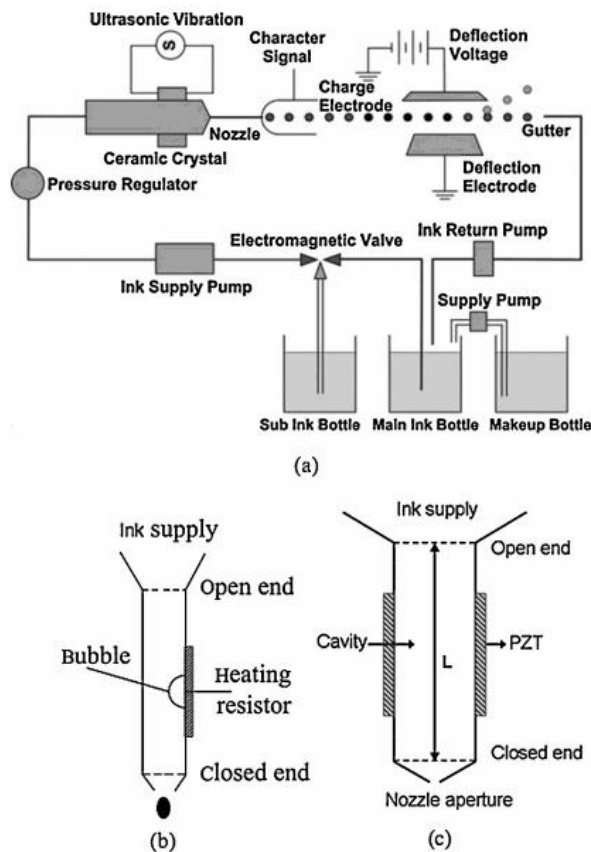
Figure 3 Inkjet printer types: (a) a continuous mode inkjet printer, (b) a thermal DOD inkjet printer, and (c) a piezoelectric DOD inkjet printer [80, 81].

However, the inkjet technology used for catalysis in this review was office inkjet printers modified to accept custom ink compositions [57]. These printers are not always practical for printing especially thicker layers or bulk objects, although printing 3D objects is possible if somewhat difficult [50]. Nonetheless inkjet printing is the basis of the Binder Jetting and Poly Jetting AM technologies [82], so office inkjet printers can be adapted for AM. As such catalytic chemistry that uses this approach was included in the review.

The nature of using modified setups is that reporting of properties such as layer thickness and speed is scarce; however, given that office printers have their own print speeds and layer thickness properties, these should be referred to in the printer manual.

In the scope of this review, Inkjet printing was used to print:

- o Metal Oxides and Mixed Metal Oxide Precursors [57-65, 83-85]

Inkjet printing is possible for any mixture meeting the material requirements for printing, see Table 3. Furthermore, Kitson et. al. [43] shows that this method may also synthesize polymers, ceramics & glasses.

2.2.2.4 DOPsL – Dynamic Optical Projection Stereolithography

Stereolithography uses UV light to photopolymerise materials layer-by-layer to make a 3D part. DOPsL is a stereolithography method that utilises a Digital Micro-Array Device (DMD) to generate the photomasks for layer-by-layer photopolymerisation of materials [54]. The mirrors allow selective exposure of UV light to photopolymerise the desired section for each layer, see Figure 4.

Typically stereolithography is slower than FDM due to curing taking up time. However it's consistently capable of small layer thickness down to 16 μm on many different printers [86]. It's also possible to print volumes up to 650 x 600 x 400 mm³ [87], although volumes like 51.2 x 38.4 x 100 mm³ [88] are more typical for desktop printers.

In the scope of this review, DOPsL was used to print a Hydrogel Polymer [54]. DOPsL is applicable to UV curable materials; this means that it can be applied to hydrogels or photopolymers.
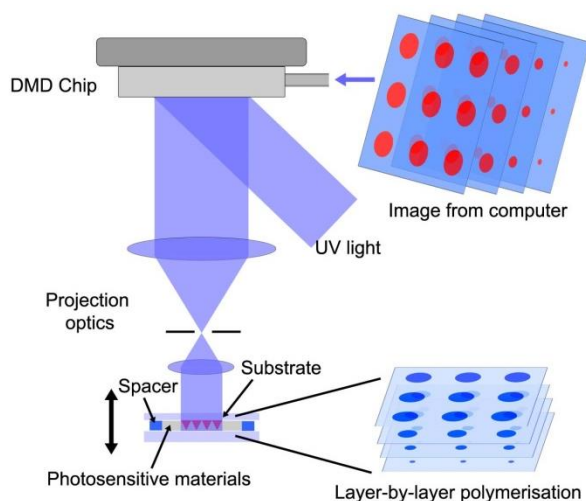
Figure 4 Schematic Diagram of Dynamic Optical Projection Stereolithography: UV-light illuminates the DMD mirror system, which generates an optical pattern according to the image flow from the control computer. The optical pattern is projected through optical lens and onto the photosensitive material to fabricate a 3D scaffold [89].

2.2.2.5 SLM – Selective Laser Melting

SLM is an AM metal powder bed process [90]. Successive layers of metal powder are deposited on top of one other and each layer has a laser scanned over it. As the SLM process proceeds, the laser scans along tracks of material which overlap and fuse [91]. As melted powder solidifies, it fuses itself to the layer deposited below. This is repeated for successive layers to make a 3D object, as in Figure 5.
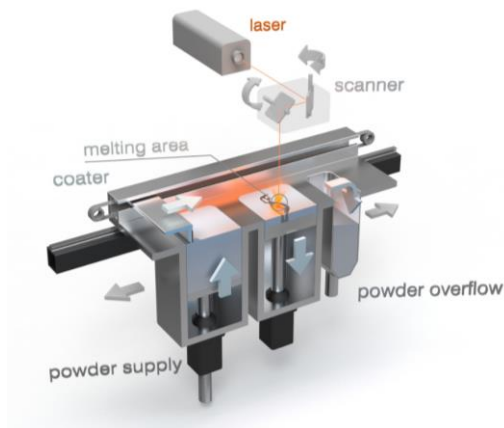
Figure 5 This LaserCUSING Diagram illustrates Concept Laser GmbH's SLM Technology [26].

Volumes as large as 600 x 400 x 500 mm^3 can be built this way [92] with layers as small as 15 microns thick [26]. Printable materials are mostly metal alloys such as Ti, Al, steels and refractory metals like CoCrMo [93]. Other specific examples are given in Table 4.

Table 4 There are a variety of alloys and materials currently utilised in SLM including [90, 94]:

Titanium	Aluminium	Tool Steel	Ni Super Alloy	Stainless Steel	Refractory
Ti-6Al-4V	Al-Si-Mg	H13	IN625	SS316, SS316L	Mo-Re
ELI Ti	AA6061	Cermets	IN718	SS347	Ta-W
CP Ti				SS420	CoCr
Γ-TiAl				17-4 PH	Alumina

Similarly, in this review, SLM was only used to print metals and alloys [55], as the high temperatures of this process make many materials, like polymers, incompatible and unbuildable.

A major disadvantage of the SLM process is the poor surface finish it produces [94]. When layer thickness and particle diameter are similar there is a potential for particles filling gaps between consecutive layers, increasing the surface roughness.

The "stair-step" effect is the stepped approximation that occurs when building inclined planes and curves using layers of finite thickness [94], as illustrated in Figure 6. This effect is present, to some extent, in most AM processes. One of the consequences of the "stair-step" effect is the additional cost of post-processing it introduces.
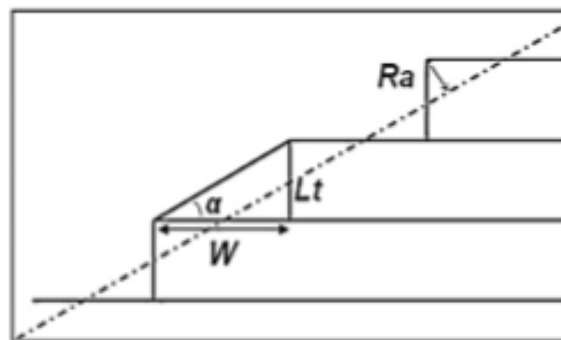
Figure 6 Schematic representation of sliced profile. The dash dotted line represents the mean location of the surface [94].

It follows that improved surface finish occurs when finer layer thicknesses are implemented [94]. Surface roughness is also expected to decrease with increasing inclination angle based on Eq. *1*. This is clearly inadequate based on the experimental data of Strano, G. et al in Figure 7 [94], who noted that the stair-step effect was not observed above a 50° inclination.

$$R_a = \frac{1}{L}\int_0^L |y(x)|\, dx = \frac{1}{4}L_t \cos(\alpha) \qquad \textit{Eq. 1 Surface roughness of an inclined plane [94].}$$
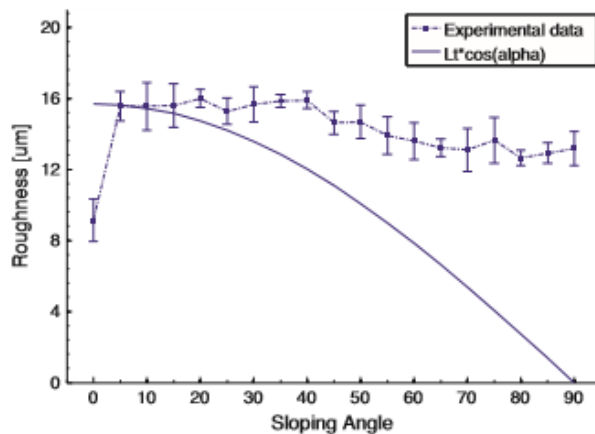
Figure 7 Comparison of experimental roughness and simulated roughness according to
Eq. 1 [94].

Where Eq. *1* most likely goes wrong is failing to incorporate the impact of poorly bonded particles on the edges of each step [94].

During SLM, each passing scan of the laser induces high thermal gradients within the melt pool [94]. When different volumes of the melt have high thermal gradients, it leads to surface tensions that produce Marangoni convection. This involves radial mass transfer to the melt pool surface such that the periphery melt pool breaks off into solid spheres of material scattered on both sides of the pool. This "balling" phenomenon limits the resolution of the SLM method by introducing discontinuous cracks in sharply detailed geometries; it can also cause delamination due to non-uniform deposition from layer to layer. In practice this decreases part density and increases surface roughness. Solutions all involve reducing the thermal gradient. This may be achieved by increasing the fluid viscosity and heating the powder bed. Another practical solution is to have adjacent laser tracks to overlap sufficiently to remelt any balling which may have occurred – which only fails for the final track. As such, the "balling" phenomenon has a greater impact on side roughness than top roughness due to the lateral scattering to both sides of the melt pool [95]. Strano, G. et al also observed that as the inclination angle increases the particle concentration stuck on the edge has been observed to increase [94].

The following formulae are useful for determining a value for surface roughness [94].

$$R_a = \frac{1}{L}\int_0^L |f(x)|\, dx$$
Eq. 2 1D surface roughness using continuous data

$$R_a \approx \frac{1}{N}\sum_{i=1}^N |f_n|$$
Eq. 3 1D surface roughness using discrete data

$$S_a \approx \frac{1}{NM}\sum_{i=1}^N \sum_{j=1}^M |f_{ij}|$$
Eq. 4 2D surface roughness using discrete data

To

Figure

Even

Limitations

Increasing the laser power can substantially increase the scan rate to achieve the same energy density as lesser laser powers. According to $V = \Delta y_s \times D_s \times v_{scan}$ *Eq. 5*, this would result in higher build-up rates [96].

$$\dot{V} = \Delta y_s \times D_s \times v_{scan}$$
Eq. 5 A standard formula to determine the build-up rate [96]

Current machines use lasers with wattages in the range of $400 - 700$ with some outliers outside this range [97].

SLM has various applications as observed in the literature, which include:

- Rapid prototyping [98]
- Dental restorations – CoCr [96]
- Hip implants – Titanium Alloys [96]
- Pneumatic valve – AlSi10Mg [96]
- Surgical instruments – Titanium Alloys [96]

A useful table of advantages and disadvantages for the SLM table can be made with reference to materials produced by Bremen S., et al. and Strano G., et al. [94, 96], see Table 5.

Table 5 The Advantages and Disadvantages of SLM according to the literature:

SLM Advantages [96]	SLM Disadvantages [94, 96]
No part-specific tooling needed.	Insufficient production speeds for industry
Hollow structures possible	Shallow or steep inclinations are problematic
High Surface Area (High Surface Roughness)	Poor Dimensional Accuracy (High Surface Roughness)
Adapted rigidity	
Graded Porosity attainable	

2.3 CATALYST IMMOBILISATION & AM MATERIALS

A primary concern for combining AM and catalysis is the immobilisation of the catalyst [47, 66]. Immobilising the catalyst species is invaluable to many chemical processes [47, 66]. The advantages include ease of recovery, recycling of the catalyst species and improved catalytic performance due to the presence of a solid support [99]. This solid support may provide chemical, thermal and mechanical stabilisation of the catalyst species [70, 99].

Heterogeneous catalysts are sophisticated materials which can be prepared by many procedures. Detailed studies on heterogeneous catalysis have been disclosed in the literature [100-105] during the last 50 years. As such this review focuses only on conventional methods for heterogeneous catalysis where they have been applied to AM structures.

In the conventional preparation of catalysts, immobilisation methods tend to focus on anchoring catalysts to supports rather than the interior surfaces of reaction vessels. Not only is AM effective at printing microfluidics [30, 31, 34, 39-41], but it's able to print 'reactionware'. A term used to describe AM structures made specifically for chemical reactions.

In the literature two strategies are used to immobilise catalysts into or onto reactionware. The main strategy for immobilising catalysts in AM structures is 'Integration': To include the catalyst species within an already-valid build material prior to the printing process or to use it as the building material outright. The less common

strategy is 'Functionalisation': coating the AM material with a catalyst as a post-treatment process.

A list of references where authors have applied AM to a catalytic reaction by integration is compiled in Table 6 and a similar list of references for AM applied to a catalytic reaction by functionalisation is compiled in Table 7.

Table 6 All known AM systems used for heteregeneous catalysis by integration in literature

Catalyst/Support – Substrate	AM Technologies	Reactions*	Ref.
Cu/Al_2O_3	Robocasting	3 Ullmann reactions	[47, 66]
Pd/C – Toluene-thinned acextoxysilicone	Robocasting	Styrene hydrogenation (Ethylbenzene synthesis)	[1]
Carbon Black – Toluene-thinned acextoxysilicone	Robocasting	Phosphomolybdic acid reduction	[1]
$BaMn_2Al_{10}O_{19-\alpha}$	Robocasting	Methane oxidation	[67]
GOx, HRP – Hydrogel	Robocasting	o-Phenylenediamine oxidation (by H_2O_2)	[70]
TiO_2 Nanoparticles	InkJet Printing	Methylene blue decomposition	[83, 84]
TiO_2 – Soda-lime glass	InkJet Printing	Dichloroindophenol decomposition	[85]
Ni, Fe, Co, Al, Cu, Sr, Cr, Zn metal oxides – FTO glass	InkJet Printing	Hydrogen & oxygen evolution (Photochemical & Photoelectrochemical)	[57]
Ni, Fe, Co metal oxides – FTO glass	InkJet Printing	Hydrogen & oxygen evolution (Electrochemical)	[58]
Ni, Fe, Co, Ti metal oxides – FTO glass	InkJet Printing	Oxygen evolution (Electrochemical & photoelectrochemical)	[59, 60]
Mg, Ni, Mn, Cr, Cu, Fe, Co, Ti metal oxides – Glass	InkJet Printing	Hydrogen evolution (Photochemical)	[61]
Fe, Cu, Cs, Nd, Co, Al metal oxides – FTO glass	InkJet Printing	Hydrogen & oxygen Evolution (Photoelectrochemical)	[62, 63]
Ti, Si, Al doped α-Fe_2O_3 – conductive glass	InkJet Printing	Oxygen evolution (Photoelectrochemical)	[64]
Ir, Ru, Pt, Rh, Pd, Mn, Al, Nb, Sn metal oxides – FTO glass	InkJet Printing	Oxygen evolution (Electrochemical)	[65]
TiO_2 – polymer	FDM	Rhodamine 6G decomposition	[79]
Polydiacetylene (PDA) nanoparticles – polyethylene glycol diacrylate (PEGDA) hydrogel matrix by addition polymerisation	DOPsL	Melittin toxin capture	[54]

*FTO glass is F-doped Tin Oxide coated glass, it's a conductive glass

**Polydiacetylene (PDA) nanoparticles – polyethylene glycol diacrylate (PEGDA) hydrogel matrix by addition polymerisation

Table 7 All known AM systems used for heterogeneous catalysis by functionalisation in literature

Catalyst/Support – Substrate	AM Technologies	Reactions	Ref.
$BaMn_2Al_{10}O_{19-\alpha}$ – α/Al_2O_3	Robocasting	Methane oxidation	[67]
ZSM-5 – 316L Stainless Steel	Robocasting	Methanol dehydration	[68]
ZSM-5 – Ti6Al4V Titanium Alloy	Robocasting	N_2O decomposition	[69]
Ni/Al_2O_3 – 316L Steel	Robocasting	CO_2 methanation	[106]
Gold & Silver Paint – Polypropylene	FDM	Electrolysis of water	[53]
IrO_2 – Stainless Steel	SLM	Oxygen evolution	[55]

These strategies will now be explored with respect to all the tabulated references (see Table 6 and Table 7) with an emphasis on the improvements AM has made possible with respect to controlling the catalytic reaction outcomes.

2.3.1 Integration Strategy

In the case of Robocasting, 'inks' of appropriate viscosities are needed for printing. Multiple authors have taken this into account when designing immobilised catalysts by the integration strategy. The complexity of catalyst integration in the build-stock can vary, authors such as Tubío, C.R., et al. [47] designed their robocasting 'ink' completely from scratch with no apparent reference to previously printable materials. Their 'ink' consisted of Al_2O_3 powder dispersed in 2.56M $Cu(NO_3)_2.2.5H_2O$ mixed with a viscosity modifier, hydroxypropyl methylcellulose, and then successively mixed with a cationic polyelectrolyte poly(ethylenimine) as a chelating agent to bind the ink. The woodpile structure produced by this material is an open, porous structure with a high surface area to volume ratio. The application of Robocasting has enabled the efficient, uniform distribution of the catalyst such that the entire surface is catalytically active. 3 Ullman reactions performed under various conditions demonstrated yields from 78% to 94% [47].

Stuecker et. al. [67] are yet another group who have effectively implemented Robocasting to print immobilised catalysts. Unusually, this group independently

employed both integration and functionalisation strategies for immobilising their catalyst, the latter of which will be spoken of under the functionalisation strategy heading. This group directly printed barium manganese hexaaluminate ($BaMn_2Al_{10}O_{19-\alpha}$) using Robocasting to make robocast FCC lattices that were capable of 100% conversion of methane by oxidation with excess oxygen in a continuous stream connected to an online Gas Chromatograph at 700°C.

A simpler approach has been demonstrated by Symes et. al. [1] whose work in reactionware involved extensive use of an acetoxysilicone polymer, sourced from "Loctite 5366 bathroom sealant". Catalyst integration was enabled by modifying this acetoxysilicone polymer with toluene to thin the ink and then load Pd/C until a paste appropriate for printing was made.

A reactionware vessel robocast from the Pd/C-loaded acetoxysilicone polymer was found useful for a reaction of 4-methoxyaniline with 5-(2-bromoethyl)phenanthridinium bromide [1]. The printed reactor volume in proportion to the reactants was used to control the reactant's stoichiometric ratios. Different primary products were procured this way. Both $C_{22}H_{20}N_2O$ at 80% conversion and $C_{21}H_{17}BrN_2O$ at 90% conversion were independently produced using reactor geometry to switch the primary product as can be seen in Figure 9.
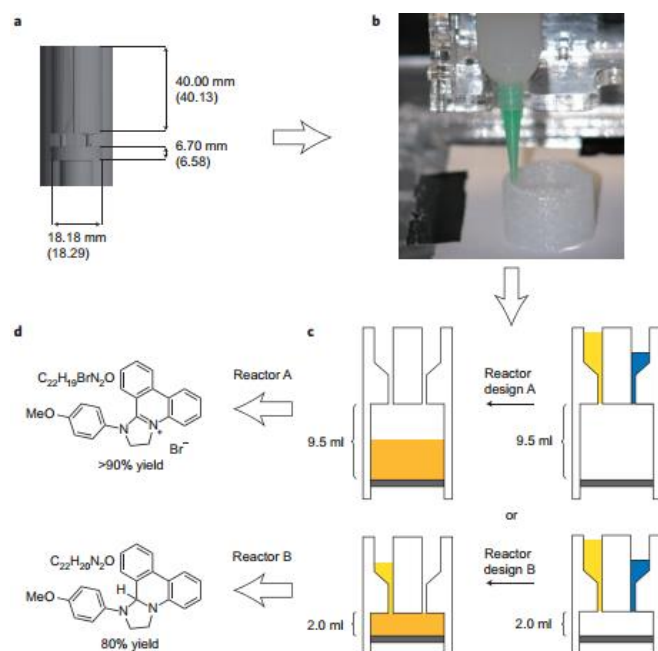
*Figure 9 A workflow for printing reactionware. **a**, A schematic for one of the AM vessels used for chemical reactions by Cronin and co-workers. **b**, A photograph of reactionware being printed. **c**, Different reactor designs can be created easily and rapidly, which allows the impact of design on outcome to be explored. **d**, Two different products can be produced selectively from a single reaction based on 'reactionware' design [1].*

AM allows for the combination of various design elements to enable well-integrated designs. The same authors [1] also produced electrochemical cells with robocasting by printing the reactionware walls with acetoxysilicone. Two parallel lines were printed on the base from toluene-thinned acetoxysilicone that incorporated carbon black, these conductive lines were connected to the relevant electrodes to enable reduction of a 5mM solution of Phosphomolybdic Acid (PMA) in 0.1 M H_2SO_4 with a -2.5 Voltage applied. The yellow solution began turning blue around the electrode in a few minutes, indicating that reduction was occurring.

Whilst uncommon, some authors have demonstrated enzymatic catalysis using a method similar to robocasting [70]. Wei et. al. printed a hydrogel mixed with a dual enzymatic system of GOx (Glucose oxidase) and HRP (Horseradish peroxidase) which, after printing, catalyse the cross-linking of the hydrogel into a structure that integrates the GOx and HRP catalysts adjacently. This combination of chemistry and AM allows the 3D construction of enzymatic catalysts within a hydrogel with a complex

configuration and excellent mechanical properties. Aside from significantly improved mechanical strength due to the cross-linking, this structure was superactive for the oxidation of o-phenylenediamine by H_2O_2.

Inkjet printing for catalysis is strongly focussed on metal oxide compositions in the literature. Metal Oxides are well known to have potential as active or supporting species in catalysis [107-109].

Metal oxides have been successfully incorporated in InkJet inks and it is common for the colloidal systems to consist of 1-30% metal precursor, 50-60% liquid carrier and 1-10% additives [50]. The liquid carrier influences the ink properties most and serves as a medium to dissolve or disperse the metal species precursor. Aqueous inks have low viscosity and high surface tension compared to non-aqueous inks; they are of low toxicity, inexpensive and stable. Unfortunately, these low drying rates make printing slow. The rapid drying rate of non-aqueous inks is great for print speed and therefore better for multilayer printing [50]. The metal species precursor forms reported include metal salt solutions [110], colloidal suspensions of metal oxide nanoparticles [111] and colloidal nanoparticles based on sol-gel chemistries [112].

Arin et. al. [83, 84] synthesized TiO_2 nanoparticle suspensions that were used in an ink for InkJet printing of homogenous TiO_2 coats on glass substrates. These coats were catalytically active for the decomposition of methylene blue under UV illumination. Likewise, Černá, M. et. al. also synthesized TiO_2 photocatalysts for printing with a modified InkJet printer [85].

In Černá, M. et. al.'s method [85] an absolute ethanol/acetyl-acetone mixture was added dropwise to titanium (IV) isopropoxide under continuous stirring to control the hydrolysis and condensation reactions. Maintaining solution developed the complex chelate. Further dropwise addition of an absolute ethanol/water mixture began the hydrolysis and condensation reactions. Polyethylene glycol (PEG) was added in different concentrations (0, 1, 4 and 16g/L).

Soda-lime glass substrates of 50 mm x 50 mm x 1.1 mm dimension were treated with sulphuric acid to prevent sodium ion diffusion then cleaned with a surfactant solution

[85]. An office inkjet printer, 'Epson R220', was cleansed with anhydrous propanol in all of its' ink tubing/canisters. The prepared sols were filtered via 0.45µm syringe filters into printing cartridges that were placed into the black cartridge position for printing purposes. A specialised holder held the glass substrates in place for grayscale printing, a method that enables position-controlled sol loading for selective catalyst concentration control. The catalyst was dried at 110°C for ½ h before calcination at 450°C for 4h (Ramp 3°C/min).

Photocatalytic degradation of 2×10^{-5} Molar aqueous 2,6 Dichloroindophenol (DCIP) was tested in a batch setup [85]. A mercury lamp supplied $10W/m^2$ for 10 minutes prior to the reaction. Every 5 minutes 2mL of reaction solution was sampled for UV-Vis analysis over a period of 30 minutes during which substantial degradation of the DCIP occurred, indicating the success of this material for demonstrating photocatalytic activity.

Perhaps most interesting is the development of brute force catalyst investigation techniques applicable to InkJet printing, whereby Katz. et. al [57] was able to print 252 metal solutions of mixed metal oxides for potential photo electrodes in one print. 8 other papers like this [58-61] also look at reactions pertaining to water electrolysis; as such a brief description of this overall reaction is included.

Electrolysis leads to the decomposition of water into oxygen and hydrogen gas [113], it involves the placement of two or three electrodes in a water-based electrolyte under an applied voltage bias and/or catalyst-activating light source. There are several relevant full and half equations of electrolysis under both acidic and basic conditions provided in Millet, P. et al.'s work [113].

There was little variation in the strategies implemented by the authors to design the 'inks' for inkjet printing of mixed metal oxide catalysts for water electrolysis. Most groups used aqueous metal nitrate precursors and metal chloride precursors with some use of metal oxalate and metal oxide precursors. Ethanol was used almost exclusively as a solvent, although Isopropanol and a 'Base ink stock' were also used. pH modifiers were the most varied element of the ink composition; acetic acid, ammonium nitrate, hydrochloric acid and nitric acid were included. Most of the

authors included a Shape directing agent (SDA), the polymer Pluronic F127, to improve printability and a couple of groups included surfactants and viscosity modifiers of diethylene glycol monobutyl and diethylene glycol respectively. This is all shown in Table 8. Every group referenced here, used drying and/or calcination to stabilise their catalyst [57-65]. The deposition substrate for all groups found was a conductive Fluorine-Doped Tin Oxide Glass [57-60, 62-65] bar one group who used uncoated glass [61] due to their testing of photocatalysis in isolation from electrocatalysis.

The trend of metal oxide inkjet catalyst synthesis is the continued improvement of throughput. Xiang et. al. [58] was able to print 231 unique mixed metal oxides of Ni, Fe and Co for screening in the photo-electro catalysis of the oxygen evolution and hydrogen evolution reactions. They could effectively isolate active compositions from 231 catalyst permutations within a minute using their electrochemical cell and the bubble screening method.

High throughput screening was also employed by Gregoire et al.'s group [59, 60] whose work explored the quaternary oxide library of (Fe Co Ni Ti). 5456 mixed metal oxides compositions were deposited on (FTO)-coated glass plates for serial screening by their custom-made scanning droplet cell to identify catalysts active for the oxygen evolution reaction. They could process one sample every 4 seconds.

Arguably the most impressive of all these examples is the work of Liu et. al. [61], in which a modified InkJet Printer could print up to 1,000,000 sol-gel catalyst formulations with up to 8 components per hour. This setup was used by the author in conjunction with multi-dimensional group testing (m-GT) to find several active catalyst species for hydrogen evolution by photo catalytically reforming a formaldehyde-water solution. 5000 catalyst species of quaternary mesoporous metal oxides $Mg_xNi_yCu_zTi_{1.0}O_w$ (0 < x, y, z < 1.0) were printed and split into 8 groups of 625 each. Each set of 625 catalyst formulations underwent batch testing in their respective groups. The photocatalytic hydrogen production was determined by Gas Chromatography after these batch reactions [61]. In their first iteration, Group 4 was most active and a further 5000 compositions were subdivided into this groups' scope

($Mg_{0.5-1}Ni_{0-0.35}Cu_{0.5-0.9}Ti_{1.0}O_w$). After the 4th iteration of this method, optimal catalyst compositions were settled upon by the authors as shown in Figure 10.

What the latter setup makes clear is that inkjet printing enables catalyst production at a quicker rate than available catalyst screening methods can match. The bottleneck for metal oxide catalyst exploration lies in high throughput catalyst screening rather than high throughput catalyst synthesis.

In the Hydrogen and Oxygen evolution reactions, photocatalysts [57, 61], electrocatalysts [58-60, 65] and photoelectrocatalysts [57, 59, 60, 62-64] have been demonstrated and ranked through various screening processes. The reaction setups correspond to which of these three latter catalyst types are being sought out.

For photochemical catalysis, there is the example of Liu et. al.'s work [61] and Katz. et. als' work [57]. Photocatalytic reformation of a formaldehyde-water solution was chosen by Liu et. al. as an efficient, low-cost batch reaction [61]. The reactions used 40mg of photocatalysts placed in 10mL of 2wt.% aqueous formaldehyde solution under constant stirring. The formaldehyde solution was N_2-treated to remove all traces of dissolved oxygen. The reaction was performed under side irradiation by a 300W Hg lamp at 25°C. GC-TCD (Gas Chromatography with Thermal Conductivity Detector) was performed to confirm oxygen removal by the N_2 pre-treatment and measure the extent of H_2 evolution quantitatively. GC-TCD was the effective quantitative screening instrument but it was the use of multi-group testing, described earlier, that enabled a 25,000-fold increase in the screening rate compared to exhaustive one-by-one screening.
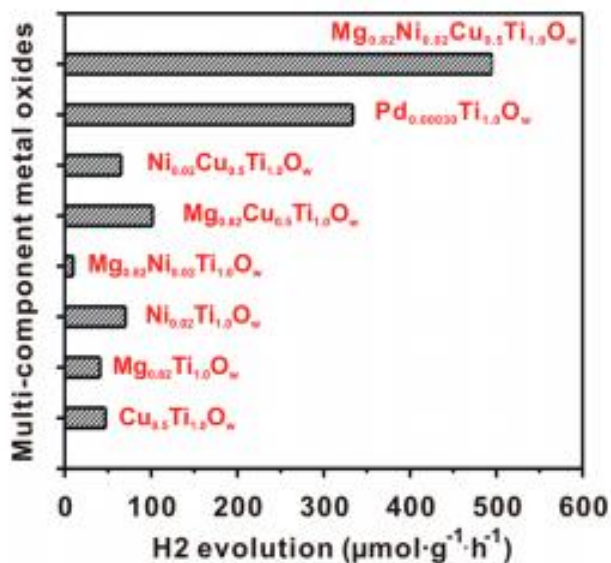
Figure 10 Photocatalytic hydrogen evolution during the liquid-phase reforming of formaldehyde-water solution over optimised $Pd_{0.00030}Ti_{1.0}O_w$, new quaternary catalyst $Mg_{0.82-}Ni_{0.02}Cu_{0.5}Ti_{1.0}O_w$ and binary and ternary combinational materials, in Liu et. al.'s work [61].

Table 8 Inkjet Ink Compositions for Catalysts in the Literature

Metal Oxide Precursors			
Nitrates [57-65]	Chlorides [59-61, 63-65]	Oxalates [65]	Oxides [61]
pH modifiers			
Acetic Acid [57, 58, 61]	Ammonium Nitrate [62]	HNO$_3$ [58-62]	HCl [59-61]
Solvents			
Ethanol [58-61]	Isopropanol [61]	Base ink stock [57]	
Shape Directing Agent	Viscosity Modifier	Surfactants	
Pluronic F127 [58-61]	Diethylene Glycol [63, 64]	Diethylene Glycol Monobutyl [63, 64]	

Katz. et. al. printed a slide of compositions to make a library of catalysts that is mobile through the action of a stepper motor over the X-Y and X-Z planes depending on the specific setup used [57]. The whole library is submerged in 1 M KOH$_{(aq)}$ and the catalysts are the effective working electrode with a Pt gauze as the counter electrode in a 2-electrode configuration. No biases are applied, instead a 150 W Xe Arc lamp provides illumination to the individual catalyst compositions and induces photocurrents whose polarity and intensity indicate whether they are active for

oxygen or hydrogen evolution. In a different setup, each sample is electrically isolated and individually connected to a custom PCB for simultaneous measurement of both the photopotential and the photocurrents of each catalyst. This parallel screening setup may allow for more rapid screening.

There are also a couple of examples of electrochemical catalysis and screening thereof [58, 65] in AM. Methods such as bubble screening [58], optical screening and pH sensitive fluorescence screening [65] have been implemented.

In Xiang et. al.'s paper electrolysis of water using a 3-electrode system with the catalysts as the working electrode was performed for several catalysts simultaneously [58]. The static aqueous solution contains TiO_2 to nucleate larger bubbles of both oxygen and hydrogen to make them more visible to the camera, with side lighting provide by LED's. At the catalyst surfaces oxygen bubbles evolve, at the Ni mesh counter electrode hydrogen bubbles evolve directly above the catalyst. Bubble screening uses binary thresholding of photos taken by a camera over time to distinguish the relative intensities of the oxygen produced by each catalyst composition. This technique is quick because it is parallel, enabling many catalysts to be tested at once. It is however, limited by the resolution of the camera & the size of the container. Figure 11 by Xiang et. al. clearly illustrates their bubble screening setup.

pH sensitive fluorescence was used by Seley et. al. [65] to screen for oxygen evolution catalysts in water electrolysis under acidic conditions. They consider ternary and quaternary mixtures of metal oxides of 5 noble metals: Ir, Ru, Pt, Rh, Pd and other metal oxides of Mn, Al, Nb and Sn. The screening method uses a pH sensitive fluorescence indicator "3-(2'-pyridyl)-[1,2,3]-triazolo[1,5- a]pyridine, (PTP)" that, because of its' chemistry, fluoresces after a short delay when adjacent to more active oxygen evolution catalysts in the acidic aqueous solution. Seley et. al. [65] conclude that small Rh additions to IrO_2 enhances its' activity but emphasize the vast number of electrocatalysts combinations that remain to be explored.
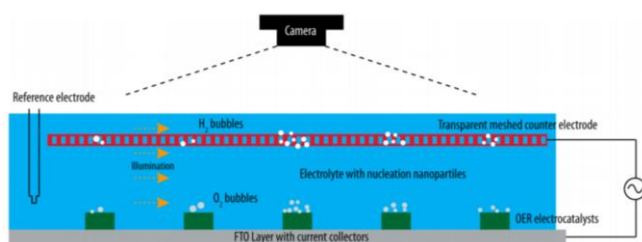
Figure 11 Cross-sectional schematic illustration of the bubble screening setup, where the green rectangles represent the testing material library, the red bars represent the transparent meshed counter electrode [58].

Most electrolysis catalyst screening methods in AM are photoelectrochemical; a Novel Scanning Droplet Cell [59, 60] was the most well-integrated setup found for linear sampling and a group of 3 papers [62-64] used electrochemical cells with impinging lasers for the photocatalytic testing.

The scanning droplet cell designed by Gregoire et. al. [59] delivers an electrolyte solution to isolated catalysts printed on conductive glass, see Figure 12. The electrolyte used is an O_2-bubbled 0.1 M NaOH aqueous solution. Cyclic voltammetry is performed on the solution contacting the catalyst. The experiment involves the use of an internal counter electrode in port F, the working electrode, which is the catalyst resting on conductive glass, and an internal capillary Ag/AgCl reference electrode which is inserted through port E. The cycling was carried out at 1 V.s-1 from -0.09 V to + 0.51 V with respect to the O_2/H_2O Nernst potential. A 2-axis translation stage was used to raster the scanning cell over the entire catalyst library. Measurement of the currents that result from the cyclic voltammetry give an indication of the relative activity of each catalyst for the oxygen evolution reaction. This same setup was used for photoelectrochemistry with the inclusion of a 2.5mW 385nm LED that flashes on and off with a 2Hz square wave profile.
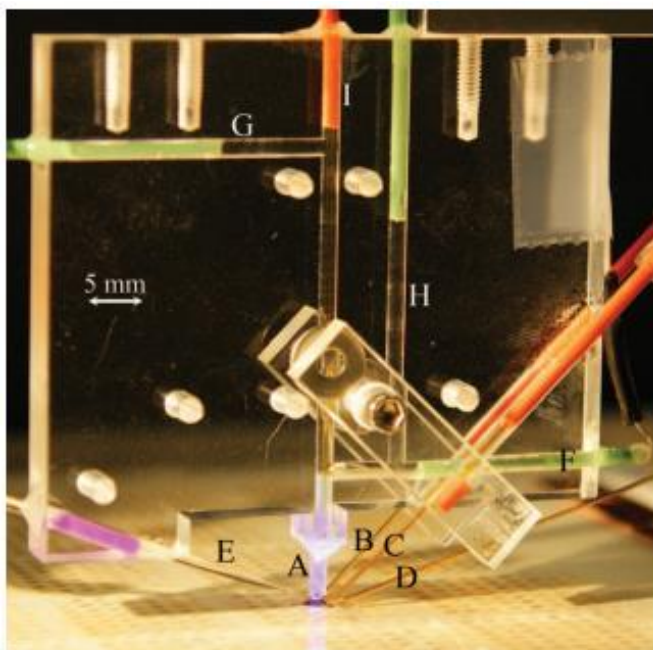
Figure 12 A photograph of the scanning droplet cell suspended over a composition library. The drop of solution at the bottom of the cell contacts a 2.5 mm-diameter region of the working electrode containing a single 1mm square sample. Nine ports (labelled A through I) are used for the solution flow and insertion of electrode and fibber optic illuminates the working electrode and produces a visible purple glow in the port A PTFE tube [59].

Gregoire et. al. used a similar setup in another paper but also performed high throughput optical screening therein [60]. Their method involved transmitting light through the catalyst and conductive glass into an integrating sphere coupled with a UV-Vis spectrometer to check photon energy ranges absorbed by the catalyst so as to identify its' effective bandgap energy.

Parkinson et. al. have 3 papers with essentially the same core elements in their methods [62-64]. An FTO glass slide was connected as the working electrode with an on-printed catalyst library in a 2-electrode configuration to a potentiostat. Pt wire looped around the perimeter of the calcined substrate acts as both a reference and a counter electrode. The glass slide was immersed in a 0.1 M NaOH aqueous solution for the electrolyte whilst positive and negative biases were applied to the substrates to check for oxygen and hydrogen evolution activities respectively [62-64]. This was performed under exposure to varying laser wavelengths, such as 514.5nm, 532nm and 632.8nm lasers. As with Katz et. al.'s work [57], the measured photocurrents for each

laser-rastered catalyst on the working electrode gave an indication of their relative activity for oxygen and hydrogen evolution reactions.

In their earliest work the measured photocurrents indicated that compositions near the Fe-Cs binary with small Cu or Nd additions were effective as oxygen evolution catalysts [62]. In further work Woodhouse et. al. [63], increased their metal nitrate concentrations. This enabled their isolation of an Fe, Co, Al oxide as a potentially effective photo anode for photo electrolysis of water [63]. He et. al. [64] investigate the effects of Ti, Si and Al dopants on α-Fe_2O_3 Photo anodes with laser induced photocurrent screening, finding that inclusions of Ti or very small inclusions of Si improve photo anodic activity of α-Fe_2O_3 catalysts.

Researchers using an FDM printer loaded with a polymer containing a TiO_2 powder dispersion managed to print a sponge-like structure. The TiO_2 inclusion remained active after printing and could demonstrate photocatalyzed degradation of Rhodamine 6G in solution. The researchers note that the maximum printable loadings of 10% TiO_2 achieve lower activity than higher loadings would enable. This makes catalysts integrated into FDM difficult to implement effectively.

The importance of properly anchoring catalyst materials to stabilise them and avoid secondary effects is expressed well in the work of Gou, M., et al. [54]. Their work uses a variant of Stereolithography called Dynamic Optical Projection Stereolithography (DOPsL) that utilises a digital micro-array device (DMD) to generate photomasks for layer-by-layer photopolymerisation of biomaterials. A modified liver lobule-configuration was printed out of photo cross linkable poly(ethylene glycol) diacrylate (PEGDA) hydrogel. The polydiacetylene (PDA) nanoparticles were synthesized from a mixture of 10,12 pentacosadiynoic acid (PCDA) and PCDA acrylamide (PCDA-A). These nanoparticles were chemically tethered, 'functionalised', by their acrylamide groups to the PEGDA hydrogel by addition polymerisation, see Figure 13.

AM by DOPsL enabled the production of remarkably complex liver-mimetic structures with features as fine as 10's of microns, see Figure 14.
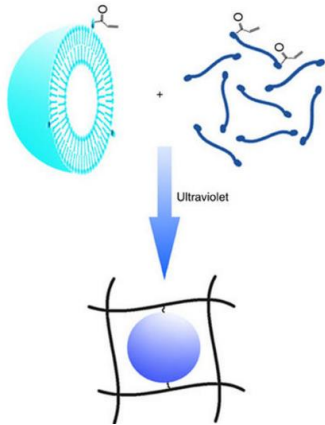
Figure 13 Schematic presentation of installing PDA nanoparticles in the network of PEGDA hydrogel. PDA nanoparticles are chemically linked to the PEGDA hydrogel network by photo crosslinking PEGDA monomer and acrylamide-modified PDA nanoparticles via addition polymerization [54].
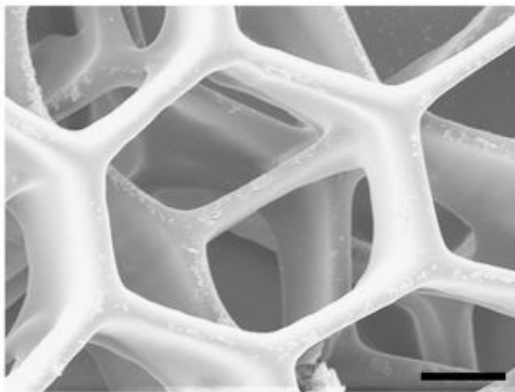
Figure 14 SEM micrograph of Gou, M. et. al.'s liver-mimetic structures made using DOPsL, the scale bar is set at 50 μm [54].

The purpose of these structures embedded with nanoparticles was to attract and capture melittin, a pore-forming toxin (PFT). Naturally this means that the nanoparticles must not dissociate from the PEGDA as that leads to secondary poisoning of the liver due to their aggregation [54]. Gou, M., et al. could achieve almost complete neutralisation of the undesired, haemolytic activity of the melittin without dissociation, as illustrated in Figure 15.
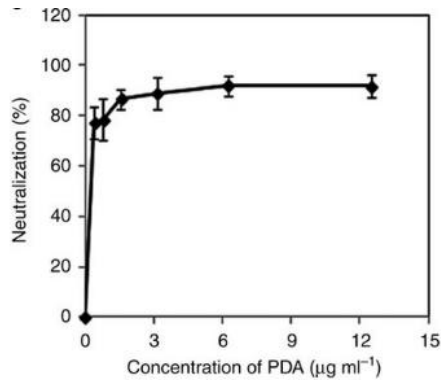
Figure 15 Quantified efficiency of neutralizing the haemolytic activity of melittin (5 µg ml−1) by PDA nanoparticles [54].

2.3.2 Functionalisation Strategy

In Ambrosi et. al.'s work [55] is demonstrated one of the only Functionalisation catalysts applied to an SLM substrate in the literature, although Yang et. al's work [114] looks like an SLM substrate they don't actually specify the printing method used. Their Ni alloy is simply described as a "3D printed Ni scaffold". Nonetheless Ambrosi et. al. uses cyclic voltammetry to apply IrO2 coatings to steel SLM substrates [55]. The powder bed approach of SLM enabled the printing of helices with significantly reduced material waste compared to subtractive manufacturing methods. The three applications of their catalyst were the Oxygen Evolution Reaction, Pseudo-capacitance functionality and a Nernstian pH sensor.

The procedure for functionalisation by cyclic voltammetry requires the preliminary printing of a steel SLM electrode for the substrate material [55]. An IrO_2 precursor was made from 75mg of $IrCl_4.H_2O$ in 50mL of Water in a 100mL beaker dissolved by stirred over 10 minutes. 180 mg Oxalic Acid was added and dissolved by 10 minutes of stirring. 450 µL H_2O_2 (30 wt.%) was added as an oxidising agent before pH was adjusted to 10.5 by using small volumes of $Na_2(CO_3)$. This solution was heat treated at 65°C for 2 hours to accelerate stabilisation of the deposition solution then refrigerated for storage. The steel was immersed in this solution in the presence of an Ag/AgCl wire reference electrode and a Pt foil auxiliary electrode. Potential scans ranging from -0.6 V to + 0.6 V with scan rate 0.05 $V.s^{-1}$ were repeated 200 times to allow deposition of an IrO_2 coat on the steel electrode. Aside from reduced material wastage during printing, the
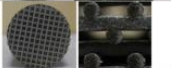
primary advantage of SLM here is the increased surface area the stainless steel has due to the processing nature of SLM.

Robocasting is the dominant AM technology for producing substrates for catalytic functionalisation. It is mostly used to produce stacked fibres oriented 90° to each other with each subsequent layer [67-69, 106]. 1-1 [68, 69, 106] and 1-3 [67, 68, 106] woodpile configurations for the fibre layering are common, although one author used a '1.3.5' configuration [69], the former 2 are illustrated in Table 9.

Structures like this are easier to produce by AM, and they are chosen to enhance the specific surface area of the catalyst and are demonstrably effective at doing so [67-69, 106].

In addition to directly printing barium manganese hexaaluminate ($BaMn_2Al_{10}O_{19-\alpha}$) using robocasting, Stuecker et. al. [67] also printed substrates made from highly pure (99.8%) Al_2O_3 that they sintered at 1650°C then functionalised with barium manganese hexaaluminate. The catalyst precursor was co-precipitated from Ba, Mn and Al salts after which were calcined at 1300°C before mixing as 15 vol.% catalyst in an aqueous slurry which is consequently dispersed in an ammonium salt of polyacrylic acid. The gas displacement method was used to clear blockages of this washcoat from the channels of the robocast monoliths, concluded by calcination at 1300°C to guarantee secure bonding of the washcoat to the substrate. Regardless of catalyst loading the robocast catalyst ($BaMn_2Al_{10}O_{19-\alpha}$) was more active than the robocast pure alumina wash coated with catalyst. The temperature sensitive activity demonstrates the dependence of conversion on ($BaMn_2Al_{10}O_{19-\alpha}$) loading clearly in Figure 16.

Table 9 Structures prepared by Lefevere et. al. for catalytic testing [68]. Reprinted from Catalysis Today, Vol.216, Jasper Lefevere, Marijn Gysen, Steven Mullens, Vera Meynen, Jasper Van Noyen, The benefit of design of support architectures for zeolite coated structured catalysts for methanol-to-olefin conversion, pp. 51-55, Copyright (2013), with permission from Elsevier.

Sample	ZSM-5 loading (g/cm³)	Support surface (cm²/cm³)	Average coating thickness (µm)	Image
3DFD 1-1	0.12	29.5	19	
3DFD 1-3	0.13	29.5	20	
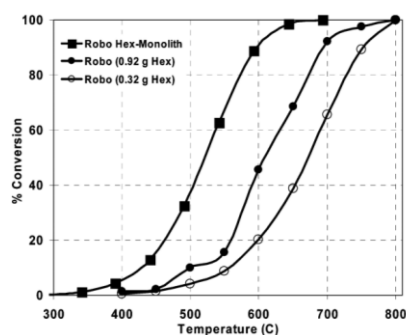
Figure 16 Comparison of pure catalyst and catalyst supported robocast FCC lattice structures [67].

Lefevere, J., et al. [68] like Stuecker et. al. [67] used robocasting to synthesize a monolith that they subsequently functionalised with their catalyst of interest. In this case a ZSM-5 catalyst was applied to 316L Stainless Steel substrates via the wash coating method [68]. Whilst ordinarily shaping 316L Stainless Steel requires high temperature processing, robocasting can print this material at room temperature. Regardless, after robocasting, the 316L Stainless steel substrate was Calcined at 1300°C for 4 h. The catalyst slurry was made from ZSM-5 powder (30wt.%) dispersed in distilled water (solvent) with colloidal silica (1wt.%) as a binder and methylcellulose (1wt.%). Gas Displacement was used in the wash coating procedure that concluded with drying at 100°C overnight and Calcination at 550°C for 3 h.

When implemented in a continuous methanol dehydration process at 250°C, the robocast functionalised 316L Stainless steel demonstrated 20% more activity than the packed bed catalyst and essentially identical conversion to the as-received cordierite honeycomb monolith. This clearly indicates the viability of robocasting for DME synthesis from methanol [68].

Noyen et. al. [69] also employs a ZSM-5 catalyst functionalised onto a robocast substrate as Lefevere, J., et al. [68] did. Their intended application was the decomposition of nitrous oxide (N_2O) in tail gases of nitric & adipic acid plants [69]. The Ti6Al4V titanium alloy robocast substrate was coated with the ZSM-5 by hydrothermal synthesis. The robocast substrate was immersed in a seeding gel compromised of Na_2O, SiO_2, tetra-propylammonium hydroxide diluted in water that was mixed with a synthesis gel of similar components in differing ratios before autoclaving at 180°C for 40 hours. After this the substrate was repetitively cleansed with bidistilled water, sonicated and dried at 60°C for 4 hours. A repetition of the latter coating procedure was performed before calcination at 550°C or 24 hours. Ion exchange of the resulting substrate was performed in 1M NH4Cl solution whilst shaking for 24 hours at RTP followed by rinsing then drying at 60°C for 24 hours. Ion exchange was likewise repeated twice. Calcination proceeded again at 550°C for 24 hours to give the H-form of the zeolite coating. Wet ion-exchange with Iron-Nitrate salts and shaking for 24 hours at RT followed by 60°C drying overnight then calcining for 24 hours at 550°C yielded the Fe-form of their zeolite.

A continuous gas-phase, stainless steel tube reactor had 10wt.% N_2O in He flowed through it and through the woodpile structured robocast substrate held in place by quartz wool [69]. The Gas Hourly Space Velocity of 10,000 mL N_2O/mL$_{catalyst}$/h was accompanied by temperature control from 200°C to 800°C at 5°C/min ramping and 120 minute isotherms. 15 min periodic sampling by online GC gave compositional analysis of the reaction for conversion and selectivity. Noyen et. al. concluded that their catalyst effectively made their substrates active for N_2O decomposition.

In Danaci. et. al.'s work [106] A Ni/Al_2O_3 catalyst slurry preparation is described in detail. A stainless steel 316L robocast structure is submersed in the slurry for 60

seconds then extracted and air dried using an air blow gun. The system was ready for catalytic reactions after 100°C overnight drying and 550°C calcination for 4 hours.

A continuous flow setup as seen in Figure 17 was used [106]. Catalysts were pre-treated by an 80%/20% H_2/He gas mixture to reduce the Ni from NiO to metallic Ni. CO_2 Hydrogenation was performed at temperatures ranging between 250°C − 450°C with a feed composition of CO_2: H_2: He = 1:4:15 at 100mL/min. Online Gas Chromatography measured the quantitative compositions of the fluids passing through it over time, CO_2 conversion was measured by a thermal conductivity detector (TCD) whilst CH_4 production was recorded using a Flame Ionisation Detector (FID) both held at 300°C during their operation. Conversion of CO_2, selectivity of CH_4 and yield of CH_4 were determined. The robocast supported catalysts were found to deliver both improved CO_2 conversion and catalyst stability for this reaction, as Figure 18 makes clear.
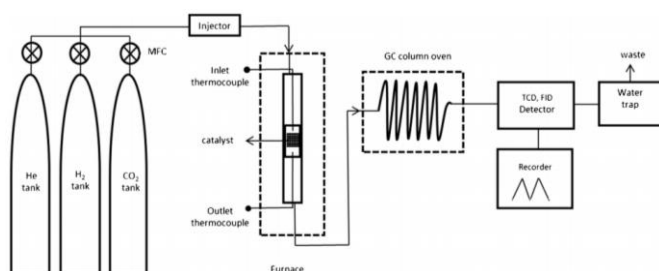
Figure 17 Danaci. et. al. [106]'s experiment setup for a methanation reaction.
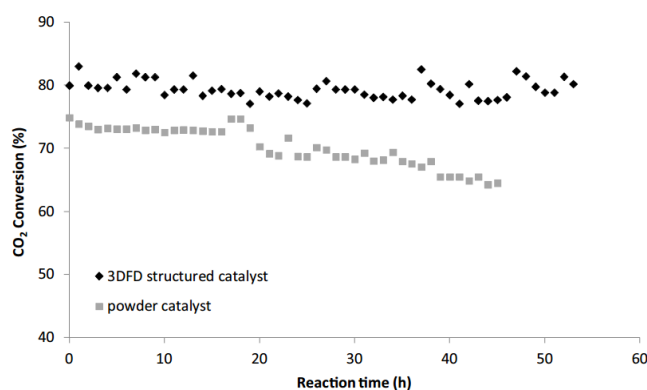
Figure 18 Stability test over packed-bed and 4B1 structured catalyst in Danaci. et. al.'s work [106]. Reaction conditions: 350°C, H_2/CO_2 = 4, WHSV 1500 h^{-1}.

AM allows for the combination of various design elements to enable well-integrated designs. Chisholm et. al. [53], used FDM to print polypropylene (PP) flow plates with 0.9mm square channels for electrolysis of water in conjunction with a proton exchange membrane (PEM) (Figure 19) and catalyst plate inserts, Iridium and Platinum both.
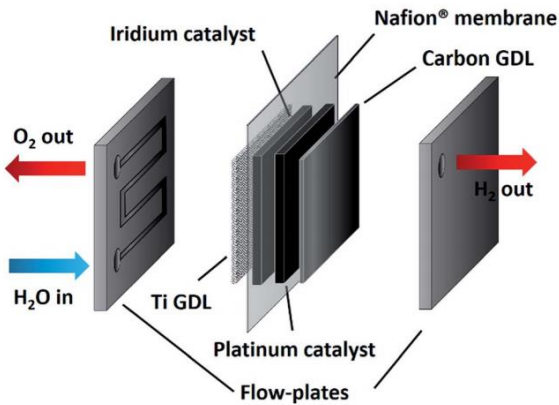
Figure 19 Chisholm et. al.'s electrolysis cell construction [53].

They functionalised their PP flow plates with silver by applying two coats of silver paint after cleansing the plates with detergent to improve adhesion. 120°C drying for 20 minutes separated each coating step. The flow plates were then suitably conductive for electrocoating with a 0.3 M $AgNO_3$ in 1 M NH_3 solution to give a 300 μm coat. A final 1.04 μm sputter coating of gold (Au) protects the silver from oxidation. Chisholm et. al. [53] concludes that the construction of electrochemical devices is viable using AM as an enabling technology.

2.3.3 Integration and Functionalisation Combined

Whilst there is both reactionware and active materials made by AM present in the literature, an uncommon outlier in the field of catalysis and AM is reactionware with demonstrated catalytic activity included. Kitson, P.J. et. al. [43, 52] have excellent work in this area and have put forward a general scheme in Figure 20, that they have implemented themselves for a multi-step reaction, their setup qualifies as using both the integration and the functionalisation Strategies. This fabrication scheme is practically applied in their own work and further demonstrated by their own figures, Figure 21 and Figure 22 [52].
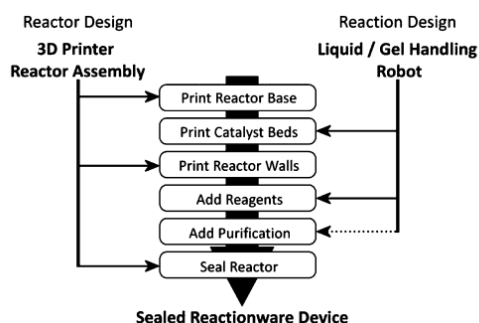
Figure 20 Fabrication scheme for the integration of AM technology with automated liquid handling to produce sealed reactionware for multi-step syntheses. Dotted line indicates the only process not automated in Kitson, P.J. et. al.'s work [52].
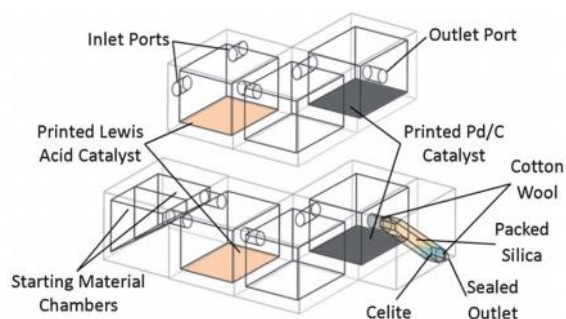
Figure 21 Schematic diagram of the 3D-printed sequential reactors; (top) open reactor featuring inlet and outlet ports for the introduction and retrieval of reactants/products, (bottom) sealed reactor with starting material reservoirs, incorporating packed silica purification column [52].

To achieve such a thoroughly integrated setup, in which the reactor, reagents and catalysts are fully integrated with AM technologies, it was necessary for Kitson, P.J. et. al. to use 2 AM technologies [43, 52]. An FDM Printer, Bits from Bytes 3DTouch, was used to print the reactor structure out of polypropylene. This material was chosen because it is compatible & insoluble with the reactants, products and solvents used in the reactions of interest [43]. To print the catalysts and deliver the reagents, a Robocasting printer, Fab@Home, was employed. In Figure 22 'a', 'b', 'c' and 'd' the base, catalysts, walls and ceiling are printed respectively.
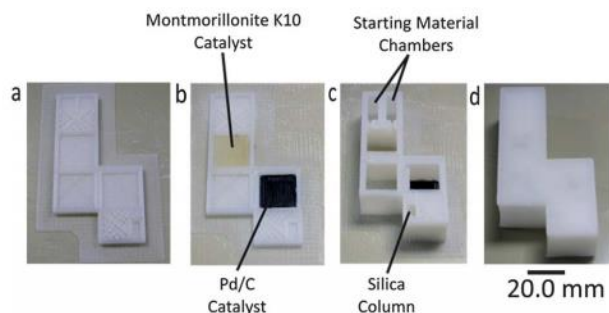
Figure 22 (a) Reactor base with purification before printing of catalyst regions. (b) Reactor base with purification column after printing of catalyst regions. (c) Fabricated Reactor with purification column after addition of starting materials, reagents and packing of silica. (d) Final sealed reactor [52].

It's important to note that the printed material had to be swapped between printers at least 4 times to complete the reactionware device [43, 52]. Whilst this is of little concern for small production runs and for reactionware innovation, it would be ideal to eliminate the use of multiple printers.

The actual inclusion of the catalyst is applied with robocasting. Both Pd/C and K10 Montmorillonite clay were separately mixed with acetoxy-silicone polymer [43, 52] for printing in separate compartments by robocasting of a reactionware vessel made with FDM. This makes the application of these catalysts both relevant to integration and functionalisation strategies. It's an integration strategy because the catalyst is directly integrated into the robocasting build material but functionalised because this catalyst system adhered to FDM-printed reactionware.

2.4 TRENDS IN AM AND HETEROGENEOUS CATALYSIS

2.4.1 Materials Palette

Although not currently demonstrated for catalysis, there are some newly printable AM materials which are likely to have value in the catalysis space. The most interesting example is graphene which has been printed by no less than three separate AM technologies; Robocasting, FDM and potentially SLM. Graphene is known to be an active catalyst and it consistently generates interest in the literature for this reason. Graphene materials are suitable for catalytic applications for several reasons, they have exceptionally high specific surface area, low density and high porosity that allows

for fluid permeation [115]. Graphene is a material known to be catalytically active with tuneability for different reactions [116].

Zhu et. al. [115] developed a method to print graphene aerogels using a graphene oxide (GO) solution with silica powder for viscosity modification and other additives. They used robocasting to print directly into an isooctane solution to avoid drying of the GO 'ink', this novel method is shown in Figure 23. Simple woodpile structures were made to demonstrate the method. Gelation occurred at 85°C in sealed glass vials, after which the wet gels were super-critically CO_2 dried before reduction at 1050°C under N_2 atmosphere. Final etching in HF acid solution removed the silica nanoparticulate filler.

Using the more common FDM technology Wei et al. [117] developed a method to produce a graphene composite with ABS and PLA polymers. A homogenous dispersion of ABS-NMP (N-methyl-2-pyrrolidone) and GO-NMP was made. Chemical reduction of GO to graphene sheets was achieved with hydrazine hydrate addition at 95°C for 1h. Slow addition of this dispersion to DI water allowed for precipitation of the synthesized composite. Centrifuging, washing, drying and heated extrusion produced a 1.75mm filament, ready for FDM printing. The advantage of this approach is that FDM printers are inexpensive, and therefore easily accessible for any laboratory to use.
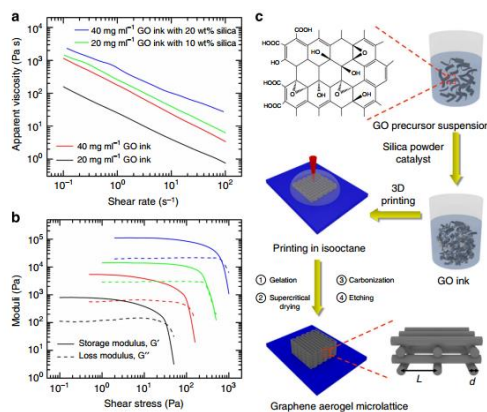
Figure 23 Schematic of Zhu et. al's graphene oxide printing process [115].

In Yang et. al's work [114] a Ni alloy template made by an AM technology, most likely SLM based off their SEM data, was thermally treated to make the surface smoother and then coated with a graphene network by the application of Chemical Vapour

Deposition (CVD) at 1000°C with Styrene as the carbon source. Further treatment in 3M HCl acid enabled the almost complete removal of the Ni template with EDS observing only trace amounts of Ni.

In a news article [118], a company named Nano Dimension announced that they are working in collaboration with Tel Aviv University on printing with Nickel Nanoparticles. Nanoparticulate Nickel materials have high potential for use as catalytically active surfaces, although not directly suggested in the news article.

An interesting article by Lau et. al. [119] adapts Selective Laser Sintering (SLS), a method currently not used in AM catalysis, to use a low energy Infra-Red laser for the sintering process. Pulsed laser ablation in liquids (PLAL) was used to synthesize colloidal Au from a Au target in an a 100mL bath of DI water. The mass of the Au target controlled the concentration of the Au colloid solution. Different masses of mesoporous ZnO were suspended in the aqueous Au colloidal solution and adsorption of the Au occurred over a few hours. Sedimentation of the functionalised microparticles led to drying at 50°C for 12h to give an Au-ZnO powder. During the SLS process, the laser induces the homogeneous nucleation of nanoparticulate Au on the surface of the ZnO micro particles. No catalysis was demonstrated by Lau et. al. [119] for their Au-ZnO SLS material, although ZnO-supported Au nanoparticles are known to be effective catalysts [120].

Other metal colloids could potentially be used as fluxes and catalysts with further adaption and material exploration using Lau et. al.'s [119] application of PLAL to functionalise metal oxide SLS powders with a metal colloid. Whilst this research area has clear potential, progress in this area will be slowed by the lack of SLS already performed for catalysis in the literature and the difficulty of readily accessing such equipment.

Given the current materials restrictions in AM technologies that use UV-curing there have been relatively few AM and catalysis articles in this space. The work of Wang et. al. [121] goes some way in improving the viability of UV-cured materials as substrates for catalysts by functionalisation and thereby as tools in reactionware. By incorporating vinyl-terminated polymerisation initiators into the UV-curable resins

used in Stereolithography various polymers may printed and post-treated by Surface-Initiated – Atom Transfer Radical Polymerisation (SI-ATRP) to gain hydrophobic or hydrophilic properties or maybe even catalytic properties by means of chelated metal catalysts. Wang's method achieved integration of the MiiCraft SLA's default material with 2-(2-bromoisobutyryloxy) ethyl methacrylate which allowed vinyl-initiated polymer coatings of PEGMA and perfluorodecyl methacrylate (PFMA).

2.4.2 Usage of AM Technologies

Whilst the categories of materials used in catalysis are diverse, there are well-defined pockets where material exploration is much more thorough. This is strongly related to the requirements associated with the feedstock materials for this process. As such Inkjet printing of mixed metallic oxides is restricted to a set of very similar ink compositions [57-65]. The variable of interest in this case is the metal in the metal precursor and so the repetition of the other components is of lesser concern. Given the number of different metals which can be printed this way, it is clearly worth continued exploration, especially given the proven strength of these materials for combinatorial and high throughput catalyst synthesis. This region of research is heavily focused on the oxygen and hydrogen evolution reactions and for these reactions there will continue to be further interest, especially with regards to both applying the known printing and screening methods on new catalyst combinations and in adapting new methods for more rapid and/or more accurate screening methods and strategies.

In the context of AM and catalysis, high throughput catalysts synthesis and screening is not seen to this extent with reactions other than oxygen and hydrogen evolution or for catalysts other than mixed metal oxides. It is therefore worth pursuing adaption of AM technologies to facilitate flexible material compositions to produce other catalyst systems with similar control of dopant concentrations. Further exploration of material compositions in the inkjet printing space may be the easiest way to achieve this because the setup already accommodates multiple printing heads; however, robocasting is also a flexible AM technology with a demonstrated ability to print supported metals, metal oxides, mixed metal oxides, metals & alloys, active carbons, hydrogels, and polymers.

If robocasting can be adapted to have multiple compositions systematically printed by one head or even multiple print heads, then high throughput combinatorial synthesis could be applied to even more material combinations and not just mixed metal oxides. In fact, some work has already been made down this path by Kokkinis et. al. [72], who utilised a two-component mixing and dispensing unit for their Robocasting printer that allowed graded compositions of two-components as desired during the printing process. Although this method has not been used for catalysis, with some adaption it is possible that this strategy may allow significant improvements for high throughput catalyst synthesis.

The other advantage to having multi-material printing capabilities is the printing of reactionware, enabling easy deposition of the catalyst wherever it is needed. Reactionware is something for which robocasting is arguably better – because it can easily print bulk objects, unlike inkjet printing. As more multi-material methods are developed, reactionware with catalysts integrated will become a growing research field. Another factor which contributes to the continued development of reactionware is modular design, the use of modular design for microfluidics is predicted as a more heavily implemented future design tool [122] because it saves a lot of time. This will progress a lot more rapidly if researchers can use an open source database for their modular components – such as Thingiverse [123].

The proliferation of inkjet printing and robocasting for catalyst synthesis comes down to their freedom for custom design of printing compositions, as already discussed. This versatility of composition is a very important aspect of design in catalysis as very specific compositions are needed to acquire the most effective catalysts.

As opposed to robocasting or inkjet printing, some AM technologies are seen very little in catalysis. FDM sees limited application in catalysis, although it is inexpensive and accessible, the material compositions that are printed are limited and the solvent inertness, temperature and pressure properties are substandard compared to materials available with other AM technologies. SLM, whilst potentially quite useful, as indicated by Ambrosi et. al.'s work [55], sees little interest in the literature, mostly because it's a less commonly available technology and it's comparatively expensive.

DOPsL and Stereolithography require a large amount of work to develop a singular catalyst system, and there is no indication in the literature that the feedstock composition design is easily transferrable to new materials and especially not to combinatorial synthesis. Other AM technologies, such as SLS, have never been applied to catalysis in the literature at all, most likely due to a combination of expense and availability of the technology.

2.5 MICRO-STRUCTURED REACTORS

Even if catalysts may be successfully immobilised on the surfaces of AM materials, there is still the question of reactor design. The motivation for this project is the production of miniature reactors for portable refining of stranded resources, such as natural gas (NG). It follows that a knowledge of micro-structured reactors is useful.

Micro-structured reactors are devices with sub-millimetre internals [20], Bakhtiary-Davijany, H., et al. [21] identified that the internal channels may range from 250 μm to 2 mm in width. Micro-structured reactors have a higher surface area to volume ratio than other reactor types leading to a higher heat transfer rate and increased catalyst-reactant interactions [23]. The flow character in these reactors is directed, symmetrical and close to laminar [21, 124, 125].

As smaller volumes are involved the operation is safer and operating windows can be made larger [20]. The utility of small volumes is the ease of controlling pressure, temperature, residence time, flow rate and flow mixing [22, 23]. In addition it's easy to meet increased demand by increasing the number of sub-units, i.e. microchannels [124]. Application of micro-structured design may be a 'drop-in' that is replacing part of a reactor design, or 'end-to-end' process intensified design that involves a fully micro-structured reactor [20].

These advantages of micro-structured reactors enable the reduction of the processing time-scale down to the minutes range for many reactions [20]. As such, micro/milli-structured reactors are a useful tool for facilitating process intensification [126]. Intensified heat and mass transfer in micro-/milli-structured components enhances the process repeatability compared to batch vessels.

Whilst micro-structured reactors have many advantages there are some phenomena and limitations which are problematic with their use. Up to a point, reducing the channel size of micro channels aids heat transfer but below a critical hydraulic diameter, the heat transfer and often, yield of a reaction, can get worse [127]. Parra, A.A.M., et al. also comments that fluid maldistribution in multichannel microreactor configurations can result in differing reaction rates and hence differing conversions of the reactants in separate channels [128]. Even the slightest dimensional difference on the micro scale of the dimensions can lead to noticeable differences in volumetric flow rate.

One issue with micro-structured reactors is the low durability of the catalyst. According to one author [124] there is limited literature on the rapid deactivation of catalysts. To counter this, higher catalyst loading and increased porosity inside the coating are ideal [129].

When SS316 was used as the reactor material, there were issues with undesired reactions such as methanation [125]. To prevent methanation, given that Fe is a catalyst for it, a coating of silicone is often utilised in the pre-heating regions. This example reveals that it's appropriate to be aware of the substrate chemistry which can be detrimental to the intended reaction if not accounted for.

Micro-structured reactors facilitate fluid flow through microchannel geometries of various designs in the literature. Garimella et. al. and Chen Y. et. al indicate that there is an extensive interest in microchannels due to their high heat transfer potential and their unique fluid flow characteristics [127, 130-133]. The geometrical variants and their impacts on fluid flow and heat transfer properties are explored in the subsequent subheading '2.5.1 Microchannel Geometries'.

2.5.1 Microchannel Geometries
2.5.1.1 Types found in literature

The following tables summarise the path, cross-section and baffle variations of the microstructures found in literature. Path variation has been arbitrarily defined as the pattern the cross-section follows along the extent of its length, see Table 10. Cross-

section is defined as the shape of a cut made laterally through the channel, see Table 11. Baffles and fins are defined here as structures located within channels or on channel walls that serve to alter fluid flow and/or heat transfer mechanisms, see Table 12. Many of the references supplied have figures or photographs of the geometry of interest.

Table 10 Path variations for microchannels

Shape	Straight	Coiled Serpentine	Curve/Wave	Serpentine	Coiled	Square Wave
Reference	[3-19]	[4]	[4, 5, 134-136]	[4, 5]	[4]	[5, 135]
Shape	Meander	Contraction-enlargement	Zigzag	Pin-hole	Sigma	
Reference	[137]	[134, 138]	[14, 134, 135, 138]	[4, 21, 139, 140]	[137]	

Table 11 Cross-section variations for microchannels

Shape	Square	Rectangular	Inverse Trapezoidal	Isosceles Right Triangle	N-shape
Reference	[6, 14, 132, 141, 142]	[8, 11, 13, 15-18, 141, 143, 144]	[143]	[132]	[141]
Shape	Diamond	Circular	Trapezoidal	Isosceles Triangle	Barrel
Reference	[143]	[7, 12, 132, 145]	[9, 10, 143, 146]	[141, 143]	[141]

Table 12 Baffle and fin variations for microchannels

Shape	Oblique Rectangle	Circular	Square	Perpendicular Rectangle	Rectangular Winglet Pair
Reference	[3, 4, 19, 147]	[138]	[138]	[3, 6]	RWP: (a) top view and (b) side view [148]
Shape	Ribs	J-shaped	Diamond	Radial Rectangle	Herringbone, Staggered Herringbone
Reference	[147]	[18]	[138]	[136]	[17, 144, 149]

2.5.1.2 Fluid Flow and Heat Transfer

Fluid flow and heat transfer in a device with micro-channels is strongly influence by the path the flow is constricted to, the cross-section of this path and any obstructing baffles or fins along the pathway. There are other influencing factors such as those suggested by Salman et.

al [150]. They identify several important variables for fluid flow and heat transfer in microchannels: size effect, rarefaction effect, surface roughness, viscous effect, electrostatic force effect, axial heat conduction in the channel wall and surface geometry. Several of these variables are explored in the following subheadings.

2.5.1.2.1 Impact of Path Variations

For the most part, variation of the path influences mixing of the fluid in the microchannel. A general principle for achieving good mixing in a microchannel, per Leung et. al.; is to have regular obstructions followed by a width constriction [15]. Another research group, Naher et. al. concluded that whilst microfluidic mixing requires the creation of swirling vortices by use of the channel geometry, it's important to create these vortexes away from dead zones [3]. The creation of vortexes within dead zones leads to undesirable back pressures.

It's common with varying path geometry for one property to be improved at the expense of another. In Jeon et al.'s work CFD simulations were performed upon various microchannel geometries to determine the most favorable design for micro-mixing [138], see Figure 24. In their setup, Inlet 1 supplied a Au nanoparticle-rich mixture and Inlet 2 supplied a $CuSO_4$ mM solution with no Au nanoparticles.
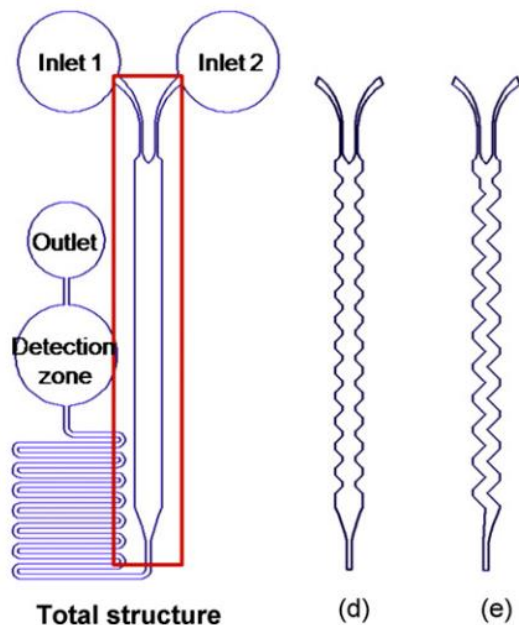
Figure 24 Figure Excerpt: Schematic geometries of micro-mixers with winding paths (d) contraction-enlargement and (e) zigzag type [138].

Jeon et. al. found out that the zigzag geometry achieved the most homogenous mixture of the two inlet flows followed by the contraction-enlargement geometry, both of which were better than the straight channel [138]. The contraction-enlargement geometry provided mixing through the variation of velocity and pressure with its differing cross-section along its length whereas the zigzag geometry utilised rapid velocity shifts at its 90° bends to facilitate effective mixing, see Figure 25. The creation of secondary flows facilitates enhanced mass and heat transfer [4].
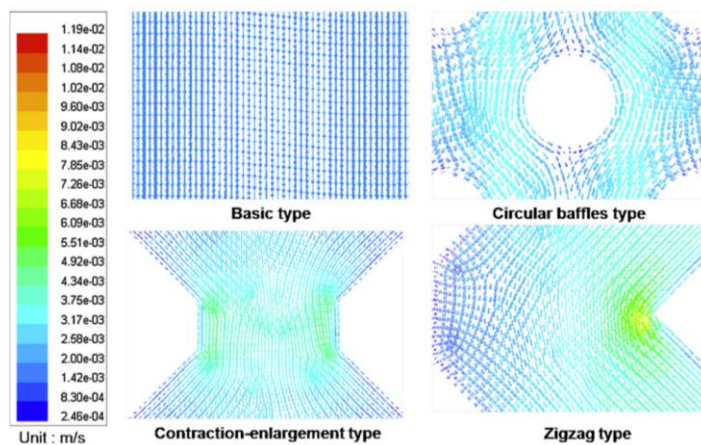
Figure 25 Velocity profiles of mixtures in different micro-mixers with vectors and contours. Secondary Flows/Velocity variations were observed near the obstructive locations [138]. The path-related geometrical variants are highlighted.

Conversely the largest pressure drop was attributed to the zigzag geometry followed by the contraction-enlargement geometry and the smallest pressure drop was for the basic, unaltered geometry [138]. A general observation may be made that, where mixing of the flow is improved the pressure drop also tends to increase – making for a difficult offset decision between mixing flows and minimizing pressure drop. Figure 26 demonstrates this well by plotting mixing efficiency with distance along the channel for each geometry type considered [138].
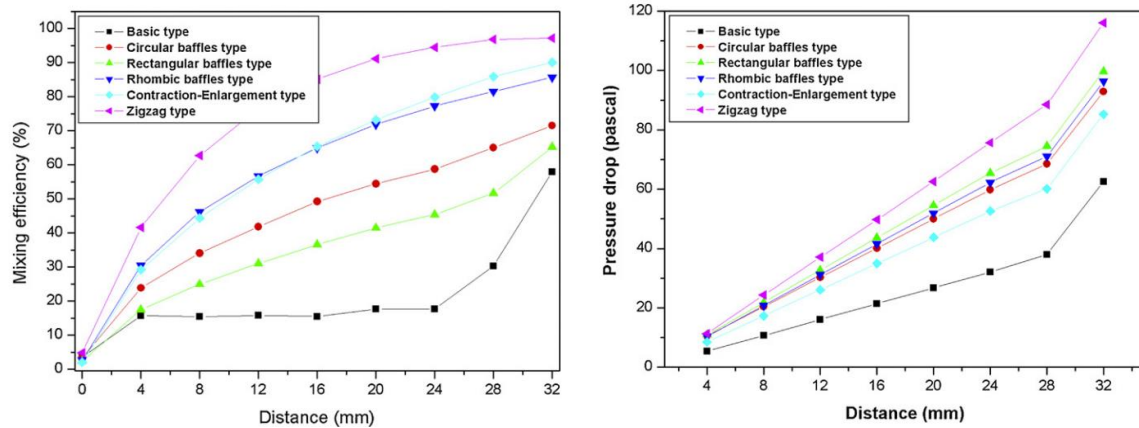
Figure 26 Simulation data for mixing efficiencies (left) and pressure drop (right) with different channel paths and micro-mixers [138].

The only geometry to have high mixing efficiency and a relatively low pressure drop simultaneously is the contraction-enlargement type [138]. Another approach to mediate this issue is the use of fractal tree-like structures. These are often observed in natural organs with a regular bifurcation shape and are able to achieve a uniform flow distribution with low pressure loss in the structure [4].

A more novel approach for the rapid mixing of reagents was developed by Zhao et. al. who utilised a geometrically-initiated production of micro-droplets [151]. Two T-junction geometries enabled the controlled generation of droplets of a dispersed phase within a continuous phase. These micro-droplets may allow compartmentalised reactions inside themselves with nano-litre to micro-litre volumes that provide rapid mixing of the reagents. Figure 27 illustrates the simulated concept of Zhao et al. [151].
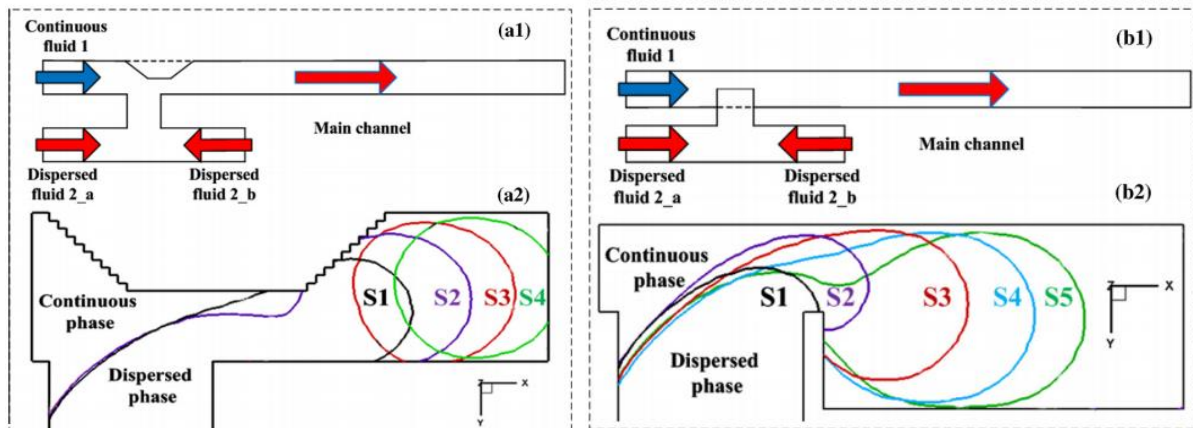
Figure 27 Schematic configurations of improved channel design ((a1) modified T-junction; (b1) micro-capillary insertion microchannel) and corresponding droplet generation steps ((a2: S1-S4) modified T-junction; (b2: S1-S5) micro-capillary insertion microchannel) [151].

Both junctions proved to be effective methods and allowed for control of the droplet generation frequency as well as the size [151]. Better internal mixing was achieved for droplets that maintained internal asymmetrical flows from the generation process.

Although path variations, mostly impact the mixing efficiency and pressure drop, they can influence other factors like the conversion of reactants. An et al. studied several path configurations and their impact on velocity, pressure drop and conversion. These configurations were tested by simulating the passage of a methane/air mixture through them. Figure 28 illustrates the steady-state velocity, pressure and conversion distributions that the CFD reported [4].
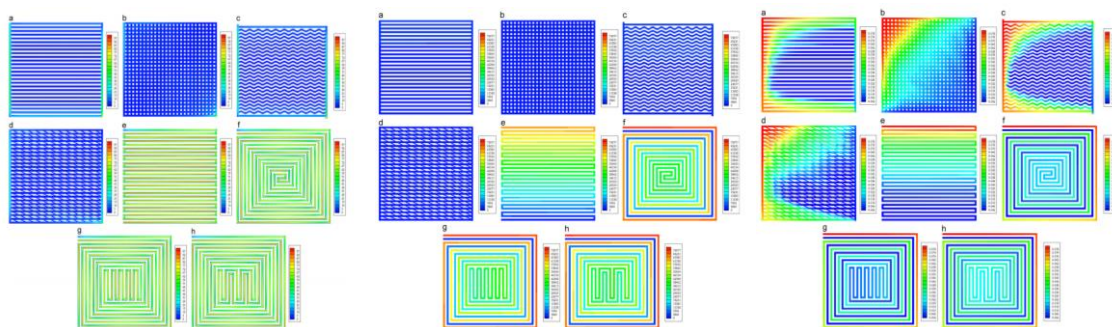
Figure 28 Contours of Velocity (Left), Pressure (Middle) and conversion (Right) at z = 5 x 10-4 m for: (a) parallel; (b) pin-hole; (c) wavy; (d) oblique fin; (e) serpentine; (f) coiled; (g) coiled with serpentine (h) coiled with double serpentine [4].

It was found that the coiled and serpentine configurations, (e) – (h), have the highest flow velocity magnitudes, whilst parallel, pin-hole, wavy and oblique fins proved to have much lower velocities in comparison [4]. However, the pressure drops of all these configurations showed the same trend. All geometries with high flow rates also suffered from significant pressure drops.

The conversion however is a slightly different story: For the coiled and s`erpentine configurations, (e) – (h), the conversion increases along the length of the channel monotonically [4]. For the parallel, wavy and oblique fin configurations an uneven conversion distribution is present. The pinhole configuration, however, displays a very high extent of conversion even though the mass distribution is uneven in each parallel channel.

Whilst the high velocities of the latter 4 configurations and their high extent of conversion makes for efficient chemical conversion it also causes a high pressure drop across the micro-reactor necessitating a large pumping power [4]. The pin-hole geometry is the only configuration which demonstrates a high conversion without suffering from a high pressure drop.

2.5.1.2.2 Impact of Cross Section

The cross-section of a microchannel is frequently reported to have a strong influence on heat transfer [130, 131, 143, 152]. Nonetheless the cross-section also influences fluid flow. Observations have been made by various authors, including Coleman et. al. [143], that a transition in flow behaviours occurs around hydraulic diameters of 5.5 mm. Gravitationally-driven stratification of flow regimes is present for D_H = 5.5 mm and greater [143] but for D_H < 5.5 mm surface tension forces dominate [130, 131, 152].

Cherlo et. al. completed experiments and simulations to observe the influence of rectangular microchannel aspect ratio on the mixing behaviours at different Reynold numbers [153], as illustrated in Figure 29. Passive micro-mixing in micro channels is desirable since it utilises static geometry to enable fully-mixed flows. T-junction engulfment flow is characterised by a break in symmetry of two pairs of counter-rotating vortices [154]. Furthermore, engulfment is desirable because it allows for effective mixing of flows without baffles [153].
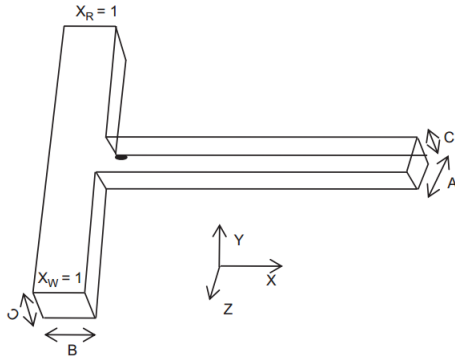
Figure 29 Schematic Representation of T-shape geometry. A, B and C are mixing channel width, inlet channel width and depth of all channels, respectively [153].

When rectangular micro channels are considered the critical Reynolds number for engulfment flow occurring at a T-junction depends on the inlet and outlet aspect ratios [153], see Eq. 6.

$$k = Re^{0.82}(B/C)^{-0.79} \left(D_h(inlets) \middle/ D_h(mixing) \right)^{-1.5} (A/C)^{0.15}$$

Eq. 6 Critical Reynolds number for engulfment flow.

The latter equation was found only to hold for A/C > 1 and B/C > 1, i.e. when the width was greater than or equal to the height for both the inlets and the outlet [153]. It follows that engulfment flow only occurred for outlet aspect ratios greater than 1, that is, those with widths greater than heights.

Aspect ratio was also found to influence the heat transfer rate; Bello-Ochende, T. et al. completed a study on the influence of hydraulic diameter and aspect ratio on the heat removal capability of a simple heat sink design [133], see Figure 30.
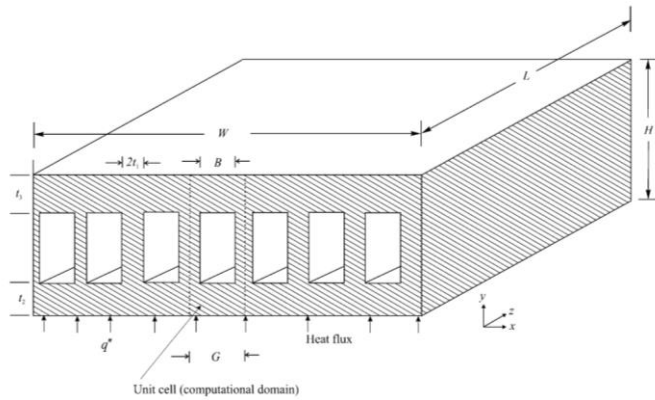
Figure 30 Micro-channel computational unit cell of Bello-Ochende T. et. al.'s heat sink [133].

An important result from this study was the prediction of a maximum thermal conductance being present for an intermediate hydraulic diameter value using the asymptote method, see Figure 31 [133].
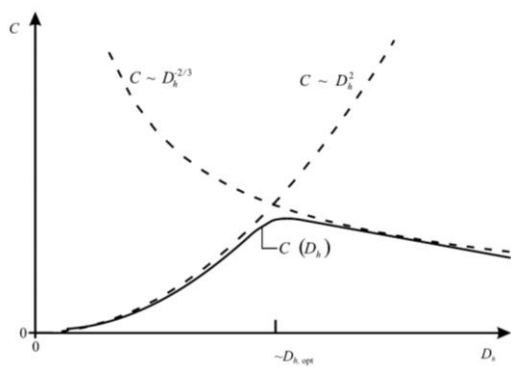
Figure 31 Thermal conductance as a function of the limits of large channel and small channel conductance relations using the asymptote method.

This led to the following simulation results which show that the maximum temperature of the heat sink can be minimized by varying the hydraulic diameter and the aspect ratio of the rectangular channels, see Figure 32 [133].
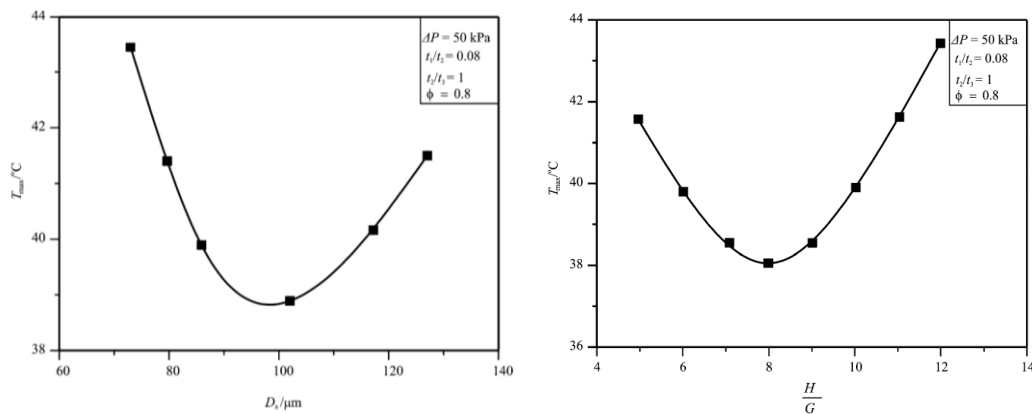
Figure 32 The effect of channel hydraulic diameter (left) and channel aspect ratio (right) on maximum Temperature in Bello-Ochende T. et. al.'s study [133].

Coleman et. al agrees with Bello-Ochende T. et. al. in that high aspect ratios are advantageous for heat transfer [143]. Within their own study, Bello-Ochende T. et al. reasons that for hydraulic diameters less than the optimal values the loss of conductance occurs because the fluid is being squeezed and overworked and for hydraulic diameters greater than the optimal value the reduction of specific surface area is responsible for the reduced conductance [133]. Salimpour et al.'s work agrees with this reasoning [132].

When working with microchannel arrays, the sheer number of microchannels can make simulations and design of microchannel arrays more complicated. Salimpour et al. used numerical modelling to find that the optimal channel configurations for unconnected channels is independent of the channel array configuration [132]. They worked on optimising a unit cell of a single channel for this reason; the smaller focus is time-saving and cost-saving.

Salimpour et al. used the Finite Volume method to calculate heat transfer of air passing through square, isosceles right triangle and circular channels at a pressure drop of Δp = 2kPa [132]. The simulated impact of the hydraulic diameter, D_h, on the volumetric dimensionless heat transfer, Q*, is illustrated in Figure 33.
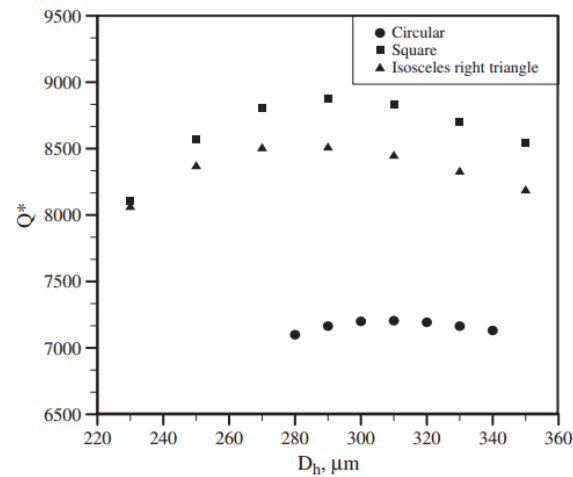
Figure 33 The effect of hydraulic diameter on the dimensionless heat transfer per unit volume, for different cross-sections with Δp = 2kPa [132].

This data supports the conclusion of Bello-Ochende, T. et. al. [133], that there is an optimal hydraulic diameter which gives the highest rate of dimensionless heat transfer [132]. However, this is not entirely independent of geometry; the Square and Isosceles right triangle had better heat transfer at their optimal hydraulic diameter and their optimal hydraulic diameter had a smaller value than that of the circular microchannels [132].

Furthermore, Salimpour et. al. found a relationship between pressure drop, optimal channel hydraulic diameter and heat transfer, see Figure 34 [132]. For all geometries considered by Salimpour et. al. the optimal hydraulic diameter for heat transfer decreased as the pressure drop increased. Conversely, the higher the allowed pressure drop the greater the heat transfer rate [132].
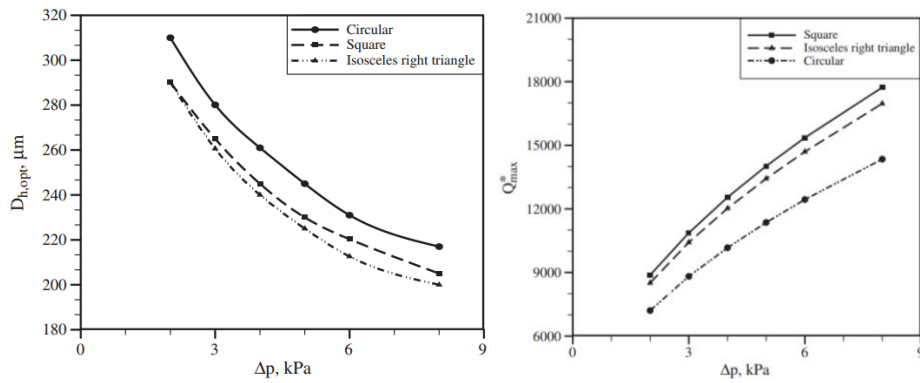
Figure 34 (Left) The effect of pressure drop on optimised channel hydraulic diameter and (Right) the maximum dimensionless heat transfer per unit volume [132].

To explore the impact of the shape of the cross-section, Coleman et. al set up the microchannel configurations in Figure 35 to assess shape-sensitivity of microchannels in their heat transfer properties [143].
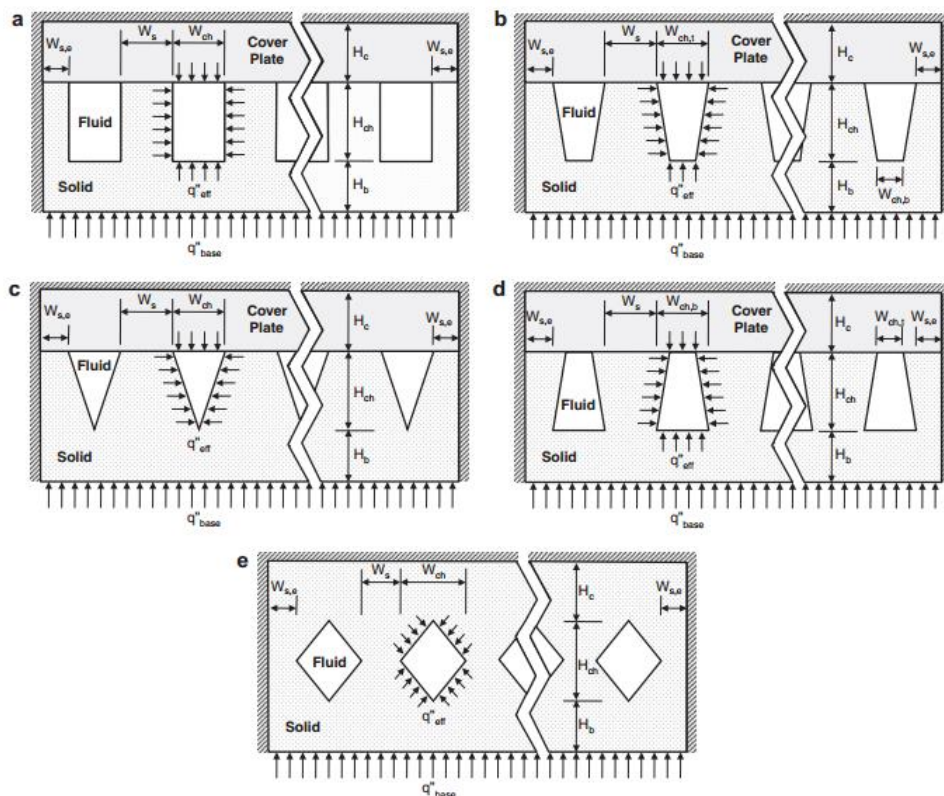
Figure 35 Schematic diagrams of micro-channel heat sinks with (a) rectangular, (b) inverse trapezoidal, (c) triangular, (d) trapezoidal and (e) diamond-shaped cross-sections, W_s is the width of spacing, W_{ch} is the channel width [143].

They found that the rectangular channels produced comparatively greater reductions in the temperature at the base and top compared to the other shapes and the diamond-shaped channels produced the least favourable outcome with higher temperatures at these locations [143]. A significant finding was that smaller channel spacing ratios 'W_s/W_{ch}' yielded greater reductions in temperature. In a similar study focusing on circular microchannel geometries Kim et. al. [145] found that cooling performance is also optimal when the spacing-to-diameter ratio of the circular channels is minimised.

Karakaya et. al. completed simulations of combustion/steam reformation coupled reactions for the geometry in Figure 36 [127], with H_2 yield as an output.
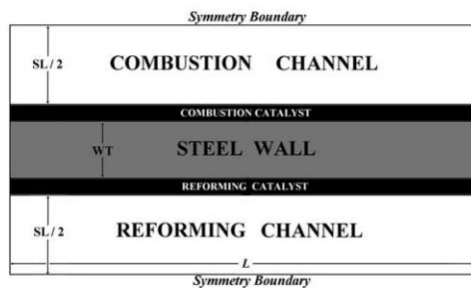
Figure 36 Microchannel geometry for Karakaya et. al.'s coupled combustion/steam reformation reactions, SL is Side Length, WT is wall thickness [127].

One of the coupled reactions was for the exothermic combustion of methanol paired with the endothermic reformation of methanol [127]. Variation of side lengths from 280 to 560μm and wall thicknesses from 100 to 400μm were applied to check the geometry sensitivity of these coupled reactions. The H_2-yield was close to the theoretical maximum of 3 for side lengths of 560μm and a wall thickness of 100μm but the H_2 yield reduced to 2.62 upon increasing wall thickness to 300μm, this was because the increased heat resistance led to lower temperatures in the endothermic reaction. However, increasing wall thickness further to 400μm increased the H_2 yield closer to 3 again, the 400 μm wall thickness increased the heat resistance enough to allow a higher temperature to develop in the combustion channel which could overcome the effect of the increased heat resistance and supply more heat to the reformation reaction.

For the 3 coupled reactions considered by Karakaya et. al. the reduction of side length from 560 to 420 μm reduced the H_2 yield by less than ~20% whereas the reduction from 420 to 280

μm caused a reduction in H_2 yield of up to ~50%. This is most likely related to these values dropping below an optimal hydraulic diameter.

2.5.1.2.3 Impact of Baffles and Fins

It is observed by several authors that the primary application of baffles and fins is to enhance mixing of flows [3, 6, 127, 136, 138, 147, 148], and often to indirectly improve the heat transfer by lieu of that mixing enhancement [4, 127]. An, H., et al. also observes that the baffles provide an increased surface area which is especially useful for catalysis [4]. Chuan et al. takes this a step further by demonstrated the effective use porous fins to facilitate mixing whilst allowing slip of the flow to reduce the pressure drop simultaneously [155].

In Karakaya et al.'s work, they considered simulations of coupled Combustion & Steam reformation reactions with and without rectangular baffles, see Figure 37 [127].
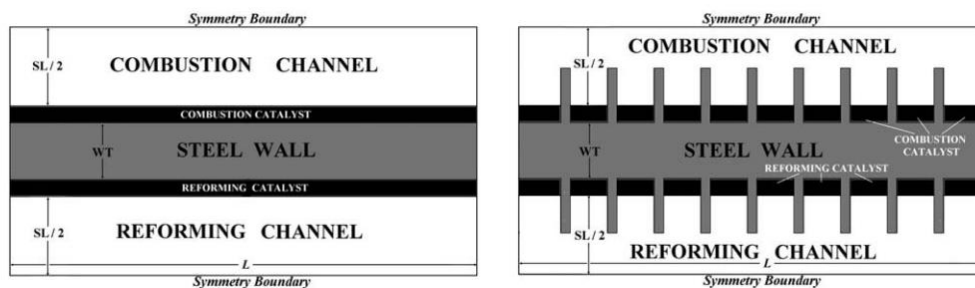
Figure 37 Microchannel geometry with and without micro-baffles, SL is Side Length, WT is wall thickness [127].

For controlled side lengths and wall thicknesses the addition of 2mm micro-baffles, 190μm long, 10mm apart led H_2 yield increased. In the coupled combustion and steam reformation of ethanol there was a ~21% increase in yield, and for propane there are a 191% increase in yield. The addition of baffles increased the heat transfer across the wall thickness leading to the increased H_2 yield [127].The presence of micro-baffles only increased the pressure drop by roughly 20 Pascals. These micro-baffles act as static mixers and improve the convective heat transfer coefficients allowing more efficient coupling of the reactions.

Gumuslu et al. modeled Fischer Tropsch synthesis for a metallic microstructured reactor with alternating reactant and cooling channel layers, see Figure 38 [6]. Their use of micro baffles in the reaction channels on the walls adjacent to the cooling channels resulted in an 11° maximum temperature reduction. Like Karakaya et. al. [127], Gumuslu G. et. al reasons that

the local heat transfer coefficient, between the catalyst coating and the wall, is improved by these static mixers [6].
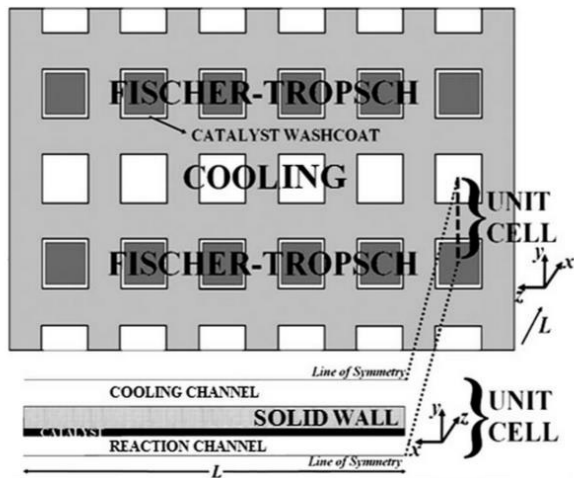
Figure 38 Heat-exchange integrated microchannel reactor system and the unit cell [6].

Jeon et. al. performed CFD upon various microchannel baffles geometries to determine the most favourable design for micro-mixing [138], see Figure 39.
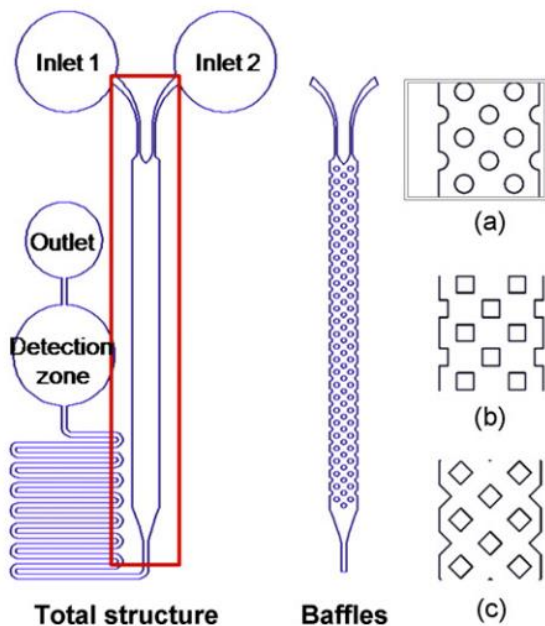
Figure 39 Figure Excerpt: Schematic geometries of micro-mixers with obstructions or winding (a) circular, (b) rectangular and (c) rhombic baffles [138].

The resulting mixing efficiencies are visible in Figure 26 [138]. Rhombic baffles gave the highest simulated mixing efficiency, followed by circular then rectangular baffles in Jeon et.

al.'s study, most likely because the rhombic baffles and circular baffles interrupt the flow less abruptly than the rectangular baffles [138].

More than one author has promoted the creation of vortices as a method to encourage mixing in microchannels [3, 148, 153]. Naher, S., et al. simulated 3 designs for mixing flows – Geometry 1 is a plain channel, Geometry 2 is a channel with rectangular baffles and Geometry 3 is a channel with angled fins, see Figure 40 [3].
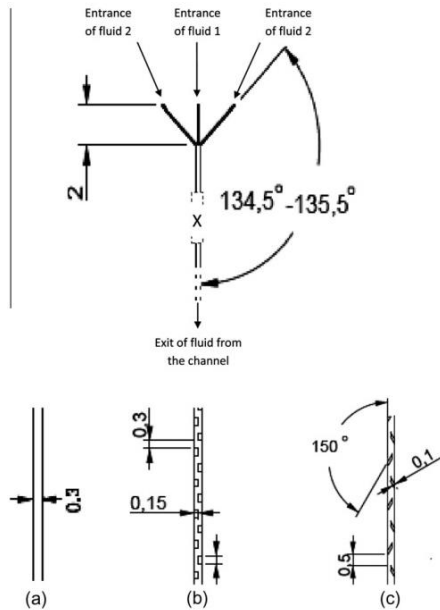
Figure 40 The top half is the common schematic of 3 different geometries of 50 mm channel. (a) - (c) shows detail inside the geometry of each channel marked by the X on the top sketch. Geometry 1 is (a), Geometry 2 is (b) and Geometry 3 is (c). The dimension are in mm [3].

The most effective mixing resulted from the angled fins, followed by the rectangular blocks, both of which were better than an unaltered micro channel, see Figure 41 [3]. The operative element in improving the mixing is the creation of vortices by surface geometries, see Figure 42.
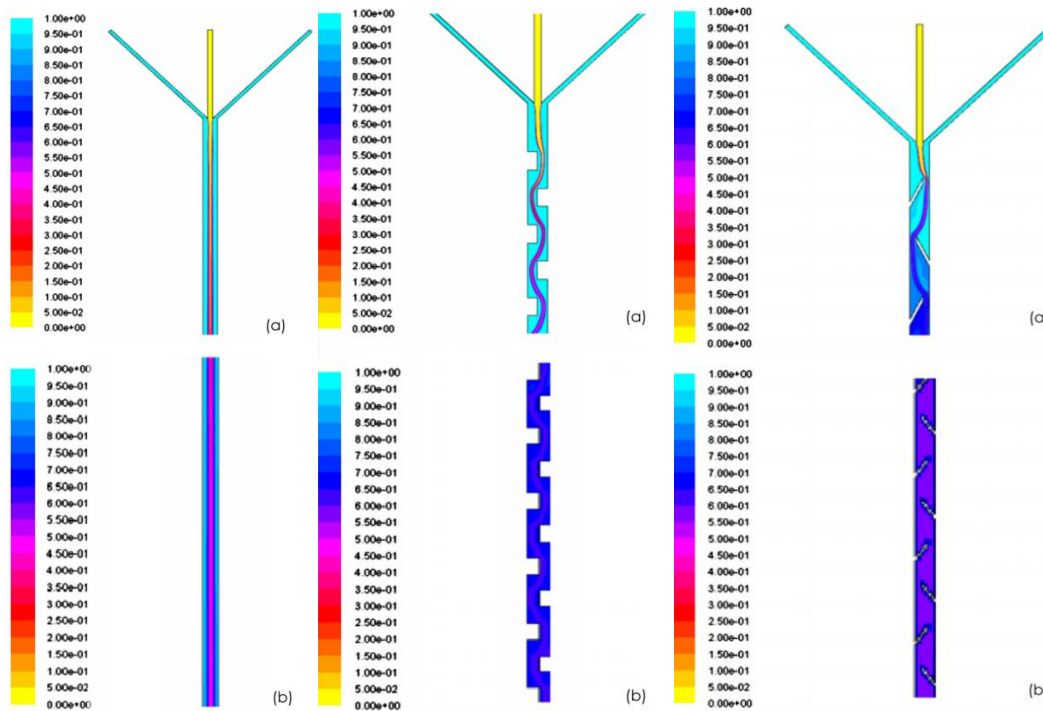
Figure 41 Fluent results along the channel for Geometry 1, 2 and 3 from left to right (a) the channel entrance and (b) the channel exit. The scale bar for the mass fraction of fluid 2 is shown on the left of each geometry [3].
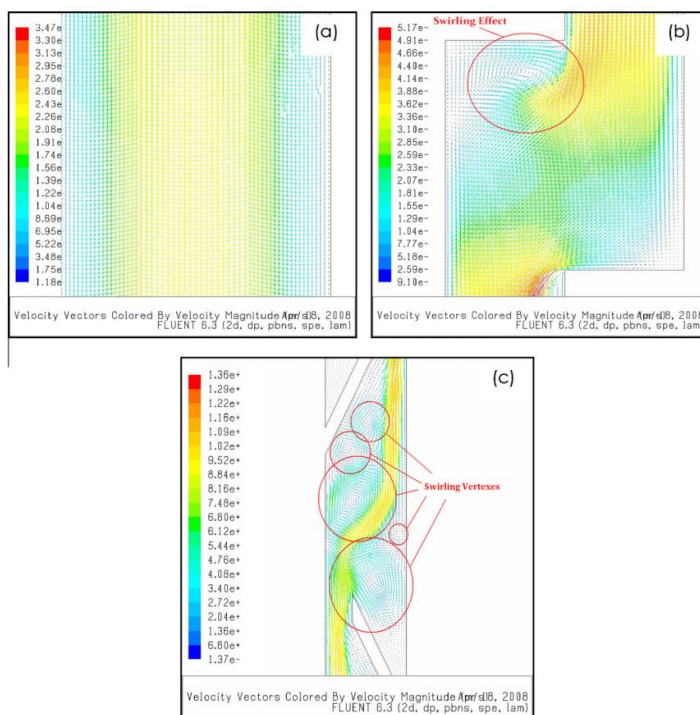
Figure 42 Velocity vectors for (a) Geometry 1, (b) Geometry 2 and (c) Geometry 3. Scale of the velocity vectors are shown in the left hand side of each image [3].

The fins typically create more vortices than the rectangular blocks, hence why they enable a much greater mixing ability compared to the open micro channel [3]. It must be noted that the vortices ought not to be present in dead zones since this creates back-pressure and doesn't improve mixing.

Further work that reinforces the usefulness of vortices for mixing was carried out by Hsiao et al. [148]. Hsiao et al. demonstrates the effectiveness of Rectangular Winglet Pairs at mixing a T-junction flow. For both convection and diffusion dominant cases of flow, RWPs improve the mixing [148]. They are most effective above a threshold Reynolds number where they generate longitudinal vortices to enhance the mixing. The optimal winglet parameters for mixing are in Table 13.

Table 13 Optimal Values for RWP positioning and sizing [148], 'D' is the distance between the front of each winglet pair, 'W_m' is the main channel width, 'h' is the winglet height and 'H' is the channel height.

Winglet Spacing	Angle of Attack	Winglet Height
$D = 1.5W_m$	$\theta = 22.5^\circ$	$h = 0.75H$

A related geometry was considered by Kim, B.S., et al. who added ribs to their microchannels to enhance mixing, see Figure 43 [147]. They found that the optimimal geometry required specific aspect ratios for the rib thickness: rib height (a: d) , the rib height: channel height (d: h) and the separation distance: rib height (b: d), and a particular angle of attack see Table 14.
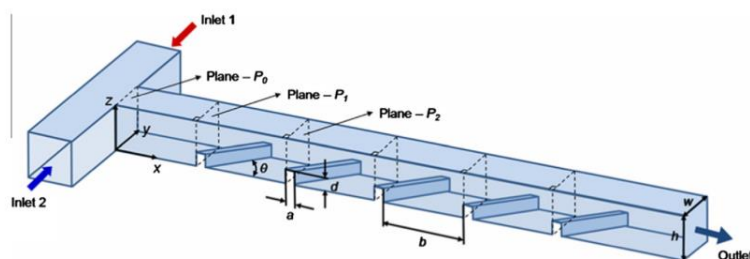
Figure 43 Schematic of a microchannel with rib-roughened mixers [148].

Table 14 Optimal values of rib position and sizing ratios for mixing in the T-junction used by Kim, B.S., et al. [147].

Angle of Attack	d/h ratio	a/d ratio	b/d ratio
θ = 35.6º	0.7	0.127	1.10

In contrast, a similar design developed by Aubin, J., D.F. Fletcher, and C. Xuereb, called a staggered herringbone structure [149] aids mixing in microchannels most when the depth of the grooves is sized at 30%-40% of the height of the channel, see Figure 44. According to the work of Kim, B.S., et al. [148] and Aubin, J. et al. [149] it would seem that the appropriate aspect ratios of grooves and ribs is not equivalent as protruding ribs are optimal at 70% of the value of the channel thickness and grooves are optimal at 30-40% of the channel thickness.
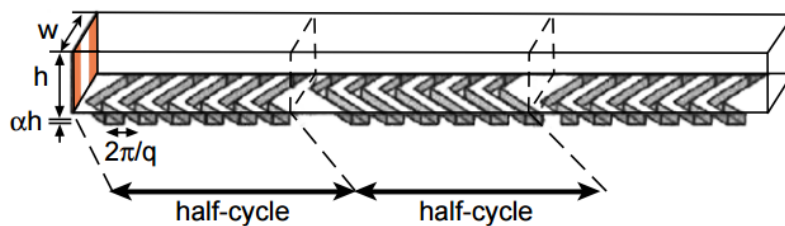
Figure 44 Geometry of Aubin, J. et al.'s staggered herringbone micromixer [149]

2.5.1.2.4 Impact of Scaling

At the reduced scale of micro reactors different forces become dominant and the impact of others becomes less important [130]. It's important to realise that macro-scale channel models do not transfer well to micro-scale channel models for this reason. For example, the large surface to volume ratio of microchannels enhances surface effects compared to macro-scaled devices [131]. Whilst surface tension becomes more important, gravitational forces become less dominant [130].

Interestingly whilst in macroscopic channels the surface roughness has little impact on fluid flow or heat transfer, in microchannels the roughness plays an important role in determining the nature of these behaviours [131]. Heat transfer was shown to increase for surfaces with a larger fractal dimension and increased roughness by Chen, Y., et al. but unfortunately the pressure drop was also higher for these surfaces. Fractal dimension is the frequency of variation in the roughness height. Likewise a higher fractal dimension and roughness

promoted turbulent flow. If the scale of the roughness is close enough to the scale of the microchannel dimensions laminar flow may be disturbed, especially near the walls.

The Bonds number, developed by Nema [152], is a dimensionless number that relates the ratio of gravitational to surface tension forces, see Figure 45,

Eq. *7* & Eq. 8.
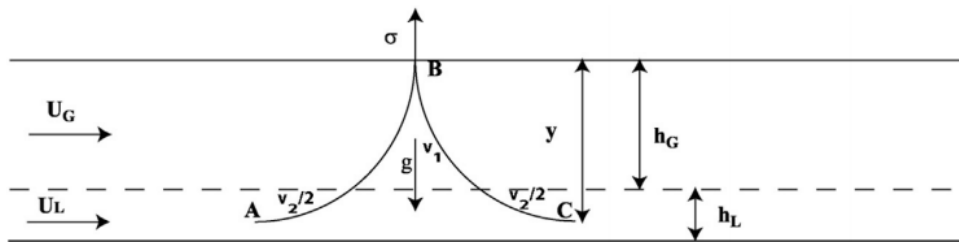
Figure 45 Liquid element force balance schematic [152]

$$Bo = \frac{(\rho_L - \rho_G) \times g \times D_H{}^2}{\sigma}$$
Eq. 7 Bonds Number

$$Bo_{critical} = \frac{1}{(\frac{\rho_L}{\rho_L - \rho_G} - \frac{\pi}{4})}$$
Eq. 8 Critical Bonds Number

When the Bonds number is less than the critical number, surface tension forces dominate; liquid slugs form as soon as the minimum liquid volume fraction to form them is present [130, 152]. Surface tension pulls the liquid film and forms a bridge across the tube. For Bond numbers greater than the critical number the liquid volume fraction needed for slug formation increases with tube diameter approaching 50% [130].

2.5.1.2.5 Impact of Reynolds Number

The effectiveness of micro-mixers at mixing depends on the Reynolds Number of the fluid flow [135]. For example, Liu et al. found that serpentine microchannels perform best for 6 < Re < 70 [5]. In this range, Liu et. al. found that a 3D serpentine microchannel provides much better mixing than square wave and straight microchannels. It's the bends in the serpentine channels strongly affecting the flow structure that enhance mixing.

For low Reynolds numbers mixing is inhibited by viscous effects and molecular diffusion is the dominant mechanism responsible for mixing [135]. In fact for low Reynolds numbers, 5 - 15, the mixing in square wave, curved and zigzag microchannels is characterised by diffusion

mixing alone [135]. At higher Reynolds numbers, 15 - 276, the presence of transverse flow enhances mixing significantly by utilising chaotic advection. Up to a Reynolds number of 50 all channels give similar pressure drops, above this the curved channel gives a slower rate of increase for its pressure drop with increasing Reynolds number.

Mixing in microchannels is heavily sensitive to the flow regime corresponding to Reynolds number, the work of Liu et al. reveals that these effects also differ when different geometries are considered.

2.5.1.2.6 Impact of Weber Number

The Weber number (We_G) is a dimensionless number that describes the ratio of vapour inertia to surface tension forces, see Eq. 9 [152].

$$We_G = \frac{\rho_G \times U_G{}^2 \times D_H}{\sigma} \qquad \textit{Eq. 9 The Weber Number}$$

This equation can be used to predict the flow regime [152]. For example, for We_G < 6 there will be pure intermittent flow and for We_G > 35 there is pure annular flow.

Garimella et al. has created some nice illustrations of different flow regimes; including annular, wavy, intermittent and dispersed, see Table 15 [130].

Table 15 Description of two-phase flow regimes and patterns [130]

ᵃNumbers in parentheses denote intensity of secondary waves.

An important criterion for micro-channel flows is the transition from intermittent flow to annular or wavy flow, although for some hydraulic diameters there is no wavy flow regime [3]. Increasing tube diameters leads to decreasing intermittent flow regime lengths.

2.5.2 Coating Methods

Whilst the loading of catalysts is typically done in one of two ways; either by coating catalyst layers on the walls or by deploying a packed bed in the microchannel [124], it's the application of wall coating which is of greatest interest to this thesis.

For the remainder of this section, common deposition methods that have been applied in the literature to adhere catalysts onto solid substrates are described. In some cases, these methods are not possible to entirely separate from their catalyst synthesis processes, such as Deposition-Precipitation. There are four sub-sections to consider, a brief section to discuss various methods of synthesizing the catalysts for mechanical deposition, a section considering ideal catalyst/support morphologies with one example, methods of mechanically applying catalyst coatings and, finally, methods to chemically apply coatings from precursors or during synthesis.

2.5.2.1 Ideal Catalyst/Support Morphologies

It is well known in literature that the morphological character of catalysts and their supports has a significant impact on various catalytic properties, not least of which is surface area [156]. It's widely known that catalytic reactions benefit from larger interfacial areas [157] and it's for this reason that catalyst supports are so commonly used, systems like this ideally have the metallic catalyst loaded such that it's highly dispersed over the support material.

Supports can perform multiple different functions in relation to the catalyst metal that they support [157]. Catalyst supports enable some control over the particle size of the catalyst, as it's possible to stabilise smaller metal particles than can be maintained by the pure metals. Supports may also contribute catalytically and may change the pH or otherwise chemically modify the metals.

Properties of interest for supported metals include [157]:

- Particle size
- Surface area
- Dispersion
- Crystal Structure
- Oxidation State

- Purity

The dispersion is the fraction of metal exposed at a surface. Hence why nanoparticles are so favourable for achieving high degrees of dispersion. Whilst there are some properties, such as those listed above, which are almost universally useful in catalysis, there is an extent to which each catalyst has specific requirements and needs that depend on the reaction they will be used for as well as the reaction conditions that are imposed upon it. For example, there are specific favourable values for properties which are ideal when making a Ni/Al_2O_3 catalyst for DRM.

Applying this to an example, in their study on Ni/Al_2O_3 activity in the dry reformation of methane, Newnham J. et. al. [24] found that of the 7, 10 and 15 wt.% Ni loadings on Mesoporous Al_2O_3 supports, the 10 wt.% loading was the most active and stable of all 3 compositions with only 2-3% activity loss in a 200 hour period. However, in their study, some issues were discovered first of foremost of which was undesired carbon deposition. Carbon deposition during methane decomposition is an issue of particular concern to the Ni/Al_2O_3 catalyst [24].

There were four main types of carbon deposition [24]:

- C_α – Amorphous
- C_β – Filamentous
- C_γ – Graphitic Carbon
- Inactive Carbon – Bulk Carbon

Amorphous carbon is exothermically consumed by the Boudard reaction as are both filamentous and graphitic carbon but bulk carbon is not and permanently deactivates catalysts [24]. Both amorphous and bulk carbons are responsible for physically blocking active sites, whereas filamentous and graphitic carbons are not. To increase catalyst life, it's necessary to prevent inactive carbon deposition on active catalyst sites. One method to achieve this is to acquire highly dispersed catalysts with low particle size and strong interactions with their supports.

Some dopants, such as Lanthanum are known to inhibit deposition of non-active filamentous and bulk carbons. The Lanthanum effected this through limiting the maximum particle size of

the Ni to 15nm [24]. High Surface area supports are found to effectively increase Ni dispersion as well as thermal stability, thus decreasing the long-term deactivation of the catalyst.

Amin et. al [158] confirms the role of Ni particle size in prolonged catalyst activity in that smaller particles are less prone to being physically blocked by Carbon deposition. The optimum Ni particle size range was identified as 6-20 nm's, as the carbon depositions this promotes are catalytically favourable rather than inhibitive. Above and below this unfavourable carbon deposition is increased.

Overall, per literature, Ni/Al_2O_3 catalysts intended for DRM are enhanced by:

- Ni particles between 6 and 20nm in size for DRM [158] – inhibits unfavourable C deposition.
- An intermediate Ni loading, reported by [24] as 10wt.% - enhances activity.
- High Surface Area Supports [24] – enhances activity.

2.5.2.2 Synthesis of Catalyst Precursors

There is an enormous variety of catalyst synthesis methods which could be considered. In most of these its' normal to create a liquid solution with catalyst precursors dissolved or suspended within it. Catalyst precursors could be metal salts [110], colloidal solutions for direct deposition, such as metal oxide nanoparticles [111] or even colloidal solutions for sol-gel chemistries [112] and these are produced by process such ion exchange or precipitation. Most catalyst preparation also involves a calcination process to chemically bond the catalyst to its' support and sometimes, to remove organic compounds used in the deposition process. In the interest of conciseness, catalyst synthesis variation will not be explored in depth here, instead any synthesis methods applied during the project will be briefly described in the experimental method.

2.5.2.3 Mechanical Deposition

2.5.2.3.1 Wash coating

Washcoats are layers bonded to the substrate with high surface areas [159]. Their main function is to provide a high surface area for dispersion of the catalyst. It should be mentioned that the usage of the terms Washcoating, Slurry coating and their derivatives is often inconsistent in the literature and care should be taken to clarify the exact meaning the author intends when they use these terms. Washcoating could broadly be taken to mean Dip Coating

[159], Flow Coating [160], Fill & Dry coating [161, 162] and possibly other methods, the important distinction is that a slurry precursor, i.e. a highly viscous solution or dispersion, is used in the process [163], this usually means coats are quite thick.

Washcoating first involves producing a slurry of the desired catalyst and/or adlayer materials [163]. Often binders are used to facilitate bonding to the substrate or adlayer. The washcoat is traditionally deposited from a water-based slurry by dip coating the substrate into the slurry [159]. In some cases, adhesion layers, known as adlayers, are applied as intermediate layers to improve adhesion of the catalyst to the substrate surface or to promote better catalyst morphology [124, 164, 165]. The idea being that direct deposition is not practical for some paired catalyst and substrate compositions so an intermediate layer which adheres effectively to both provides a solution to the problem. For example, Hwang, S. M. et. al. found that their catalyst coating was much more effective with an intermediate adhesive layer [161]. It follows that washcoating and many of the mechanical deposition methods are techniques rarely used in isolation. For example, Peela N.R. et al. applied washcoating then impregnation in series [166].

2.5.2.3.2 Dip Coating

To dip coat a substrate, the substrate is immersed into a solution of the desired coating material, it's then withdrawn, drained and dried by baking [167]. The downsides of this approach, as evident in Figure 46, include the double-sided coverage and the subsequent wastage of material due to the need for an excess of solution of the catalyst material required for this process.
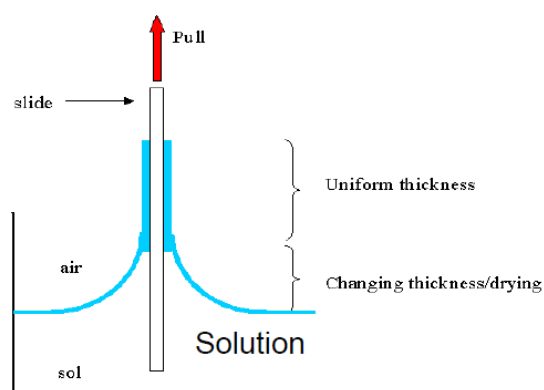
Figure 46 The Dip Coating Process [168].

The speed at which the substrate is drawn dictates the thickness of the coat according to $H = \frac{0.94(\mu v)^{\frac{2}{3}}}{\gamma^{\frac{1}{6}}(\rho g)^{\frac{1}{2}}}$ Eq. 10.

$$H = \frac{0.94(\mu v)^{\frac{2}{3}}}{\gamma^{\frac{1}{6}}(\rho g)^{\frac{1}{2}}}$$ *Eq. 10 the Landau and Levich equation [168].*

This method allows for control of the layer thickness with good uniformity [168].

2.5.2.3.3 Gas Displacement/Flow Coating

This method is a deposition method usable for slurries [160]. It is a two-step process: First the capillary is filled with a viscous fluid and secondly it is cleared by gas being forced through it, as illustrated in Figure 47. Other sources use the term 'Flow Coating' instead [161]. Sometimes surface treatments, such as acid etchants are used to prepare the capillary for coating [160].
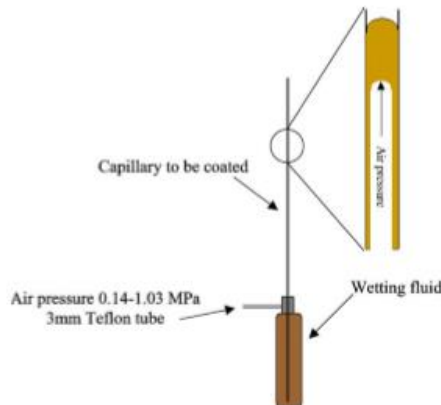
Figure 47 Experimental setup for Gas-Displacement washcoating of capillaries [160].

2.5.2.3.4 Fill and Dry Coating

Fill and dry coating involves filling channels in a micro-structured reactor with the catalyst slurry then room temperature drying and calcination [161, 162]. The liquid components of the solution or slurry evaporate leaving behind a coating on all the walls of the filled geometry.

2.5.2.3.5 Spin Coating

Spin coating involves placing an appropriate dispersion onto the centre of a substrate on a rotatable platform [169]. This platform begins to rotate at high velocity after this dispersion is placed and it spreads out to form a layer over the substrate. In some cases, rotation may begin before deposition of the dispersion.

2.5.2.3.6 Drop Casting

This method involves dropping the solution, usually by pipette, onto the substrate. Subsequent evaporation will occur over a long time or in a shorter time if heating is applied to enhance the drying rate [168].

Binda, M. suggests that the film thickness is proportional to the solution concentration but also indicates that there can be difficulties in achieving fine control over the thickness and the uniformity thereof [168]. Figure 48 illustrates this process [168].
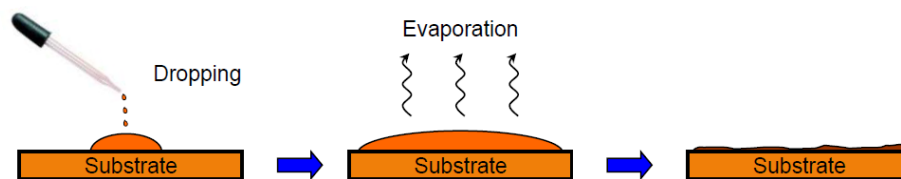
Figure 48 - The Drop-casting Process [168].

2.5.2.3.7 Cold Spraying

Cold spraying begins with the feedstock preparation [170]. The desired deposition materials are mixed in powdered form in the appropriate ratios. The mixture is then deposited at high pressure through a nozzle which rasters over the substrate. During this process, it's not uncommon for particles to cause superficial surface damage to the substrate as they impact.

2.5.2.3.8 Physical Vapour Deposition (PVD)

There are various processes which fall into this category but all of them work along the same principles [171]. To begin with material is vaporized from the source by elevated temperature & vacuum or gaseous plasma. This material, usually a thin disc of pure metal, is transferred to the substrate using a vacuum and condenses upon the substrate as well as every available interior surface of the vacuum chamber.

Thermal evaporation uses heat to cause vaporization of the source whereas Sputter-Coating uses accelerated gas ions, i.e. plasma, to bombard the source and sputter atoms from it. Condensation in both methods is similar [171]. Figure 49 from Sigma-Aldrich illustrates the Sputter Deposition Process, a sub-type of PVD:
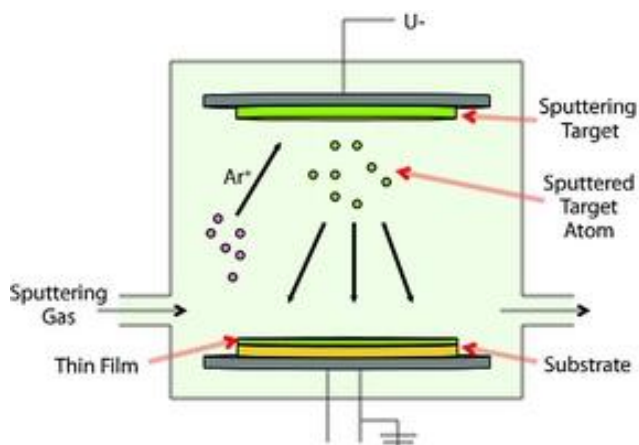
Figure 49 A diagram of Sputter Deposition, produced by Sigma-Aldrich [171].

2.5.2.4 Chemical Deposition

2.5.2.4.1 Chemical Vapor Deposition (CVD)

To achieve deposition using this method the substrates are placed within an air-tight chamber [172]. Reactant gases are injected into this chamber and pass to the other side whilst undergoing reactions. Along the way some of the reactant gas impinges on the substrate where chemical reactions on the surface form the desired film. By-products are continuously removed from the chamber.

2.5.2.4.2 Impregnation

A metal precursor is added to the substrate by applying a solution with a volume chosen in relation to the porosity of the substrate [173]. Capillary action draws the solution into the pores until the pores are full, further impregnation occurs by diffusion, albeit much slower. The process is finished by drying overnight in a low temperature furnace and then calcination at a high temperature [174].

There are two subcategories to impregnation worth noting: Incipient Wetness Impregnation and Wet Impregnation [175]. Incipient Wetness Impregnation uses a solution volume less than the pore volume of the support enabling capillary action to rapidly draw the solution into the pores whereas Wet Impregnation uses an excess solution volume [174].

2.5.2.4.3 Deposition-Precipitation

This method involves simultaneous deposition and synthesis of the catalyst by co-precipitation [175]. The distinction of this process from co-precipitation is that it also involves precipitation of the metal precursors directly onto the support material. Co-precipitation

begins with mixing of aqueous solutions containing the metal precursors, most often in the form of nitrates [175]. A basic pH precipitating agent and the metal precursors are slowly added to deionised water with vigorous stirring under mild heating at a controlled pH value. This precipitate is then filtered, thoroughly dried and calcined.

2.5.2.4.4 Anodic Oxidation

In this method, the substrate is attached to an anode whilst being fully immersed in a bath of dilute acid [176, 177]. During the process oxygen is evolved from the bath and oxidizes the surface of the substrate creating a shallow oxide layer.

2.5.2.4.5 Electrochemical Deposition

Electrochemical Deposition methods produce a metal oxide or metal salt coating on their substrates by electrolysis of a solution containing the desired metal ion or complex [178]. Electrochemical deposition, also called electrochemical plating, involves the reduction of metal ions from aqueous, organic, fused-salt or otherwise described electrolytes. The reduction of metal ions in an aqueous solution, requires an electron input, see Eq. 11 [179].

$$M^{z+}_{solution} + ze^- \rightarrow M_{lattice} \qquad \textit{Eq. 11 The reduction of metal ions in an aqueous solution}$$

Electrodeposition involves the electron supply being provided from an external current [179]. Electroless plating uses a reducing agent in the solution as a source of electrons [180, 181]; no external electric current is required for this process. In both cases, the substrate is a conductive electrode onto which these metal ions deposit when they are reduced.

2.5.2.4.6 Sol-Gel Deposition

A sol is a solid particle dispersion on a micron to sub-micron scale (0.1 – 1 micron) in a liquid with only Brownian motion suspending the particles [182]. A gel is liquid-solid dispersion in which a solid-network contains liquid components. Sol-Gel Deposition begins with the desired colloidal particles dissolved into a liquid to form a sol [182]. The sol is deposited by spraying, dipping or spinning or some other mechanical method. The solid particles are polymerised to produce a continuous gel network. Suitable drying and calcination thermally removes organic and some inorganic components to form an amorphous or crystalline coating.

2.6 LITERATURE REVIEW SUMMARY

This review presented an overview of various AM technologies in the context of heterogeneous catalysis, the nature of materials used for each technology, their capabilities, and limitations.

However, combining these two fundamentally different fields, Heterogeneous Catalysis and AM, was shown to involve significant technical challenges and needs fundamental understanding both in terms of the chemistry and AM technologies. Nonetheless there is an abundance of literature concerning microchannels and coating methods for catalysts, so given that AM technologies can make these miniature reactors there is a strong platform from which to develop functionalised micro-reactors for various applications. Three reactions, DRM, 4-Nitrophenol (4-NP) reduction and glycerol acetalisation were reviewed with the intent to develop surfaces capable of supporting these reactions.

As a tool, AM is an enabling technology. AM has been demonstrated capable of printing complex designs, with catalysts functionalised on surfaces or Integrated into the build materials. AM has even been shown to allow control of reactant stoichiometry through geometry design and has enabled bio mimicry down to the scale of 10's of microns. The efficient use of catalysts has been enabled through this less wasteful manufacturing method and designs with integrated features aside from catalysts, such as proton exchange membranes and purification columns are possible.

In addition, AM is clearly effective at rapid, iterative testing of designs, that is, rapid prototyping. AM is also highly useful in specific material categories of catalyst exploration and has exceptional potential for broader catalyst exploration if material restrictions can be overcome and multi-material systems can be implemented with more AM technologies. AM will continue to find further use in Heterogeneous Catalysis as innovative technologies are developed and a wider range of materials becomes readily available.

CHAPTER THREE – EXPERIMENTAL METHOD

To tackle the major aim "To develop, produce and test miniature, functionalised reactor components made by SLM, both in liquid and gaseous phase catalytic reactions", it's necessary to prioritise some primary objectives before others. Given that the catalysts are the most important aspect of the miniature reactor components, the deposition methodology for catalysts was therefore the first objective to be addressed. To assess the success of meeting this objective, SEM/EDX characterisations were undertaken to gain knowledge of the catalyst morphology and any substrate interactions with the SLM printing materials. The focus of this chapter is, therefore, the coating methods and their outcomes.

Whilst Chapter 2's Literature Review addresses the immobilisation of catalysts on various AM substrates, this chapter is concerned with the immobilisation of catalysts on SLM substrates only. SLM is advantageous in that complex geometries with highly roughened surfaces are produced, enabling increased surface area for catalyst interaction on the macro-scale, by design, and on the micro-scale, by the SLM surface character.

In chapter 2, only two examples of catalysts immobilised on SLM substrates were mentioned; Ambrosi et. al.'s work applied cyclic voltammetry to coat IrO_2 on helical steel printed by SLM [55], whilst Yang et. al's work used an unnamed metallic printing method that appears to be SLM to create a destructible Ni alloy template for 1000°C CVD of graphene using a styrene carbon source [114]. Both cases are isolated examples of catalyst immobilisation on an SLM substrate. The scarcity of alternate methods to deposit catalysts on SLM substrates in the literature is notable and is indicative of the difficulty of applying catalysts to SLM substrates. However, there are simpler catalyst immobilisation methods available. Solvent-based deposition approaches for functionalising SLM substrates with a catalyst; such as drop-casting and fill & dry coating were trialled in this project.

Three major challenges are identified in this work; firstly, that the coatings must adhere and do so in sufficient quantities to be of some use, secondly that they remain adhered during and after the reactions and thirdly that the catalyst is active despite of, or because of, interactions with elements in the SLM substrate alloy. The first of the three challenges is addressed here in the Experimental Method for a variety of metal, metal oxide and acidic catalyst systems which are grouped accordingly.

Other objectives, such as the development of geometries for batch and continuous reactions are addressed briefly to allow a rapid transition to address the objectives associated with testing the catalysts later.

The flow chart in Figure 50 summarises the general method of this work.
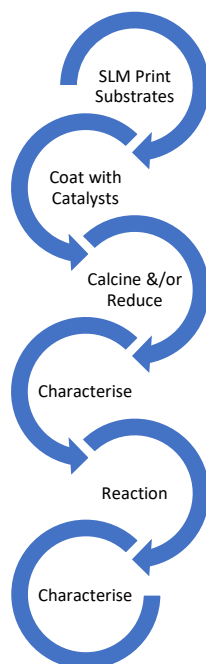
Figure 50 A flow chart of the general methodology used for most experiments

3.1 SUBSTRATE PREPARATION

3.1.1 Build Parameters & Materials

The flat, plate substrates were used for developing the catalytic functionalisation process were printed with SLM 125/250 HL metallic 3D printers using 17-4 PH or Ti6Al4V. The process parameters are described in Table 16.

Table 16 SLM process parameters for printing with Ti6Al4V and 17-4 PH

Parameter	Value
Layer Thickness	30 μm
Laser Power	100 W
Scan Speed	385 mms^{-1}
Build Angle	90°, Vertical
Hatch Distance	0.12 μm

These parameters were applied to both 17-4 PH and Ti6Al4V, the compositions of which are detailed in Table 17 and Table 18.

Table 17 17-4 PH stainless steel SLM powder composition

17-4 PH Composition	Fe	C	Mn	P	S	Si	Cr	Ni	Cu	Nb + Ta
Reference **[183-185]**	Base	<0.07	<1.00	<0.040	<0.030	<1.00	15.00-17.00	3.00-5.00	3.00-5.00	0.15-0.45

Table 18 Ti6Al4V Titanium alloy SLM powder composition

Composition (wt. %)	Fe	Ti	C	V	Al	H	N	O
Ti6Al4V (Grade 5) [94, 98]	0.40	Bal.	0.08	3.5-4.5	5.5-6.75	0.15	0.05	0.2

3.1.1.1 SLM Substrate Characterisation

After SLM printing plates in Ti6Al4V, of 10 x 5 x 2 mm^3 dimensions, according to the build parameters in section 3.1.1, SEM imaging was undertaken. In Figure 51 it was observed that most partially fused particles were ~27μm in diameter with some approaching ~50μm. To gather an approximate particle size distribution quickly, the particle size analysis was performed on the cross-section of the Ti6Al4V sample shown in part by Figure 51 using the particles visible on the sectioned surface. It's recognised by the author that this will produce data less than or equal to the true particle distribution because the particles may be sectioned at positions which are less than their full diameter. Nonetheless there are clear peaks in the particle distribution which give an approximate indication of the particle sizing as being primarily ~27 microns or ~39 microns with outlying particles sized as small as 12.8 microns and as large as 54.0 microns. The underlying substrate of the as-manufactured plate had a wavy roughness; both this and the surface particles gave micro and macro roughness leading to a high overall surface area for these materials. To determine if the SLM process was introducing a distinct surface roughness for a Ti6Al4V plate compared to that of a machined Ti6Al4V plate, SEM images are contrasted in Figure 53.
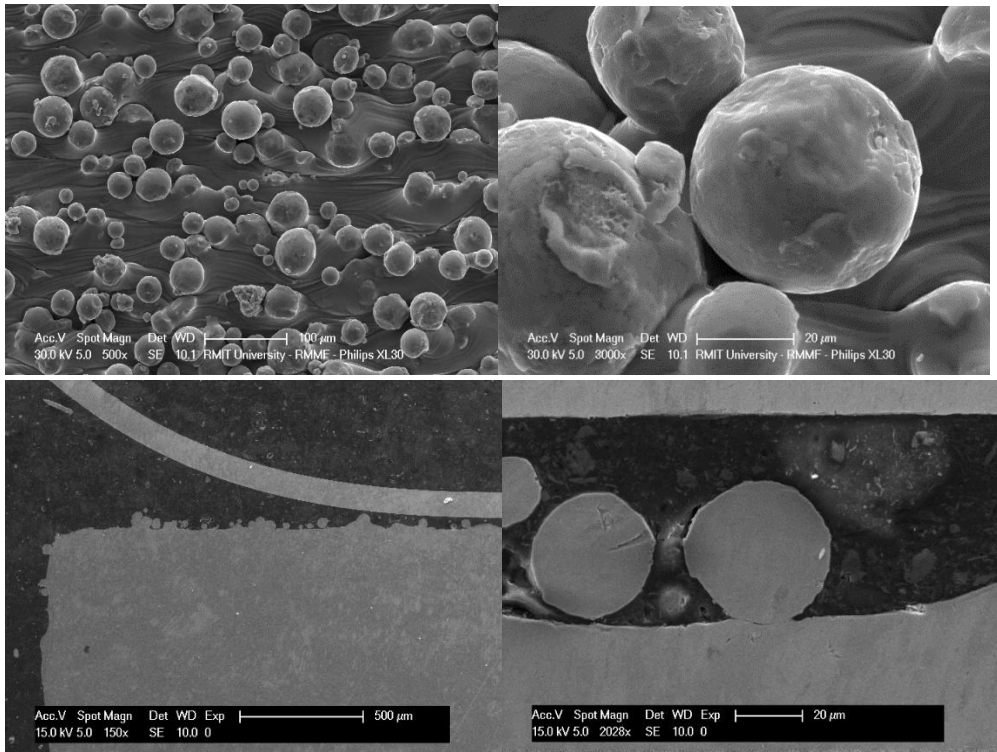
Figure 51 SEM micrographs of an as-manufactured Ti6Al4V cross-section (Top) Surface (Bottom) Cross-section
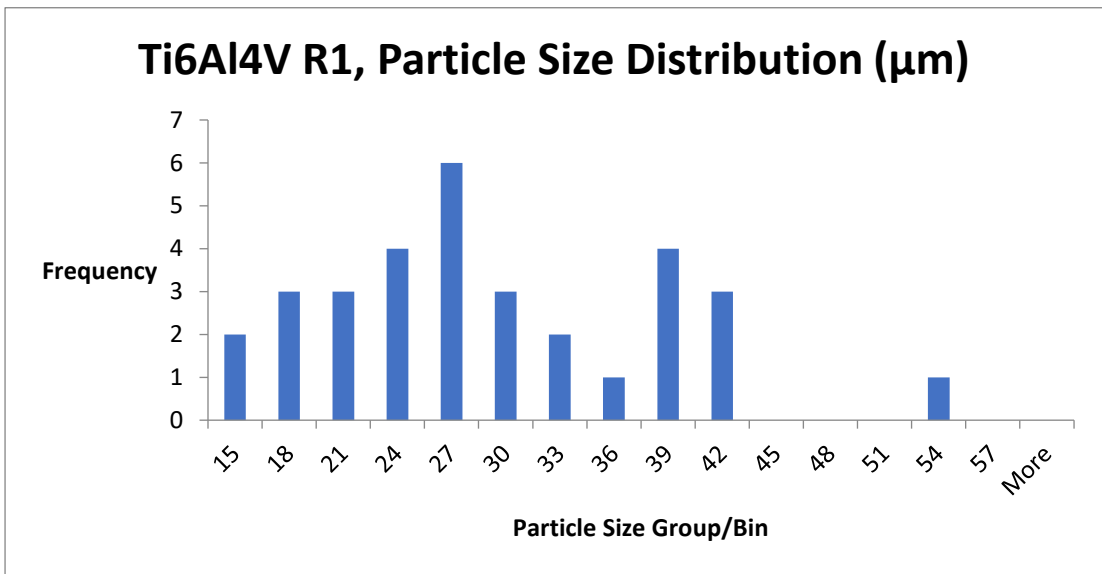
Figure 52 Particle Size Distribution for as-manufactured Ti6Al4V cross-section.
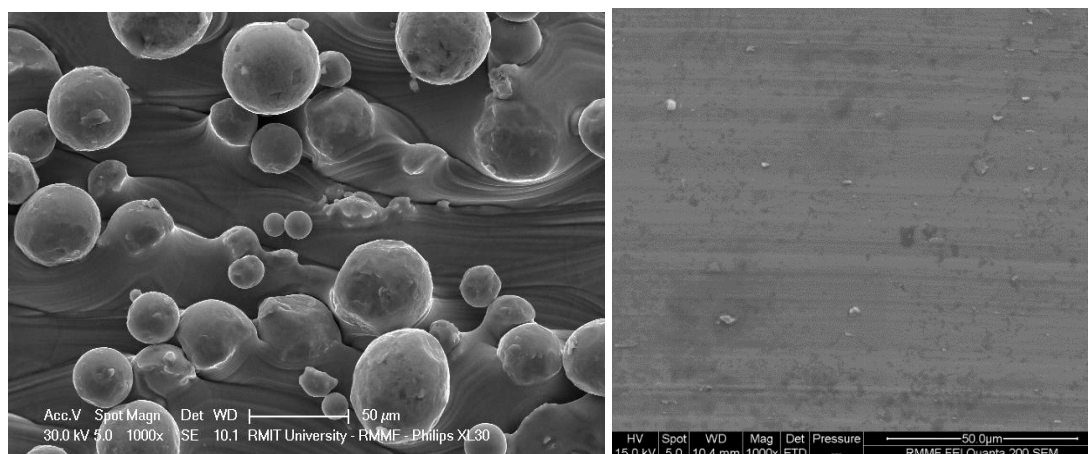
Figure 53 SEM micrographs of (left) An SLM-printed Ti6Al4V surface and (right) A CNC-machined Ti6Al4V surface.

As demonstrated by the micrographs in Figure 53 the roughness of an SLM substrate is visibly distinct from a machined piece of the same alloy. After machining the surface of a Ti6Al4V plate there is no longer any underlying wavy roughness and the SLM particles were completely removed, this demonstrates that machined Ti6Al4V alloys have substantially less surface area than the SLM-printed Ti6Al4V substrates. This is important because high surface area is one of the primary reasons SLM is favourable for printing of catalyst supports.

Various calcination procedures were appplied to Ti6Al4V to ascertain the impact this had on the alloy but also for use in creating a baseline for the impact of the coatings applied to the surface, consider Figure 54.
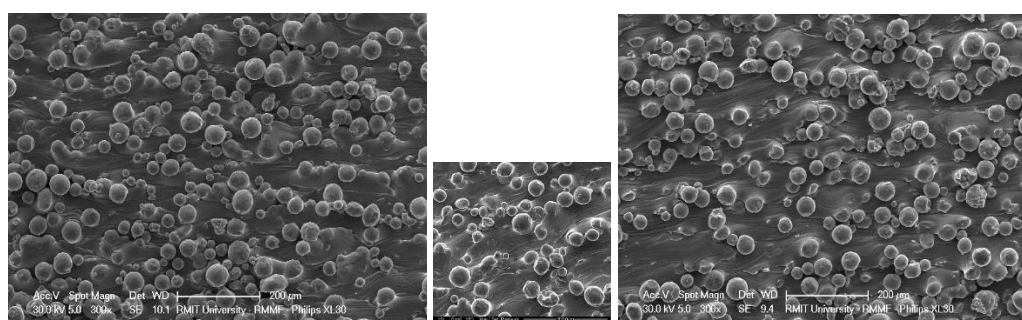
Figure 54 (Left) As-manufactured Ti6Al4V (Middle) Ti6Al4V calcined at 550ºC/2h (Right) Ti6Al4V calcined at 500ºC/4h, all three images have equivalent scales.

Figure 54 shows the representative SEM images of Ti6Al4V substrates after calcination at various temperatures. There were no variations observed in the character of their surface

morphologies with any set of calcination conditions. EDX did not provide strong evidence of any variation of the elemental distribution which appeared to be uniform distribution of Ti, Al and V as expected in the as-manufactured alloy.

To gain more information about the physical and chemical properties of Ti6Al4V, HTXRD was performed. The HTXRD data in Figure 55 reveals that as temperature increases the (110) peak shifts to lower 2θ angles. This suggests that the lattice parameter for the related plane is increasing – as is expected for increasing temperatures. It's also possible that the expansion of lattice volume is being caused by crystal minimisation to a nanoscale size range. There is also a moderate extent of peak broadening present with rising temperature as well as significant peak broadening upon the temperature being lowered back to 323 K again. Peak broadening like this suggests an increased polydispersity – this means that a larger range of crystallite sizes may be present for the material being observed, Ti6Al4V. Alternately the peak broadening could be due to crystallite microstrain. There is not enough data to make a definite conclusion as to the reason for shifting of the 2θ value.
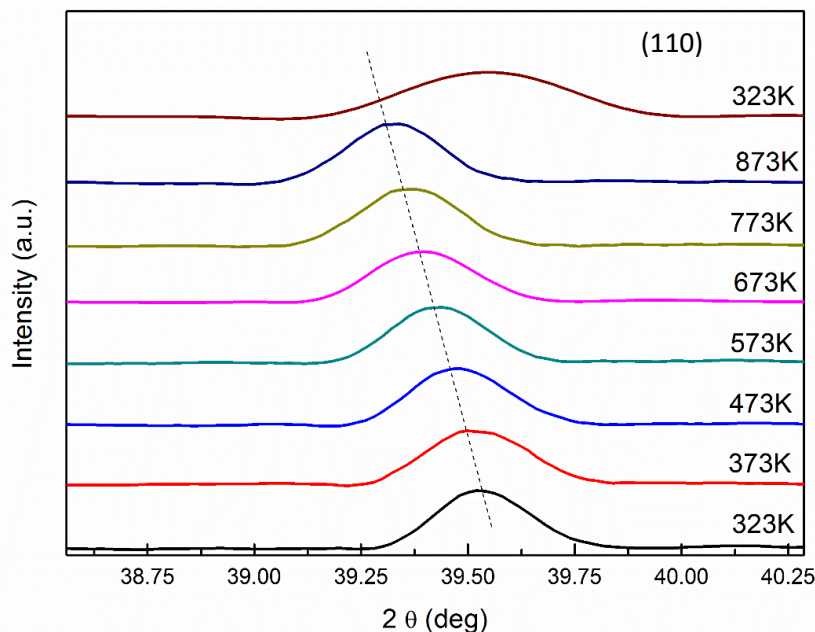
Figure 55 600ᵒC HTXRD of (110) Plane of Ti6Al4V Plate (10 x 5 x 2 mm³)

Given that the peaks' location is at an angle usually associated with a beta-induced (110) plane, it's possible that the β-phase is nucleating in small volumes as the temperature rises. This may also be explained by the occurrence of grain-growth of any already-present β-phase crystals. The increased peak width at lower temperatures may be the result of higher

temperatures decreasing the peak width and thereby obscuring the influence of the newly nucleated β particles.

For chemically specific information, X-Ray Photoemission Spectroscopy was performed under vacuum on the same substrate before and after the heat treatment at 600°C in ambient atmosphere. Two excerpts of the XPS spectrum were focussed upon; in Figure 56 the 2p orbital energy of the element Ti and in Figure 57 the 2p orbital energy of the elemental Al.
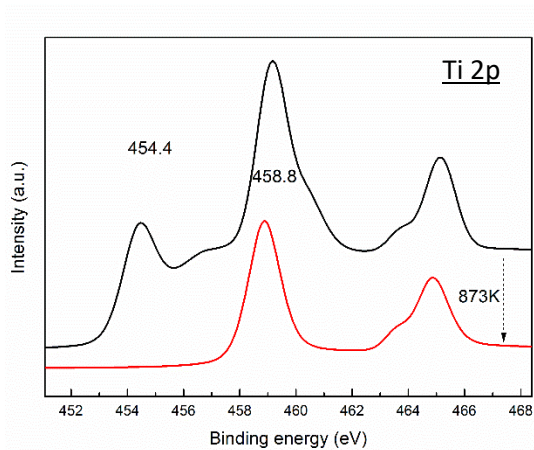
Figure 56 XPS core level spectra of Ti 2p from a Ti6Al4V substrate before and after 600°C calcination.

In Figure 56 the reduction of the 454.4 eV peak after 600°C heating, associated with metallic Titanium that is not oxidized, and the concomitant increase of the 458.8 eV peak, associated with oxidised Titanium (TiO$_2$), indicate that the elemental titanium which caused the 454.4 eV peak has been entirely replaced by the oxidized titanium that causes the 458.8 eV peak. This means that the titanium oxide layer has increased in thickness below the depth at which XPS measures surface compositions.
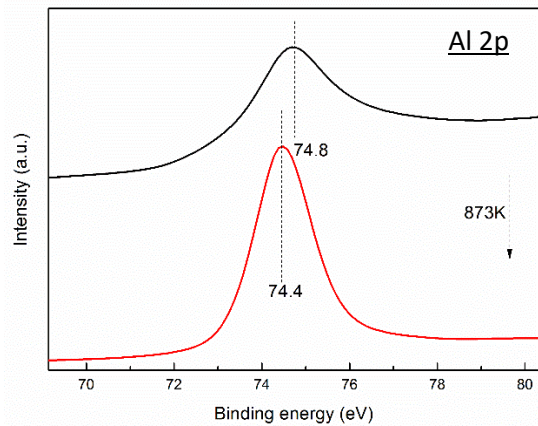
Figure 57 XPS core level spectra of Al 2p from a Ti6Al4V substrate before and after 600°C calcination.

XPS studies of Al showed much better changes. As shown in Figure 57, a significant compositional change is revealed. Prior to heating the Al: Ti ratio at the surface was 4:1, after heating it was changed to 1:1. A fourfold increase in the Al: Ti ratio has occurred at the surface. This indicates that heating to 600°C has caused diffusion of aluminium from the bulk of the material to the surface, where it may be observed by the XPS technique. In addition to this the single peak of Al in Figure 57 shows that the Al is completely oxidised.

In Figure 58 it's observed that for 17-4 PH steel there are relatively fewer SLM particles fused to the surface of 17-4 PH compared to the Ti6Al4V alloy, this reveals that it's less rough than Ti6Al4V and therefore has a smaller surface area to volume ratio. Another observation of importance is the consistent presence of pores all through the bulk of the 17-4 PH steel. Voids such as these are not consistently present on the Ti6Al4V substrate at all. Overall the default structural properties of Ti6Al4V are better than 17-4 PH, as Ti6Al4V is closer to 100% density and has a higher surface roughness.
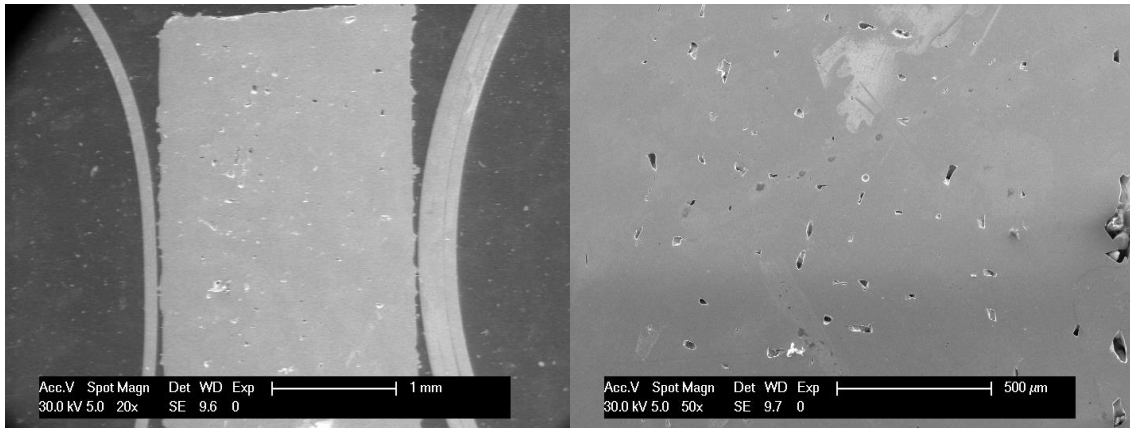
Figure 58 SEM micrographs of the 17-4 PH cross-section.

3.1.2 Geometries for Reaction Testing

Flat substrates were mainly printed to identify, optimise and characterise the various catalyst coating processes. However, for some catalytic processes more complex geometries were applied to demonstrate feasibility of the SLM-printed substrates as chemical reactors. For the DRM reaction, a geometry with 2 open ends was needed because the reaction can only be tested in a continuous configuration. For the build material, 17-4 PH was used rather than Ti6Al4V as it possesses better high temperature stability. As such cylinders with parallel square micro-channels were printed from 17-4 PH in a cylinder shape, see Figure 59 & Figure 60 for the printed cylinders & sections of their CAD files respectively.
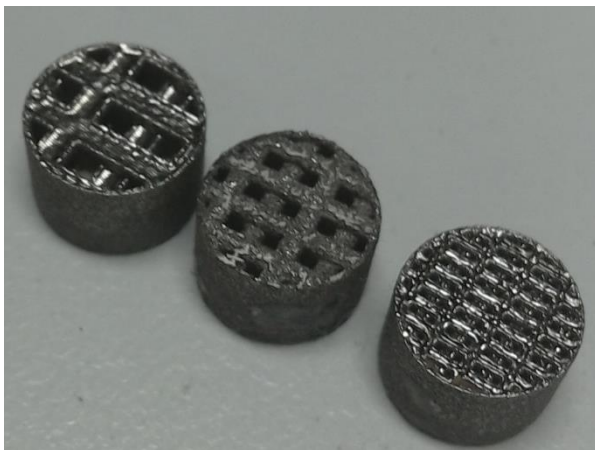
Figure 59 SLM-printed DRM Monoliths with 1.5, 1.0 and 0.5mm channels.
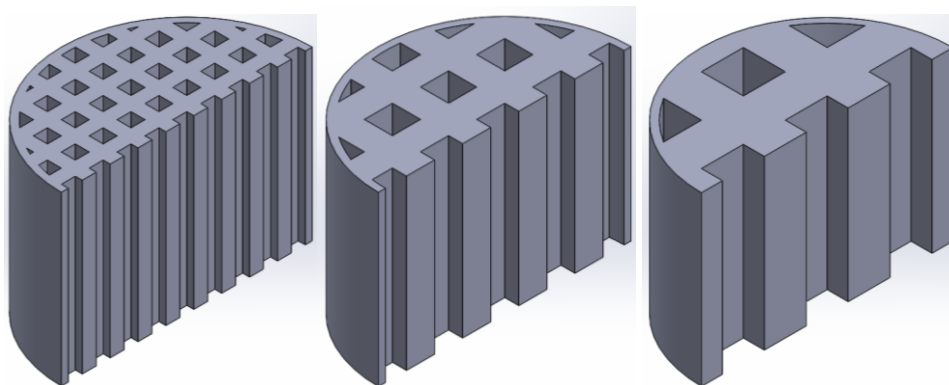
Figure 60 Solidworks screenshots of half-section isometric views of DRM reactor designs with hydraulic diameter 0.5, 1.0 and 1.5 mm.

Furthermore, a half-open geometry was also designed for testing batch reactions. It was named a 'reactionware teapot'. It consists of a cylinder closed on one end, with a lattice providing an increased surface area for any catalyst materials deposited internally, see Figure 61.
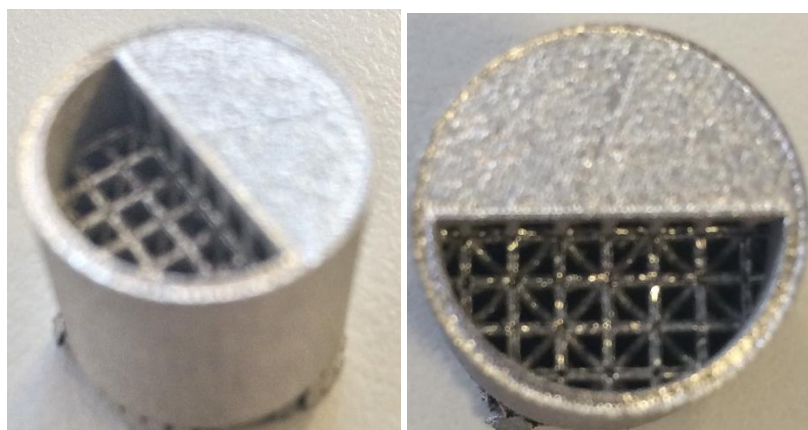
Figure 61 Photographs of reactionware used for glycerol acetalisation

3.2 SEM/EDX SAMPLE PREPARATION
SLM substrates with catalysts deposited on them were characterised by SEM/EDX maps to:

- Confirm deposition of the coating materials
- Determine the distribution of the catalyst deposition including
  - The extent of surface coverage,
  - The homogeneity or discontinuity and,
  - The particle morphology – such as spherical or rod-like

- Identify chemical Interactions with the substrate

For SEM/EDX analysis, mostly the planar substrates were considered, as opposed to the more complex geometries, as planar geometries made sample preparation easiest.

To acquire SEM images two co-operative approaches were applied. In the first approach the coated sample was simply placed coated-side up towards the electron column without any sectioning so that the lateral distribution of coated materials could be observed. This has the drawback of allowing only inferences to be made about coating thickness – especially for continuous coats.

To address this, the second approach involved making a perpendicular section in the sample and mounting one half in a conductive resin so that the thickness of any coatings could be observed.

For this process, samples were sectioned using a circular saw then one half was held vertically in place inside a cylindrical, heated compression chamber with a metallic clip. Conductive phenolic resin was poured around the sample, then was set by heat and pressure. To make the surface viable for SEM/EDX characterisation, polishing was necessary for the resin-embedded, sectioned sample. Hand polishing with 400, 600, 800 and 1200 grit sizes was used with each grinding application perpendicular to the last.

A Kent 3 polishing machine was used to apply a smoother polish, starting with 3μm for 10 minutes, 1μm for 10 minutes and a colloidal silica polish for 15-30 minutes. The samples were then ready for SEM/EDX examination and photography.

It should be noted that whilst the cross-sectional approach occasionally worked, it proved ineffective for discontinuous & particulate coatings of catalysts and for mechanically weak continuous coatings which would often disintegrate during the sectioning process. This makes it difficult to judge if the cross-sectional SEM/EDX data corresponds to the true cross-section of the materials present.

3.3 INSTRUMENT OPERATION AND PARAMETERS

SEM, EDX, XRD, XPS, GC & UV-Visible machines/spectrometers were used for analyses in this thesis, this section briefly describes their operating conditions and the specific machines used.

The parameters used for SEM and EDX varied from accelerating voltages as low as 10kV up to 30kV with spot sizes at 5 or 6, all of which is specifically captioned in all captured SEM images. Secondary Electron Imaging was used exclusively in preference to Back-Scattered Electron Imaging because it provides data relevant to the surface, where the catalyst is situated, rather than the bulk which is not of interest for this thesis. Furthermore, based on availability three microscopes were used for imaging, a Philips XL30 SEM, a Nova NanoSEM and an FEI Quanta 200 SEM. With all these instruments, the software used for EDX was Aztec in its' Quantitative mode.

XRD was performed using a Bruker D8 X-ray diffraction instrument and an operating voltage of 40 kV with a current of 40 mA with CuKa radiation and equipped with an Antonn Paar Heating accessory. This accessory allowed HTXRD so that the impact of calcination temperature on the crystal structure of Ti6Al4V substrates and other samples could be considered. When the Anton Paar was applied, a temperature profile was chosen to vary temperatures at an hourly interval starting from 50°C and raising to 100, 200, 300, 400, 500 and 600°C with 1 hr holding times at the elevated temperature and 1 hr relaxation times at 50°C. XRD scans were programmed to be performed during the elevated temperature holding times.

XPS measurements were obtained using a Thermo K-Alpha XPS instrument at a pressure lower than 1×10^{-9} Torr with core levels aligned with a C1s binding energy of 284.6 eV. The spectra of known elements were selected to assess variations in peak intensities associated with different reduction states, such as metallic Ti and TiO.

For both GC-MS and GC-FID the column a wax column was used with a length of 30mm and a diameter of 0.25mm. The temperature profile applied for glycerol acetalisation was an initial column temperature of 70°C held for 30 seconds prior to increasing at 15 degrees per minute up to 250°C and holding for 5 minutes. A carrier gas of H_2 was used with a Split Ratio of 100. When an FID detector was used, it's temperature was 250°C. This worked out to be a total program time of 17.5 minutes.

For UV-Visible Spectroscopy, an Agilent Technologies instrument: UV Cary 60 UV-Vis, was used with a scan rahenge of 800 – 200nm. Prior to any reaction, the UV-Vis spectrometer was calibrated using DI-H_2O in a 1mL cuvette. To prepare for the reaction, one flask was put aside

for each substrate to be tested. The sampling process required taking 100μL of the reaction mixture and diluting it with 400μL of H_2O before placing it in the UV-Vis Spectrometer. Once the reaction began, at this point and every 5 minutes afterwards, a sample was taken for UV-Vis spectroscopy. The reaction and sampling process were continued for 2 hours or until UV-Vis data indicated the completion of the reaction.

3.4 PROPERTIES OF CHEMICALS USED

3.4.1 Chemical Reagents

The following table summarises the properties all chemicals used as reagents in the DRM, 4-NP reduction and Glycerol Acetalisation reactions.

Table 19 Reagent suppliers, purities and other relevant information

Reagent Name	Reagent Formula	Supplier	Purity	Minor Impurities
Methane	CH_4 (g)	BOC	>99.995%	N_2<30ppm O_2<5ppm H_2O<10ppm CO<10ppm CO_2<10ppm Hydrocarbons<30ppm
Carbon Dioxide	CO_2 (g)	BOC	>99.99%	H_2O<10ppm Hydrocarbons<20ppm O_2/N_2<70ppm
Hydrogen Gas	H_2 (g)	BOC	>99.999%	O_2<1ppm Hydrocarbons<1ppm N_2<4ppm H_2O<4ppm
Helium Gas	He (g)	BOC	>99.999%	O_2<2ppm H_2O<2ppm N_2<4ppm
Argon Gas	Ar (g)	BOS	>99.999%	Hydrocarbons<0.2ppm CO<0.2ppm CO_2<0.5ppm O_2<1ppm H_2O<2ppm N_2<5ppm
4-Nitrophenol	$O_2NC_6H_4OH$ (s)	Fluka-Analytical	>99.5%	Ca<10ppm Cd<5ppm Co<5ppm Fe<5ppm K<50ppm Mg<5ppm Ni<5ppm Pb<5ppm Zn<5ppm Cr<5ppm Cu<5ppm Mn<5ppm Na<50ppm
Milli-Q water	H_2O (l)	RMIT:CAMIC	18.2MΩ @ 25°C	None specified.
Sodium Borohydride	$NaBH_4$ (s)	Sigma-Aldrich	>98%	Silica and Magnesium Carbonate, Iron cations.
Glycerol	$HOCH_2CH(OH)CH_2OH$ (l)	Gold Cross	Not specified.	H_2O
Solketal, (DL-1,2 – Isopropylideneglycerol)	$C_6H_{12}O_3$ (l)	Sigma-Aldrich	>97%	None specified.
Acetone	CH_3COCH_3	Chem-Supply	>99%	H_2O<0.5% Ignition Residue<0.005% Acetic Acid<0.0002%

3.4.2 Catalyst/Support Synthesis Chemicals

The following table summarises the properties all chemicals used in catalyst and support synthesis for the DRM, 4-NP reduction and Glycerol Acetalisation reactions, except where already mentioned under the Chemical Reagents section.

Table 20 Synthesis Chemical suppliers, purities and other relevant information

Reagent Name	Reagent Formula	Supplier	Purity	Minor Impurities
Acetonitrile	CH_3CN	Unichrom	>99.7%	Acidity<0.005% H_2O<0.1%
Citric Acid Monohydrate	$HOC(COOH)(CH_2COOH)_2.H_2O$	Merck	>99.5%	Cl<0.002% Oxalates<0.05% SO_4<0.005% Cu<0.001% Fe<0.001% Pb<0.001% Sulfated Ash<0.05% 7.5%<H_2O<9%
Dodecylamine	$CH_3(CH_2)_{11}NH_2$	Sigma-Aldrich	>98%	None specified.
Dichloromethane	CH_2Cl_2 (l)	Chem-Supply Pty Ltd	>99.5%	Non-volatiles<0.01% H_2O<0.01%
Chloroauric Acid	$HAuCl_4$ (aq)	Sigma-Aldrich	~50% Au basis	None specified.
Palladium Chloride – Cyclooctadiene ligand	$PdCl_2$-COD (s)	Synthesized by Steven Priver	N/A.	Potentially traces of: COD, H_2O, EtOH, HCl.
Oleic Acid	$CH_3(CH_2)_7CH=CH(CH_2)_7COOH$ (l)	Sigma-Aldrich	>90%	None specified.
Copper(II) Oxide*	Cu(II)O (s)	Sigma-Aldrich	>98%	None specified.
Aqueous Zinc Oxide**	ZnO (aq)	Kannan?	50 wt.% in H_2O	None specified.
Nickel Nitrate hexahydrate	$Ni(NO_3)_2{\cdot}6H_2O$ (s)	Aldrich	Ni component > 94.5%	None specified.
Aluminium Hydroxide	$Al(OH)_3$ (s)	Sigma-Aldrich	Al_2O_3 50-57 wt.%	Aluminium Carbonate
Rhodium Chloride	$RhCl_3$ (s)	Sigma-Aldrich	>98%	None specified.
Magnesium Hydroxide	$Mg(OH)_2$ (s)	Sigma-Aldrich	>95%	NH_4^+<0.05% Na<0.005% Cu<0.0005% Pb<0.001% Zn<0.001% Fe<0.02% K<0.005% Cl<0.5% Al<0.02% Ca<0.7%
Iron(III) Chloride	$FeCl_3$ (s)	BDH Chemicals	>98%	HCl<0.03% SO_4<0.02% Pb<0.005%

*Particle Sizing <10μm's
**CuO nanoparticles all < 100nm, and <35nm on average

3.5 CATALYST SYNTHESIS AND DEPOSITION

All the flat, SLM substrates were coated with catalysts that consist of metal, metal oxide or metal chloride compositions. Different coating approaches were applied for different catalysts as described in this sub-section.

3.5.1 Metals

3.5.1.1 Au Nanoparticles

Nanoparticulate Au is known to be an effective catalyst for both oxidation and reduction reactions [186] and TiO_2 is a consistently used as a support for Au nanoparticles [187]. Therefore, Ti6Al4V was used as a substrate for Au nanoparticles. To deposit Au on an SLM substrate, we need to form Au nanoparticles prior to deposition. Au nanoparticles were prepared as follows. Au Nanoparticle synthesis began with the preparation of 4 different solutions. 0.526g citric acid monohydrate ($C_6H_8O_7.H_2O$) was dissolved in 100mL water to make a ~2.5×10^{-2} M solution, 0.1907g sodium borohydride ($NaBH_4$) was dissolved in 50mL water to make a ~0.1 M solution, 18.5mg dodecylamine ($C_{12}H_{27}N$) was dissolved in 50mL of dichloromethane (DCM) to make a 1.0×10^{-3} M solution and 4mL of 3.3×10^{-3} M chloroauric acid ($HAuCl_4$) was diluted up to 500mL with H_2O to make a 2.5×10^{-4} M $HAuCl_4$ solution.

The HAuCl solution was stirred whilst 5mL of citric acid solution was added, followed immediately by addition of 15mL of sodium borohydride solution. Citric acid peptised the Au nanoparticles to prevent their aggregation. Sodium borohydride reduced the Au oxidation state from +3 to 0. After stirring overnight, 50mL of dodecylamine ($C_{12}H_{27}N$) in DCM solution were added to the solution. The solution was then poured into a separating funnel, settled and the wine-red DCM solution was extracted.

Rotary evaporation removed the DCM solvent, leaving the Au nanoparticles as a residue. This residue was dissolved in a smaller volume of 5mL of DCM to make a 2.64×10^{-3} M Au nanoparticle solution. Drop casting by micro-pipette in various amounts on Ti6Al4V was applied. Alternate deposition procedures were also tested, as follows:

Horizontal Immersion: Substrates immersed horizontally in an Au nanoparticle solution.
50µL Drop Casting: 50µL of Au nanoparticle solution micro-pipetted onto substrates.
300uL Drop Casting: 300µL of Au nanoparticle solution micro-pipetted onto substrates.
Vertical Immersion: Substrates immersed vertically in an Au nanoparticle solution.

Some samples were left after drying but for the remainder, various calcination procedures were implemented at 400 – 600°C for 2-4 hours in static air or flowing 4% H_2 in N_2.

In Figure 62 the first coating Au nanoparticles on Ti6Al4V may be observed, it was calcined at 500°C/4h, with an ID of [HI Au NP-T-500°C/4h]. Most observed Au particles are sub-micron in diameter so they can be confidently described as nanoparticles. Their deposition behaviour is to deposit on both the SLM particles and the underlying surface. The dispersion extends all over the substrate surface with low relative surface coverage.
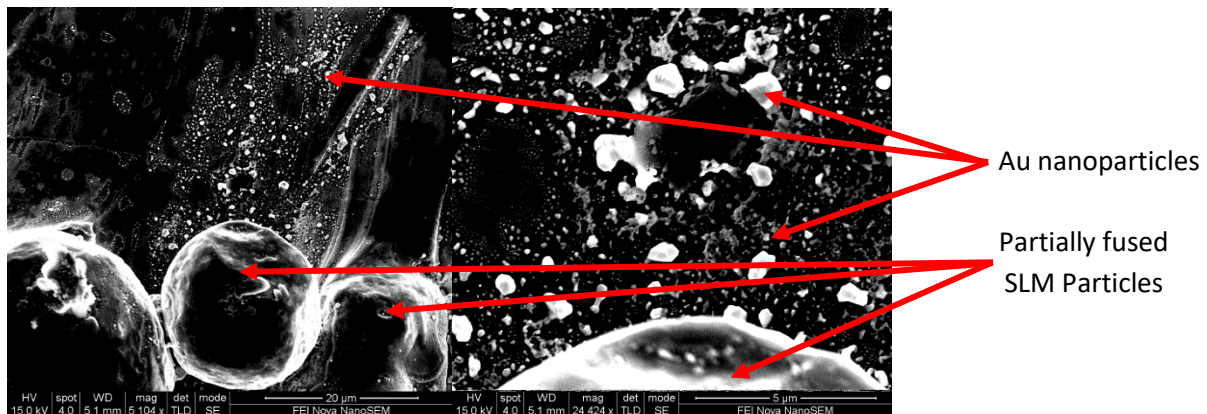
Figure 62 SEM micrographs of [HI Au NP-T-500°C/4h]

Various other calcination conditions were applied giving subtle structural distinctions to the structure of the Au on the Ti6Al4V substrates. For both the following sample IDs; [HI Au NP-T-500°C/3h] and [HI Au NP-T-600°C/3h], two distinct regions were found. In the sparse regions, there was less Au present than in the dense regions. An example of a sparse region may be seen in the top right and bottom right micrographs of Figure 63 & Figure 64; the Au was present as discrete nanoparticles. These regions often had Au nanoparticles distributed in layers, possibly due to patterns created by drying of the DCM solvent used for deposition – although such layering was less prevalent for the [HI Au NP-T-600°C/3h] system. A typical example of a dense region was present on the top middle micrograph of Figure 63 & Figure 64; the Au was present as a percolated, continuous thin film. The percolation of the continuous thin films of Au in the dense regions is most likely due to the boiling & evaporation of the ligand dodecylamine which was used as a surfactant to fix the Au to the Ti6Al4V surface.

In addition, observation of the bottom middle micrograph of Figure 63 & right-side micrograph of Figure 65, shows that both samples have wrinkles present on the surface, which were more abundant for 600°C calcination than 500°C calcination. It's suggested that

the Ti6Al4V alloy is being degraded in some way, especially given that Ti oxidises so easily, although the EDX images in Figure 66 do not clarify how.
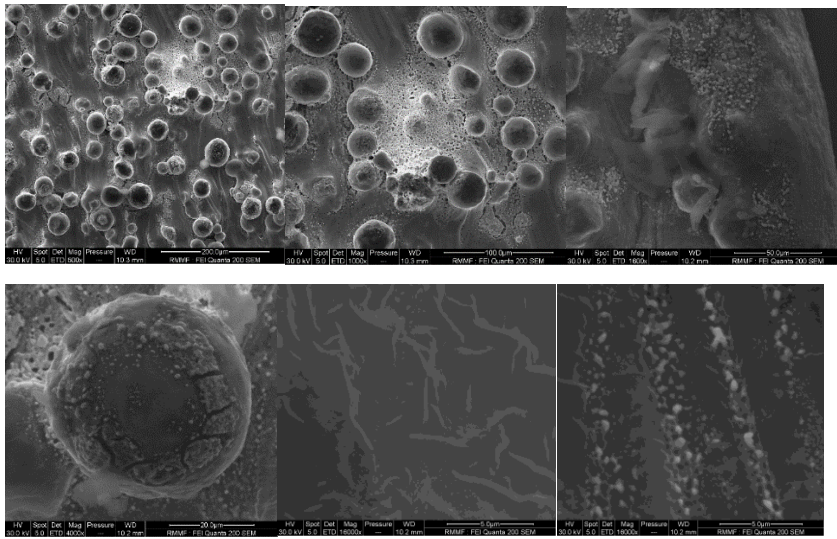
Figure 63 SEM micrographs of [HI Au NP-T-500ºC/3h]
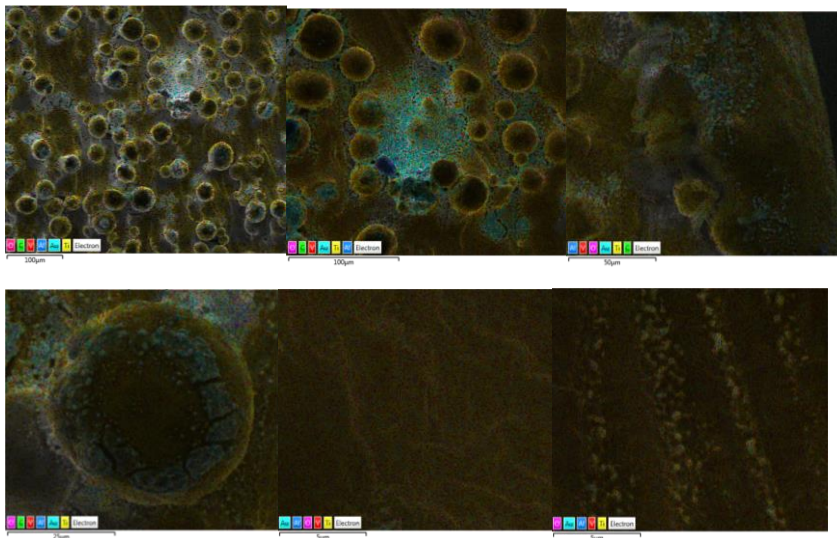
Figure 64 Corresponding EDX micrographs of [HI Au NP-T-500ºC/3h]
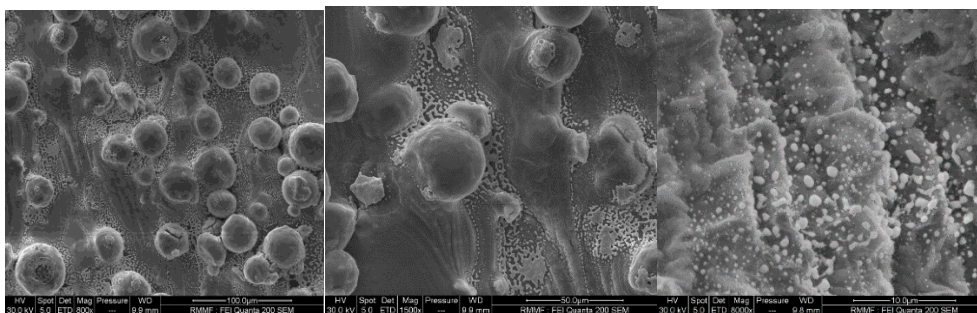
Figure 65 SEM micrographs of [HI Au NP-T-600°C/3h]
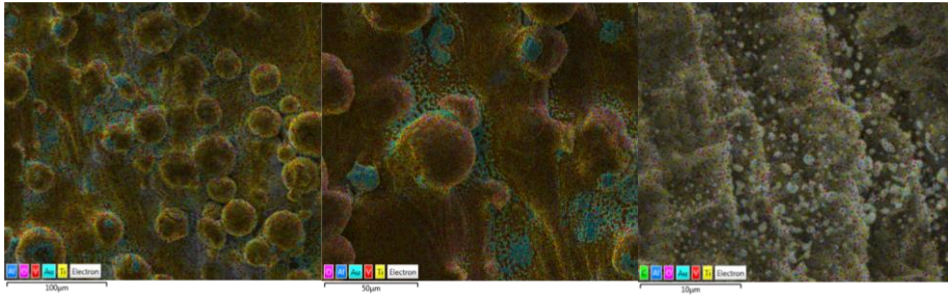
Figure 66 Corresponding EDX micrographs of [HI Au NP-T-600°C/3h]

To enable a contrast on the impact of oxidising and reducing atmospheres, SEM/EDX data was collected for the [300µL Au NP-T-H$_2$ 400°C/3h] sample. The Au distributions on calcined (static air) and reduced (4% H$_2$ in N$_2$) Au nanoparticles coatings are distinct from each other which can be clearly seen from the images shown in Figure 125 & Figure 67.

Although [HI Au NP-T-500°C/3h] and [HI Au NP-T-600°C/3h] are characterised as having some percolated continuous thin films of Au, [300µL Au NP-T-H$_2$ 400°C/3h] exhibited no such percolation and in the regions of dense Au deposition the Au was distributed as discontinuous islands rather than a continuous thin film. It's highly probable that the reducing atmosphere left the dodecylamine on the Ti6Al4V – which explains why the Au-dense regions are not percolated. This conclusion is supported by the observation that there is still carbon present on the [300µL Au NP-T-H$_2$ 400°C/3h] substrate after heat treatment, see Figure 68.

The carbon distribution on [300µL Au NP-T-H$_2$ 400°C/3h] is mostly uniform over the Ti6Al4V substrate, although given that it produces a much weaker signal than Au, no strong correlations can be made between Au and C distribution. Like [HI Au NP-T-400°C/4h], [300µL Au NP-T-H$_2$ 400°C/3h] has Au nanoparticles smaller than 1 micron all over its' surface, as shown in Figure 67. Unlike the calcined Au nanoparticle coatings, the reduced Au nanoparticle coating also had Au nanoparticles as large as 10's of microns all over its' surface. These larger particles appear to be aggregates of smaller Au nanoparticles. If that is case then the oxidising atmosphere appears to prevent this particle aggregation, whereas the reducing atmosphere promotes this aggregation.
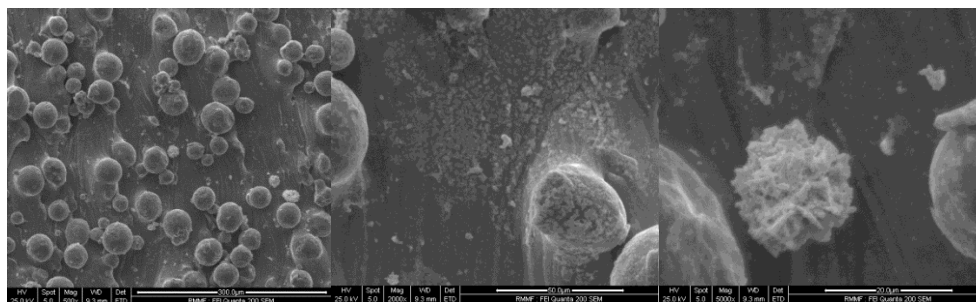
Figure 67 SEM micrographs of [300μL Au NP-T-H_2 400°C/3h]
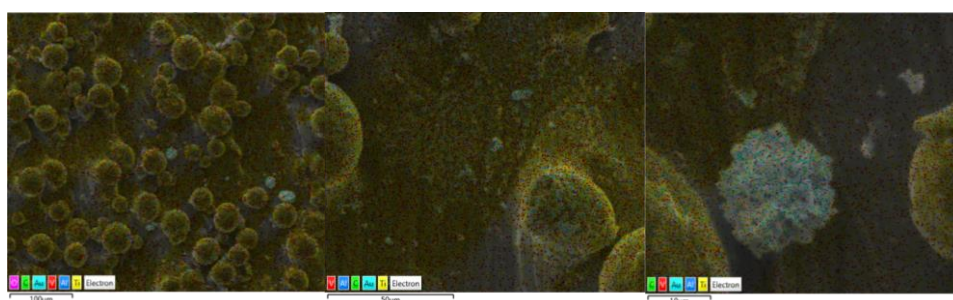
Figure 68 Corresponding EDX micrographs of [300μL Au NP-T-H_2 400°C/3h]

Further SEM and EDX data is explored within the context of the relevant reaction in Chapter 5.

3.5.1.2 Pd Nanoparticles

Pd is a well-known catalyst for hydrogenation, reduction, and C-C coupling reactions [188-190]. Like Au coating on an SLM substrate, Pd nanoparticles were prepared prior to its' deposition. A couple of different methods were trialled for coating Pd Nanoparticles.

Pd nanoparticle synthesis is as follows. 14.196mg $PdCl_2$-COD (Cyclo-octadiene ligand) was dissolved in 50mL of DCM to make a 1.0 x 10^{-3} M solution, similarly 9.2675mg of DDA (Dodecylamine) was also dissolved in 50mL DCM to make a 1.0 x 10^{-3} M solution* and 9.4575mg of $NaBH_4$ was dissolved in 25mL water to make a 0.1 M solution. The $PdCl_2$-COD and DDA solutions were mixed together then the 25mL of $NaBH_4$ solution was added immediately afterwards and stirring continued until there was no further colour change after 10 minutes.

*In a method variant 15.9μL oleic acid replaced DDA as an alternative ligand.

For the DDA ligand variant, most of the Pd was observed resting as a particle dispersion on top of the water the sodium borohydride was dissolved in, instead of being dispersed as very fine particles homogenously throughout the DCM. Nonetheless Ti6Al4V substrates were dip-coated using this floating layer then dried or calcined at 400°C for 4h.

For the oleic acid ligand variant, after mixing the $PdCl_2$-COD with Oleic Acid and $NaBH_4$, the DCM solvent resulted in a dispersion of Pd particles throughout the DCM. This was subsequently evaporated using a rotary evaporator at 180rpm and 350 Torr, leaving a black precipitate thought to be Pd nanoparticles. Concentration of this precipitate in 10mL of DCM made a 5.0×10^{-3} M solution. Unlike the DDA ligand variant, this method involved the use of drop-casting by micro-pipette on Ti6Al4V rather than dip-coating. Substrates were then dried or calcined at 400°C for 3 hours in static air.

A more direct approach dissolved 2mg of $PdCl_2$(COD) in 2mL DCM then drop-casting 100µL of this solution onto a Ti6Al4V substrate. 400°C Reduction occurred for 3h 15m in a flowing 4% H_2 in N_2 atmosphere.

All SEM, EDX and other data associated with Pd nanoparticles is included in Chapter 5, in the context of their application to 4-NP reduction.

3.5.2 Metal Oxides & Metals on Metal Oxides
3.5.2.1 CuO

CuO is known as an important catalytically active metal oxide for CO_2 hydrogenation to methanol, although it's usually grouped with other metal oxides to improve its properties [191]. A commercially available CuO powder dissolved in a solvent was drop casted in this project. CuO synthesis begins with the dissolution of 17.0 mg of Cu(II) Oxide power into 5mL water. After thorough stirring, 100µL of solution is drop-cast by micro-pipette onto the 10 x 5 mm^2 face of a Ti6Al4V substrate. Overnight drying precedes 500°C calcination for 4 hours.

From the SEM micrographs of Figure 69 and the Layered EDX map of Figure 70 it is clearly seen that the CuO is uniformly distributed all over the Ti6Al4V substrate. These data demonstrated that the CuO is present as rough, percolated, discontinuous aggregates, where it's deposited on the protruding particles. Conversely, the CuO is present as a rough, percolated, continuous coating on the underlying substrate leaving neglible gaps through

which the Ti6Al4V is exposed. The high roughness of the CuO is favourable for catalytic applications and supplements the process-induced roughness of the SLM substrates. Overall this is an excellent catalyst coating with a more-than sufficient loading.
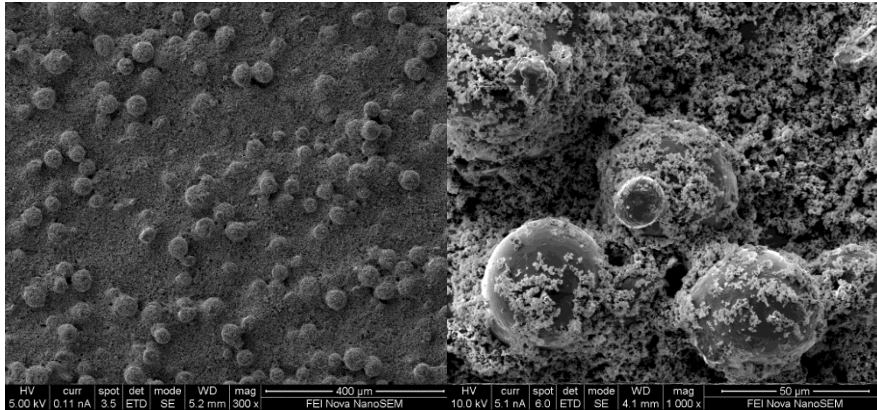
Figure 69 SEM micrograph of CuO-coated Ti6Al4V surface, heated to 500ºC for 4 hours
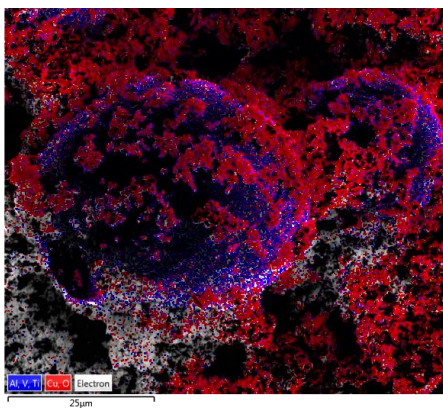
Figure 70 EDX micrograph of CuO-coated Ti6Al4V surface at 2000x, heated to 500oC for 4 hours

3.5.2.2 ZnO

The ZnO catalyst is an important photo-catalyst and is applied to photocatalytic degradation of dyes [192]. The steps for ZnO synthesis and deposition were performed as follows.

A commercially available ZnO aqueous dispersion, with a density of 1.7mg ZnO/mL, was drop-casted by micro-pipette onto the 10 x 5 mm^2 face of a Ti6Al4V substrate with a volume of 100μL. After drying in ambient air the substrate was calcined at 500ºC for 4 hours.

The results of this method are shown in the surface SEM & EDX data of Figure 71 and Figure 73, and in the cross-sectional SEM data of Figure 72.
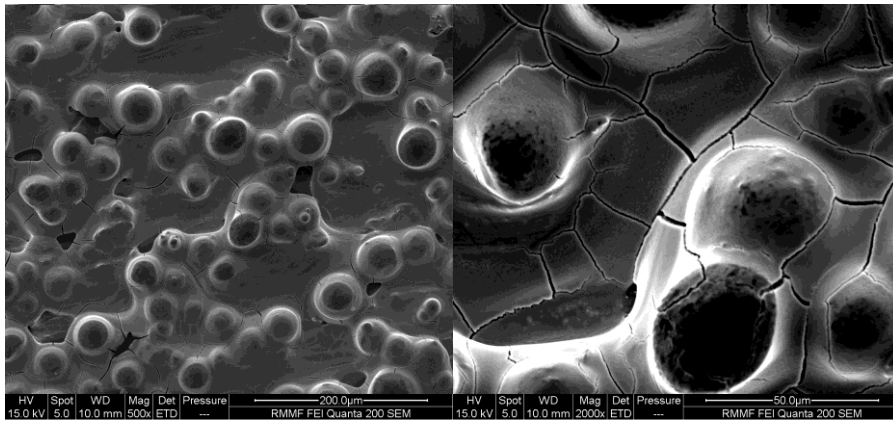
Figure 71 SEM micrographs of ZnO-coated Ti6Al4V surface, heated to 500ºC for 4 hours
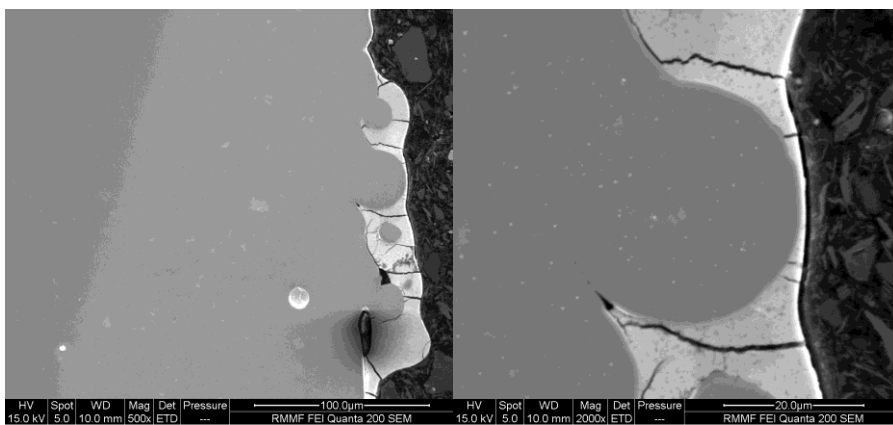
Figure 72 SEM micrographs of ZnO-coated Ti6Al4V cross-section, heated to 500ºC for 4 hours
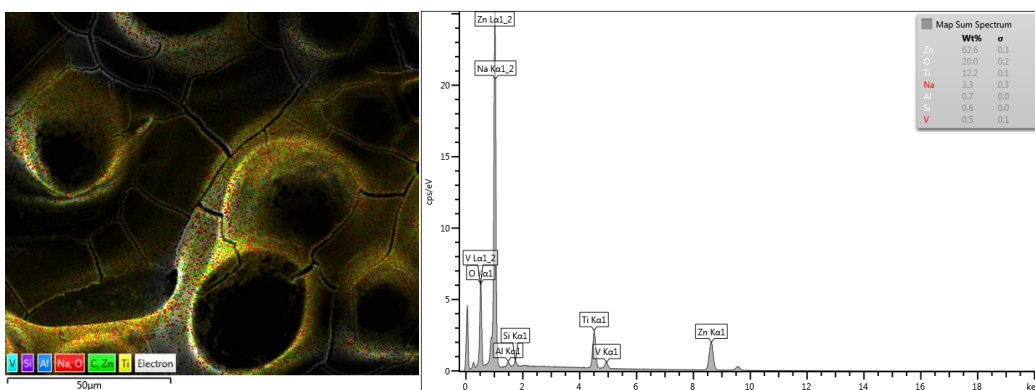
Figure 73 EDX micrograph and Quantitative Spectrum of ZnO-coated Ti6Al4V surface at 2000x, heated to 500ºC for 4 hours

In the cross-sectional micrographs of Figure 72, the ZnO coating was observed as thicker on the underlying layer and thinner on the tops of the SLM particles. In the EDX micrograph and quantitative spectra of Figure 73 ZnO is shown to have an excellent relative surface coverage

of ~60% when only including the Zn and ~80% when also including the O, although the true ZnO coverage will be in the range of 60% - 80% as not all the O is associated with the Zn. Some thicker regions of ZnO coatings adjacent to SLM particles indicate that the SLM particles anchor the ZnO coating.

Cracking is clearly present in all the SEM data of Figure 71 and Figure 72 as well as the EDX data of Figure 73. This cracking primarily occurs perpendicular from the substrate-coat interface to the upper surface through the ZnO and is less often parallel to the Ti6Al4V substrate. This suggests that the ZnO coat is mechanically weaker than the substrate & furthermore, its' suggested that the ZnO cracking mostly occurs due to a difference in thermal expansion as well as, potentially, a difference in crystal structure mismatch.

3.5.2.3 CuZnO

Mixed metal oxides of CuO/ZnO are commonly used for the selective conversion of syngas into methanol [193]. The steps for CuO/ZnO synthesis and deposition were performed as follows:

1. Pour 5 mL of aqueous ZnO dispersion into a vial.
2. Add 17.0 mg of Cu(II) Oxide powder to this vial.
3. Drop-cast 100μL of solution by micro-pipette onto the 10x5mm face of a Ti6Al4V substrate.
4. Dry in ambient atmosphere.
5. Place coated substrate in a furnace to heat at 500°C for 4 hours.

The results of this method are shown in the SEM data of **Error! Reference source not found.**Figure 74, in the EDX data of Figure 75, in the XRD of Figure 76 and the XPS data of Figure 77.
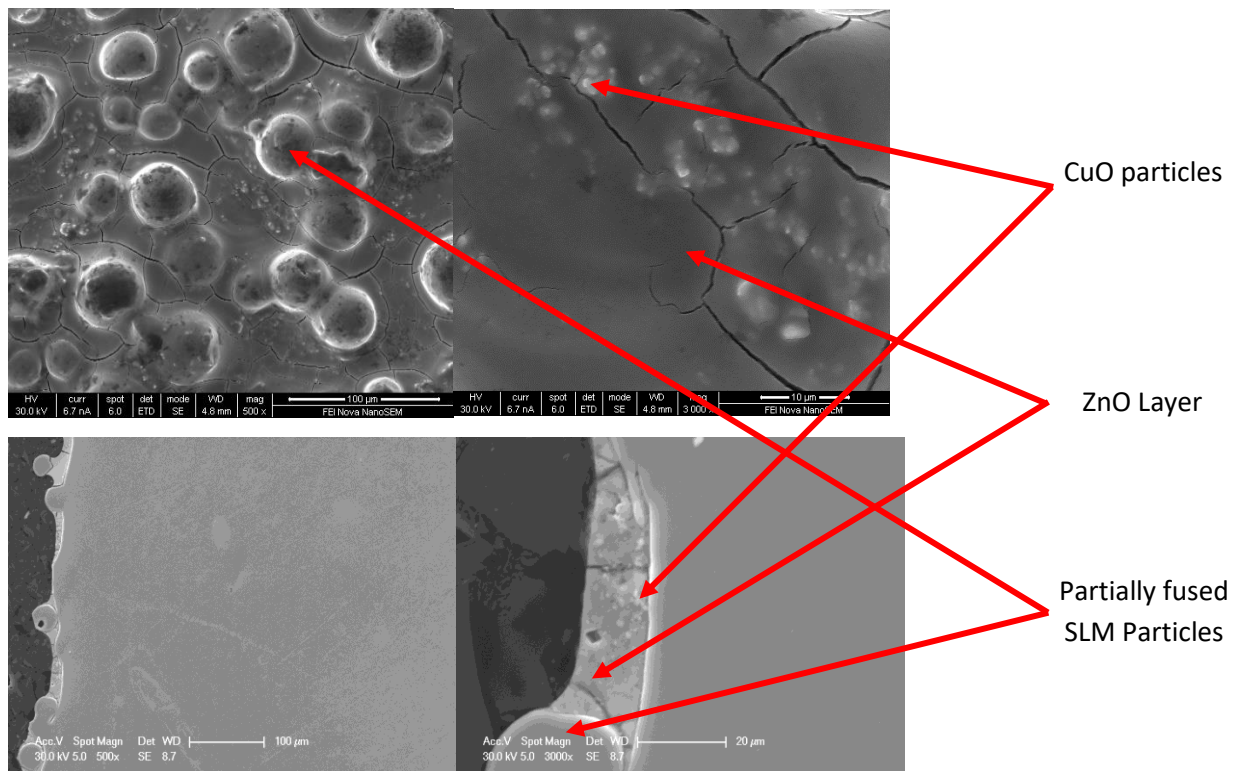
Figure 74 SEM micrographs of CuZnO-coated Ti6Al4V heated to 500°C for 4 hours (top) surface (bottom) cross-section

The SEM micrographs of Figure 74, clearly reveal that the addition of CuO to the ZnO coating has had little impact on the extensive cracking of the ZnO coating. This is particularly evident in the 3000x magnification images in which cracking has occurred despite the immediate presence of submerged CuO particles.

Only after 30kV accelerating voltages were used, did both the ZnO and the CuO become visible in the surface EDX mapping of Figure 75, otherwise under 10kV only the ZnO coating was visible. Increased beam interaction volumes occur at higher beam voltages indicating that the CuO is at present below the surface of the ZnO coating. This is clearly confirmed by the Cu K series EDX map of the substrate cross-section in Figure 75 which directly shows that the CuO is mostly submerged within the smoother ZnO layer. As for the pure ZnO coating the Zn EDX map of the CuZnO coating reveals that the ZnO layer is thickest below the protruding substrate particles, and has only a light coat on top of them.
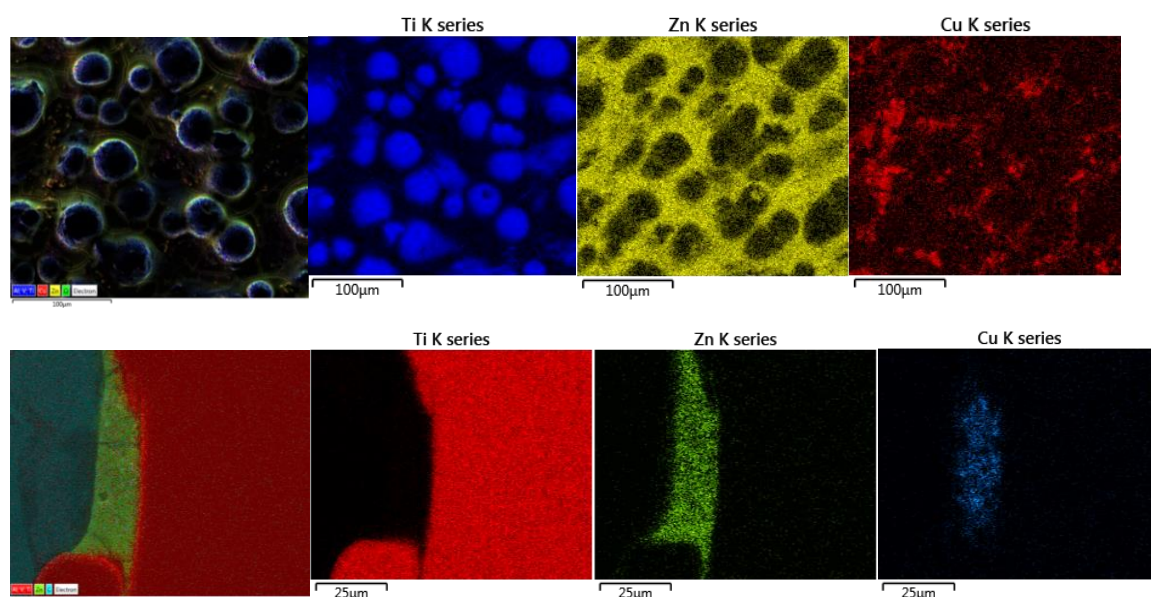
Figure 75 EDX micrographs of CuZnO-coated Ti6Al4V heated to 500°C for 4 hours (top) surface (bottom) cross-section

The XRD data shown in Figure 76 indicates that the CuO present in the CuO and the CuZnO depositions are not primarily crystalline but are primarily amorphous, conversely the XRD shows that ZnO phase that exhibits strong crystallinity for both the ZnO and CuZnO depositions. However, there are certain crystalline phases corresponding to CuZnO that were present in the mixed CuO and ZnO coated substrate.
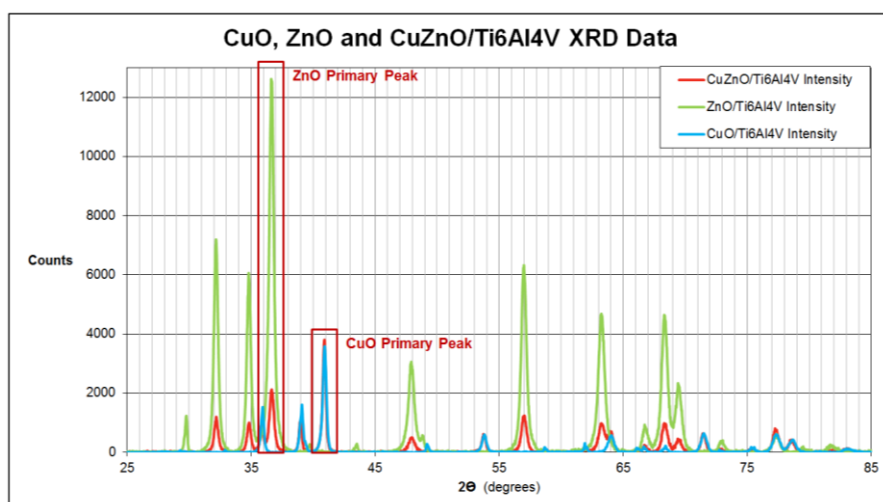
Figure 76 XRD Data for CuO, ZnO and CuZnO (500°C/4h)

The XPS data shown in Figure 77 indicated the presence of a mixed metal oxide phase on the surface that corresponds to CuZnO. The CuZnO surface has greatly reduced but still noticeable

CuO peaks as there is substantially less CuO near the surface, whilst the CuZnO surface has mildly reduced ZnO peak intensities and peaks which are shifted across in the ZnO regions. Horizontal peak-shifts are indicators of the presence of a mixed metal oxide. The CuO, ZnO and CuZnO catalysts have potential, further work will be required for testing and this was outside the scope of the thesis.
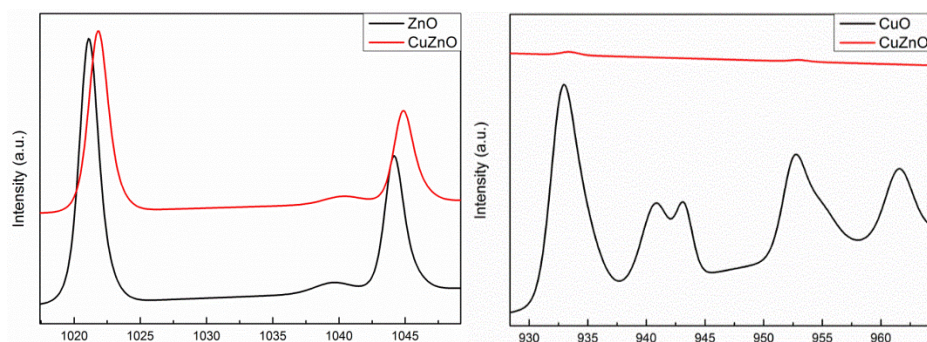
Figure 77 XPS Data for CuO, ZnO and CuZnO (500ºC/4h)

3.5.2.4 NiO

Nanostructured NiO has been demonstrated as a catalyst after its activation by a reducing atmosphere [194]. Since most of Ni catalyst reactions are high temperature, stainless steel was used for a substrate instead of the titanium alloy Ti6Al4V.

Preliminary plate coatings of NiO on 17-4 PH began with the dissolution of 495.5mg $Ni(NO_3)_2$ in 5mL of water. This solution was drop-cast on a flat 17-4 PH substrate until the surface was covered in the deposition solvent. Oven drying was applied at 100ºC to evaporate the aqueous solvent before calcination at 500ºC for 4 hours.

Secondary plate coatings of NiO on 17-4 PH were synthesized and deposited with the same method, albeit at a calcination temperature of 550ºC rather 500ºC. For the reactionware cylinder pictured in Figure 59, a fill and dry method was used to coat the inner walls of the SLM-printed DRM monoliths with 1.5mm wide channels. The base of the cylinder was sealed with Kapton tape to ensure the solvent remained in contact with the walls long enough to deposit the NiO there. An additional step immediately in the reactor was reduction in a reducing atmosphere intended to convert the NiO to Ni metal. All SEM and EDX data is explored within the context of the reaction in Chapter 4.

3.5.2.5 Al₂O₃

Alumina can act as an adlayer for any catalyst and SLM substrate. It not only adheres to metals like Ni on stainless steel, it also acts as a support to disperse catalysts such as Ni [195].

Coatings of Al_2O_3 on 17-4 PH steel, began with 1.56 g $Al(OH)_3$ powder dissolution in 5mL of water. This solution was drop-cast on a flat 17-4 PH substrate until the surface was covered in the deposition solvent. Oven drying was applied at 100°C to evaporate the aqueous solvent before calcination at 500°C for 4 hours.

The SEM data of Figure 78 reveals the character of the Al_2O_3 deposition on 17-4 PH. The Al_2O_3 deposits as particles primarily on the underlying layer with few exceptions. These particles are visibly faceted and have a low relative surface coverage of only ~4.4wt.% Al unevenly distributed across the entire substrate according to the quantitative spectra of Figure 79. This faceting increases the surface area of the deposited Al_2O_3. Furthermore, the Al_2O_3 particles appear to frequently deposit adjacent to the larger SLM particles.

From EDX data shown in Figure 79, it becomes apparent that some particles other than Al_2O_3 are present on the surface of the alloy, namely Si. Considering that there is a strong correlation of the O with the Al and a correlation of the O with the Si this confirms that the Al is present as Al_2O_3 and that the Si is present SiO_2. Although there are other known alloying elements in this alloy which could form particles, for example Cu is known to play an active role in precipitation hardening of 17-4 PH steels, nonetheless, its suggested that Si was prevalent because it's atomic weight is the lowest of all the metallic/semi-metallic elements present. More specifically, during the calcination process it's postulated that lighter elements are diffusing to the surface where they have visibly precipitated out of the solid solution.

Al_2O_3 particles

Partially fused SLM Particles
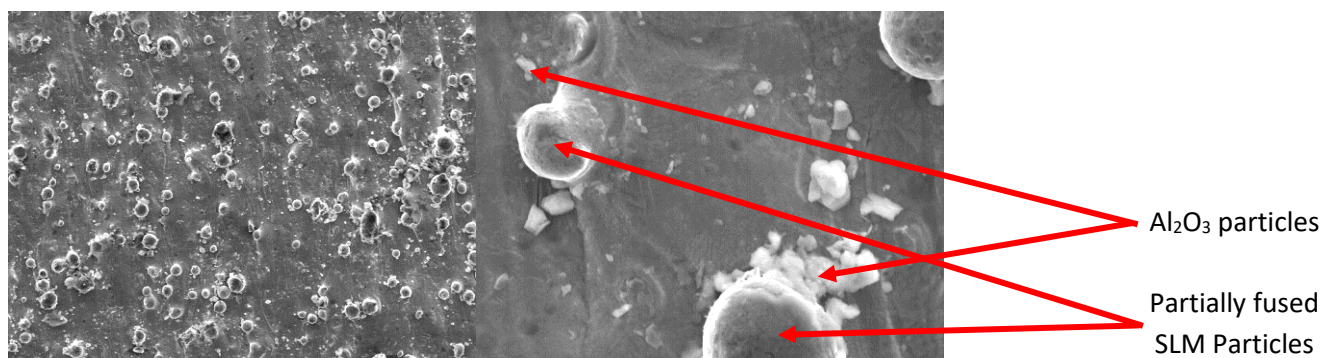
Figure 78 SEM micrographs of the Al_2O_3 coated 17-4 PH surface, heated to 500°C for 4 hours.
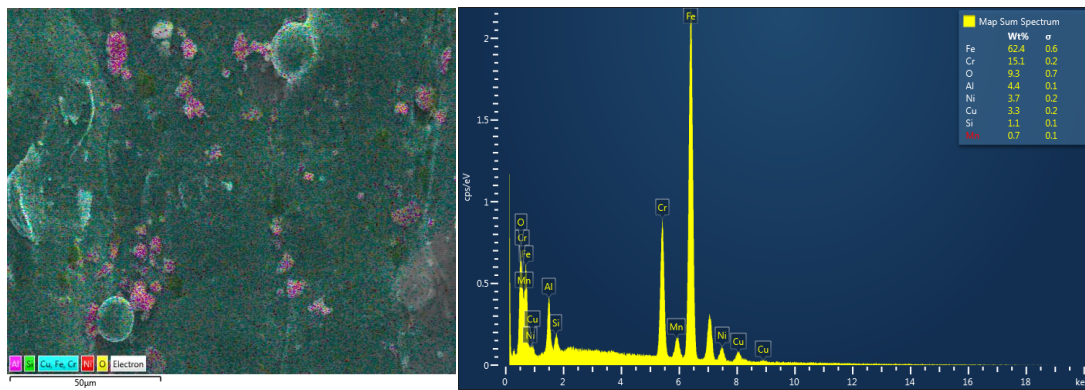
Figure 79 EDX micrograph and quantitative spectrum of Al$_2$O$_3$-coated 17-4 PH surface at 200x, heated to 500°C for 4 hours.

Coatings of Al$_2$O$_3$ on Ti6Al4V alloy, began with 1.56 g Al(OH)$_3$ powder dissolution in 5mL of water before oven drying was applied at 120°C for 1 hour to evaporate the aqueous solvent. Halfway through drying a few drops of water were pipetted into the container to consolidate the Al(OH)$_3$ powder. After drying was completed the powder was scraped into an eppendorf flask and a drop of water was added to make a slurry from the dried Al$_2$O$_3$ powder. This slurry was drop cast by micro-pipette upon the 10x5mm face of a Ti6Al4V substrate before calcination at 550°C for 4 hours. The results of this method are shown in the surface SEM data of Figure 80.

Inspection of SEM micrographs in Figure 80 reveals a similar pattern of deposition for Al$_2$O$_3$ on Ti6Al4V as for 17-4 PH steel. The Al$_2$O$_3$ still coats primarily on the underlying layer of the Ti6Al4V substrate with faceted particles and a small extent of surface coverage over the entire substrate. The Al$_2$O$_3$ particles are anchored by the larger protruding Ti6Al4V particles similar to those on 17-4 PH steel.
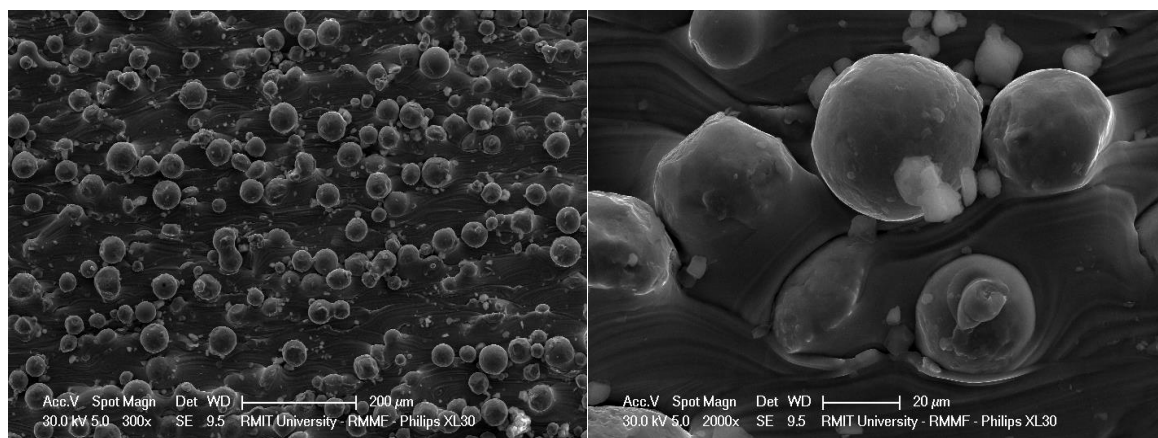
Figure 80 SEM micrographs of the Al₂O₃ coated Ti6Al4V surface, heated to 500°C for 4 hours.

3.5.2.6 Rh/Al₂O₃

Alumina-supported Rh is a catalyst system known for its application to the catalytic partial oxidation of methane to the gaseous products, CO and H_2 [196].

Coatings of Rh/Al₂O₃ on Ti6Al4V alloy were produced as follows. Dissolution of 522.5mg of RhCl₃(s) in 250mL of water in a volumetric flask was applied to make a 10mM RhCl₃(aq) solution. 1.5663 g of Al(OH)₃(s) was dissolved separately in an excess volume of water to which 9.8mL of the 10mM RhCl₃(aq) solution was mixed in before oven drying was applied at 120°C for 1 hour to evaporate the aqueous solvent. After drying was complete the powders were scraped into an eppendorf flask and a drop of water was added to make a slurry from the dried powders. This slurry was drop cast by micro-pipette upon the 10 x 5 mm² face of a Ti6Al4V substrate before calcination at 550°C for 4 hours. The results of this method are shown in the surface SEM & EDX data of Figure 81 and Figure 82, in the XPS data of Figure 83 and in the XRD data of Figure 84 and Figure 85.

From observations made by visual inspection, after calcination the surface of one side of the substrate was covered in a thin, black coating in contrast to the white flaky coating present on the Ti6Al4V substrate receiving only Al₂O₃ without the Rh.

In the SEM & EDX micrographs of Figure 81 and Figure 82 Al₂O₃ exhibits similar, if not slightly larger relative surface coverage for Rh/Al₂O₃ compared to just Al₂O₃ deposition. The Al₂O₃ seems more aggregated and less dispersed, as observable by its larger particle size. The surface area to volume ratio it offers is therefore, slightly less than for pure Al₂O₃ deposition.

Rh Nanoparticles are not clearly visible in SEM or directly visible in EDX, nonetheless EDX does reveal a low concentration dispersion of Rh uniformly deposited over the substrate.
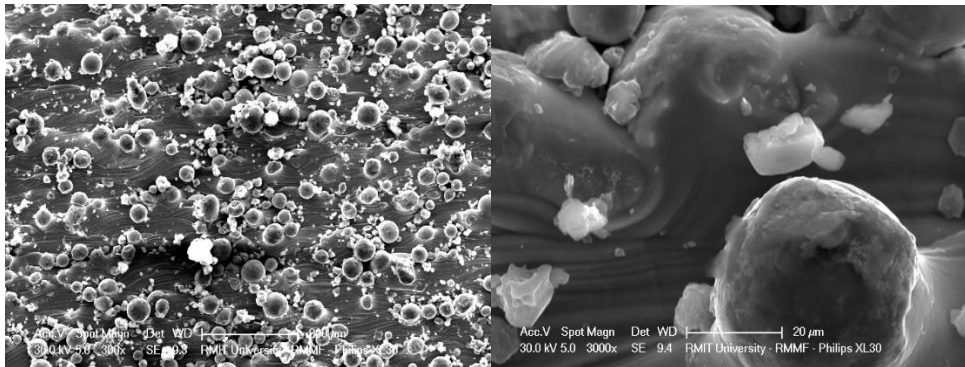
Figure 81 SEM micrographs of the Rh/Al₂O₃ coated Ti6Al4V surface, heated to 550ºC for 4 hours.
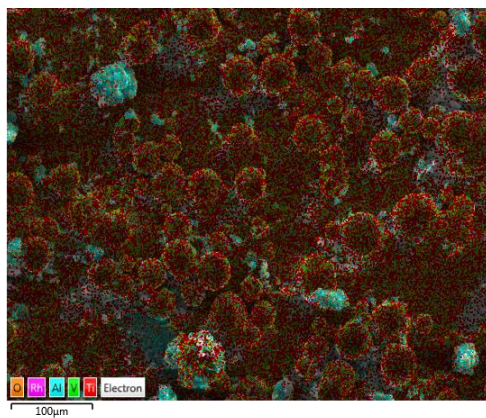
Figure 82 EDX micrographs of the Rh/Al₂O₃ coated Ti6Al4V surface, heated to 550ºC for 4 hours.

Figure 83 shows the XPS data of a Rh/Al$_2$O$_3$ coated SLM substrate used to study the nature of the Rh deposition. The appearance of the Rh 3d level spectra clearly shows that Rh is present with its characteristic peaks at ~308.5eV. This energy corresponds to the trivalent state of Rh preferentially in its oxidised form. From the peak intensity ratios of Ti and Rh on Rh/Al$_2$O$_3$ coated Ti6Al4V, there is a ~2:9 ratio of Rh: Ti on the surface.
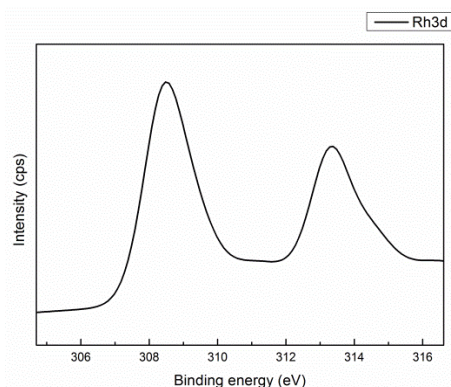
Figure 83 XPS Spectra samples; Characteristic Rh binding energy Peaks on Rh/Al₂O₃ coated Ti6Al4V substrate.

XRD patterns of materials related to Rh/Al$_2$O$_3$ deposition on Ti6Al4V were collected and are shown in Figure 84 and Figure 85. It's clearly seen that the changes in the peak position and peak width correlate to changes in the interplanar spacing and average crystallite size, respectively. Calcination shifts the XRD peaks across to the right; this suggests that calcination of the Ti6Al4V leads to an increased interplanar spacing, whilst Al$_2$O$_3$ and Rh have little further impact on the average crystallite size. Furthermore, calcination also correlated with a decreased full width half maximum value of the peak. This correlates to a decreased polydispersity of the crystallite sizing. Again, Al$_2$O$_3$ and Rh addition had little additional impact on this outcome.
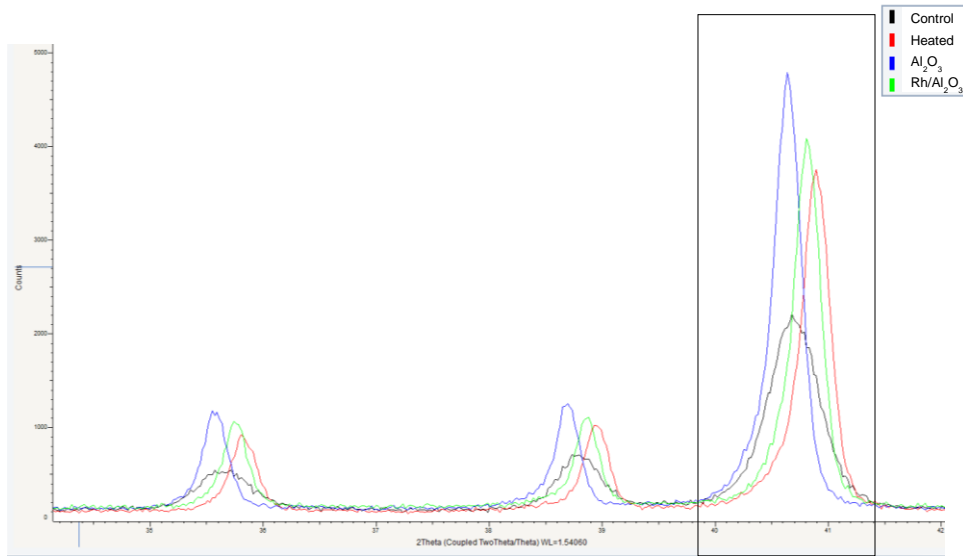
Figure 84 XRD Data for Rh/Al₂O₃ coated Ti6Al4V surface, heated to 500ºC for 4 hours & other samples indicated in the key. The peak of interest for analysis is highlighted with a black rectangle.
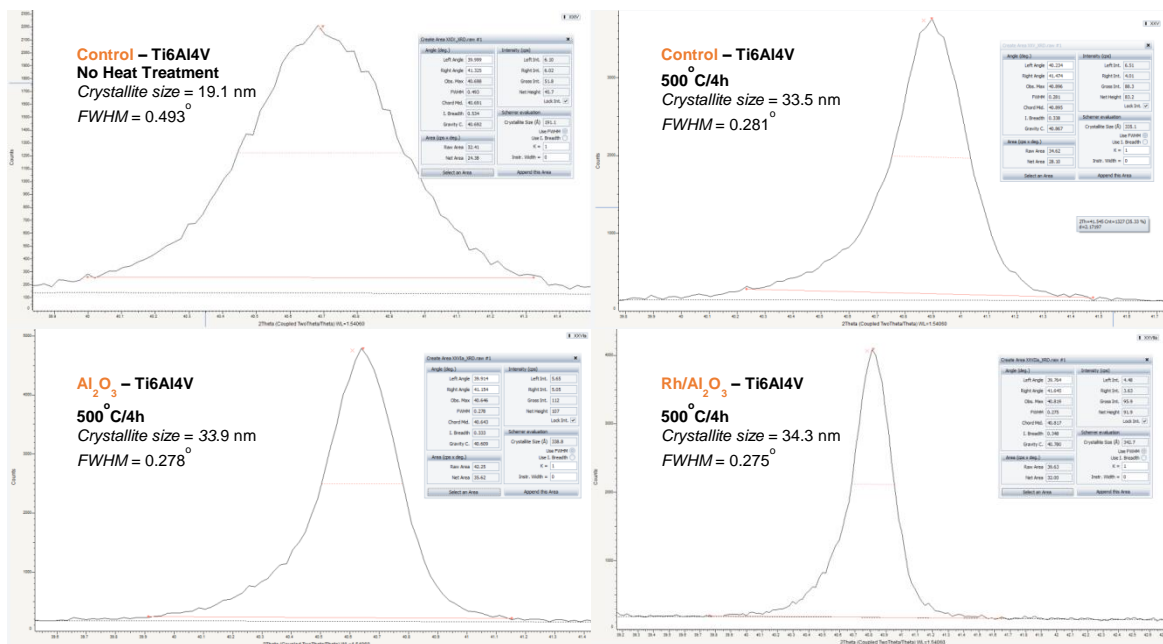
Figure 85 XRD peak variations for the plain, 500ºC/4h heated, Al₂O₃ and Rh/Al₂O₃ coated Ti6Al4V surfaces, heated to 500ºC for 4 hours. Images not on equivalent scales.

3.5.2.7 NiO/Al₂O₃

Preliminary plate coatings of NiO/Al_2O_3 on 17-4 PH steel, began with 1.56 g $Al(OH)_3$ powder first dissolved in 5mL of water, then 495.5mg $Ni(NO_3)_2$ was also dissolved in the same solution. This solution was drop-cast on a flat 17-4 PH substrate until the surface was covered in the

deposition solvent. Oven drying was applied at 100°C to evaporate the aqueous solvent before calcination at 500°C for 4 hours.

Secondary plate coatings of NiO/Al_2O_3 on 17-4 PH were calcined at 550° rather than 500°C. There was a slight difference in the method used for the synthesis of the NiO/Al_2O_3 here; rather than using 5mL of water for both the 495.5mg $Ni(NO_3)_2$ and the 1.56g $Al_2(OH)_3$, both these precursors were dissolved in their own 5mL of water and then 1mL of each was mixed together. This means that the concentration of the deposition solution was halved for both the $Ni(NO_3)_2$ and the $Al_2(OH)_3$. The solution was drop-cast on the 17-4 PH substrate as in the preliminary method before drying and 550°C calcination for 4 hours.

For the reactionware cylinder pictured in Figure 59, a fill and dry method was used to coat the inner walls of the SLM-printed DRM monoliths with 1.5mm wide channels. The base of the cylinder was sealed with Kapton tape to ensure the solvent remained in contact with the walls long enough to deposit the NiO/Al_2O_3 there. An additional step immediately in the reactor was reduction in a reducing atmosphere intended to convert the NiO to Ni metal. All SEM and EDX data is explored within the context of the reaction in Chapter 4.

3.5.2.8 NiO/MgAl₂O₄

$NiO/MgAl_2O_4$ began with the dissolution of 495.5mg of $Ni(NO_3)_2$ in 5mL water, 0.725g of $Mg(OH)_2$ in 5mL of water and 0.78g of $Al_2(OH)_3$ in 5mL of water. 1mL of each solution was mixed together, applying a 1/3 dilution to each component of the solution. The solution was drop-cast on the 17-4 PH substrate as in the preliminary method before drying and 550°C calcination for 4 hours. For the reactionware cylinder pictured in Figure 59, a fill and dry method was used to coat the inner walls of the SLM-printed DRM Monoliths with 1.5mm wide channels. The base of the cylinder was sealed with Kapton tape to ensure the solvent remained in contact with the walls long enough to deposit the $NiO/MgAl_2O_4$ there. An additional step immediately in the reactor was reduction in a reducing atmosphere intended to convert the NiO to Ni metal. All SEM and EDX data is explored within the context of the reaction in Chapter 4.

3.5.3 Acid Catalysts

3.5.3.1 FeCl₃ on Ti6Al4V & 17-4 PH

Lewis acid and Bronsted acid catalysts play a key role in the petroleum and fine chemical industries. For example, the Lewis acid catalyst, $FeCl_3$, has been applied to fuel purification [197]. In this project, $FeCl_3$ coating of 17-4 PH and Ti6Al4V began with the dissolution of 0.811g $FeCl_3$ in 100mL of acetonitrile to make a 5×10^{-2} M solution. 150μL of this solution was drop-cast by micro-pipette onto flat Ti6Al4V & 17-4 PH substrates. An alternate applied coating method was vertical immersion of the flat Ti6Al4V & 17-4 PH substrates in 400μL of the 50 mM $FeCl_3$ in acetonitrile in an eppendorf flask left to dry. Substrates were either used after this drying process or the subsequent 400°C/3h calcination.

When applying this coating to the 'reactionware teapot' visible in Figure 61, a different approach was necessary for coating, although the rest of the method was the same as for the flat substrates. The 50mM solution of $FeCl_3$ in acetonitrile was poured straight into the reactionware vessel which was dried at 100°C using direct contact of the base with a hot plate. As before, calcination at 400°C for 3 hours was applied to set the coating into the substrate and fully remove the acetonitrile. All SEM and EDX data is explored within the context of the relevant reaction in Chapter 5.

3.6   REACTION SETUPS

For all 3 reactions, SLM substrate-supported catalysts were investigated using SEM/EDX pre-reaction and/or post-reaction, all other reaction-specific information is covered in the following subsections.

3.6.1 DRM Reaction Setup

The preliminary coats associated with the DRM reaction were not for catalyst testing purposes, they were to demonstrate a method that enabled deposition of the catalyst material on SLM substrates. This was because the catalyst testing procedure was time-consuming and impractical for initial testing. It was therefore much better to initially develop coating methods assessed by SEM/EDX characterisation rather than reactions, since characterisation was faster. Since the process occurs at high temperatures, the catalysts were coated onto SLM-printed Stainless Steel substrates.

The DRM reaction was performed with catalyst-coated SLM substrates based on Danaci et al.'s method [106]:

1. Insert the coated cylinder with square channels into heated, steel tube, see Error! Reference source not found..

2. Allow a 33% H_2/He mix to flow at 800°C to reduce the coated 17-4 PH cylinders.

3. Allow a 1:1 mix of CH_4: CO_2 diluted by He to flow at 700°C and 800°C.

4. The reaction continued for 15 hours unless:

    a. Catalytic activity ceased due to catalyst poisoning.

    b. Excessive pressures halted the reaction.

5. Online Gas Chromatography was used to determine the concentrations of H_2, CO_2 and CH_4 during the reaction.
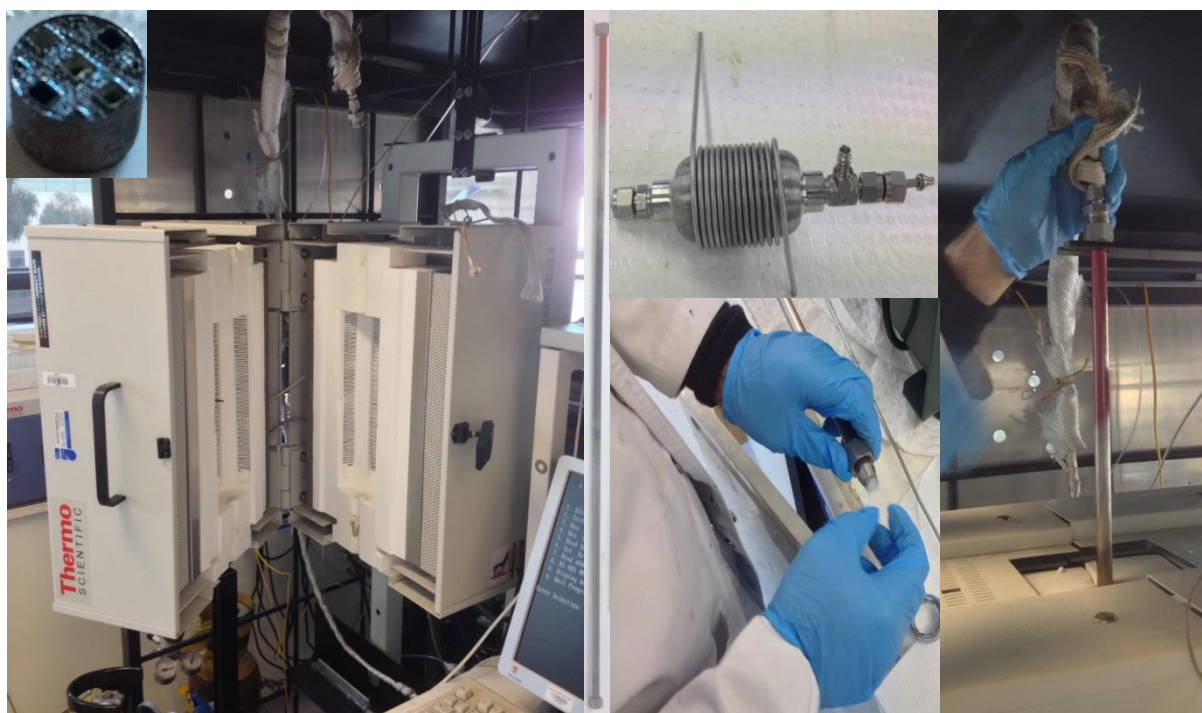
Figure 86 DRM continuous reactor setup. (Top Left) Coated Pin-hole cylinder ready for insertion. (Left) Open heating unit with steel cylinder removed. (Middle Left) Steel Cylinder that contains reactants, pin-hole cylinder and products. (Middle Top) Water Trap. (Middle Bottom) Inserting the pin-hole cyinder between 2 pieces quartz wool to hold it in place. (Right) Sealing the assembly in preparation for the reaction.

3.6.2 4-NP Reduction Reaction Setup

As reported in literature [204], 4-NP cannot be reduced by $NaBH_4$ to form 4-AP unless a catalyst is involved. 4-NP shifts from colourless to yellow over the 5.4 to 7.5 pH range [210].

Given that 4-NP is yellow in DI water and is colourless when converted to 4-AP, there is a clear visual indication when a 4-NP reduction reaction is progressing well. For quantitative evaluation it's useful to apply UV-Visible spectroscopy, to measure the relative presence of a $NaBH_4$-induced intermediate, 4-Nitrophenolate, according to the 400nm peak and the 4-AP product according to the 300nm peak [204].

For reactant ratios, it's common to use high proportions of $NaBH_4$ in the mole ratios of 4-NP: $NaBH_4$ as it's advantageous for an excess of $NaBH_4$ to be present for these reactions. To this end, it's reported that Srisombat et al. used a 4-NP: $NaBH_4$ mole ratio of 1:63.75 [204], Park et al. used 1:164.7 [211] and Ma et al. used 1:400 [212].

From these reports, the method was developed and refined over time. The earliest steps for preparing the reactants and performing the reaction were as follows: 3783 mg $NaBH_4$(s) was dissolved in 100mL H_2O to make a 0.1 M $NaBH_4$(aq) solution and 13.911 mg 4-NP was dissolved in 100mL H_2O to make a 0.001 M 4-NP (aq) solution.

Prior to the reaction, the UV-Vis spectrometer was calibrated using DI-H_2O in a 1mL cuvette. One flask was put aside for each substrate to be tested then 10mL of the 4-NP solution was poured into each flask, then the temperature and stirring speeds for the reaction were set at the desired values. From here a stirrer & an SLM sample substrate were placed into each flask and 10mL of $NaBH_4$ solution was added in last. This gave final concentrations of 0.05 M $NaBH_4$ solution & 0.0005 M 4-NP solution. Once the $NaBH_4$ was added the reaction began, at this point and every 5 minutes afterwards, a sample was taken for UV-Vis spectroscopy. The reaction and sampling process were continued for 2 hours or until UV-Vis data indicated the complete reduction of 4-NP.

3.6.3 Glycerol Acetalisation Reaction Setup

The last reaction of interest is glycerol acetalisation wherein glycerol reacts with acetone to form solketal. Aside from converting glycerol, any catalyst used must be selective towards the 5-membered ring solketal, instead of the 6-membered ring acetal. Esteban et al. observed that initial molar ratios of acetone: glycerol ('M') of 2:1 to 6:1 are most common but points out that others have used ratios as high as 20:1 in their work [214]. Furthermore, they found that solketal yield increases with increasing M up to 12:1 which was the highest ratio in their work. Fonseca et al. reported a similar result [215]. It's not clear what the upper boundary of

this effect is but it's evident that up to a 12:1 ratio increasing the initial acetone concentration is beneficial to the solketal yield.

Taking these into account but not increasing the scope to explore new aspects of the reaction chemistry, the methods developed were made with the intent of assessing the effectiveness of the innovative catalyst systems synthesized in this project. The preliminary reactions were performed as follows: 0.1 mmol glycerol and 0.3 mmol of acetone were mixed at RTP in a reaction flask before inserting the SLM substrate-supported catalyst system. The reaction proceeded for 2h before removing the substrate and performing GC-MS on the resulting reaction mixture. This enabled a rough initial estimate to be made regarding the viability of each catalyst system.

For the initial reaction setup for the reactionware 0.5mL glycerol and 0.5mL acetone were mixed then transferred to the reactionware vessel. A further 0.5mL of acetone was added to flush the glycerol further into the reactionware lattice and increase the acetone: glycerol ratio. Sonication of the vessel indirectly through a beaker aided the mixture in progressing further into the lattice. During the reaction, the vessel was sealed with parafilm, then left at RTP for 2 hours as the reaction to progressed. After this period inversion of the vessel and sonication in 10mL of methanol enabled the extraction of any acetone, glycerol and solketal. Qualitative analysis of the extracted reaction mixture was performed using GC-MS. Regeneration of the catalyst and the removal of remnant liquids in the reactionware vessels occurred through oven drying at 100°C overnight.

Later, more quantitatively accurate methods of analysis were carried out by the GC-FID technique. To begin with the external standards were needed to allow meaningful interpretation of the GC-FID spectra. External standards were created for the solketal reactions, as follows: 1mmol glycerol was measured by mass as 0.09209382g (approximated to 0.092g) in a 10mL measuring flask. 1mmol Solketal was measured in volume as 124.33µL (approximated to 124µL) and pipetted into the same flask. This mix was diluted to 10mL using methanol as a solvent. The resulting concentrations were 0.1M solketal and 0.1M glycerol in methanol solution. Extracts from this volume were diluted to make standards of 0.075M, 0.05M & 0.025M concentrations of both reagents. 0.1M, 0.075M, 0.05M & 0.025M concentrations were run through the GC-FID setup to ascertain the linear responses of

glycerol and solketal. That is, a correlation between peak area and concentration was found for both glycerol and solketal, thus enabling a quantitative measurement of glycerol acetalisation. More specifics of the calculations used in this methodology and the calibration curves this generated are detailed in Appendix A.

3.7   SUMMARY AND CONCLUSIONS

In summary, various methods which have been used to apply coats of metals and metal oxides to SLM substrates. These metals and metal oxide coatings are of well-known catalyst systems, the use of which has precedents in the literature. Their uniformity and other coating properties were characterised by SEM, EDX, XPS and XRD.

SLM substrates were found to undergo some structural changes during calcination. The titanium alloy, Ti6Al4V was observed with XPS data to have surface concentrations of Al increase 4-fold during calcination, on the other hand SEM & EDX data revealed that a variety of Silicates with Mn or Al formed during calcination for the 17-4 PH steel substrate, the concentration of which appeared to correlate to the coating material involved.

Post calcination of these materials suggests that it's possible that this induces precipitation of the lighter alloying elements at the surface. In the case of 17-4 PH steel, the Si rises to the surface, in the case of Ti6Al4V, the Al rises to the surface. Furthermore, it's suggested that the reason for this is that the diffusivities of these lighter elements are higher than the other alloy components and that, as the temperature of the plate increases towards the outside surface, diffusion of the light elements provides a heat transfer enhancing mechanism to equilibrate the temperature difference. If this heat transfer mechanism were present, slow heating rates should inhibit this behaviour.

The consequence of unanticipated precipitation of alloying elements is that unintended metallic oxides or mixed metallic oxides may be present and in addition, sometimes the creation of mixed metallic oxides with coating materials may occur. Catalyzed reactions are known to be sensitive to dopants such as these, even in small concentrations [61], making the response of SLM parts to scenarios like oxidizing atmospheres problematic if not thoroughly characterised and controlled.

With respect to the SLM substrate materials, Ti6Al4V was found to be better than 17-4 PH due to the presence of less alloying components leading to less complex interactions of the substrate with the catalyst. Furthermore, the rougher surfaces of Ti6Al4V gave rise to higher surface to volume ratios for the catalyst to deposit on than for 17-4 PH steel. The number of successfully coated material deposition methods applied and characterised is an indication of the viability of SLM substrates for functionalisation with the intent of facilitating heterogeneous catalytic reactions.

CHAPTER FOUR – VAPOUR PHASE REACTIONS ON AM SUBSTRATES

4.1 INTRODUCTION

In the previous chapter, various metal and metal oxide coatings were applied to SLM substrates. To demonstrate their potential in heterogeneous catalytic processes, it is important to test their catalytic efficiency. In chapter 4, Ni has been coated on 17-4 PH substrates with and without various supporting materials. To apply these materials, Ni-catalysed reactions were considered. One of the major processes to which Ni catalysts are traditionally applied is the CO_2-reforming of methane gas into syngas. The primary source of methane is natural gas (NG), of which methane is the major component.

One third of the 170 Trillion Cubic Metres (TCM) of NG is stranded gas [1], mostly due to high transport costs. This makes on-site processing, with portable miniature reactors, desirable to decrease costs. NG is converted to syngas from methane gas then syngas is converted to methanol and finally methanol is dehydrated to DME. There are a few different reactions which may produce syngas [124, 198, 199]:

$$CH_4 + H_2O \leftrightarrow CO + 3H_2 \qquad \qquad \textit{Eq. 12 Steam methane conversion (SMC)}$$

$$CH_4 + \frac{1}{2}O_2 \leftrightarrow CO + 2H_2 \qquad \qquad \textit{Eq. 13 Catalytic partial oxidation (CPOx)}$$

$$CH_4 + CO_2 \rightarrow 2CO + 2H_2 \qquad \qquad \textit{Eq. 14 Dry reforming of methane (DRM)}$$

One of the big advantages of DRM compared to SMC or CPOx is that it uses CO_2 rather than O_2 or H_2O to produce syngas from methane, this is more environmentally friendly [24]. Although Dry Reforming of Methane consists of several smaller steps, two broad processes

involved are Methane Decomposition and the Boudouard Reaction, shown in

Eq. *15* and   Eq. *16* respectively [24].
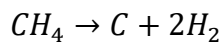
$$CH_4 \rightarrow C + 2H_2$$ *Eq. 15 Methane decomposition*
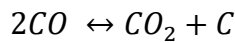
$$2CO \leftrightarrow CO_2 + C$$ *Eq. 16 The Boudouard reaction*

Multiple authors confirm that for transition metal catalysts, methane cracking is a rate-limiting step in the Dry Reforming of Methane [200-202]. Silverwood et al. explores the Dry Reforming of Methane mechanisms, accounting for adsorption of the reactants – which is the role of the catalysts used for this reaction [203].

The methane cracking reaction is broken into five steps. The CH_4 gas is first adsorbed onto a catalyst and then H atoms dissociate from the carbon atom whilst remaining adsorbed to the catalyst [203]. H dissociation from the C atom occurs as described four times. The end result is one Carbon atom and four Hydrogen atoms adsorbed on a catalyst surface. The H atoms pair up to form Hydrogen Gas then desorb from the catalyst in a process known as Hydrogen Evolution. The C atom may undergo one of two processes, the first and preferred reaction is the reverse Boudouard reaction, the second and detrimental reaction is polymerisation whereby the atomic carbon forms amorphous carbon. Both the rate of the reverse Boudouard reaction and the subsequent desorption of the CO afterwards are relevant in minimising the formation of amorphous carbon. This is important to consider because carbon formation over catalysts deactivates them and leads to flow blockage of the reactants and products [24]. All of these reaction stages are shown in equations and a reaction scheme present in Silverwood et al.'s work in Figure 87 and Figure 88, respectively [203].

$$CH_{4(g)} \rightarrow CH_{4(ad)} \quad k_1$$

$$CH_{4(ad)} \rightarrow CH_{3(ad)} + H_{(ad)} \quad k_2$$

$$CH_{3(ad)} \rightarrow CH_{2(ad)} + H_{(ad)} \quad k_3$$

$$CH_{2(ad)} \rightarrow CH_{(ad)} + H_{(ad)} \quad k_4$$

$$CH_{(ad)} \rightarrow C_{(ad)} + H_{(ad)} \quad k_5$$

$$2H_{(ad)} \rightarrow H_{2(ad)} \quad k_6$$

$$H_{2(ad)} \rightarrow H_{2(g)} \quad k_7$$

$$CO_{2(g)} + C_{(ad)} \rightarrow 2CO_{(ad)} \quad k_8$$

$$CO_{(ad)} \rightarrow CO_{(g)} \quad k_9$$

$$nC_{(ad)} \rightarrow C_{n(ad)} \quad k_{10}$$
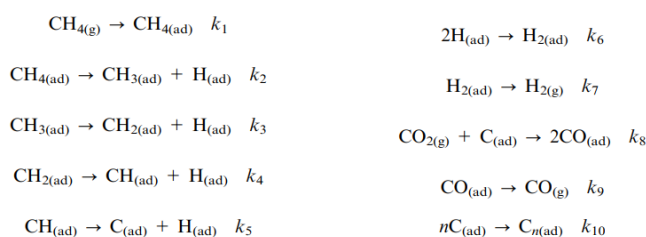
Figure 87 Reaction stages occurring during Dry Reforming of Methane [203].
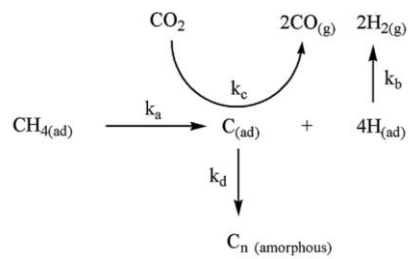
Figure 88 Silverwood et al.'s reaction scheme for Dry Reforming of Methane [203].

Three major challenges were identified in this work, as described in the Experimental Method. First, that the coatings need to be present in appropriate amounts, secondly that they may remain adhered during the reactions and thirdly that the catalyst is active despite interactions with elements in the SLM substrate alloy. All three of these challenges are addressed using DRM applied to select catalyst coatings of interest. The reactions of Ni, Ni/Al$_2$O$_3$ and, Ni/MgAl$_2$O$_4$ calcined at 550°C/4h then reduced and reacted at 700°C or 800°C in a 17-4 PH cylinder are highlighted.

Summary and conclusions finish this chapter with future recommendations for method and issues to be aware of in future work.

4.2 DRY REFORMING OF METHANE

The few catalysts applied to DRM were trialled for deposition on planar substrates and catalyst testing was performed in cylindrical square-channelled substrates, see Table 21. During catalytic reaction testing, only one adjustment to method was applied, see Table 22.

Table 21 – 17-4 PH samples trialled for catalytic activity in dry reforming of methane & their assigned sample ID

Sample ID	Sample Preparation
[A-p]	NiO/Al$_2$O$_3$-17-4 PH 550°C/4h calcination (10 wt.% Ni)
[A-c]	Ni/Al$_2$O$_3$-17-4 PH 550°C/4h calcination (10 wt.% Ni), then 800°C/- reduction
[B-p]	NiO/MgO-17-4 PH 550°C/4h calcination (10 wt.% Ni)
[B-c]	Ni/MgO-17-4 PH 550°C/4h calcination (10 wt.% Ni), then 800°C/- reduction
[C-p]	NiO/MgAl$_2$O$_4$-17-4 PH 550°C/4h calcination (5 wt.% Ni)
[C-c]	Ni/MgAl$_2$O$_4$-17-4 PH 550°C/4h calcination (5 wt.% Ni), then 800°C/- reduction
[D-p]	NiO/MgAl$_2$O$_4$-17-4 PH 550°C/4h calcination (10 wt.% Ni)
[D-c]	Ni/MgAl$_2$O$_4$-17-4 PH 550°C/4h calcination (10 wt.% Ni), then 800°C/- reduction
[E-p]	NiO -17-4 PH 550°C/4h calcination
[E-c]	Ni -17-4 PH 550°C/4h calcination, then 800°C/- reduction

*These catalysts demonstrated noticeable activity

Table 22 Dates of reactions, complications and the corrections made for glycerol acetalisation

Substrates Tested	CH$_4$: CO$_2$ Gas Flow Temperature	Issues & Adjustments
[E-c]	700°C	Low conversion.
[A-c]	700°C	Low conversion, try higher temperature.
[C-c]	800°C	Conversion measurable but still minimal.

*Not a reaction but an action of another kind, clarified under 'Substrates Tested'

Of the 5 prepared reaction cylinders, Ni [E-c], Ni/Al$_2$O$_3$ [A-c], Ni/MgO [B-c] & 2 Ni/MgAl$_2$O$_4$ [C-c] & [D-c] on 17-4PH, 3 were tested; Ni [E-c], Ni/Al$_2$O$_3$ [A-c], and one Ni/MgAl$_2$O$_4$ [C-c] on 17-4 PH. First Planar substrates; [A-p], [C-p], [E-p] then their paired reaction cylinders; [A-c] and [E-c], were imaged under the SEM for microstructural analysis whilst EDX was applied for elemental analysis. The planar samples were only coated & calcined, whereas the reaction cylinders subsequently endured a higher temperature reducing atmosphere and the DRM reactants passing through them, both of which are intended to convert the nickel oxides to metallic nickel.

The catalyst outcomes from metallic Nickel on 17-4 PH Steel, [A-c], was negligible conversion of CH$_4$ or CO$_2$, see the GC-FID data in **Error! Reference source not found.** within Appendix C. This GC-FID data was not converted to a conversion vs. time graph because the peaks indicate that the conversion of CO$_2$ and CH$_4$ to H$_2$ and CO was not very high.

SEM characterisation of NiO coatings on 17-4 PH steel, shows how the substrate surfaces were changed due to oxidizing calcination for both the preliminary coating on a plate, see Figure 91, Figure 92, Figure 93, & Figure 94, and for a 2nd coating on another plate using a slightly higher calcination temperature (550°C instead of 500°C), see Figure 89, Figure 96, Figure 95, and Figure 97. Further characterisation of the NiO coating applied to the used reaction cylinders revealed the impact of the reducing reaction, as shown in Figure 90, Figure 99, and Figure 100.

After drying, the 2nd coating appeared as a very thin translucent green layer on the 17-4 PH substrate with a moderate degree of wetting. After 550°C/4h calcination the 17-4 PH coated in NiO acquires a brown-grey colour and the wetting remains unchanged, as shown in Figure 89. After the reaction the cylinder is coated in a thin gray coating of material, as shown in Figure 90, which EDX, see Figure 96, Figure 97, confirms is partly due to carbon deposition.

Figure 89 NiO on 17-4 PH plate after 550°C/4h calcination; Sample ID [E-p].

Figure 90 (Left) Unaltered 17-4 PH cylinder (Middle, Right) Ni on 17-4 PH cylinder after 550°C calcination & 700°C reduction Sample ID [E-c]

The calcined NiO and NiO/Al_2O_3 coated plates made for SEM & EDX characterisation of the coating without a reducing atmosphere do not exhibit the same coating character as their preliminary coating equivalents, even though the only difference is 500°C calcination for preliminary coatings instead of 550°C calcination for these later coatings.

Considering the preliminary coating shown in Figure 91, Figure 92, Figure 93, and Figure 94. There is a very high relative surface coverage of NiO with clear indications of SLM particles anchoring the NiO deposits. This is most strongly confirmed by typical quantitative spectra

paired with a layered EDX map in Figure 92, which indicates that the wt.% of Ni on the surface is 30.8 wt.%.

There are regular discontinuous islands of NiO observable in Figure 91 distributed all over the substrate. However, a gap in the NiO deposition is visible in Figure 93. Given that there was nothing chemically or physically distinct observed in this region to account for this, it's not clear why this occurred. In addition, there were other unexpected particles present; looking at the EDX Maps in Figure 94 shows a region consisting of the elements Mn, Al and Si.
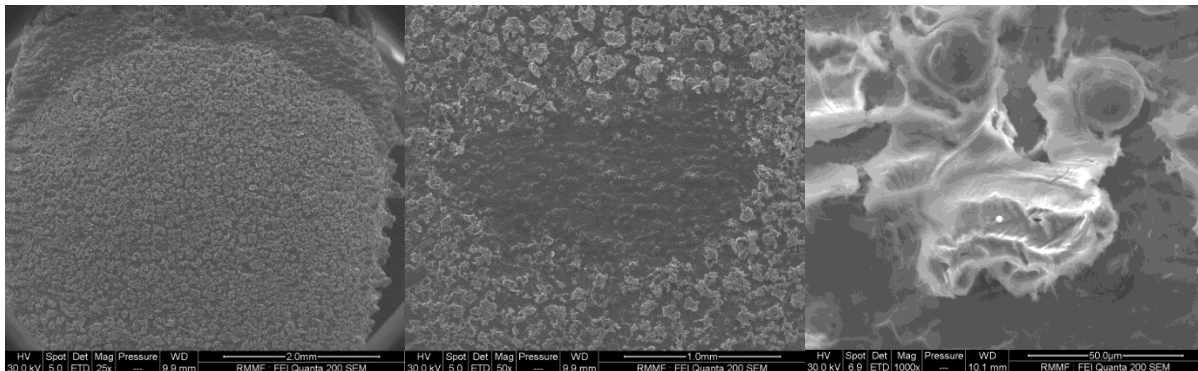
Figure 91 SEM micrographs of the preliminary plate coating: NiO coated 17-4 PH surface, heated to 500ºC for 4 hours.

Figure 92 (Left) A layered EDX Map showing a typical distribution of NiO on the preliminary coating of 17-4 PH (Right) Related quantitative spectra.
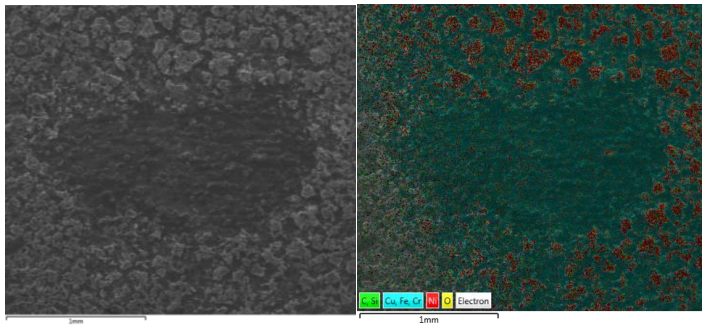
Figure 93 EDX micrographs of the preliminary plate coating: NiO coated 17-4 PH surface, heated to 500ºC for 4 h, Site 1.
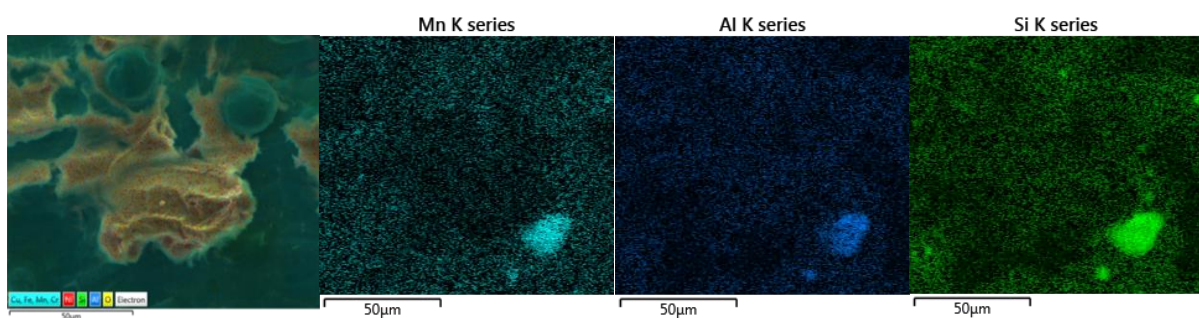
Figure 94 EDX micrographs of preliminary plate coating: NiO coated 17-4 PH surface, heated to 500ºC for 4 hours, Site 2.

Whilst the 2nd 17-4 PH plate coated with Ni has regions similar to the preliminary plate coating, as shown in the right SEM micrograph of the 2nd plate coating in Figure 95, this is mostly not the case. The regular pattern of discontinuous islands visible on the preliminary plate coating, as shown in Figure 91, was replaced by irregular discontinuous islands with thin ridges of NiO coating for the 2nd 17-4 PH plate. In fact the overall deposition pattern looks like that of the preliminary 10wt.% Ni, Ni/Al$_2$O$_3$ deposition, see Figure 103, as there appears to be a lot of material being lost during the calcination procedure. Furthermore, it's suggested that the Ni coating would be continuous if no material were lost during calcination, as shown in the left micrograph of Figure 95. Regardless, there is less Ni present for this later coating than the preliminary coating.
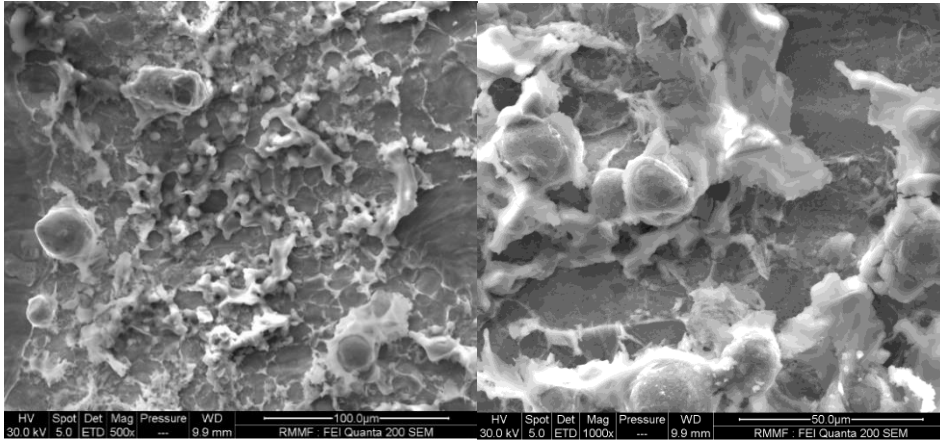
Figure 95 SEM micrographs of the 2nd plate coating: NiO coated 17-4 PH surface, heated to 550°C for 4 hours

This poor adhesion is most likely due to a difference in surface chemistry as the EDX Maps reveal, see Figure 96. Although there are regions with the expected compositions in the 2nd plate coating such as NiO and silicates, see Figure 97, there were some unexpected K and Na oxide dispersions which might originate from contaminants in the $Ni(NO_3)_2$ precursor solution ingredients again see Figure 96. It's suggested that K and/or Na_2O has deposited preferentially to Ni thus preventing the formerly seen, thorough coverage of Ni on 17-4 PH. Looking at the K & Na maps as shown in Figure 96, it's notable that the distributions of the K & Na coincide with lower concentrations of Ni.
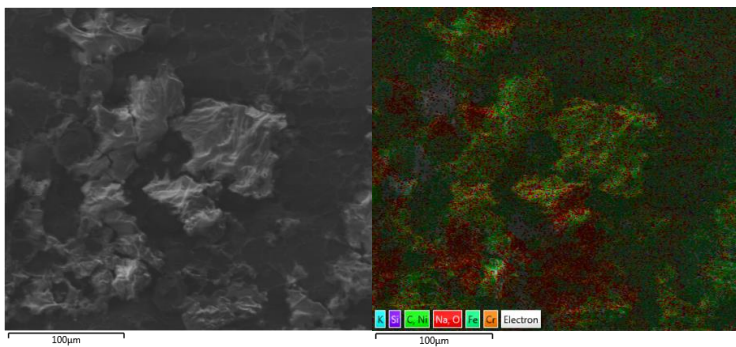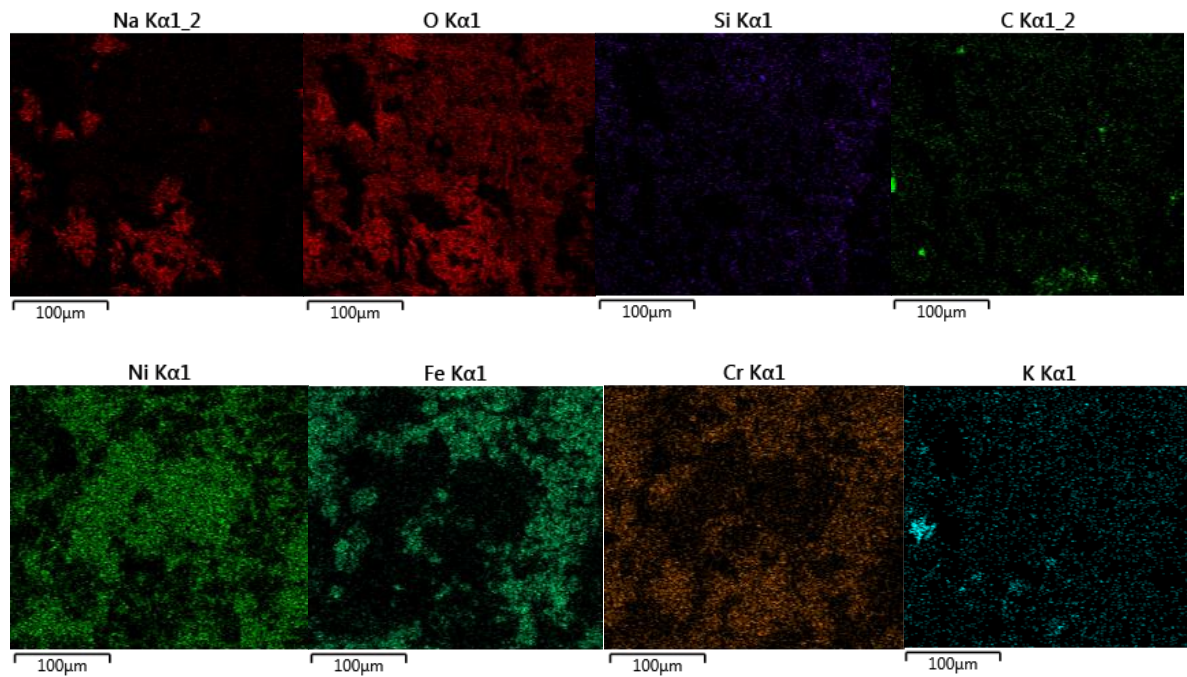
Figure 96 EDX micrographs of the 2nd plate coating: NiO coated 17-4 PH surface, heated to 550°C for 4 hours; (Top Left) 400x SEM site, (Top right) 400x EDX Map Overlay, (Bottom 2 rows) EDX Element Maps, Site 1.
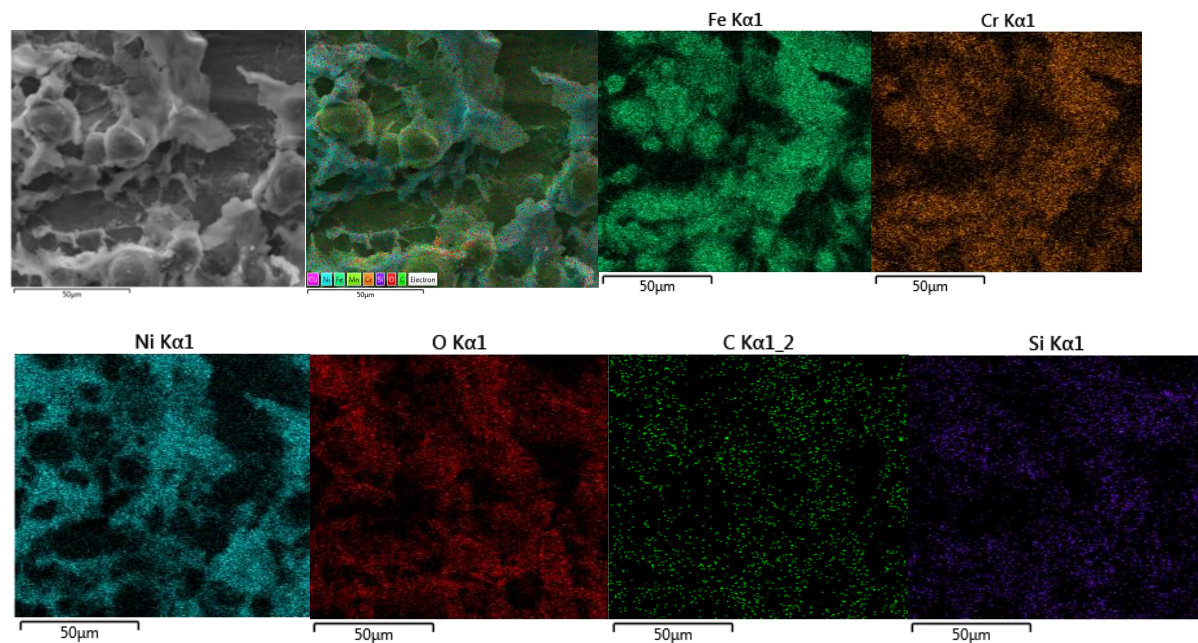
Figure 97 EDX micrographs of the 2nd plate coating: NiO-coated 17-4 PH surface, heated to 550°C for 4 hours, Site 2.

Regardless of unexpected variations in surface chemistry, the use of NiO is not effective for DRM, it's necessary to reduce this material to metallic Ni to have an active catalyst material.

A contrast of the SEM & EDX characterisation data from before and after the reaction, see Figure 98, reveals that the NiO of the calcined substrate was successfully reduced to a metallic Ni by the reducing atmosphere. This is evident from three pieces of information; the coated NiO shifted from its' discontinuous island character to a combination of discontinuous islands and particulate Ni, the data of the EDX maps in Figure 100 where O is concentrated on Fe, away from the Ni and the Ni:O weight percentage ratios of the EDX data shift from 32.9%:15.6% (~2:1) in the calcined substrate to 56.0%:6.0% (~9:1) in the reduced substrate, with respect to EDX data collected from the micrographs in Figure 98. Viewing the Ni deposition character before and after the reaction reveals just how much reduction has impacted the Ni surface morphology, see Figure 98.
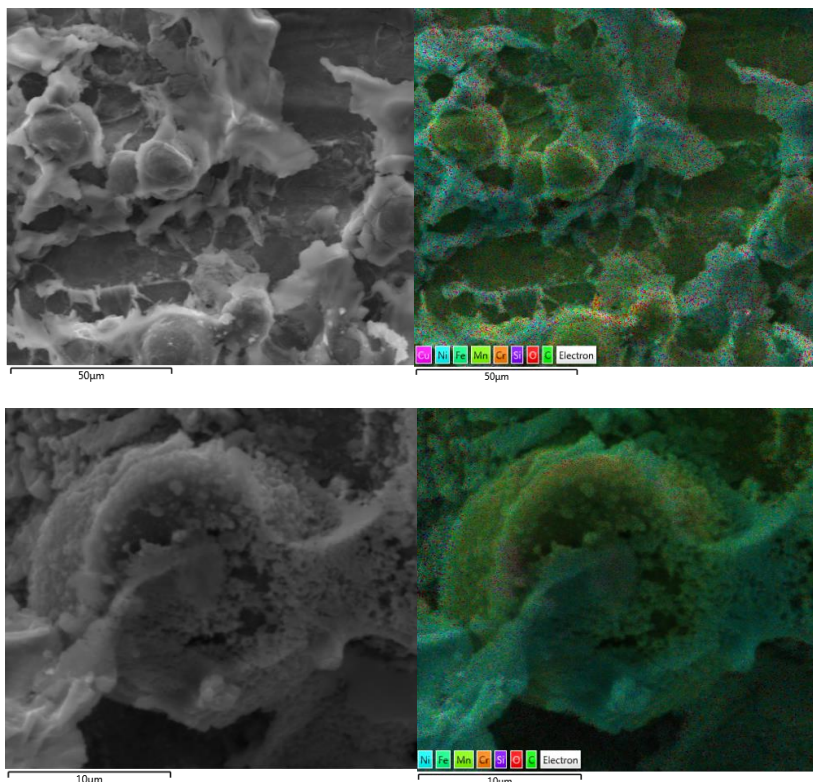
Figure 98 A contrast of Ni surface morphologies. (Top) NiO-coated 17-4 PH surface, heated to 550°C for 4 hours, 1000x magnification SEM Image (Left) & EDX Overlay (Right). (Bottom) Ni coated 17-4 PH surface, heated to 550°C for 4 hours then reduced at 700°C in CH_4 & H_2, 5000x magnification SEM Image (Left) & EDX Overlay (Right).

In addition to a reduced Ni state, the Ni-coated 17-4 PH cylinder used in the DRM reaction showed a significantly different surface chemistry and morphology to its paired coating on the 17-4 PH plate, see Figure 99 and Figure 100. After the reaction, on the cylinder there were discontinuous Ni islands 100's of microns across, covering most of the surface and the visible edges of the micro channels. Particulate Ni was found within and adjacent to these islands whilst Si particles were found aggregated in a few local regions as in the preliminary plate coatings. Oddly, none of the K particles or Na_2O could be found on the cylinder suggesting that the reducing atmosphere has entirely removed these materials or that the K and Na oxide were contaminants associated with the 17-4 PH plate substrate.

It is unusual that this material was not active given that Ni is known to be active for dry reforming of methane. Its' suggested that either some inactive carbon deposition on the Ni due to methane decomposition, see Figure 100 and Eq. *15*, or sintering of the catalyst, see Figure 98, or one of the alloying elements, such as Mn or Si, is responsible for poisoning the catalyst.
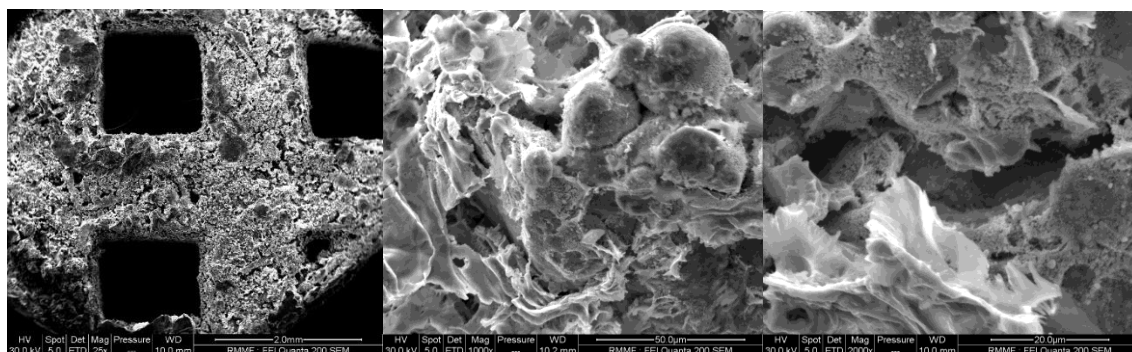
Figure 99 SEM micrographs of the cylinder coating: Ni coated 17-4 PH surface, heated to 550ºC for 4 hours then reduced at 700ºC in CH_4 & H_2.

Figure 100 EDX micrographs of the cylinder coating: Ni-coated 17-4 PH surface, heated to 550ºC for 4 hours then reduced at 700ºC in CH₄ & H₂.

Following the Ni on 17-4 PH coating was the Ni/Al$_2$O$_3$ on 17-4 PH coating. Unfortunately, the GC-FID data that resulted from this reaction was erratic and no means was found to identify which peaks corresponded to which compounds, as such the GC-FID data could not be interpreted.

However, SEM/EDX characterisation provided useable data of the NiO/Al$_2$O$_3$ coatings on 17-4 PH steel, and showed how the substrate surfaces were changed due to oxidizing calcination for both the plate preliminary coatings, see Figure 103, Figure 104, and Figure 105, and for a 2nd coating on another plate using a slightly higher calcination temperature (550ºC instead of 500ºC), see Figure 101, Figure 108, and Figure 109. Further characterisation of the NiO/Al$_2$O$_3$ coating applied to the used reaction cylinder revealed the impact of the reducing reaction, see Figure 102, Figure 110, Figure 111, and Figure 112.

After applying and drying the NiO/Al$_2$O$_3$ on 17-4 PH coating for the 2nd plate, an inhomogenous distribution of the coating was observed with clusters of intense green thicker than the underlying mild green coating and poor wetting of the surface. After 550ºC/4h calcination the 17-4 PH coated in NiO/Al$_2$O$_3$ acquires a dirty-brown colour and the wetting is similar to the dried coating and, unlike the NiO coating, the 17-4 PH substrate acquires a

bronzed colour, see Figure 101**.** After the reaction the cylinder is coated in a thin black coating of material, see Figure 102. SEM/EDX characterisation of this cylinder revealed that the charcoal black colour is partly due to the presence of carbon.

Figure 101 NiO/Al$_2$O$_3$ on 17-4 PH plate after 550°C/4h calcination; Sample ID [A-p].

Figure 102 (Left) Unaltered 17-4 PH cylinder (Middle, Right) Ni/Al$_2$O$_3$ on 17-4 PH cylinder after 550°C calcination, 700°C reduction & reaction; Sample ID [A-c]

As mentioned earlier for NiO, variability of coating morphology occurred for NiO/Al$_2$O$_3$ with only a 50°C increase in calcination temperature from 500°C for the preliminary coating, see Figure 103, to 550°C, see Figure 108, for the secondary plate coating.
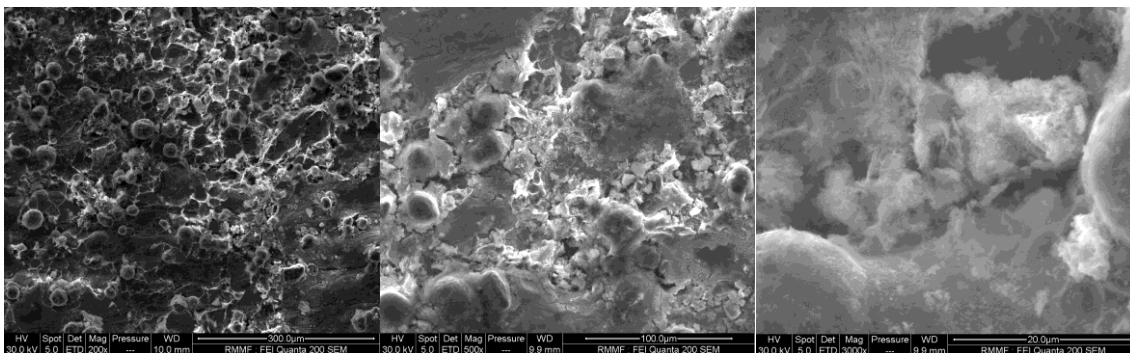
Figure 103 SEM micrographs of the preliminary coating: 10wt.% Ni, NiO/Al$_2$O$_3$ coated 17-4 PH surface, heated to 500°C for 4 hours

Considering the preliminary NiO/Al$_2$O$_3$ coating shown in, Figure 103, Figure 104, and Figure 105, in which ridges of NiO, Al$_2$O$_3$ and/or Ni, Al mixed metal oxide deposits are observable all over the substrate surface, see the left micrograph of Figure 103. These deposits lie preferentially on the underlying substrate. They appear to be the remnants of large amounts

of material lost during calcination. The remnants Ni and Al tend to be aggregated separately from one another and are distributed all over the substrate unevenly. Although it appears that the remnant particles are not strongly interacting. It is suggested that a mixed metal oxide of Ni and Al was removed by the calcination procedure.
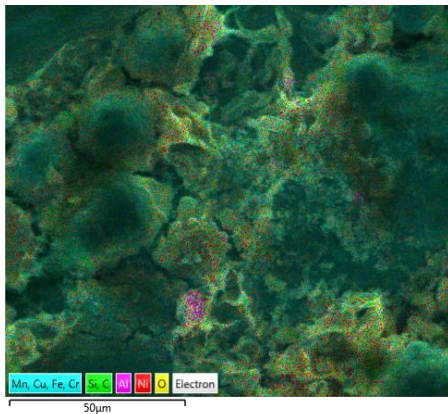
Figure 104 EDX micrographs of the preliminary coating: 10wt.% Ni, NiO/Al$_2$O$_3$-coated 17-4 PH surface, heated to 500°C for 4 hours
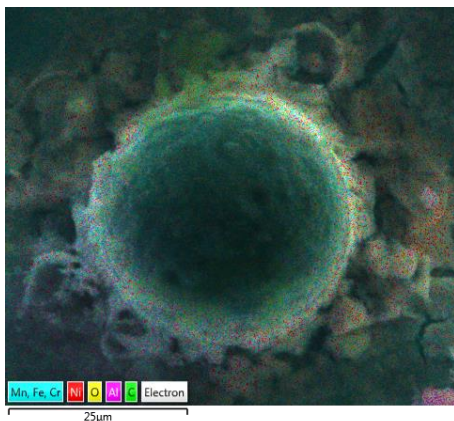
Figure 105 EDX micrographs of the preliminary coating: 10wt.% Ni, NiO/Al$_2$O$_3$-coated 17-4 PH surface, heated to 500°C for 4 hours

The preliminary coating of NiO/Al$_2$O$_3$ and NiO show similar amounts of Ni (27.4wt.% and 30.8wt.% respectively) and therefore, coverage of Ni on the surface of their 17-4 PH substrates, see the layered EDX maps and quantitative spectra of typical regions in Figure 106. It's noted that lower proportions of Al$_2$O$_3$ were observed than the 10wt.% loading of Ni in the NiO/Al$_2$O$_3$ would infer. It's evident that NiO bonds with a greater affinity to the 17-4 PH alloy than the Al$_2$O$_3$ in the coating solution. Regardless, as with most of the depositions, the

deposits were found preferentially on the underlying surface and some of the EDX maps show clear anchoring of the coating, NiO in particular, see Figure 105.
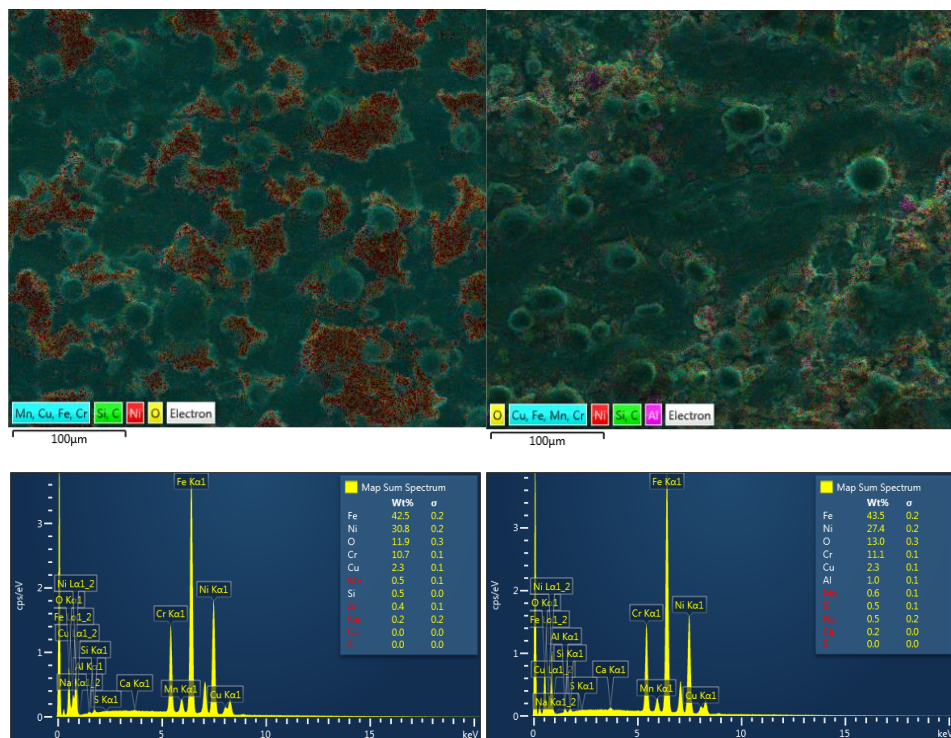
Figure 106 (Left) A layered EDX Map showing a typical distribution of NiO on the preliminary coating of 17-4 PH with quantitative spectra attached below. (Right) A laye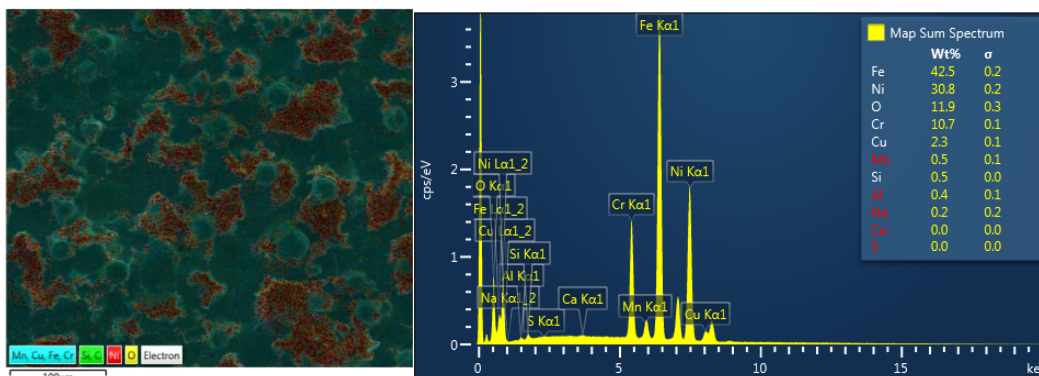red EDX Map showing a typical distribution of NiO/Al$_2$O$_3$ on the preliminary coating of 17-4 PH with quantitative spectra attached below.

A contrast between typical regions of NiO and NiO/Al$_2$O$_3$ reveals some key changes in the NiO distribution behaviour caused by the presence of Al$_2$O$_3$, see Figure 106. The preliminary NiO coating forms evenly dispersed disconnected NiO islands in sizes ranging from 10's of μm's to 100's of μm's across. The preliminary NiO/Al$_2$O$_3$ coating forms uneven distributions of more closely clustered and smaller NiO and Al$_2$O$_3$ islands 10's of μm's across, leaving some regions of the 17-4 PH surface entirely uncoated and unaffected by their presence. The Al$_2$O$_3$ islands tend to coincide with the NiO islands, rarely occurring entirely in isolation from them. Unlike the NiO preliminary coating, the NiO/Al$_2$O$_3$ preliminary coating did not show any strong evidence of silicate particles consistently precipitating at its' surface.

Likewise, the 2nd plate coating of NiO/Al$_2$O$_3$ on 17-4 PH was also observed to have negligible numbers of silicate particles forming, see Figure 108 and Figure 109. For NiO/Al$_2$O$_3$, unlike the

preliminary and secondary coats of NiO on 17-4 PH, the preliminary and secondary coats of NiO/Al_2O_3 on 17-4 PH are quite similar. Especially with respect to the loading of Ni which only changed from 27.4wt.% in the preliminary coating to 27.8wt.% in the secondary coating, see Figure 107. Conversely the Al loading is substantially higher at 5.3wt.% in the secondary coating compared to 1.0 wt.% in the preliminary loading. With only a 50°C increase in calcination temperature there is currently no explanation provided for this Al concentration difference. Al distribution nonetheless follows a similar pattern for the secondary coating, see Figure 109, as it does for the preliminary coating, see Figure 104; a dispersion of discrete Al_2O_3 islands, although the Al_2O_3 is visibly embedded underneath the NiO in the secondary coating.
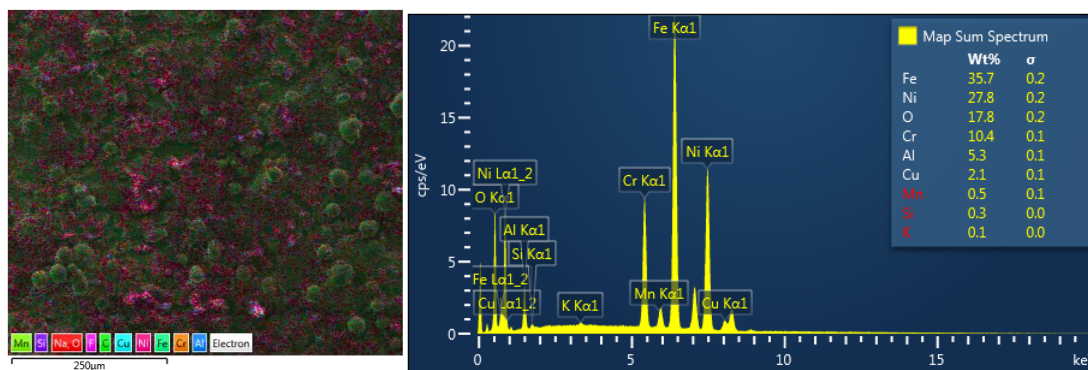
Figure 107 (Left) A layered EDX Map showing a typical distribution of NiO/Al_2O_3 on the 2nd plate coating of 17-4 PH. (Right) The corresponding quantitative spectra.

However, the major distinction between preliminary coatings and secondary coatings for NiO/Al_2O_3 is the morphology of the coatings. Whilst the preliminary coating consisted of NiO and Al_2O_3 islands made distinct by what appears to be shrinkage and/or evaporation cracks, in the secondary coating, the NiO is wispy and more continuous with no distinct NiO islands. There is less evidence of traces of Ni, and Al oxides and its' suggested that less material loss has occurred from the secondary coating.
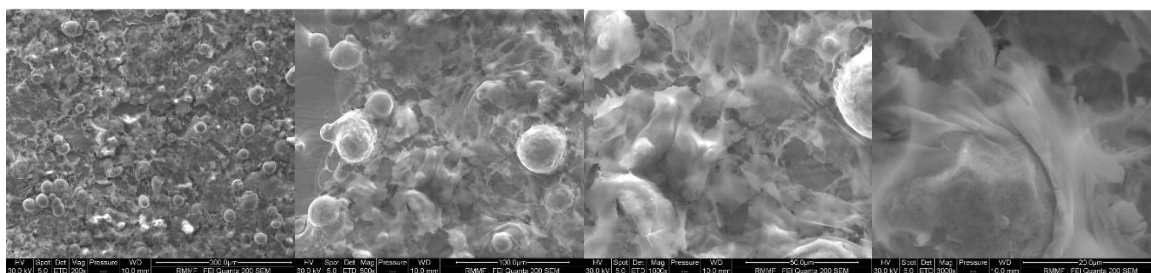
Figure 108 SEM micrographs of the 2nd plate coating: 10wt.% Ni, NiO/Al2O3 coated 17-4 PH surface, heated to 550°C for 4 hours.
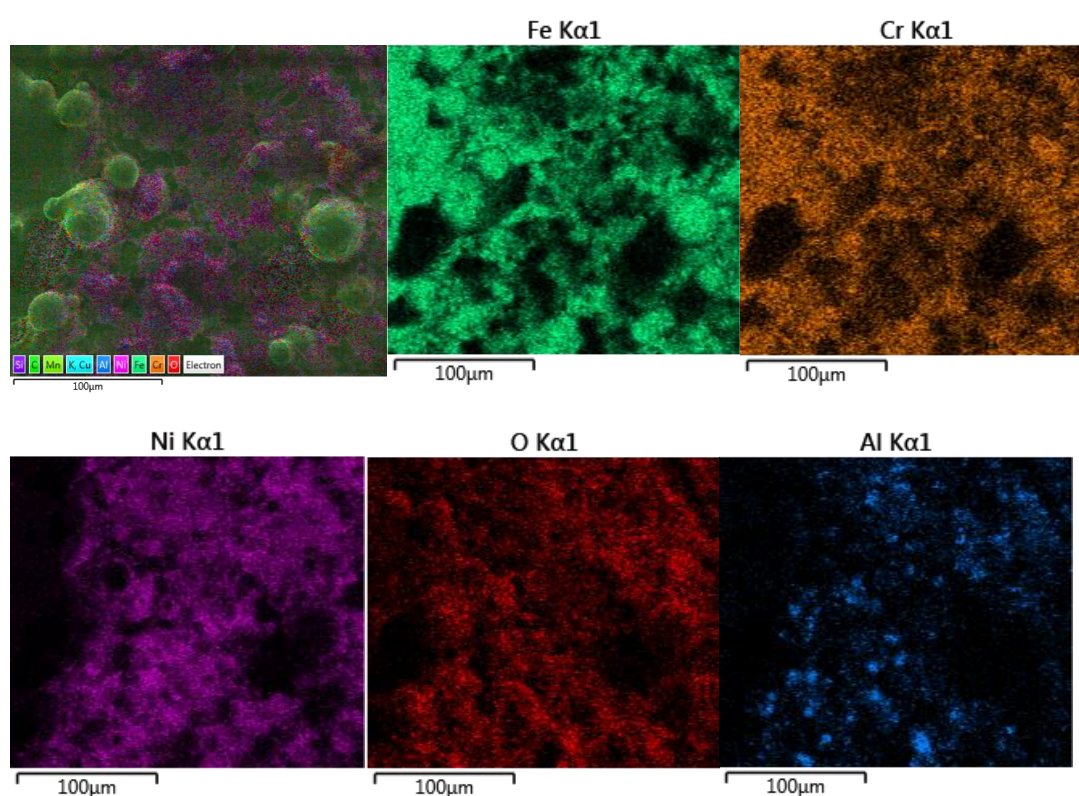
Figure 109 EDX micrographs of the 2nd plate coating: 10wt.% Ni, NiO/Al2O3-coated 17-4 PH surface, heated to 550°C for 4 hours.

As for pure NiO coating, so also for NiO/Al_2O_3 coating its necessary to reduce the NiO to Ni for its effective use as a catalyst in the DRM reaction. However, looking at all EDX spectrums taken of the cylinder after the reaction, including Figure 112, there is neither a strong positive nor a strong negative correlation between the Ni and the O. This makes the oxidation state of the Ni ambiguous.

The typical loading of Ni after the reaction is only moderately reduced by the reaction from 27.8wt.% Ni to 26.1wt.% Ni and the Ni distribution has changed quite substantially. Instead

of the wispy, almost continuous distribution of Ni present on the secondary plate coating, there are clusters of Ni and potentially a particulate Ni distribution. There are regions where the underlying substrate of 17-4 PH appears heavily percolated and it's not clear whether a very thin layer of percolated Ni might be present or not, see Figure 112. Other regions, see Figure 111, are more like the distribution apparent for the preliminary NiO on a 17-4 PH plate, see Figure 93, in that they consist of discrete Ni (or potentially NiO) islands 100's of μm's across.

Although there are no unexpected particles present for the Ni/Al_2O_3 coating on the 17-4 PH steel according to the EDX, there are some odd structures apparent at very high magnifications – those greater than 15,000x make this observation clearest, consider the 15,000 and 30,000x magnfications of Figure 110. Irregular strings of material which are compositionally indistinct on the low-resolution EDX maps are of an unspecified material. It's suggested that this is filamentous carbon or carbon nanotubes.
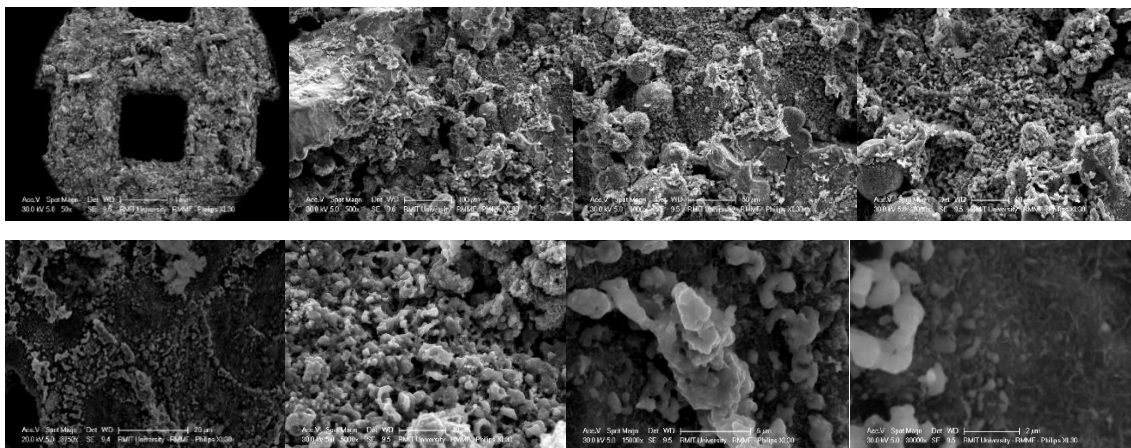
Figure 110 SEM micrographs of the cylinder coating: 10wt.% Ni, NiO/Al_2O_3 coated 17-4 PH surface, heated to 550ºC for 4 hours then reduced at 700ºC in CH_4 & H_2.
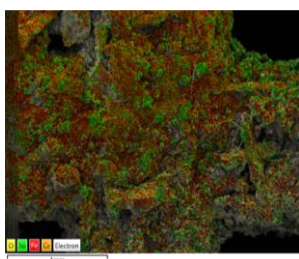
Figure 111 Dispersion of Ni on NI/Al_2O_3 coated cylinder after 700ºC reducing reaction.
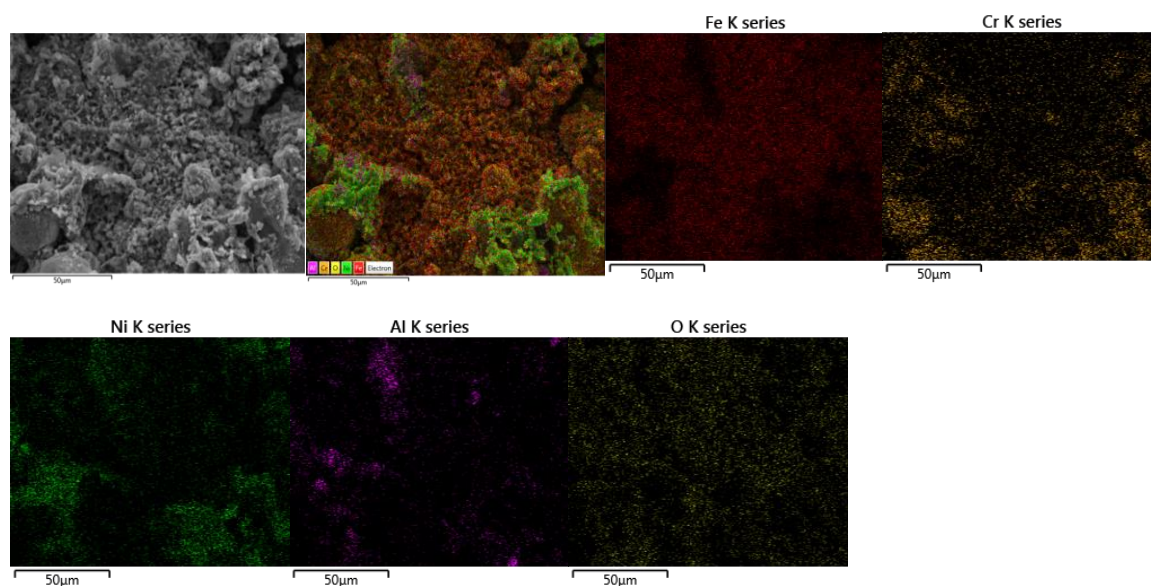
Figure 112 EDX micrographs of the cylinder coating: NiO/Al$_2$O$_3$-coated 17-4 PH surface, heated to 550°C for 4 hours then reduced at 700°C in CH$_4$ & H$_2$.
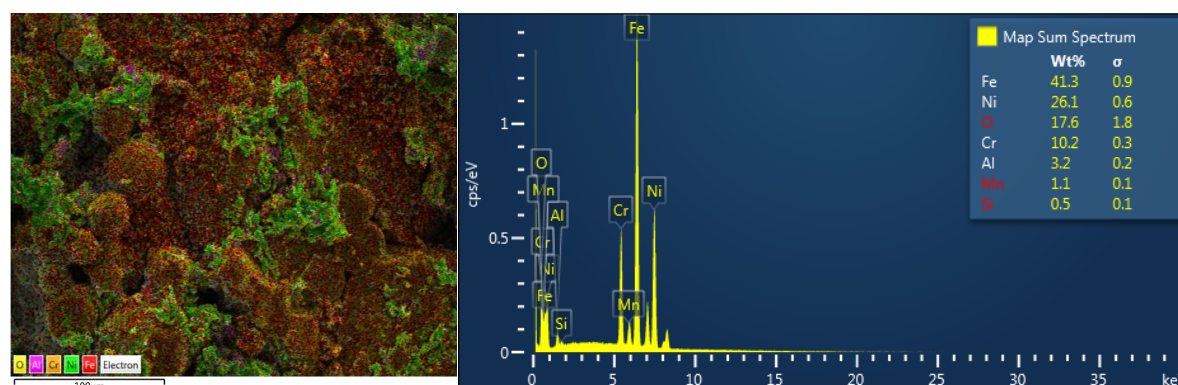
Figure 113 (Left) A layered EDX Map showing a typical distribution of Ni/Al$_2$O$_3$ on the cylinder coating of 17-4 PH after a reaction. (Right) The corresponding quantitative spectra.

This Ni/Al$_2$O$_3$ coating also proved to be inactive, so further modification was made to see what improvements MgO could make as a support in a NiO/MgAl$_2$O$_4$ coating, furthermore a higher temperature was trialed for this last substrate to increase the reaction rate and to favour higher conversion. This yielded the best result of all 3 tested systems. The reaction outcome from metallic nickel supported by magnesium alumina on 17-4 PH steel with 5wt.% Ni, [C-c] was a small conversion of CH$_4$ & CO$_2$, see the GC-FID data in Figure 114.

Figure 114 Online GC-FID Data for Ni/MgAl$_2$O$_4$ on 17-4 PH Steel

This data was converted to a conversion vs. time graph, see Figure 115, in which there is a variance of catalyst activity over time. Although there is an initial growth in conversions over the 1st 3 hours, the reaction never converts enough CH$_4$ or CO$_2$ to justify further use of these catalyst materials without further adaptation. Given the deactivation of the catalyst, it's suggested that one or more of the various alloying elements in the 17-4 PH steel was responsible for this loss of activity due to temperature-enhanced diffusion allowing enhanced interactions of these elements.

Figure 115 Online conversion for Ni/MgAl$_2$O$_4$ on 17-4 PH Steel

To discern the morphology change caused by reduction, SEM/EDX was performed on the planar substrate, see Figure 116, and Figure 118, and the cylinder was prepared for similar characterisation. Unfortunately, the sample was misplaced and this latter characterisation had to be excluded. Nonetheless the following data serves to reveal the nature of the originally deposited catalyst coating.

For the $NiO/MgAl_2O_4$ deposited on 17-4 PH, after drying, a homogenous, uniformly thick, pale milky-green deposition of the coating was observed with good wetting over the surface. After calcination at 550°C/4h the coat was a light brown colour and there was visible cracking. For the cylinder, after calcination before the reaction, a brown coating was visible covering all the visible internal geometry, to the extent of flow being partially blocked by coat thickness in some channels. Sapphire-blue particles were visible to the naked eye. It's suggested that these are Ni-based particles although these weren't visibly apparent on the coated plates.

The SEM/EDX data for the $NiO/MgAl_2O_4$ deposition shows a much thicker coating than any previous coating used for DRM, see Figure 116. Overall the morphology is characterised by thickly coated regions which flake away at the edges into more sparse clusters of particles of the coating materials. Unfortunately, attempts to measure coating thickness by imaging a section of this substrate are not effective due to the loss of coating caused by the sectioning process. Nonetheless it is noted that, the loading of the coating elements is quite different, see Figure 117. The Ni loading is 5.6 wt.% and the Al is further reduced at only 0.9 wt.%. The reason for this of course is the preferential deposition of the Mg at 35.5wt.% The proportion of Ni:Mg is closer to the deposition solution ratio than in any other context. It's suggested that the Mg also has good affinity with the 17-4 PH and this is why it coats so much better than the Al. Furthermore, it's observed that the desired $MgAl_2O_4$ phase is definitely not occuring to any notable extent as all Al particles are clearly distributed with no particular correlation to the Mg. Nonetheless, as for the NiO preliminarily coated 17-4 PH plate, there is observed on the $NiO/MgAl_2O_4$ coated 17-4 PH plate, an ample number of silicate-based particles, see Figure 118.

One unfavourable trend is observed in the relative distribution of Mg and Ni in Figure 118. Where Mg concentrations are highest there is less Ni concentrated and vice-versa; these materials preferentially deposit away from each other which is not preferable as the role of

MgO, MgAl$_2$O$_4$ and Al$_2$O$_3$ is primarily to provide an underlying support for Ni and protect these particles from sintering. Furthermore, there is no strong evidence of any particulate Ni and there is very little in the way of particulate Mg or Al either. This suggests that the calcination process may have caused sintering to some extent, however this is difficult to verify as there is no SEM data for the substrate prior to calcination.
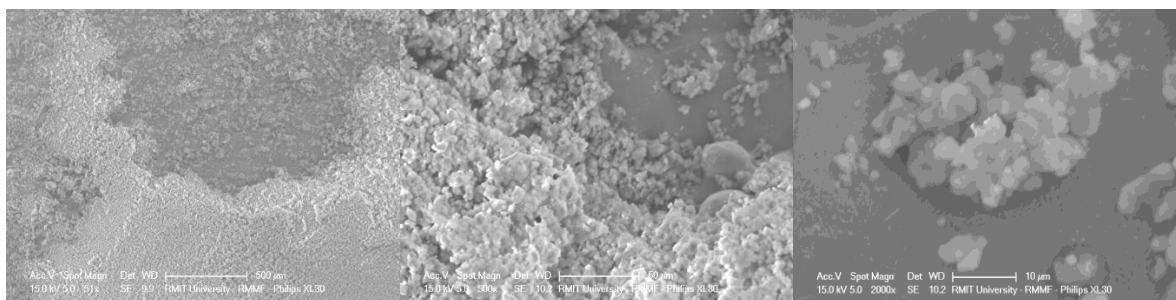
Figure 116 SEM micrographs of: NiO/MgAl$_2$O$_4$ coated 17-4 PH plate, heated to 550ºC for 4 hours
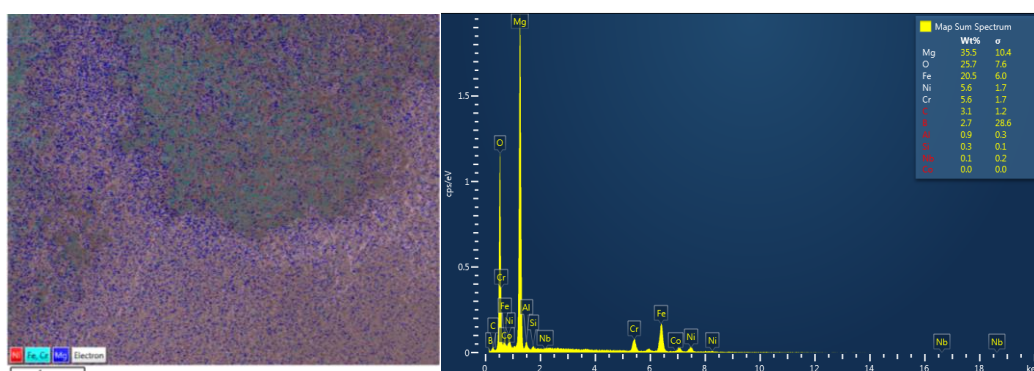
Figure 117 (Left) A layered EDX map showing a typical distribution of Ni/MgAl$_2$O$_4$ on the cylinder coating of 17-4 PH after a reaction. (Right) The corresponding quantitative spectra.

The two differences which contributed to making this catalyst system active were the inclusion of MgO and the increased reaction temperature from 700ºC to 800ºC. Due to the limited number of reactions undertaken, it was not possible to separate the effect of these factors from each other. Regardless, these changes led to a system which demonstrated some initial catalyst activity for DRM, the catalyst was mildly active and stuck to the 17-4 PH alloy initially. Whether it remained afterwards could not be determined due to the loss of the sample.
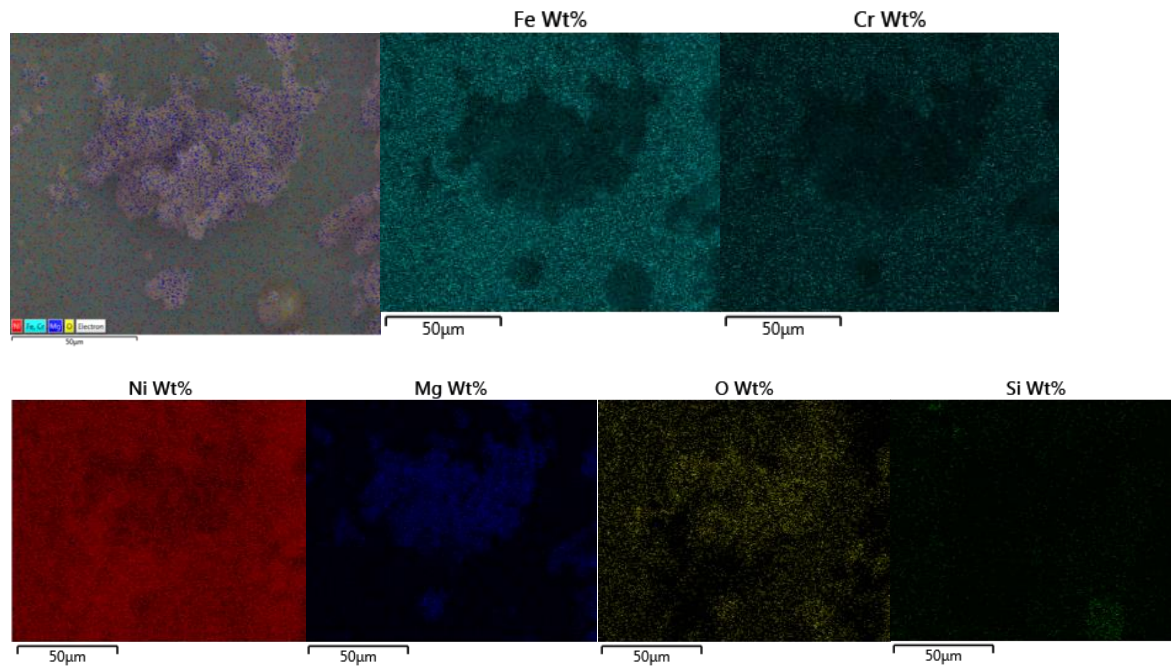
Figure 118 EDX micrographs of: NiO/MgAl₂O₄-coated 17-4 PH plate, heated to 550°C for 4 hours.

4.3 SUMMARY AND CONCLUSIONS

All preliminary and secondary plate coatings were observably distinct with only a 50°C increase in calcination temperature and no other changes in method. Furthermore, not all elements in the catalyst coating solution deposit with equal efficiency; Ni and Mg were found to deposit preferentially to Al which always coated in disproportionately small amounts. Furthermore, some elements precipitated or coated the 17-4 PH substrate instead of the catalyst; deposits of K and Na coincided with regions of low catalyst coating content, making the removal of elements inducing such effects favourable for better catalyst coating.

The work performed on DRM is not, by any means, close to commercial application. However, the brief activity demonstrated by the Ni/MgAl₂O₄ (5wt.% Ni) catalyst ([C-c]), is enough for a proof of concept. It indicates that the use of SLM is valid to the objective: "Design/Print geometries for continuous reactions with high Surface Area to Volume Ratios & without removable internal support structures." Given the rapid deactivation of the catalyst, it's suggested that one or more of the various alloying elements in the 17-4 PH steel were responsible for this loss of activity due to temperature-enhanced diffusion allowing enhanced interactions of these elements. Alternately deposited carbon may have blocked the active

sites of the catalyst or other interactions with the reactants and products could be responsible for catalyst deactivation.

Nonetheless, there are several points at which this research may be furthered; investigation of the origins of stray inclusions such as K or Na should be undertaken so that these unintended inclusions may be controlled or removed entirely. In addition, the use of more stable alloys such as anInconel alloys is suggested – they are well-known for their extreme temperature resistance, a property which 17-4 PH poorly mirrors. As to the coating content, the loading of the constituents should reflect the ratios which are known to be effective, whilst Mg and Ni coated well, Al did not – this must be improved if Al is to be used as a support.

It would also be beneficial for more thorough studies to be undertaken on the impact of temperature on reaction outcomes for functionalised SLM-based substrates. Especially where alloys such as 17-4 PH steel are concerned as they have many elemental components.

Overall it has been found that better understanding of the interactions between the deposited catalyst and the SLM substrate are needed, especially where the SLM alloy used is a complex system consisting of many elemental components. Adherence of the catalyst is not as great an issue as the chemical stability of the catalyst – pressure exerted by gases didn't notably strip the catalyst from the substrates, however the elevated temperature and, possibly, unintended reactions have chemically degraded the substrate alloy and catalyst so they are ineffective for catalysis and unsuited for extended high temperature exposure.

CHAPTER FIVE – LIQUID PHASE REACTIONS ON AM SUBSTRATES

5.1 INTRODUCTION

In the previous chapter, it was shown that catalyst coated monoliths exhibit moderate catalytic activity towards DRM. In this chapter SLM substrate-supported catalysts were tested for their catalytic applications in liquid phase heterogeneous catalysis. Therefore, the reactions were undertaken as batch type processes, as this is a more compatible approach for liquid phase reactions. Two representative reactions chosen for this project were 4-NP reduction and glycerol acetalisation.

4-NP is a toxic, organic pollutant introduced to water by industrial sources [204]. The product of 4-NP reduction is 4-Aminophenol (4-AP), a product which is useful for antipyretic and analgesic drugs [204]. 4-NP reduction can be described by Eq. 17 and Figure 119. In this work NaBH$_4$ is used to reduce the 4-NP to 4-AP.

$2C_6H_4NO_2OH \rightarrow 2C_6H_4NH_2OH + H_2O$ *Eq. 17 4-NP Reduction (Not balanced) [204].*
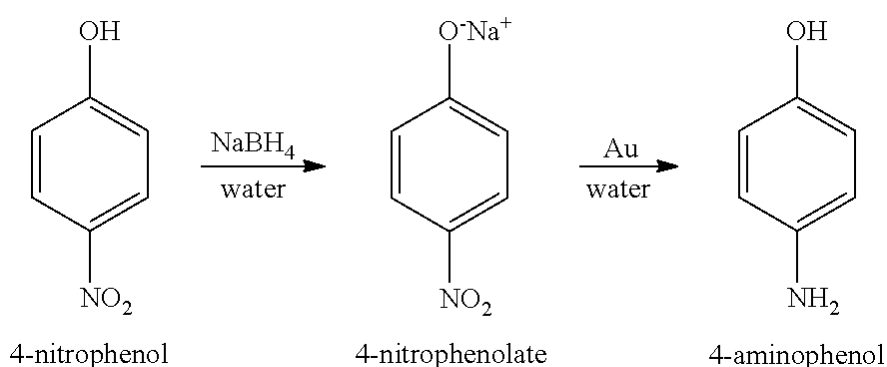
Figure 119 Schematic of 4-NP reduction to 4-AP via 4-Nitrophenolate [205].

Wang et al. describes a reaction mechanism for the anaerobic, catalytic reduction of 4-Nitrophenol in a recent paper, as illustrated in Figure 120 [206]. When in a solution with NaBH$_4$, 4-Nitrophenol converts to 4-Nitrophenolate with a Na$^+$ atom present in place of the H in the hydroxyl group. Once the BH$_4^-$ and 4-Nitrophenolate adsorbed onto the catalyst surfaces, electron transfer occurred from the donor BH$_4^-$ to the 4-NP acceptor. The catalysts acted as an electron transfer medium between the 2 reactants. Once the 4-nitrophenolate receives the electrons, BH$_4^-$ ions act as a H source allowing 4-AP to form as the final product

[207]. The key role of the catalysts in this reaction is the adsorption of 4-Nitrophenolate and BH_4^- ions to facilitate electron transfer.
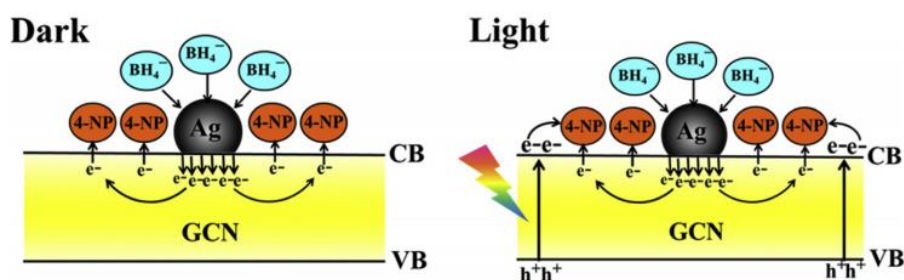
Figure 120 Mechanism of catalytic reduction of 4-NP with the Ag/GCN composite [206].

Conversely, glycerol is not toxic but instead will be ubiquitous as future glycerol supply is anticipated to increase with the use of the biodiesels that produce it as a by-product [208]. To utilise this, glycerol can be converted to more valuable products such as biodiesel fuel additives like solketal, see Figure 121.
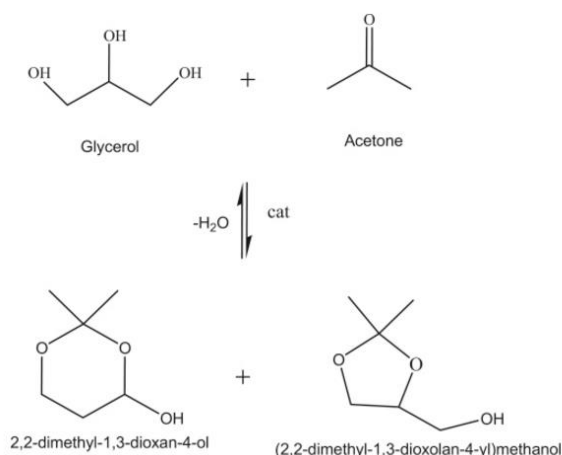
Figure 121 Unbalanced Glycerol Acetalisation according to Gadamsetti et al. [210].

A reaction mechanism for glycerol acetalisation with acetone and a mesoporous silica-supported Molybdenum Phosphate catalyst is also shown by Gadamsetti et al. in Figure 122 [210]. The general mechanism is thought to begin with a lone pair of electrons on an outer glycerol oxygen atom attacking the positively charged carbonyl carbon of the acetone to form an intermediate compound called Hemiketal. Meanwhile, a hydroxyl group has adsorbed to the catalyst surface. The nucleophilic attack of the secondary glycerol hydroxyl group upon the tertiary carbon of the hemiketal forms solketal whilst the hemiketal is indirectly adsorbed

to the catalyst via another hydroxy group. The catalyst's role here is to adsorb hydroxy groups in order to adsorb the intermediate hemiketal and enable a nucleophilic reaction to occur.
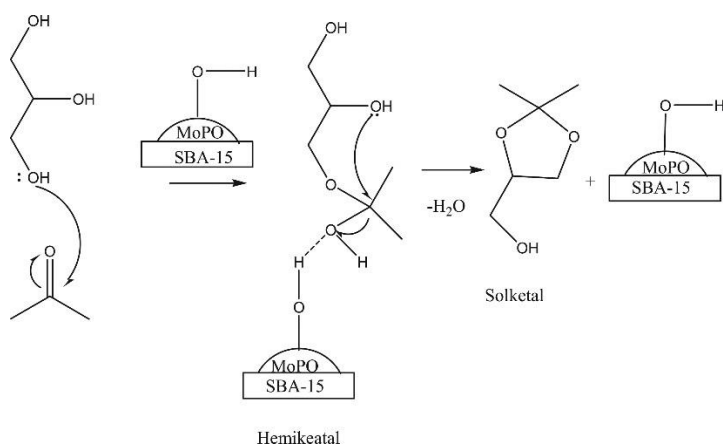
Figure 122 Possible reaction mechanism of glycerol acetalization with acetone over MoPO/SBA-15 catalysts [210].

Three major challenges were identified in this work, as described in the introduction to the Experimental Method. All three of these difficulties will be addressed here using 4-NP reduction and glycerol acetalisation applied to select catalyst coatings of interest. For 4-NP reduction, the reactions of Au nanoparticles dried or calcined at 400°C/4h and Pd nanoparticles dried or calcined at 400°C/3h on Ti6Al4V substrates are highlighted. Likewise, the solid-acid catalyst $FeCl_3$ calcined at 250°C/4h is highlighted in its application to glycerol acetalisation.

The focus of this chapter is the catalysts coated and their reaction activity in 4-NP reduction and glycerol acetalisation as well as the impact of the reaction on the catalyst and its' underlying SLM substrate.

5.2 4-NITROPHENOL REDUCTION

All samples trialled in 4-NP reduction reactions are listed in Table 23 paired according to a sample ID and the related preparation methodology, whilst all the dates of these reactions and their complications are outlined in Table 24.

Table 23 - Ti6Al4V samples trialled for catalytic activity in 4-nitrophenol reduction & their assigned Sample ID

Sample ID	Sample Preparation
-	Au nanoparticle (NP) Coatings
[HI Au NP-T-Dried]	*Horizontally Immersed, Dried
[HI Au NP-T-400°C/4h]	*Horizontally Immersed, 400oC/4h
[HI Au NP-T-400°C/3h]	Horizontally Immersed, 400oC/3h
[HI Au NP-T-500°C/3h]	Horizontally Immersed, 500oC/3h
[HI Au NP-T-500°C/4h]	Horizontally Immersed, 500°C/4h
[HI Au NP-T-600°C/3h]	Horizontally Immersed, 600°C/3h
[50µL Au NP-T-Dried]	50µL drop-cast, dried
[50µL Au NP-T-400°C/3h]	50µL drop-cast, 400°C/3h
[300µL Au NP-T-Dried]	300µL drop-cast, dried
[300µL Au NP-T-400°C/3h]	300µL drop-cast, 400°C/3h
[300µL Au NP-T-H_2 400°C/3h]	300µL drop-cast, H_2 400°C/3h
[VI Au NP-T-Dried]	Vertically Immersed, Dried
[VI Au NP-T-400°C/3h]	Vertically Immersed, 400°C/3h
-	Mixed Coatings
[100µL Au NP/PdCl$_2$(COD) T-H_2 400°C/3h]	Au NP, PdCl$_2$ 300µL, H_2 400°C/3h
[DDA-Pd HI Au NP-T-400°C/3h]	Au NP Dried, DDA-Pd Dip Coat, Aqueous NaBH4, 400°C/3h (Sequential)
[DDA-Pd HI Au NP- (400°C/3h)²]	Au NP, DDA-Pd Dip Coat, Aqueous NaBH4, 400°C/3h (Sequential)
[HI Au NP/CNT-T-400°C/3h]	Au-NP, CNT's-Ti6Al4V H_2 400°C/3h
-	Uncoated Ti6Al4V
[T]	Plain Ti6Al4V
[T-400°C/3h]	400°C/3h Ti6Al4V
[T-500°C/3h]	500°C/3h Ti6Al4V
[T-600°C/3h]	600°C/3h Ti6Al4V
[T-H_2 400°C/3h]	H_2 400°C/3h Ti6Al4V
-	Pd NP Coatings
[DDA-Pd-T-Dried]	*DDA-Pd Dip Coat, Aqueous NaBH$_4$, dried
[DDA-Pd-T-400°C/3h]	*DDA-Pd Dip Coat, Aqueous NaBH$_4$, 400°C/3h
[Oleic-Pd-T-Dried]	Oleic Acid-Pd, Drop-cast, Direct NaBH$_4$
[Oleic-Pd-T-400°C/3h]	Oleic Acid-Pd, Drop-cast, Direct NaBH$_4$, 400°C/3h
[PdCl$_2$(COD)-T-H_2 400°C/3h]	PdCl$_2$ 300µL, H_2 400oC/3h
[CNT-T-H_2 400°C/3h]	CNT's-Ti6Al4V H_2 400°C/3h
-	No Catalyst

*These catalysts demonstrated noticeable activity

Table 24 Dates of reactions, complications and the corrections made for glycerol acetalisation

Substrates Tested	Remarks
[HI Au NP-T-Dried], [T], [HI Au NP-T-400°C/4h], [T-400°C/3h], [HI Au NP-T-500°C/3h], [T-500°C/3h], [HI Au NP-T-600°C/3h], [T-600°C/3h].	Applied at RTP without stirring. [HI Au NP-T-Dried], [HI Au NP-T-400°C/4h] were active. Trial heating and stirring.
No Catalyst, [HI Au NP-T-Dried], [HI Au NP-T-400°C/3h].	50°C/200rpm
[T], [T-400°C/3h].	Temperature & stirring rpm not recorded.
Improvement identified.	Reactant mass >> Catalyst mass, consider decreasing reactant volume
[VI Au NP-T-Dried], [VI Au NP-T-400°C/3h].	Temperature & stirring rpm not recorded.
[DDA-Pd-T-Dried]$_1$, [DDA-Pd-T-400°C/3h]$_1$.	100°C/500 rpm. Both samples were active.
[DDA-Pd-T-Dried]$_2$, [DDA-Pd-T-400°C/3h]$_2$.	100°C/500 rpm. Both samples were inactive.
[DDA-Pd HI Au NP-T-400°C/3h], [DDA-Pd HI Au NP-T- (400°C/3h)^2].	Used 15/08/16 Concentrations.
[Oleic-Pd-T-Dried]	Temperature & stirring rpm not recorded.
[Oleic-Pd-T-400°C/3h]	Temperature & stirring rpm not recorded.
[PdCl$_2$(COD)-T-H$_2$ 400°C/3h], [300μL Au NP-T-H$_2$ 400°C/3h], [T-H$_2$ 400°C/3h], [100μL Au NP/PdCl$_2$(COD) T-H$_2$ 400°C/3h].	[100μL Au NP/PdCl$_2$(COD) T-H$_2$ 400°C/3h]

In the preliminary testing, [HI Au NP-T-Dried] & [HI Au NP-T-400°C/4h] samples exhibited moderate reduction of 4-nitrophenol whereas [T], [T-400°C/3h], [HI Au NP-T-500°C/3h], [T-500°C/3h], [HI Au NP-T-600°C/3h] & [T-600°C/3h] were inactive. This was qualitatively assessed by visual inspection of the reaction solution colour. A clear solution had most 4-nitrophenol reduced, and a rich-yellow solution had little-to-no 4-nitrophenol reduced. These substrates were all SEM imaged & EDX mapped.

The [HI Au NP-T-Dried] sample is distinct from all the calcined samples in that the Au is not primarily nanoparticulate but rather it's distributed within or adjacent to amorphous carbon matrix as clusters of nanoparticles, larger in size than microns, as shown in Figure 123. This is most strongly evidenced by the close overlap of the carbon and Au EDX Maps, as shown in

Figure 124. The carbon originates from the Au nanoparticle synthesis process in the form of the ligand; dodecylamine. There are also Al₂O₃ particles present on the surface, though relatively few of them.
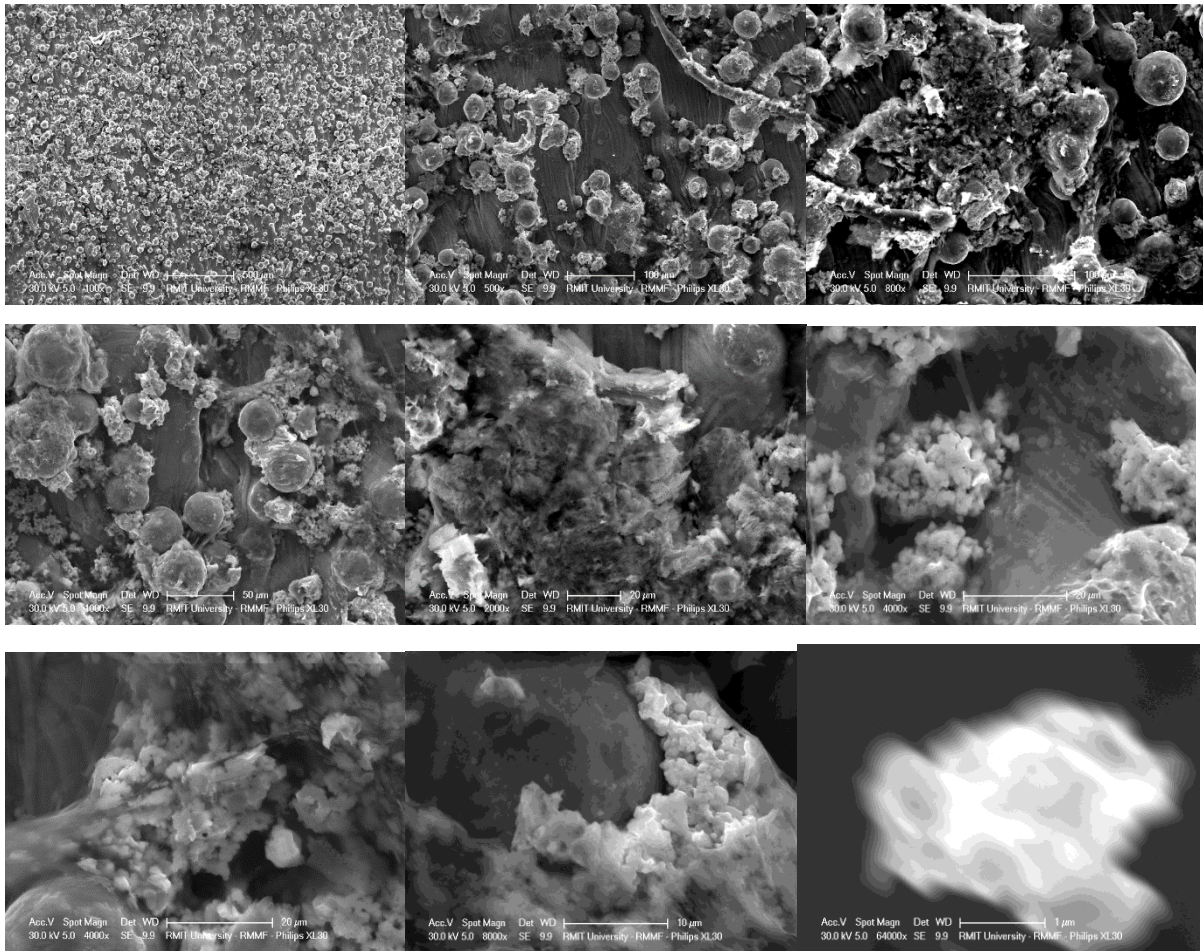
Figure 123 SEM micrographs of [HI Au NP-T-Dried].
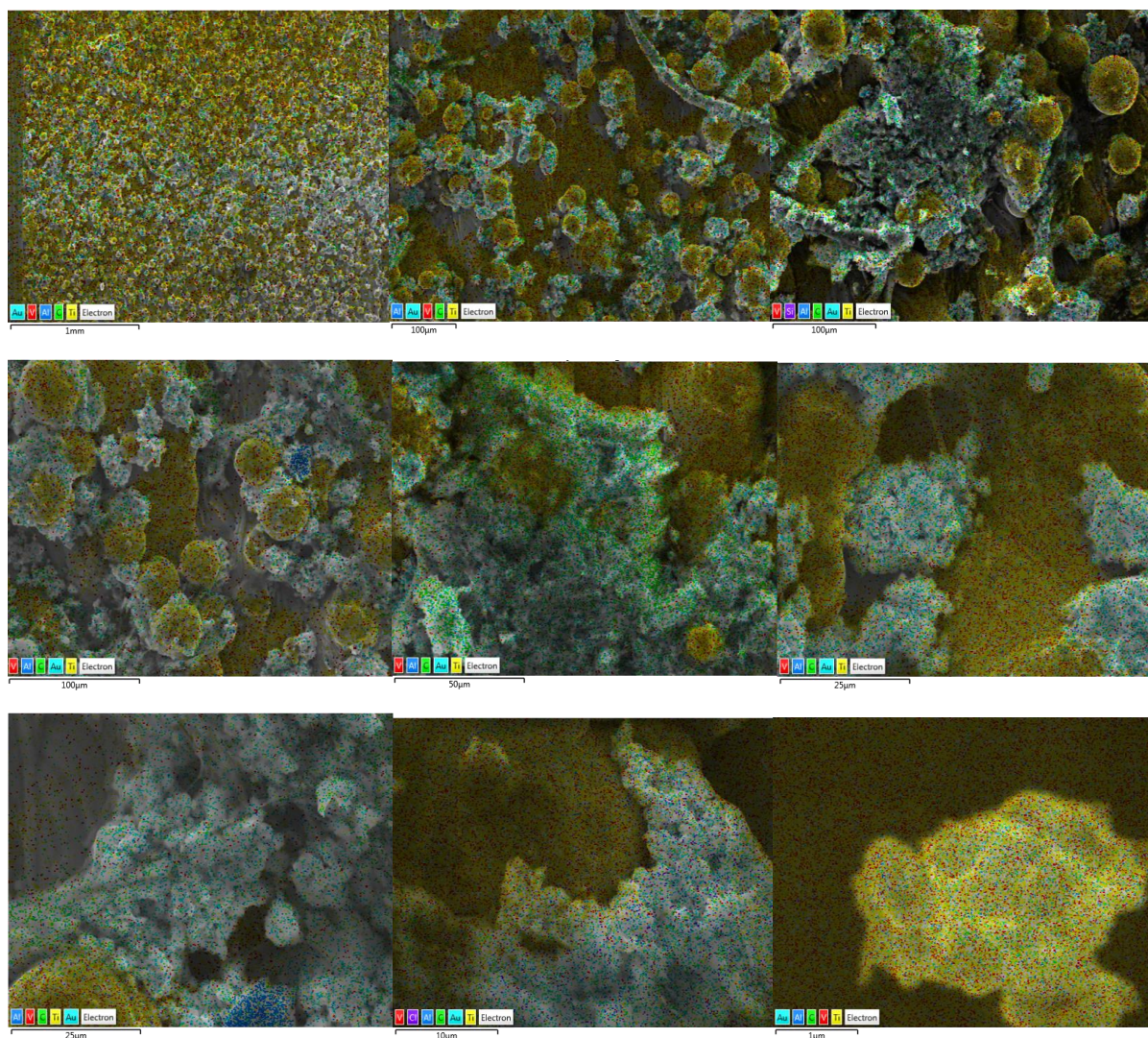
Figure 124 Corresponding EDX micrographs of [HI Au NP-T-Dried]

Like the former sample, [HI Au NP-T-Dried], [HI Au NP-T-400°C/4h] was found to be highly active for nitrophenol reduction. Unlike the former sample, [HI Au NP-T-Dried], [HI Au NP-T-400°C/4h] has absolutely no carbon present, nor do any of the other calcined samples, as can be seen in Figure 125 and Figure 126. This indicates that calcination has not deactivated the Au nor does the amorphous carbon appear responsible for any nitrophenol reduction.

The two region types found on [HI Au NP-T-500°C/3h] and [HI Au NP-T-600°C/3h] were also present on [HI Au NP-T-400°C/4h], although much more of the Au was distributed than formerly described in the dense regions of [HI Au NP-T-500°C/3h] and [HI Au NP-T-600°C/3h] and on [HI Au NP-T-400°C/4h] there was no indication of the 'wrinkling' observed on the 500°C and 600°C calcined samples.
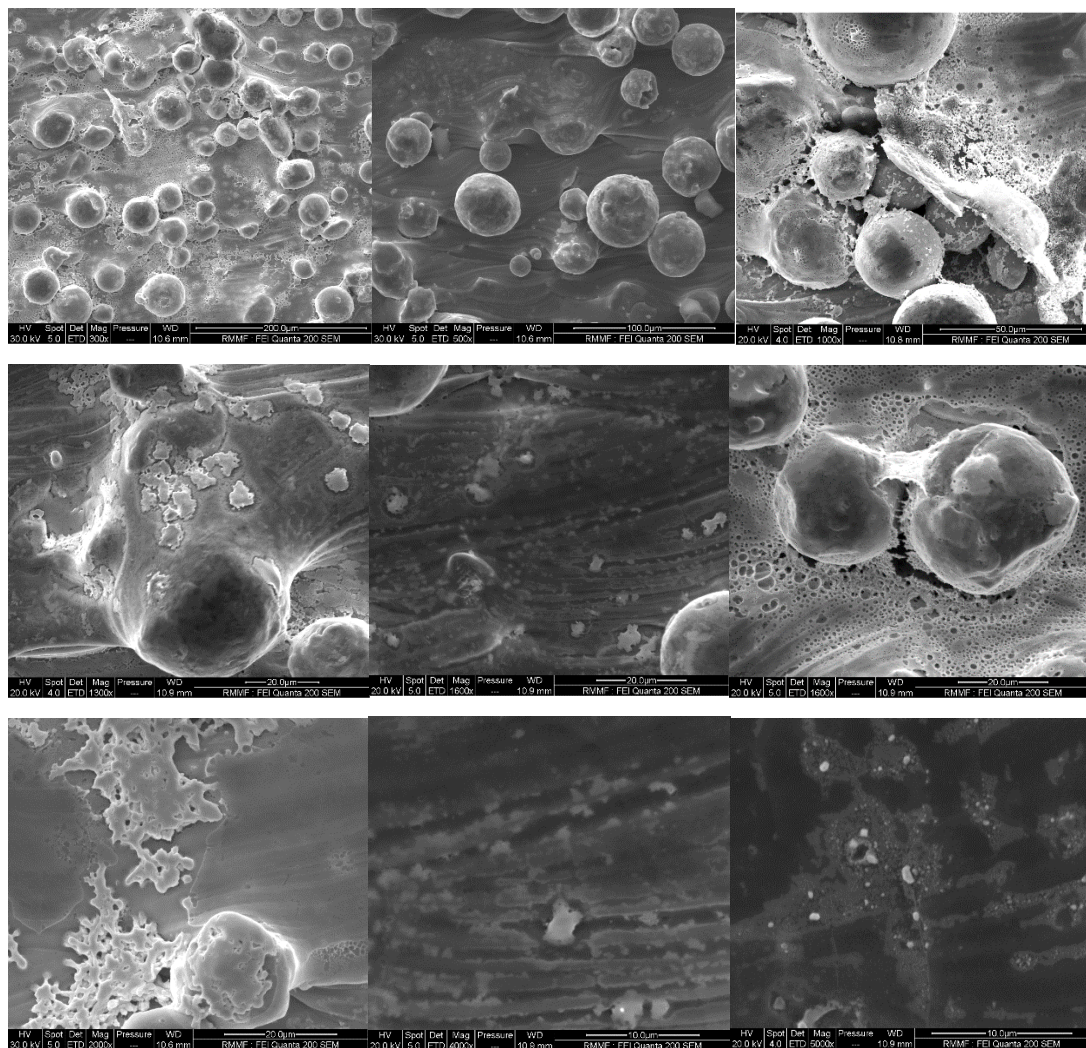
Figure 125 SEM micrographs of [HI Au NP-T-400ºC/4h] before reacting
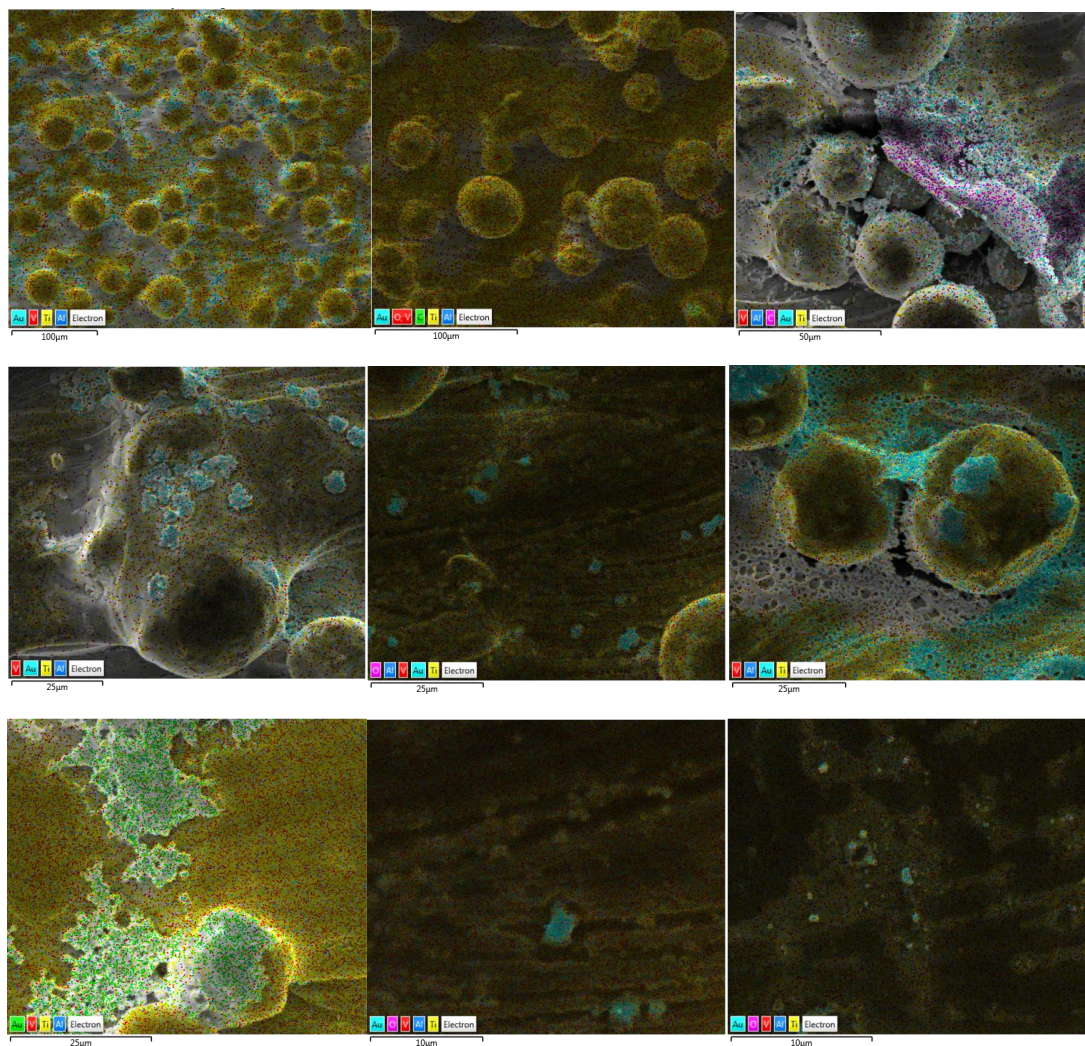
Figure 126 Corresponding EDX micrographs of [HI Au NP-T-400ºC/4h] before reacting

To understand why this catalyst deactivated during 4-NP reduction SEM/EDX analysis was performed on the same substrate again after the reaction. Figure 127 reveals that leaching of the catalyst during the reaction was minimal. It's important to keep any leaching of the catalyst into the reaction solution to a minimum as this is advantageous towards getting better results. The morphology of [HI Au NP-T-400ºC/4h] before and after reacting, changes only slightly. There are two regions described on the [HI Au NP-T-400ºC/4h] substrate before the reaction, the sparse and the dense regions of Au, but only the dense regions of Au are present after the reaction. More specifically the dense regions of Au after the reaction, though originally consisting of continuous percolated thin Au films, now appear to consist of solid hubs of thin Au film scattered amidst larger regions of heavily percolated thin Au films. These appear to be more percolated than prior to the reaction.
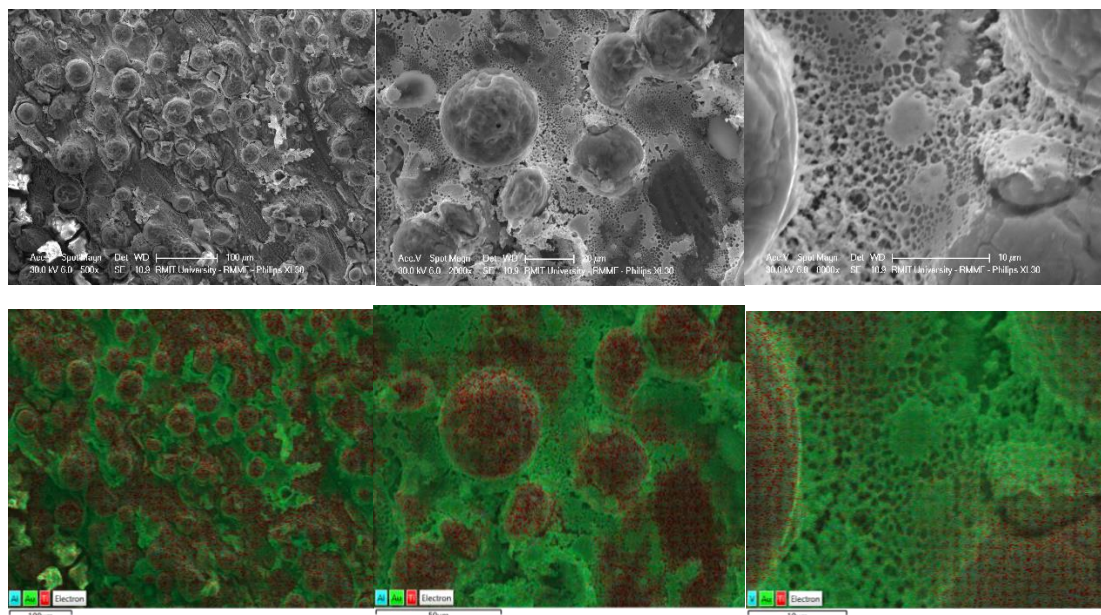
Figure 127 SEM & EDX micrographs of [HI Au NP-T-400°C/4h] after reacting

However, the most useful information is identifying the absence of nanoparticulate Au, which could be missing for a few possible reasons. As with other catalysts leaching may be responsible for catalyst deactivation. It is suggested that the nanoparticulate Au may have been stripped away as the Au active sites are attached to 4-NP or 4-AP by adsorption. The latter is most likely as amino groups are known to have strong interactions with Au [213]. Other potential causes for the loss of Au nanoparticles could include the aggregation of the Au from sparse regions into dense regions or the formation of intermetallic bonds of Au nanoparticles with elements of the TI6Al4V substrate.

Another 2 catalysts of interest synthesized were [DDA-Pd-T-Dried] and [DDA-Pd-T-400°C/3h]. These were quantitatively tested under new reaction conditions, by changing steps 1, 2 and 4 of the reaction setup. Instead of dissolving 3783 mg $NaBH_4$(s) in 100mL H_2O to make a 0.1 M $NaBH_4$(aq) solution, 1514.8 mg $NaBH_4$(s) was dissolved in 100mL H_2O to make a 4.0×10^{-2} M $NaBH_4$(aq) solution. Likewise, instead of dissolving 13.911 mg 4-NP in 100mL H_2O to make 0.001 M 4-NP(aq) solution, 5.564 mg 4-NP was dissolved in 100mL H_2O to make 4.0×10^{-4} M 4-NP(aq) solution. Finally, a temperature of 100°C and a stirrer speed of 500rpm was applied.

After making these adaptations to the method [DDA-Pd-T-Dried] and [DDA-Pd-T-400ºC/3h] were applied to the 4-NP reduction reaction with ongoing UV-Visible spectroscopy assessing the quantitative extent of 4-NP reduction. Figure 128 and Figure 129 show this UV-visible data for for [DDA-Pd-T-Dried] and [DDA-Pd-T-400ºC/3h] respectively.
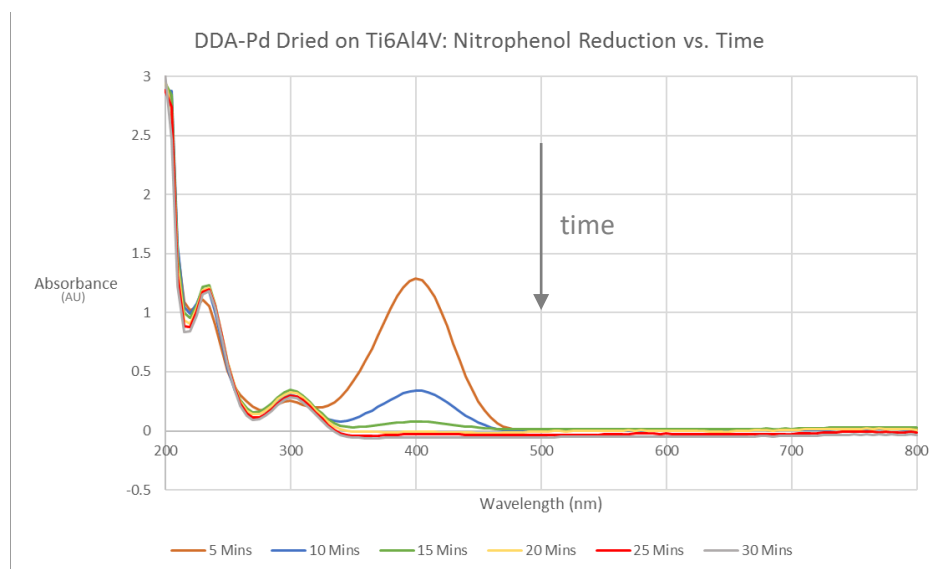
Figure 128 Nitrophenol reduction w.r.t. time for [DDA-Pd-T-Dried].
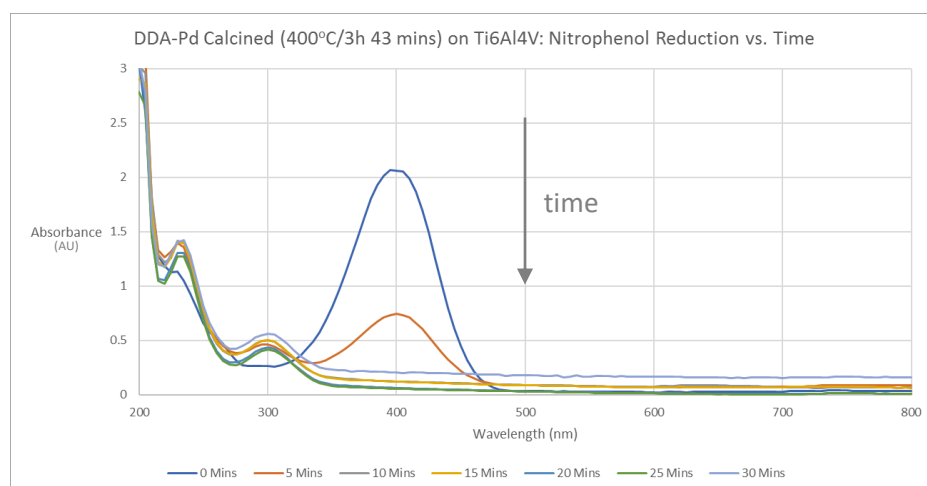
Figure 129 Nitrophenol reduction w.r.t. time for [DDA-Pd-T-400ºC/3h].

Complete reduction of 4-NP occurred for both samples within 20 minutes. Although, as may be noted in Figure 130 the calcined DDA-Pd sample reduced the Nitrophenol within 10 minutes which is notably quicker than its' dried counterpart at 20 minutes.
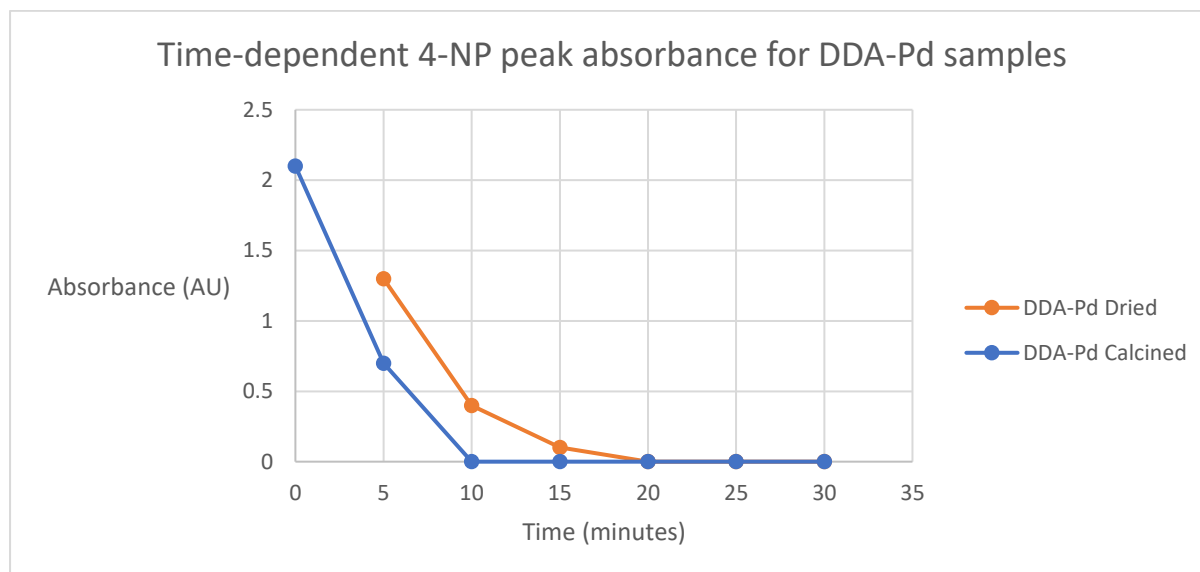
Figure 130 Approximate 4-NP peak absorbance w.r.t. time for calcined and dried DDA-Pd

For both [DDA-Pd-T-Dried] & [DDA-Pd-T-400°C/3h], the catalyst was leached from its Ti6Al4V substrate and was visible as black particles resting on the reaction fluid surface after the reaction. These catalysts were applied to much less concentrated 4-NP than the former successful catalyst systems with higher temperatures and stirring speeds than [HI Au NP-T-Dried] and [HI Au NP-T-400°C/4h]. Either way, to endurance test these 2 catalyst systems, [DDA-Pd-T-Dried] and [DDA-Pd-T-400°C/3h], both were quantitatively tested a 2nd time for 4-NP reduction. For 50 minutes, neither sample demonstrated any reduction in the 400nm peak and therefore showed no activity at all.

To ascertain why the samples were deactivated SEM/EDX characterisation was performed on the samples before and after a reaction, as shown in Figure 131 & Figure 132 for the characterisation before the reaction. However, this data produced an unexpected result. The Pd nanoparticles thought to be deposited all over the TI6Al4V titanium alloys were, in fact, barely present at all. For [DDA-Pd-T-400°C/3h]$_0$, the substrate prior to a reaction, only trace elements of Pd were detected by EDX, but not enough for true mapping to identify any particles much less enough to identify a deposition pattern. Instead, there was extensive coverage of the Ti6Al4V surface by a Na oxide coating present as faceted rods, particle clusters and amorphous continuous islands of Na oxide. It's probable that the Na oxide coating originated from the NaBH$_4$ used as a reducing agent in the Pd NP synthesis process. The solid

aggregate floating on the Pd NP solution during Pd catalyst synthesis was most likely precipitated Na-containing crystals rather than Pd crystals as was suspected at the time.

Even though Pd was present on the substrates in trace quantities, with EDX data from different images giving weight percentages ranging from 0.2 – 1 wt.% Pd, it catalysed the 4-Nitrophenol reduction in the first cycle for both substrates. SEM imaging of these same substrates after the reaction, shows that there was nothing distinguishable on their surfaces at all. The substrates perfectly resembled a Ti6Al4V substrate with no coating, as such the loss of catalyst mass was close to 100%. This confirms that the Na oxide was not chemically anchored to the substrate and that leaching is responsible for the deactivation of this catalyst. It follows that no regeneration process could recover the former activity of this sample and that the Ti6Al4V substrate does not directly contribute as a catalyst to this reaction. SEM/EDX data reveals nothing of interest for [DDA-Pd-T-400ºC/3h]$_1$ and is therefore not included here.
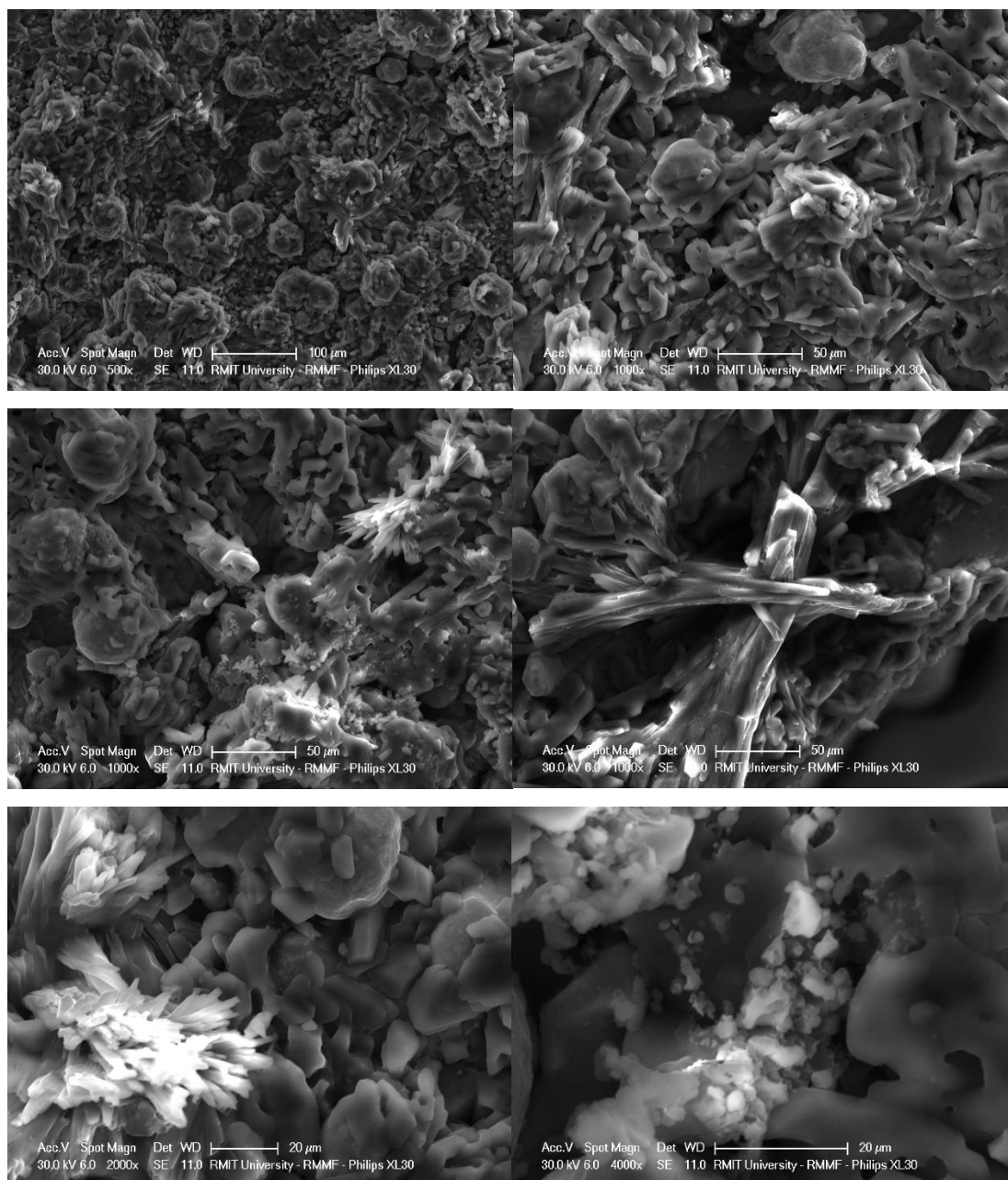
Figure 131 SEM micrographs of [DDA-Pd-T-400ºC/3h].
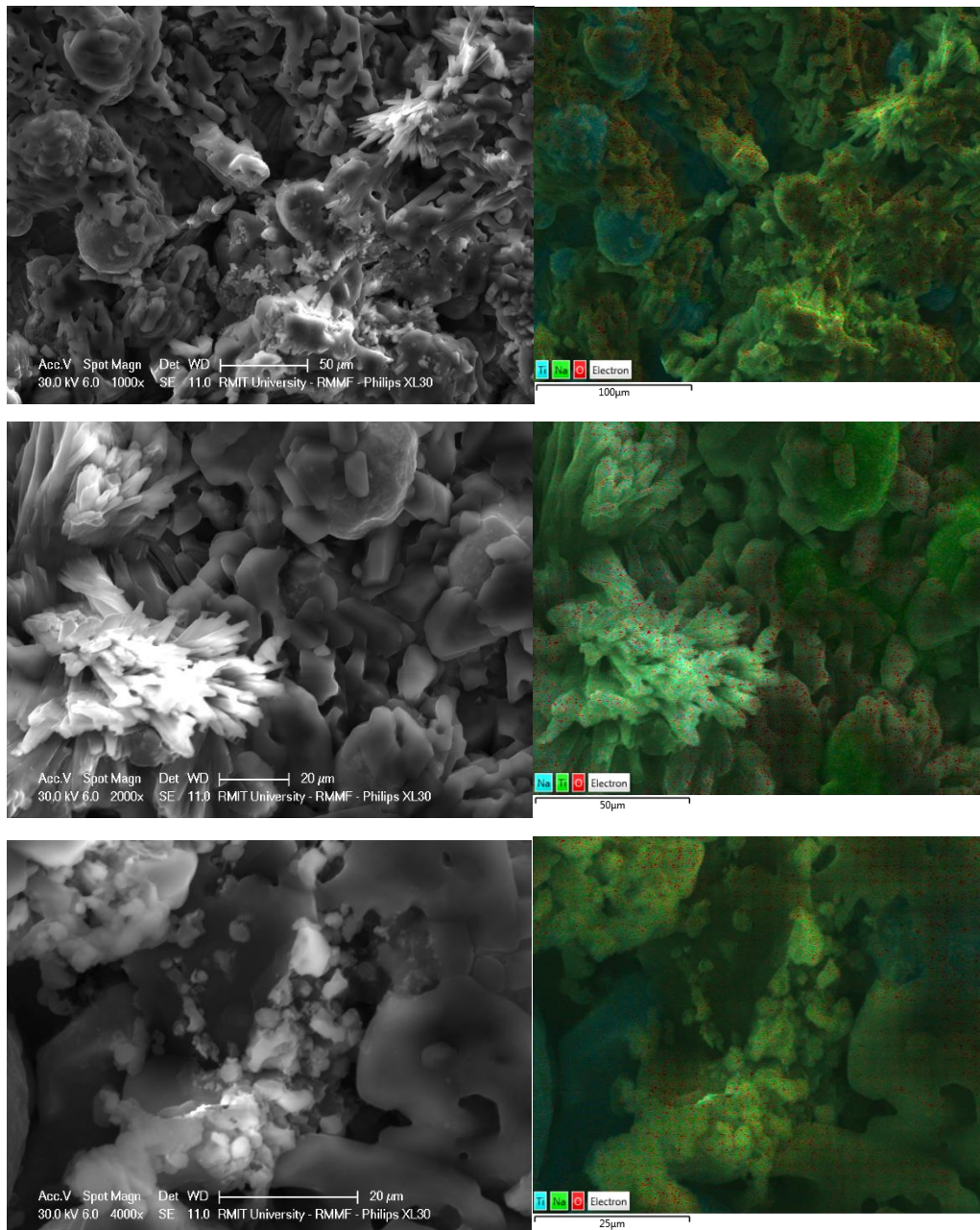
Figure 132 Paired SEM & EDX micrographs of [DDA-Pd-T-400ºC/3h]

5.3 GLYCEROL ACETALISATION

Various solid acid catalysts were trialled for deposition and catalyst testing on Ti6Al4V substrates for glycerol acetalisation, as shown in Table 25.

Table 25 Ti6Al4V samples trialled for catalytic activity in glycerol acetalisation & their assigned Sample ID

Sample ID	Sample Preparation
[FeCl$_3$-T-400°C/3h]	Ti6Al4V Vertically Immersed in FeCl$_3$, 400°C/3h
[FeCl$_3$-T-Dried]	Ti6Al4V Vertically Immersed in FeCl$_3$, Dried
[FeCl$_3$-S-400°C/3h]	17-4 PH Vertically Immersed in FeCl$_3$, 400°C/3h
[FeCl$_3$-S-Dried]	17-4 PH Vertically Immersed in FeCl$_3$, Dried
[T]	*Plain Ti6Al4V*
[T-400°C/3h]	*400°C/3h Ti6Al4V*
[S]	*Plain 17-4 PH*
[S-400°C/3h]	*400°C/3h 17-4 PH*
[FeCl$_3$-T-250°C/4h]	Ti6Al4V Vertically Immersed in FeCl$_3$, 250°C/4h
[FeCl$_3$-T$_R$-400°C/4h]	Ti6Al4V Reactionware Vertically Immersed in FeCl$_3$, 400°C/4h
[FeCl$_3$-T$_R$-250°C/4h]	Ti6Al4V Reactionware Vertically Immersed in FeCl$_3$, 250°C/4h
[FeCl$_3$-T$_R$-Dried]	Ti6Al4V Reactionware Vertically Immersed in FeCl$_3$, Dried

*This catalyst showed noticeable activity

The order of testing, complications the reactions introduced and how the method was optimised afterwards are recorded in Table 26. If not otherwise stated, all reactions used are fresh substrates in their first reaction.

Table 26 Reactions performed and remarks on their setup for glycerol acetalisation, ordered sequentially.

Substrates Tested	Remarks
[FeCl$_3$-T-400ºC/3h], [FeCl$_3$-T-Dried], [FeCl$_3$-S-400ºC/3h], [FeCl$_3$-S-Dried].	GC-MS available, wait for GC-FID for quantitative data.
[T], [S], [T-400ºC/3h], [S-400ºC/3h].	GC-MS available, wait for GC-FID for quantitative data.
[FeCl$_3$-T$_R$-Dried], [FeCl$_3$-T$_R$-400ºC/3h].	GC-MS available, wait for GC-FID for quantitative data.
[FeCl$_3$-T-Dried], [FeCl$_3$-T-250ºC/4h], [FeCl$_3$-T$_R$-Dried], [FeCl$_3$-T$_R$-250ºC/4h].	GC-MS available, wait for GC-FID for quantitative data.
External Standards Calibrated.	GC-MS available, wait for GC-FID for quantitative data.
[FeCl$_3$-T-Dried], [FeCl$_3$-T-250ºC/4h], [FeCl$_3$-T$_R$-Dried], [FeCl$_3$-T$_R$-250ºC/4h].	
[FeCl$_3$-T-Dried]$_2$, [FeCl$_3$-T-250ºC/4h]$_2$, [FeCl$_3$-T$_R$-Dried]$_2$, [FeCl$_3$-T$_R$-250ºC/4h]$_2$.	Acetone evaporating during reaction. Use a condenser for planar substrates. Halt use of reactionware until a catalyst yields a good result.
Problem Identified.	Glucose contaminated. New source of glucose procured.
External Standards Recalibrated.	
[FeCl$_3$-T-Dried], [FeCl$_3$-T-250ºC/4h].	
[FeCl$_3$-T-Dried]$_2$, [FeCl$_3$-T$_R$-Dried].	

*Not a reaction, an action clarified under 'Substrates Tested'

The initial work identified the viability of FeCl$_3$ catalyst on Ti6Al4V & 17-4 PH alloys for the glycerol acetalisation reaction. Observation of the GC-MS spectra from 4 reactions, as shown in Figure 147, Figure 148, Figure 149 and Figure 150 of Appendix B, indicated that sample ID's [FeCl$_3$-S-Dried], [FeCl$_3$-S-400ºC/3h], [FeCl$_3$-T-Dried] & [FeCl$_3$-T-400ºC/3h] were all acetalizing glycerol to solketal but not with 100% conversion in any case, as some glycerol was still present for each substrate afterwards.

This gave enough information to clarify that FeCl$_3$ deposited on 17-4PH & Ti6Al4V substrates have potential to catalyse glycerol acetalisation. To determine if the underlying substrate materials were in any way directly responsible for glycerol acetalisation, both plain &

400°C/3h samples of Ti6Al4V & 17-4 PH were trialled for glycerol acetalisation and found to have no observable conversion of glycerol to solketal. Therefore, the primary active component is $FeCl_3$ although it cannot be ruled out that Ti6Al4V or 17-4 PH do not function as supports for the $FeCl_3$ catalyst.

To elucidate which aspects of the coated morphology are responsible for the conversion of glycerol subsequent characterisation of the $FeCl_3$ coatings on the SLM substrates was performed. [$FeCl_3$-S-Dried], [$FeCl_3$-S-400°C/3h], [$FeCl_3$-T-Dried] and [$FeCl_3$-T-400°C/3h] were thus imaged by SEM & EDX. A few deposition patterns were observed for $FeCl_3$ dried on Ti6Al4V, as shown in Figure 133, Figure 134, and Figure 135. There were regions of thin films of $FeCl_3$ visible on the surface, as shown in Figure 135. These films were cracked and only covered a small fraction of the surface. It's suggested that during deposition of $FeCl_3$, rapid evaporation of the acetonitrile solvent led to rapid contraction of the fresh $FeCl_3$ coating and, therefore, is responsible for the cracks in the coating. Furthermore, there are a few micron-sized particles, the contrast for which suggests a composition of Fe, FeO or $FeCl_3$.
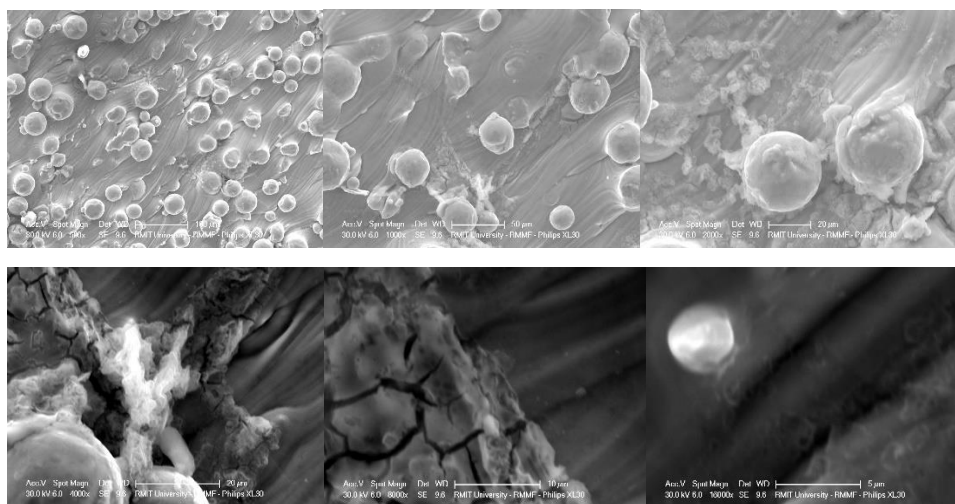
Figure 133 SEM images of Ti6Al4V vertically immersed in $FeCl_3$ solution: (Top Left) – 500x, (Top Middle) – 1000x, (Top Right) – 2000x, (Bottom Left) – 4000x, (Bottom Middle) – 8000x, (Bottom Right)– 16000x.

After calcination of $FeCl_3$ on Ti6Al4V, as shown in Figure 136 and Figure 137, there were some changes in the $FeCl_3$ coating morphology. The Cl concentrations were much lower after calcination than prior to it, although there were some regions of $FeCl_3$ thin films which were protected by the SLM particles, there remains little Cl regardless. There is less thin film of

$FeCl_3$ present than before and further cracking during calcination occurred to the extent of discontinuity. Compositionally the thin films now have negligible Cl concentrations. These thin films have also precipitated higher contrast particles which were speculatively identified as iron oxide particles because of the locally increased O concentrations. Both the loss of Cl concentration and the precipitation of iron oxide particles were suggested as being responsible for the extended cracking of the $FeCl_3$ thin films. In addition, nanoparticulate Fe seemed to be present, as the dispersion of high contrast nanoscale particles at higher magnifications infers.
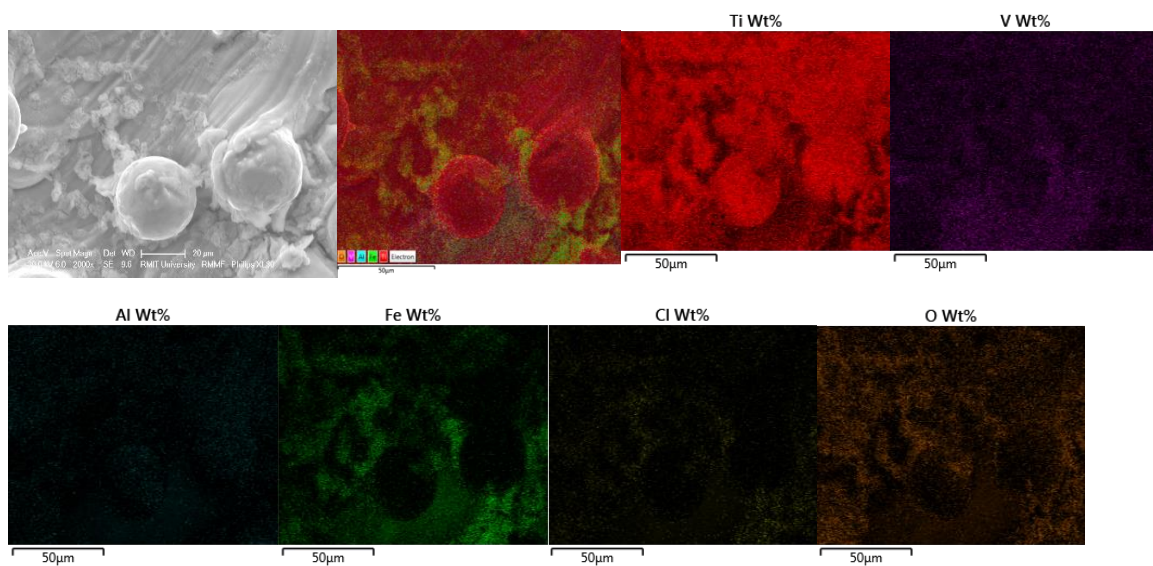
Figure 134 EDX of Ti6Al4V vertically immersed in FeCl$_3$ solution: (Top Left) – 2000x SEM site, all other tiles as-labelled spectra.
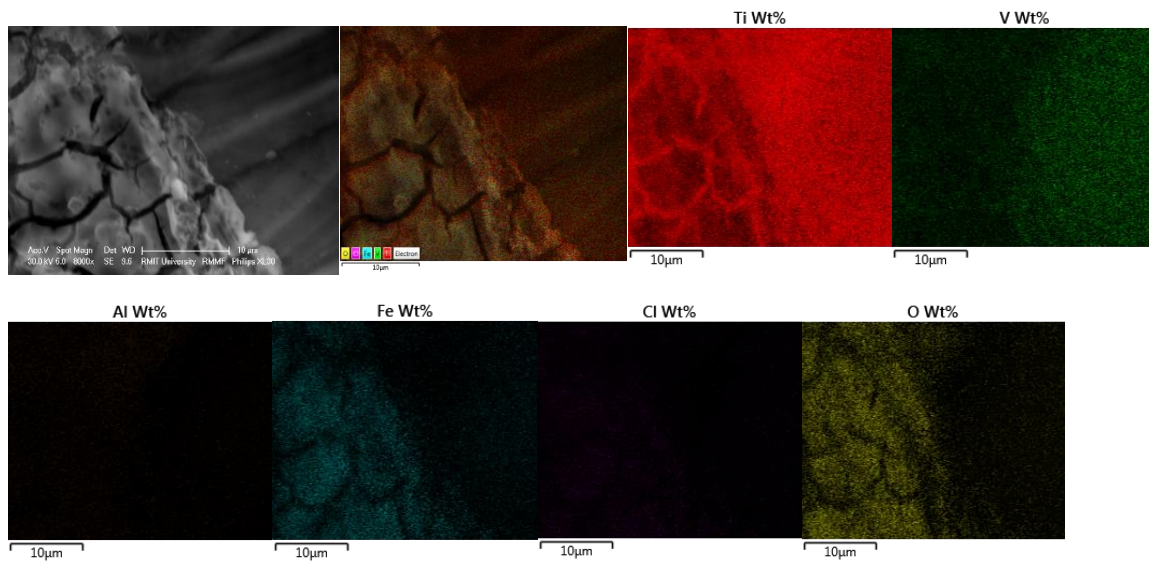
Figure 135 EDX of Ti6Al4V vertically immersed in FeCl₃ solution: (Top Left) – 8000x SEM site, all other tiles as-labelled spectra.

Overall, the observations about effects of calcination are suggestive of FeCl$_3$ decomposition to iron oxide and, therefore, calcination at 400°C/3h renders less catalytic activity.
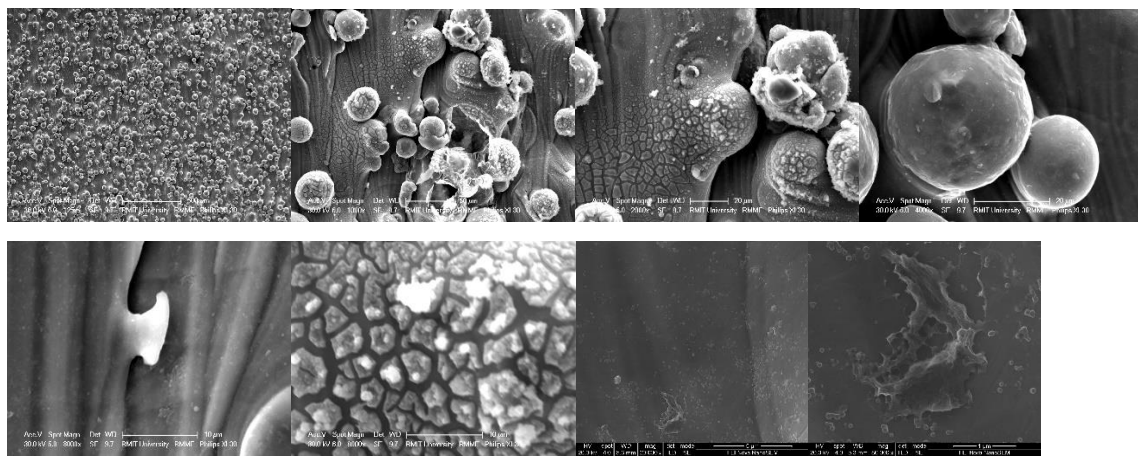
Figure 136 SEM images of Ti6Al4V vertically immersed in FeCl₃ solution & calcined at 400°C/3h of Magnification: 125, 1000, 2000, 4000, 8000, 8000, 20000 and 50000 from top left to bottom right.
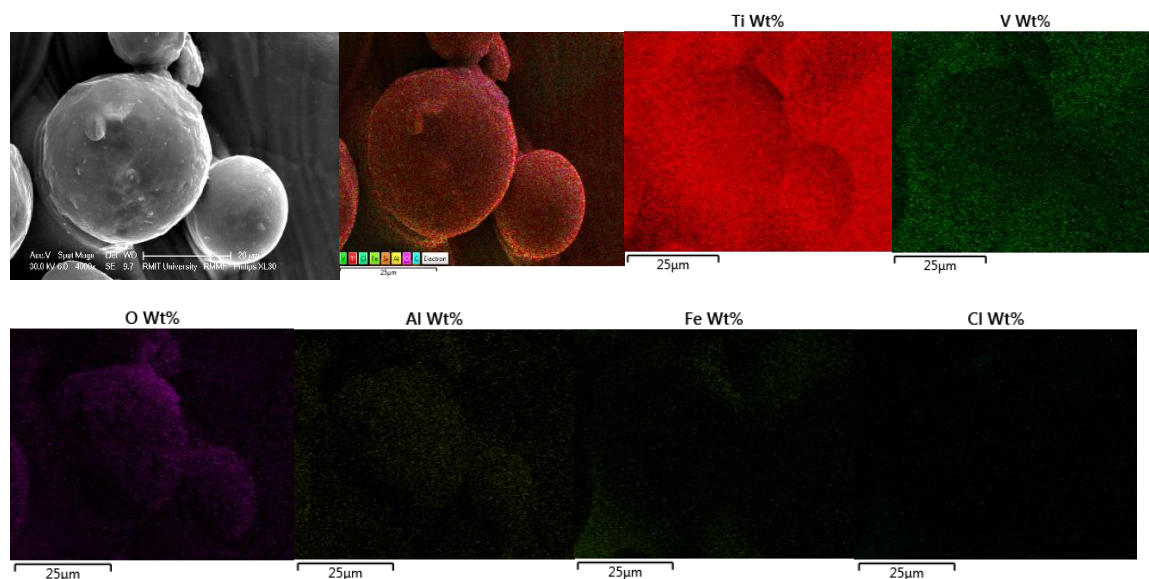
Figure 137 EDX of Ti6Al4V vertically immersed in FeCl3 solution & calcined at 400°C/3h: (Top Left) – 4000x SEM site, all other tiles as-labelled spectra.

The morphology of $FeCl_3$ on 17-4 PH before calcination is like $FeCl_3$ on Ti6Al4V before calcination, see Figure 138 & Figure 139. The $FeCl_3$ was distributed as a thin film with hints of thicker layers of $FeCl_3$ detaching from the 17-4 PH substrate. As shown in the Cl map in Figure 139, there is also cracking at the edge of the thin film coverage, potentially due to the aforementioned loss of $FeCl_3$. As for Ti6Al4V, the deposited $FeCl_3$ thin films have cracked, again, probably due to rapid shrinkage as the acetonitrile solvent evaporates. However, in this case, the cracking was so severe it appears the $FeCl_3$ crumbled off the surface, as in Figure 139.

In Figure 139 an aluminosilicate particle is visible. The substrate, 17-4 PH is known to have trace concentrations of these lighter elements, so it's likely that calcination induced the precipitation of this particle at the surface from the bulk of the steel.
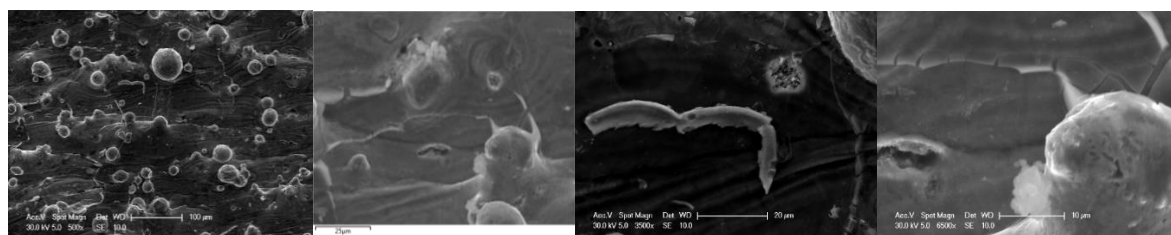
Figure 138 SEM images of 17-4 PH vertically immersed in FeCl3 solution: (Top Left) – 500x, (Top Middle) – 2500x, (Top Right) – 3500x, (Bottom) – 6500x
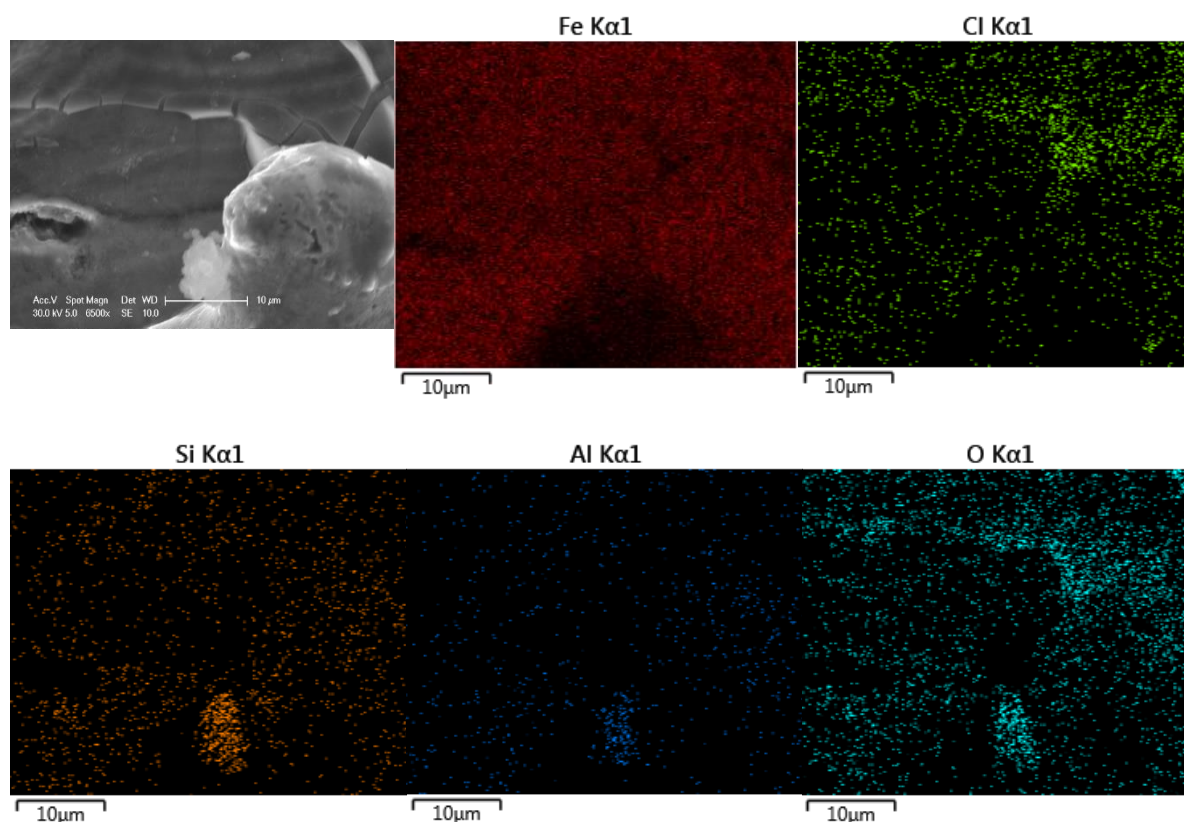
Figure 139 EDX Maps of 17-4 PH vertically immersed in FeCl₃ solution: (Top Left) – 6500x SEM site, all other tiles as-labelled spectra.

After Calcination, as shown in Figure 140, Figure 141 and Figure 142, there was no thin film of FeCl₃ visible, instead sparse micron-scaled particles of no consistent shape were distributed all over the surface. In addition, the EDX Maps, as shown in Figure 141 & Figure 142, do not reveal any Cl to be present. Therefore, it's highly likely that some of these are Fe particles. However, as the base constituent of 17-4 PH Steel is Fe it isn't easy to distinguish Fe originating in the coat and the substrate, either by SEM contrast or by EDX elemental analysis. In the case of Figure 142, the particle is not Fe or Cr-based as these two metals are deficient at this location. Instead a concentration of Cu, Mg, Al, Si and O suggest the presence of a complex non-ferrous oxide. Again, the presence of aluminium is unexpected on the calcined sample given that it's not an intended coating, although this is consistent with the dried sample. The magnesium is also unexpected on the calcined substrate but was not visible on the dried substrate at all.

It's concluded that because of the absence of Cl and the change in morphology from a thin film to a particulate distribution that $FeCl_3$ has decomposed to FeO as suggested for the Ti6Al4V substrate. To aid in reaching this conclusion, the substrate coating is a rusty brown-red colour – the colour of FeO.
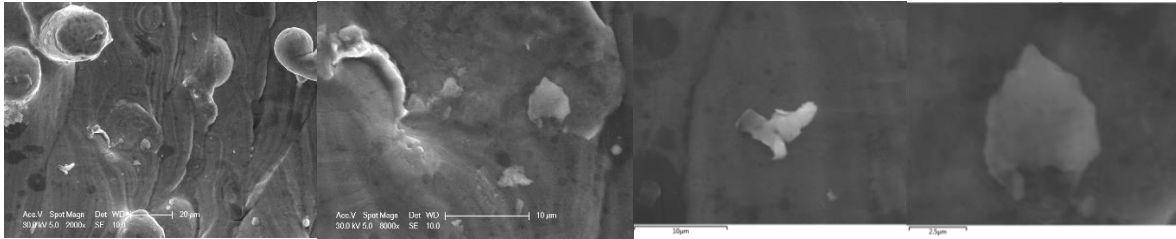
Figure 140 SEM images of 17-4 PH vertically immersed in FeCl₃ solution & calcined at 400°C/3h: (Far Left) – 2000x, (Left) – 8000x, (Right) – 10000x, (Far Right) – 25000x.
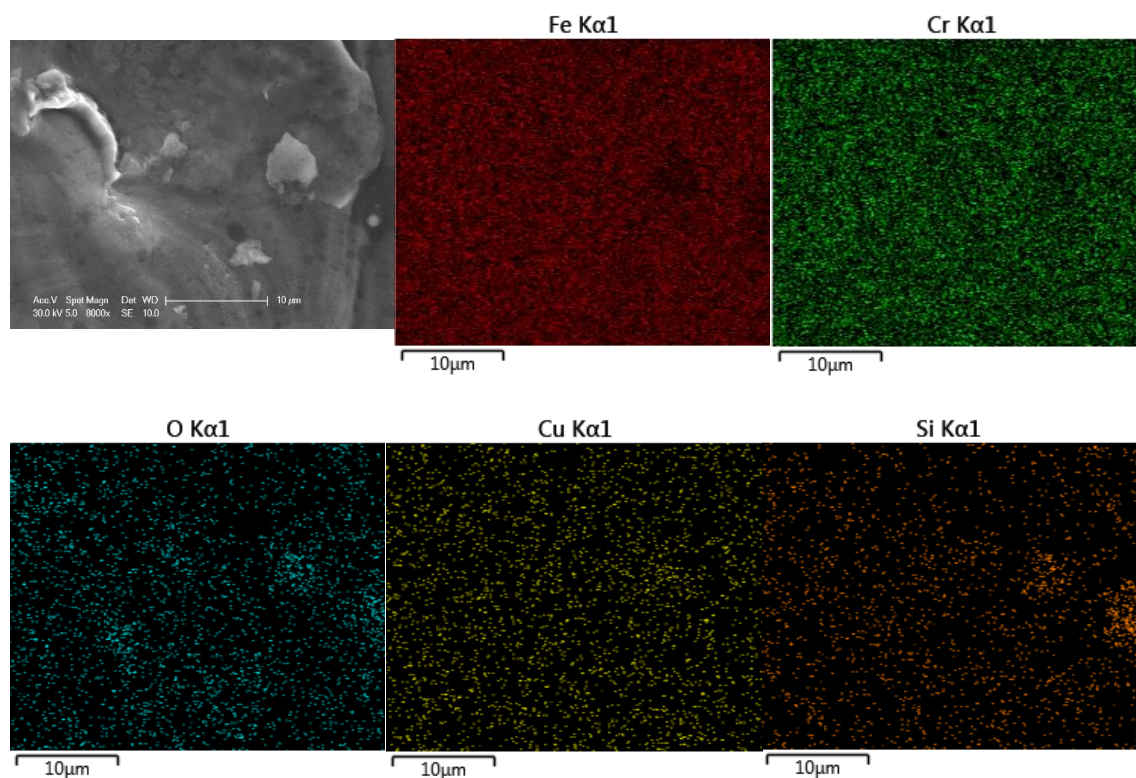
Figure 141 EDX maps of 17-4 PH vertically immersed in FeCl₃ solution & calcined at 400ºC/3h: (Top Left) – 8000x SEM site, all other tiles as-labelled spectra.
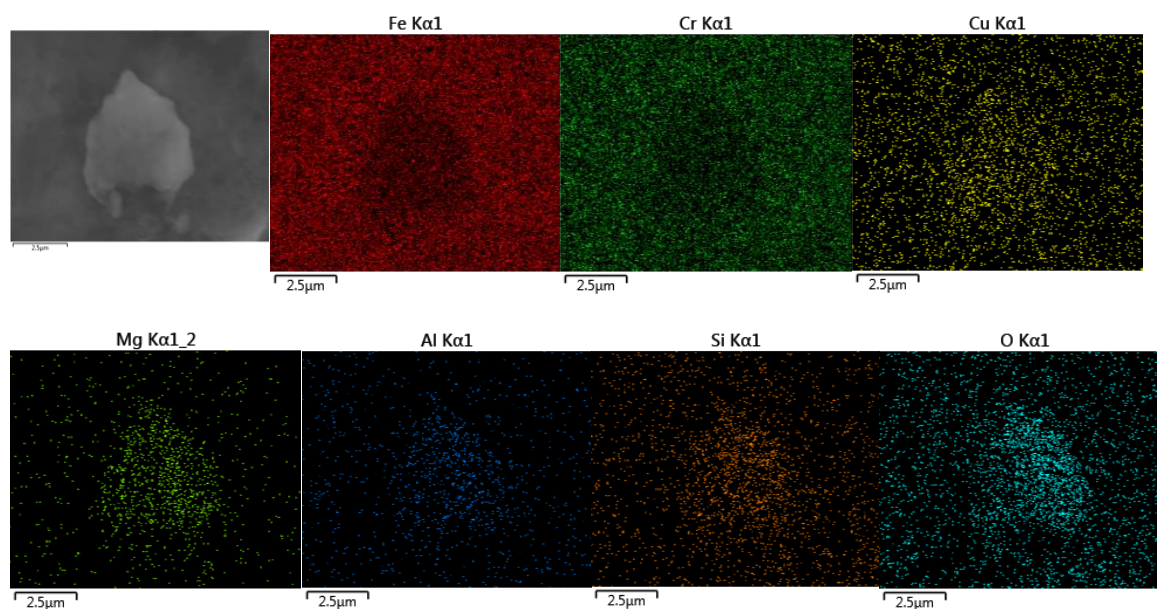
Figure 142 EDX Maps of 17-4 PH vertically immersed in FeCl3 solution & calcined at 400ºC/3h: (Top Left) – 8000x SEM site, all other tiles as-labelled spectra.

Given that planar substrates qualitatively worked for glycerol acetalisation, it was decided to apply the FeCl₃ coatings to reactionware vessels. Glycerol acetalisation was then performed

in these vessels. The reaction fluid after 2 hours of reacting was discoloured by the catalyst materials as evidenced when extracted in methanol by sonication. For the $FeCl_3$ dried reactionware [$FeCl_3$-T_R-Dried], the reactionware vessel divulged a yellow coloured liquid during sonication – some of the coated catalyst was detached. Whereas for the $FeCl_3$ calcined reactionware [$FeCl_3$-T_R-400ºC/3h] the reactionware vessel divulged a red coloured liquid during sonication. Aside from indicating leaching of the catalyst, the colour of the catalyst in solution indicates its' composition. The yellow colour corresponds to the $FeCl_3$-loaded deposition solution and the red colour is suggestive of haematite. It's therefore suggested that the catalyst has decomposed to FeO from $FeCl_3$ due to calcination.

The GC-MS data in Appendix D as shown in **Error! Reference source not found.** and Error! Reference source not found. indicates that some acetal and solketal are produced by both dried and 400ºC/3h calcined $FeCl_3$ on TI6Al4V reactionware, as with the planar substrates, and likewise, there remains some unreacted glycerol after the 2h reaction period.

It was realised that $FeCl_3$ starts decomposing at 280ºC, melts at 306ºC and boils at 315ºC, given that $FeCl_3$ seems to be decomposing there's a need to process the $FeCl_3$ at lower temperatures. So, new substrates were prepared to account for this. 2 Ti6Al4V plates and 2 Ti6Al4V reactionware vessels were coated in $FeCl_3$ and 1 of each were calcined at 250ºC/4h instead of 400ºC/3h. All 4 substrates were applied to glycerol acetalisation and produced the GC-MS chromatograms and highlighted mass spectra in **Error! Reference source not found.** and **Error! Reference source not found.** which also indicate that solketal and acetal are produced by these catalysts**.**

Later GC-FID analyses were carried out to do the quantitative analysis. External standards were prepared for quantitative analysis by GC-FID using the method described in the **Error! Reference source not found.**.

4 new Ti6Al4V substrates were coated in $FeCl_3$ as before and were then applied to glycerol acetalisation. This required the method adapted for use with GC-FID instead of GC-MS. The

first results achieved this way are detailed in Table 27. However, the loss of liquids during handling made one reaction unmeasurable, that of [FeCl$_3$-T$_R$-Dried]$_1$.

Table 27 Conversion calculations for sample ID: [FeCl$_3$-T-Dried]$_1$, [FeCl$_3$-T-250ºC/4h]$_1$, [FeCl$_3$-T$_R$-Dried]$_1$ & [FeCl$_3$-T$_R$-250ºC/4h]$_1$

Sample ID	GC Peak Areas				Molarity		
	Solketal	Acetal	S + A	Glycerol	Solketal	S + A	Glycerol
[FeCl$_3$-T-Dried]$_1$	7126	0	7126	13820	0.000657024	0.000657024	0.00395639
[FeCl$_3$-T-250ºC/4h]$_1$	0	0	0	25989.7	0	0	0.074403313
[FeCl$_3$-T$_R$-250ºC/4h]$_1$	0	0	0	10417.8	0	0	0.029824078

Sample ID	Moles			Balanced moles		Glycerol conversion	Glycerol remaining
	Solketal	S + A	Glycerol	Solketal	Glycerol		
[FeCl$_3$-T-Dried]$_1$	6.57024E-06	6.57024E-06	3.95639E-05	0.000142416	0.000857584	**14.24%**	**85.76%**
[FeCl$_3$-T-250ºC/4h]$_1$	0	0	0.000744033	0	0.001	**0.00%**	**100.00%**
[FeCl$_3$-T$_R$-250ºC/4h]$_1$	0	0	0.000298241	0	0.001	**0.00%**	**100.00%**

The initial quantitative data, as shown in Table 27, is at odds with the formerly performed GC-MS data. The data suggests that the calcination of 250ºC is killing the catalysts ability to convert glycerol as the only active sample was the [FeCl$_3$-T-Dried]$_1$. This sample gave only 14.24% conversion of the glycerol. It's not clear why this is the case and further investigation of this behaviour was not viable in the scope of this project, although possibly this is due to sintering or decomposition of the catalyst. However, Table 28 also provides some key information that aids in understanding this data.

Table 28 Material losses due to reaction/sampling for sample ID: [FeCl$_3$-T-Dried]$_1$, [FeCl$_3$-T-250ºC/4h]$_1$, [FeCl$_3$-T$_R$-Dried]$_1$ & [FeCl$_3$-T$_R$-250ºC/4h]$_1$

Sample ID	Moles Total	Moles Lost	Percent Moles Retained	Percent Moles Lost
[FeCl$_3$-T-Dried]$_1$	0.00004613	0.00095387	4.61%	95.39%
[FeCl$_3$-T-250ºC/4h]$_1$	0.00074403	0.00025597	74.40%	25.60%
[FeCl$_3$-T$_R$-Dried]$_1$	0.00000000	0.00100000	0.00%	100.00%
[FeCl$_3$-T$_R$-250ºC/4h]$_1$	0.00029824	0.00070176	29.82%	70.18%

The percentage of moles lost during reactions for the planar substrates and the reactionware is too high for the data to remain representative. The only exception to this was the [FeCl$_3$-T-250ºC/4h]$_1$ sample which retained almost 75% of the total reaction mass. 3 potential sources of liquid losses are suggested:

- Evaporation,

- Adsorption &

- Viscous interactions with SLM particles

Any evaporation losses are more likely to occur from the solketal which boils at 188°C than the glycerol which boils at 290°C, although neither liquid should be evaporating at room temperature and pressure. Although evaporation of acetone with a boiling point of 56°C, is much more probable, this doesn't relate to the losses of solketal and/or glycerol for which the mole total is calculated. Regardless, glycerol is far more viscous than the other liquids and it's possible that this viscosity has led to glycerol being trapped between the micron size SLM particles on the surface of the SLM printed parts. In addition, it's possible that adsorption of glycerol or solketal on the surface of the SLM substrate led to losses of these liquids during the removal of the SLM part from the reaction mixture. Any of these issues could have caused liquid losses.

A few concerns about the validity of using the reactionware became apparent during redesign of the experimental method. There were 4 major issues, as follows:

A. Rapid evaporation of acetone and open-topped reactionware causing material losses.

B. No internal mixing is possible by stirring during the reaction as there isn't enough room.

C. Glycerol is viscous and gets trapped easily in the lattice causing poor mass balance.

D. Internally obscured geometry causes difficulty in seeing liquid trapped inside.

Given that condensers wouldn't collect the evaporated materials back into a reactionware vessel, the first issue (A) can't be easily addressed, however the second issue (B) can be resolved by moving the reactionware using external means, the third issue (C) can be overcome by extended sonication of the reactionware in a methanol solution. This serves to extract more of the glycerol and other reagents into the methanol solution. The fourth issue (D) is less critical, it necessitates extended sonication as the lack of visual indicators makes it difficult to clarify when enough sonication has been performed. Regardless further reactions used only planar substrates to accelerate the experimentation.

To enable better retention of the liquids and therefore the mass balance, the reaction

[FeCl$_3$-T-Dried]$_1$ and [FeCl$_3$-T-250°C/4h]$_1$ was repeated with a condenser. GC-FID data was collected from these 2 reactions with much improved liquid retention, as shown in

Table 29. The percentage of material lost was reduced to a range of ~1-6% compared to the previous range of ~25-95%, as shown in Table 28. Therefore, it's now reasonable to claim that the GC-FID data outcomes, as shown in Table 30, are representative of the reaction.

Table 29 Material losses due to reaction & sampling for sample ID: [FeCl$_3$-T-Dried]$_1$, [FeCl$_3$-T-250°C/4h]$_1$.

Sample ID	Moles Total	Moles Lost	Percent Moles Retained	Percent Moles Lost
New [FeCl$_3$-T-Dried]$_1$	0.00095549	0.00006304	93.81%	6.19%
New [FeCl$_3$-T-250°C/4h]$_1$	0.00100457	0.00001287	98.74%	1.26%

A very small conversion of 0.45% was observed for the 250°C/4h calcined plate, as shown in Table 30. Due to the temperature fluctuations of the furnace during calcination, the temperature extended 20°C above the programmed temperature, the 250°C becoming 270°C, its' suggested this led to decomposition and deactivation of the FeCl$_3$ catalyst. Conversely the dried plate converted 53.55% of the glycerol to solketal which is the best result to date and merited further iterative testing of this catalyst.

Table 30 Conversion calculations for new copies of both sample ID's: [FeCl3-T-Dried]$_1$ & [FeCl3-T-250°C/4h]$_1$

Sample ID	GC Peak Areas				Molarity		
	Solketal	Acetal	S + A	Glycerol	Solketal	S + A	Glycerol
[FeCl$_3$-T-Dried]$_1$	600545.6	8275.9	608821.5	187169.4	0.05079114	0.05149108	0.04405781
[FeCl$_3$-T-250°C/4h]$_1$	5388.6	1929.1	7317.7	424139.2	0.00045574	0.00061889	0.09983813

Sample ID	Moles			Balanced Moles		Glycerol conversion (2 s.f.)	Glycerol remaining (2 s.f.)
	Solketal	S + A	Glycerol	Solketal	Glycerol		

[FeCl$_3$-T-Dried]$_1$	0.00050791	0.00051491	0.00044058	0.00054142	0.00046964	**53.55%**	**46.45%**
[FeCl$_3$-T-250°C/4h]$_1$	0.00000456	0.00000619	0.00099838	0.00000462	0.00101117	**0.45%**	**99.55%**

Having found a good setup for the reaction and a decent catalyst activity, a 2nd iteration of glycerol acetalisation for the dried FeCl$_3$ Ti6Al4V plate & a similarly coated fresh reactionware vessel was performed, see Table 31 & Table 32. The mole balance data for the plate sits close to 5% error which is acceptable, see Table 31, notably the reactionware mole balance was far better in this case compared to the earliest work with reactionware, see Table 27 and Table 28, due most likely to extensive sonication.

Table 31 Material losses due to reaction & sampling for [FeCl$_3$-T-Dried]$_2$ & [FeCl$_3$-T$_R$-Dried]$_1$

Sample ID	Moles Total	Moles Lost	Percent Moles Retained	Percent Moles Lost
[FeCl$_3$-T-Dried]$_2$	0.00107629	- 0.00005342	105.22%	-5.22%
[FeCl$_3$-T$_R$-Dried]$_1$	0.00068097	0.00033865	66.79%	33.21%

Table 32 Conversion calculations for [FeCl$_3$-T-Dried]$_2$ & [FeCl$_3$-T$_R$-Dried]$_1$

Sample ID	GC Peak Areas				Molarity		
	Solketal	Acetal	S + A	Glycerol	Solketal	S + A	Glycerol
[FeCl$_3$-T-Dried]$_2$	0	0	0	457236.6	0.00000000	0.00000000	0.10762892
[FeCl$_3$-T$_R$-Dried]$_1$	0	0	0	289293	0.00000000	0.00000000	0.06809668

Sample ID	Moles (Based on 10mL)			Balanced Moles		Glycerol conversion	Glycerol remaining
	Solketal	S + A	Glycerol	Solketal	Glycerol		
[FeCl$_3$-T-Dried]$_2$	0.00000000	0.00000000	0.00107629	0.00000000	0.00102287	**0.00%**	**100.00%**
[FeCl$_3$-T$_R$-Dried]$_1$	0.00000000	0.00000000	0.00068097	0.00000000	0.00101961	**0.00%**	**100.00%**

These 2 reactions revealed no conversion of the glycerol for either reaction, see Table 32. It's concluded that the 1st reaction for [FeCl$_3$-T-Dried] completely detached the catalyst from its' underlying Ti6Al4V substrate and, given that FeCl$_3$ is the active component of the FeCl$_3$/Ti6Al4V system, that there was no catalyst remaining to enable any conversion. To make the FeCl$_3$ on Ti6Al4V system viable it's necessary to anchor the catalyst to the Ti6Al4V without decomposing the FeCl$_3$, this means temperatures lower than 250°C are needed. It's possible that 200°C could be a better calcination temperature, or the use of an adlayer coating could enable better adherence. Nonetheless, further exploration of this catalyst is outside the scope of this work.

5.4 SUMMARY AND CONCLUSIONS

There were four highly active catalyst systems deposited on SLM substrates for 4-NP reduction, which have been demonstrated: [HI Au NP-T-Dried], [HI Au NP-T-400ºC/4h], [DDA-Pd-T-Dried] and [DDA-Pd-T-400ºC/3h].

All four substrates effectively reduced 4-NP to 4-AP, [HI Au NP-T-Dried] and [HI Au NP-T-400ºC/4h] both succeeded within a day and [DDA-Pd-T-Dried] and [DDA-Pd-T-400ºC/3h] succeeded within 20 and 15 minutes respectively.

Whilst initial adherence was good for [HI Au NP-T-Dried], [HI Au NP-T-400ºC/4h], [DDA-Pd-T-Dried] and [DDA-Pd-T-400ºC/3h], the leaching resistance during the 4-NP reduction was poor for small particles on [HI Au NP-T-Dried] and [HI Au NP-T-400ºC/4h] and all coating materials on [DDA-Pd-T-Dried] and [DDA-Pd-T-400ºC/3h]. Alternately the Au nanoparticles of [HI Au NP-T-Dried] and [HI Au NP-T-400ºC/4h] may have been lost due to their aggregation or the formation of intermetallic bonds of Au nanoparticles with the Ti6Al4V substrate. Any of these reasons could be responsible for catalyst deactivation. Furthermore, if leaching is responsible, it's suggested this was caused by adsorption of 4-NP and particularly 4-AP on the Au nanoparticles, thereby stripping them off the Ti6Al4V substrate.

For glycerol acetalisation the most active catalyst was the $FeCl_3$ catalyst, [$FeCl_3$-T-Dried] which demonstrated valuable properties towards catalysis. This catalyst gave a good initial adherence and glycerol conversion of 53.55% but leached during glycerol acetalisation.
Overall, it has been found that where a catalyst is active it will be easily leached into the solution. It's suggested that this correlation of highly active catalysts with catalysts vulnerable to leaching comes down to the common factor of strong interactions with the reagents, such as by adsorption of the reagents by the catalyst surface. Furthermore, it's suggested that these reagent-catalyst interactions must be greater in strength than the adhesion forces present between the catalyst and the SLM substrate to strip the catalyst off the SLM surface. Conceptually, increasing the bonding strength between the catalyst and the SLM substrate is the strategy suggested to counter this issue.

An ideal catalyst would have achieved these three properties together, excellent conversion of reactants, persistent adhesion of the catalyst during reactions and excellent retention of

the active catalyst morphologies during reactions. For further research, it is recommended to pursue the improved adhesion of known effective catalysts or to further improve the extent of conversion for already strongly adhered catalysts.

CHAPTER SIX – CONCLUSIONS & FUTURE RESEARCH

This section will address the extent to which the research aims & objectives were met, the accuracy of the research hypothesis and the data found to answer the research questions.

6.1 MEETING THE RESEARCH AIMS AND OBJECTIVES

The major research aim of this project was *"To develop, produce and test miniature, functionalised reactor components made by SLM, both in liquid and gaseous phase catalytic reactions"*. This objective has been addressed in various ways.

Several different geometries were printed by SLM & used for testing. Plates and a reactionware teapot were used for batch reaction testing, whilst cylinders with parallel, square channels & an open VFBCC lattice structure were used for continuous flow reaction testing.

3 reactions were performed over the course of this project: the gaseous phase DRM reaction and the liquid phase 4-NP reduction, & glycerol acetalisation reactions. Catalysts were functionalised on SLM substrates for all reactions.

The major research aim was met, all systems considered were explored & assessed to some extent. The 1st Primary Engineering Objective was to *"Design/Print geometries for batch reactions without removable internal support structures"*. This was initially achieved by a simple rectangular or square plate for preliminary batch reaction tests then later achieved by the design of a reactionware teapot filled with a lattice that could also contain the reactants. This latter design didn't require removable internal support structures. Whilst the reactionware teapot was applied to glycerol acetalisation and could be made to contain the necessary glycerol and acetone, there were design issues which require further solutions. These design elements, problems & suggested solutions are as follows:

Design Element: The reactionware is open at the top.

Design Problem: Evaporation of reactants & products, primarily acetone.

Suggested Solution: Design a plug to seal the gap. Use in conjunction with Kapton tape.

Design Element: Closed geometry & lattice structure.

Design Problem: The interior is difficult to see, especially due to the lattice structure. This makes it difficult to ascertain the liquid entrainment.

Suggested Solution: Perform mass balances with GC-FID & measure mass before & after reactions.

Design Element: Miniature geometry

Design Problem: No mixing is possible by stirring during the reaction.

Suggested Solution: Stir the reaction mix by rotating the whole vessel.

Design Element: Lattice structure with small spacing.

Design Problem: Glycerol is very viscous and will not move easily out of the lattice once entrained due to the high surface tensions involved. Furthermore, this complicates the mass balance.

Suggested Solution: Extend sonication time & increase the methanol volume used for sonication.

Whilst there are issues associated with the use of this vessel for glycerol acetalisation, of the 4 issues, 3 can be solved by improved method and only 1 needs to be solved by variation or improvement of the design itself. This research aim is therefore partially completed with the recognition that after a simple modification to the design, the reactionware is completely feasible for use in glycerol acetalisation provided the catalyst system is viable.

The 2nd Primary Engineering Objective, *Design/Print geometries for continuous reactions with high Surface Area to Volume Ratios & without removable internal support structures*, was achieved by multiple designs. The earliest designs were cylinders with parallel, square channels allowing flow, this design was adapted to include plates parallel to the flow with an intersecting pin-hole configuration.

To address the sub-objective, *Identify the geometry with lowest pressure drop*, these adapted designs were subject to variants in the shapes used for the pin-hole configuration and the trend was that pin-holes without size variation or tortuous paths generated the smallest pressure drops.

Considering the primary objective, the cylinders with parallel, square channels were applied to DRM in a continuous setup, although there was a design problem to be address:

Design Element: Free volume is too low & channel width is too small.
Design Problem: Pressure build-up during the reaction, forced the reaction to stop early.
Suggested Solution: Improve the free volume or increase the channel width in a new design.

A later design addressed this objective properly by increasing the free volume substantially, such that no further issues were encountered with excessive pressures during reactions. This design is a simple VFBCC lattice structure, which is an overlay of the BCC & FCC lattice structures with vertical elements added for SLM building stability. This latter design was fit for DRM, so this Research Objective has been met.

The 1st Primary Chemistry Objective, *Develop & Implement a deposition method for catalysts of known gaseous phase reactions, including: catalytic partial oxidation (CPOx), the dry reforming of methane (DRM) & methanol synthesis (MS)*, was achieved for various catalysts to varying degrees of success.

The catalyst coatings successfully deposited then tested for DRM on 17-4 PH steel include:
1. Al_2O_3,
2. Metallic Ni,
3. Ni/Al_2O_3 &
4. $Ni/MgAl_2O_4$.

Although Al_2O_3 bonded moderately well to the 17-4 PH, the MgO and Ni materials were adhered exceptionally better. Furthermore, successful coatings were made for Catalytic Partial Oxidation of Methane and Methanol Synthesis catalysts, although testing these catalysts in reactions was outside the scope of the project.

Results from the DRM catalysts show minimal or no activity, however, they demonstrate that the coating methods applied in the Experimental Method for these materials are feasible. It's apparent that some substantial improvement is required for the catalysts to be commercially

viable, nonetheless this work serves to demonstrate the feasibility of using SLM materials as substrates for catalysts in gaseous phase reactions. Because active catalyst depositions have been conceived and demonstrated it follows that this Research Objective has been met.

The 2nd Primary Chemistry Objective, *Develop & Implement a deposition method for catalysts of known liquid phase reactions, including: 4-Nitrophenol reduction & glycerol acetalisation,* was achieved for various catalysts to varying degrees of success.

The catalyst coatings successfully deposited then tested for 4-NP reduction include:

1. Au nanoparticles on Ti6Al4V Titanium Alloy

    ⎯ Includes several variants in method.

2. Pd nanoparticles on Ti6Al4V Titanium Alloy

    ⎯ Includes a few variants in method.

3. Mixed Au & Pd nanoparticles on Ti6Al4V Titanium Alloy

The catalyst coatings successfully deposited then tested for glycerol acetalisation include:

1. $FeCl_3$ on Ti6Al4V Titanium Alloy

2. Al_2O_3 on Ti6Al4V Titanium Alloy & 17-4 PH Stainless Steel

    ⎯ Includes 6 Variants

The methods were more effective in some cases & less in others. The general trend was that immersing substrates in the coating fluid was, by far, more effective than drop-casting the reaction fluid onto the substrates. This distinction was explored in the 4-NP reduction reaction. Regardless, there are a few competing needs when it comes to producing an effective catalyst for any reaction which these reactions have made apparent. These needs are ordered by priority:

1. The catalyst system must be able to convert the reactants to the products desired.

2. The catalyst system must be adhered well enough to resist dissolution in reagent solvents.

3. The catalyst should be able to be regenerated by repeating its' calcination procedure.

The applied catalysts satisfy only need 1 by being active, such as 400ºC/3h calcined $FeCl_3$ on Ti6Al4V with its ~53% conversion of the glycerol reactant, or dried DDA-Pd on Ti6Al4V with its qualitative conversion of 4-NP to 4-AP. However, both systems suffered from leaching of the catalyst in their respective reaction solvents and thus did not satisfy Need 2 or Need 3. As such, no catalyst system was found to satisfy all 3 of these needs.

Given that a couple of implemented catalyst systems were active it can be considered that this research objective has been partially met. Although it would be preferable if all 3 needs could be met for a catalyst system, the first need is of greatest importance for this research objective.

The primary chemistry research objectives, *Test catalysts under batch reaction conditions* & *Test the best catalysts under continuous reaction conditions*, were met based on the methodologies provided in the Experimental Method chapter.

The underlying secondary chemistry objectives, *Measure conversion and selectivity by GC-FID/MS &/or UV/Vis* & *Perform these methods for further data – XRD, XPS & SEM/EDX*, were met & reported in *Chapter 3: Vapour Phase Reactions on AM substrates* & *Chapter 4: Liquid Phase Reactions on AM substrates* in the context of the results for each different reaction. Characterisation data was not always collected in the interests of saving time – as inactive systems are of less interest.

All research objectives were met to some extent and explored within the context of this research project: *Investigation of Catalytic Reactions on Additively Manufactured Substrates*.

6.2 ADDRESSING THE RESEARCH HYPOTHESES

The primary hypothesis was that "Catalyst-loaded solvents can be used effectively for the functionalisation of complex geometries made by SLM". This hypothesis is confirmed, as considered in the latter section, several catalysts were anchored effectively using a catalyst-loaded solvent to deliver the catalyst to the SLM substrate surface.

Accounting only for tested catalysts, the following systems were created by using a catalyst-loaded solvent to functionalise an SLM substrate:

1. Al_2O_3 on 17-4 PH Stainless Steel

1. Metallic Ni on 17-4 PH Stainless Steel

2. Ni/Al_2O_3 on 17-4 PH Stainless Steel

3. $Ni/MgAl_2O_4$ on 17-4 PH Stainless Steel

4. Au nanoparticles on Ti6Al4V Titanium Alloy

    —— Includes several variants in method.

5. Pd nanoparticles on Ti6Al4V Titanium Alloy

    —— Includes a few variants in method.

6. Mixed Au & Pd nanoparticles on Ti6Al4V Titanium Alloy

7. $FeCl_3$ on Ti6Al4V Titanium Alloy

It is true that catalyst-loaded solvents can be used effectively for the functionalisation of complex geometries made by SLM.

The secondary hypotheses, *SLM substrates can effectively anchor catalysts on their surface to stabilise them* & *SLM substrates can be effective supports for both gaseous and liquid phase catalysts*, are true according to the latter list of SLM catalyst systems. However, there has been no evidence that *SLM substrates can act as catalyst supports to increase the conversion or alter selectivity.* On the contrary, SLM substrates seem to frequently deactivate any catalysts placed upon them, making it very difficult to find catalysts which are both functionalise and retain activity. This latter hypothesis was not true, SLM substrates typically deactivate catalysts and none to date have improved the activity of any catalyst employed.

The research questions are best addressed in *Chapter 4: Vapour Phase Reactions on AM substrates* & *Chapter 5: Liquid Phase Reactions on AM substrates* where the discussions associated with answering them are part of the flow of these chapters.

6.3 SUMMARY AND FINAL CONCLUSIONS

The research aims, objectives, hypotheses and questions have been addressed satisfactorily. The work done on the project, "Investigation of Catalytic Reactions on Additively Manufactured Substrates", has made it clear that this little-explored area of research has potential.

However, there are still some major challenges for future research to address:

1. An Improved Catalyst Synthesis Strategy:

    1.1. Brute force catalyst synthesis & testing methods are one valid path.

    1.2. Catalyst synthesis & testing methods based on fundamental understanding

    1.3. A combined strategy including fundamental understanding & brute force methods is
    ideal

2. Refining methods for functionalising the catalysts onto SLM substrates with more reliable
distribution over the substrate surface, a task made challenging by SLM surface
roughness.

3. The lack of fundamental understanding of the interactions of SLM substrates with their
functionalised catalyst systems.

This is a promising field of research which is almost untouched, it's worth further exploration
as the combination of SLM & heterogeneous catalysis has many positive possibilities, the
creation of miniature, & therefore portable, reactors for DME synthesis being one such
commercially interesting application.

REFERENCES

1. Symes, M.D., et al., *Integrated 3D-printed reactionware for chemical synthesis and analysis.* Nat Chem, 2012. **4**(5): p. 349-354.
2. Mardani, S., et al., *Development of a unique modular distillation column using 3D printing.* Chemical Engineering and Processing: Process Intensification, 2016. **109**: p. 136-148.
3. Naher, S., et al., *Effect of micro-channel geometry on fluid flow and mixing.* Simulation Modelling Practice and Theory, 2011. **19**(4): p. 1088-1095.
4. An, H., et al., *Computational fluid dynamics (CFD) analysis of micro-reactor performance: Effect of various configurations.* Chemical Engineering Science, 2012. **75**: p. 85-95.
5. Liu, R.H., et al., *Passive mixing in a three-dimensional serpentine microchannel.* Microelectromechanical Systems, Journal of, 2000. **9**(2): p. 190-197.
6. Gumuslu, G. and A.K. Avci, *Parametric analysis of Fischer-tropsch synthesis in a catalytic microchannel reactor.* AIChE Journal, 2012. **58**(1): p. 227-235.
7. Matkovic, M., et al., *Experimental study on condensation heat transfer inside a single circular minichannel.* International Journal of Heat and Mass Transfer, 2009. **52**(9–10): p. 2311-2323.
8. Bavière, R., M. Favre-Marinet, and S. Le Person, *Bias effects on heat transfer measurements in microchannel flows.* International Journal of Heat and Mass Transfer, 2006. **49**(19–20): p. 3325-3337.
9. Wu, H.Y. and P. Cheng, *An experimental study of convective heat transfer in silicon microchannels with different surface conditions.* International Journal of Heat and Mass Transfer, 2003. **46**(14): p. 2547-2556.
10. Qu, W., G.M. Mala, and D. Li, *Heat transfer for water flow in trapezoidal silicon microchannels.* International Journal of Heat and Mass Transfer, 2000. **43**(21): p. 3925-3936.

11. Park, H.S. and J. Punch, *Friction factor and heat transfer in multiple microchannels with uniform flow distribution.* International Journal of Heat and Mass Transfer, 2008. **51**(17–18): p. 4535-4543.

12. Owhaib, W., C. Martín-Callizo, and B. Palm, *Evaporative heat transfer in vertical circular microchannels.* Applied Thermal Engineering, 2004. **24**(8–9): p. 1241-1253.

13. Minakov, A., et al., *Investigation of slip boundary conditions in the T-shaped microchannel.* International Journal of Heat and Fluid Flow, 2013. **43**: p. 161-169.

14. Ren, Y. and W.W.-F. Leung, *Flow and mixing in rotating zigzag microchannel.* Chemical Engineering Journal, 2013. **215–216**: p. 561-578.

15. Leung, W.W.-F. and Y. Ren, *Crossflow and mixing in obstructed and width-constricted rotating radial microchannel.* International Journal of Heat and Mass Transfer, 2013. **64**: p. 457-467.

16. Lee, P.-S., S.V. Garimella, and D. Liu, *Investigation of heat transfer in rectangular microchannels.* International Journal of Heat and Mass Transfer, 2005. **48**(9): p. 1688-1704.

17. Hassell, D.G. and W.B. Zimmerman, *Investigation of the convective motion through a staggered herringbone micromixer at low Reynolds number flow.* Chemical Engineering Science, 2006. **61**(9): p. 2977-2985.

18. Lin, Y.-C., Y.-C. Chung, and C.-Y. Wu, *Mixing enhancement of the passive microfluidic mixer with J-shaped baffles in the tee channel.* Biomedical Microdevices, 2007. **9**(2): p. 215-221.

19. Suha, Y., et al., *Numerical and experimental study on a channel mixer with a periodic array of cross baffles.* Journal of Mechanical Science and Technology, 2007. **21**(3): p. 549-555.

20. Hessel, V., *Special Issue: Design and Engineering of Microreactor and Smart-Scaled Flow Processes.* Processes, 2015. **3**(1): p. 19-22.

21. Bakhtiary-Davijany, H., et al., *Characteristics of an Integrated Micro Packed Bed Reactor-Heat Exchanger for methanol synthesis from syngas.* Chemical Engineering Journal, 2011. **167**(2–3): p. 496-503.

22. Rahman, M.T. and E.V. Rebrov, *Microreactors for Gold Nanoparticles Synthesis: From Faraday to Flow.* Processes, 2014. **2**(2): p. 466-493.

23. Cao, E., et al., *Enhanced Performance of Oxidation of Rosalva (9-decen-1-ol) to Costenal (9-decenal) on Porous Silicon-Supported Silver Catalyst in a Microstructured Reactor.* Processes, 2014. **2**(1): p. 141-157.

24. Newnham, J., et al., *Highly stable and active Ni-mesoporous alumina catalysts for dry reforming of methane.* International Journal of Hydrogen Energy, 2012. **37**(2): p. 1454-1464.

25. Anjaneyulu, C., et al., *Influence of La on reduction behaviour and Ni metal surface area of Ni–Al2O3 catalysts for COx free H2 by catalytic decomposition of methane.* International Journal of Hydrogen Energy, 2015. **40**(9): p. 3633-3641.

26. ConceptLaser. *LaserCUSING® - Laser melting with metals*. Available from: https://www.concept-laser.de/en/technology/lasercusingr.html.

27. Kiwi-Minsker, L. and A. Renken, *Microstructured reactors for catalytic reactions.* Catalysis Today, 2005. **110**(1–2): p. 2-14.

28. Kwon, P., et al., *Processing Issues in Fabricating Ceramic Micro-Heat Exchangers by Joining Components*, in *Advances in Joining of Ceramics*. 2006, John Wiley & Sons, Inc. p. 209-219.

29. Kurzrock, R. and D.J. Stewart, *Click chemistry, 3D-printing, and omics: the future of drug development.* Oncotarget, 2016. **7**(3): p. 2155-2158.

30. He, Y., et al., *Developments of 3D Printing Microfluidics and Applications in Chemistry and Biology: a Review.* Electroanalysis, 2016. **28**(8): p. 1658-1678.

31. Gross, B.C., et al., *Evaluation of 3D Printing and Its Potential Impact on Biotechnology and the Chemical Sciences.* Analytical Chemistry, 2014. **86**(7): p. 3240-3253.

32. Richards, D.J., et al., *3D Printing for Tissue Engineering.* Israel Journal of Chemistry, 2013. **53**(9-10): p. 805-814.

33. Bose, S., S. Vahabzadeh, and A. Bandyopadhyay, *Bone tissue engineering using 3D printing.* Materials Today, 2013. **16**(12): p. 496-504.

34. Rezende, R.A., et al., *Scalable Biofabrication of Tissue Spheroids for Organ Printing.* Procedia CIRP, 2013. **5**: p. 276-281.

35. Tasoglu, S. and U. Demirci, *Bioprinting for stem cell research.* Trends in Biotechnology, 2013. **31**(1): p. 10-19.

36. Rengier, F., et al., *3D printing based on imaging data: review of medical applications.* International Journal of Computer Assisted Radiology and Surgery, 2010. **5**(4): p. 335-341.

37. Shirazi, S.F.S., et al., *A review on powder-based additive manufacturing for tissue engineering: selective laser sintering and inkjet 3D printing.* Science and Technology of Advanced Materials, 2015. **16**(3): p. 033502.

38. Kirchmajer, D.M., R. Gorkin Iii, and M. in het Panhuis, *An overview of the suitability of hydrogel-forming polymers for extrusion-based 3D-printing.* Journal of Materials Chemistry B, 2015. **3**(20): p. 4105-4117.

39. Tseng, P., et al., *Research highlights: printing the future of microfabrication.* Lab on a Chip, 2014. **14**(9): p. 1491-1495.

40. Bhattacharjee, N., et al., *The upcoming 3D-printing revolution in microfluidics.* Lab on a Chip, 2016. **16**(10): p. 1720-1742.

41. Pohanka, M., *Three-Dimensional Printing in Analytical Chemistry: Principles and Applications.* Analytical Letters, 2016: p. null-null.

42. Ambrosi, A. and M. Pumera, *3D-printing technologies for electrochemical applications.* Chemical Society Reviews, 2016. **45**(10): p. 2740-2755.

43. Kitson, P.J., et al., *3D printing of versatile reactionware for chemical synthesis.* Nat. Protocols, 2016. **11**(5): p. 920-936.

44. Johnson, R.D., *Custom labware: Chemical creativity with 3D printing.* Nat Chem, 2012. **4**(5): p. 338-339.

45. Sun, J., et al., *An Overview of 3D Printing Technologies for Food Fabrication.* Food and Bioprocess Technology, 2015. **8**(8): p. 1605-1615.

46. Stanton, M.M., C. Trichet-Paredes, and S. Sanchez, *Applications of three-dimensional (3D) printing for microswimmers and bio-hybrid robotics.* Lab on a Chip, 2015. **15**(7): p. 1634-1637.

47. Tubío, C.R., et al., *3D printing of a heterogeneous copper-based catalyst.* Journal of Catalysis, 2016. **334**: p. 110-115.

48. Dickson, M.J., *Plant Design*, in *Process Understanding*. 2011, Wiley-VCH Verlag GmbH & Co. KGaA. p. 283-305.

49. Capel, A.J., et al., *Design and additive manufacture for flow chemistry.* Lab on a Chip, 2013. **13**(23): p. 4583-4590.

50. Liu, X., et al., *Recent advances in inkjet printing synthesis of functional metal oxides.* Particuology, 2015. **19**: p. 1-13.

51. Crawford, S., *How 3-D Printing Works*, HowStuffWorks.com, Editor. 2011.

52. Kitson, P.J., et al., *Combining 3D printing and liquid handling to produce user-friendly reactionware for chemical synthesis and purification.* Chemical Science, 2013. **4**(8): p. 3099-3103.

53. Chisholm, G., et al., *3D printed flow plates for the electrolysis of water: an economic and adaptable approach to device manufacture.* Energy & Environmental Science, 2014. **7**(9): p. 3026-3032.

54. Gou, M., et al., *Bio-inspired detoxification using 3D-printed hydrogel nanocomposites.* Nat Commun, 2014. **5**.

55. Ambrosi, A., J.G.S. Moo, and M. Pumera, *Helical 3D-Printed Metal Electrodes as Custom-Shaped 3D Platform for Electrochemical Devices.* Advanced Functional Materials, 2016. **26**(5): p. 698-703.

56. Solutions, S. *SELECTIVE LASER MELTING MACHINE SLM 280 2.0*. Available from: https://slm-solutions.com/products/machines/selective-laser-melting-machine-slm-280-20.

57. Katz, J.E., et al., *Combinatorial synthesis and high-throughput photopotential and photocurrent screening of mixed-metal oxides for photoelectrochemical water splitting.* Energy & Environmental Science, 2009. **2**(1): p. 103-112.

58. Xiang, C., et al., *High-Throughput Bubble Screening Method for Combinatorial Discovery of Electrocatalysts for Water Splitting.* ACS Combinatorial Science, 2014. **16**(2): p. 47-52.

59. Gregoire, J.M., et al., *Scanning droplet cell for high throughput electrochemical and photoelectrochemical measurements.* Review of Scientific Instruments, 2013. **84**(2): p. 024102.

60. J. M. Gregoire, C.X., S. Mitrovic, X. Liu, M. Marcin, E. W. Cornell, J. Fan and J. Jin, *Combined Catalysis and Optical Screening for High Throughput Discovery of Solar Fuels Catalysts.* Electrochemical Society, 2013. **160**(4): p. F337-F342.

61. Liu, X., et al., *Inkjet Printing Assisted Synthesis of Multicomponent Mesoporous Metal Oxides for Ultrafast Catalyst Exploration.* Nano Letters, 2012. **12**(11): p. 5733-5739.

62. Woodhouse, M., G.S. Herman, and B.A. Parkinson, *Combinatorial Approach to Identification of Catalysts for the Photoelectrolysis of Water.* Chemistry of Materials, 2005. **17**(17): p. 4318-4324.

63. Woodhouse, M. and B.A. Parkinson, *Combinatorial Discovery and Optimization of a Complex Oxide with Water Photoelectrolysis Activity.* Chemistry of Materials, 2008. **20**(7): p. 2495-2502.

64. He, J. and B.A. Parkinson, *Combinatorial Investigation of the Effects of the Incorporation of Ti, Si, and Al on the Performance of α-Fe2O3 Photoanodes.* ACS Combinatorial Science, 2011. **13**(4): p. 399-404.

65. Seley, D., K. Ayers, and B.A. Parkinson, *Combinatorial Search for Improved Metal Oxide Oxygen Evolution Electrocatalysts in Acidic Electrolytes.* ACS Combinatorial Science, 2013. **15**(2): p. 82-89.

66. *Catalysis Research; Findings from University of Santiago Yields New Findings on Catalysis Research (3D printing of a heterogeneous copper-based catalyst).* Chemicals & Chemistry, 2016: p. 699.

67. Stuecker, J.N., et al., *Advanced Support Structures for Enhanced Catalytic Activity.* Industrial & Engineering Chemistry Research, 2004. **43**(1): p. 51-55.

68. Lefevere, J., et al., *The benefit of design of support architectures for zeolite coated structured catalysts for methanol-to-olefin conversion.* Catalysis Today, 2013. **216**: p. 18-23.

69. Van Noyen, J., et al., *Ceramic Processing Techniques for Catalyst Design: Formation, Properties, and Catalytic Example of ZSM-5 on 3-Dimensional Fiber Deposition Support Structures.* International Journal of Applied Ceramic Technology, 2012. **9**(5): p. 902-910.

70. Wei, Q., et al., *Printable hybrid hydrogel by dual enzymatic polymerization with superactivity.* Chemical Science, 2016. **7**(4): p. 2748-2752.

71. Eqtesadi, S., et al., *Poly-(lactic acid) infiltration of 45S5 Bioglass® robocast scaffolds: Chemical interaction and its deleterious effect in mechanical enhancement.* Materials Letters, 2016. **163**: p. 196-200.

72. Kokkinis, D., M. Schaffner, and A.R. Studart, *Multimaterial magnetically assisted 3D printing of composite materials.* Nat Commun, 2015. **6**.

73. Miranda, P., et al., *Mechanical properties of calcium phosphate scaffolds fabricated by robocasting.* Journal of Biomedical Materials Research Part A, 2008. **85A**(1): p. 218-227.

74. Rombouts, M., et al., *The production of Ti-6Al-4V parts with controlled porous architecture by three-dimensional fiber deposition*, in *Innovative Developments in Design and Manufacturing*. 2009, CRC Press.

75. Schlordt, T., et al., *Robocasting of alumina hollow filament lattice structures.* Journal of the European Ceramic Society, 2013. **33**(15–16): p. 3243-3248.

76. Review, M.T. *Robocasting*. Intelligent Machines 1999; Available from: https://www.technologyreview.com/s/400400/robocasting/.

77. Additively, *Fused Deposition Modeling (FDM)*.

78. Imaginables. *Ultimaker 3 Extended*. 2017; Available from: http://imaginables.com.au/collections/3d-printers/products/ultimaker-3-extended.

79. *Nanoparticles; Researchers use 3-D printing to create structure with active chemistry.* NewsRx Health & Science, 2016: p. 256.

80. Maier, W.F., K. Stöwe, and S. Sieg, *Combinatorial and High-Throughput Materials Science.* Angewandte Chemie International Edition, 2007. **46**(32): p. 6016-6067.

81. Tekin, E., P.J. Smith, and U.S. Schubert, *Inkjet printing as a deposition and patterning tool for polymers and inorganic particles.* Soft Matter, 2008. **4**(4): p. 703-713.

82. Additively. *Overview over 3D printing technologies*. [cited 2017 23/01/2017]; Available from: https://www.additively.com/en/learn-about/3d-printing-technologies.

83. Melis, A., et al., *Deposition of photocatalytically active TiO 2 films by inkjet printing of TiO 2 nanoparticle suspensions obtained from microwave-assisted hydrothermal synthesis.* Nanotechnology, 2012. **23**(16): p. 165603.

84. Arin, M., et al., *Low temperature deposition of TiO2 layers from nanoparticle containing suspensions synthesized by microwave hydrothermal treatment.* Journal of Sol-Gel Science and Technology, 2013. **66**(1): p. 100-111.

85. Černá, M., M. Veselý, and P. Dzik, *Physical and chemical properties of titanium dioxide printed layers.* Catalysis Today, 2011. **161**(1): p. 97-104.

86. Additively. *Stereolithography (SL)*. Available from: https://www.additively.com/en/learn-about/stereolithography.

87. Shining3D. *SLA 3D Printer*. Available from: http://en.shining3d.com/3d_printing-168.html?gclid=CKzR14Xak9ICFYgJvAodqJkKkw.

88. 3D, A. *Explorer DLP 3D Printer*. 2017; Available from: http://aussie3d.com/products/explorer-dlp-3d-printer?utm_medium=cpc&utm_source=googlepla&variant=17165643205&gclid=CI_v88DXk9ICFY0DKgodPTQO7w.

89. Zhang, A.P., et al., *Rapid Fabrication of Complex 3D Extracellular Microenvironments by Dynamic Optical Projection Stereolithography.* Advanced Materials, 2012. **24**(31): p. 4266-4270.

90. Frazier, W., *Metal Additive Manufacturing: A Review.* Journal of Materials Engineering and Performance, 2014. **23**(6): p. 1917-1928.

91. Yadroitsev, I., et al., *Factor analysis of selective laser melting process parameters and geometrical characteristics of synthesized single tracks.* Rapid Prototyping Journal, 2012. **18**(3): p. 201-208.

92. Additively. *Laser Melting (LM)*. Available from: https://www.additively.com/en/learn-about/laser-melting.

93. Srivatsan, T.S. and T.S. Sudarshan, *Additive Manufacturing*. 2015, Boca Raton, UNITED STATES: CRC Press.

94. Strano, G., et al., *Surface roughness analysis, modelling and prediction in selective laser melting.* Journal of Materials Processing Technology, 2013. **213**(4): p. 589-597.

95. Mumtaz, K. and N. Hopkinson, *Top surface and side roughness of Inconel 625 parts processed using selective laser melting.* Rapid Prototyping Journal, 2009. **15**(2): p. 96-103.

96. Bremen, S., W. Meiners, and A. Diatlov, *Selective Laser Melting.* Laser Technik Journal, 2012. **9**(2): p. 33-38.

97. Solutions, S. *Selective Laser Melting Systems: Metal Additive Manufacturing Systemn*. 2017; Available from: http://slm-solutions.us/selective-laser-melting-systems/.

98. Venkatesh, K.V. and V.V. Nandini, *Direct Metal Laser Sintering: A Digitised Metal Casting Technology.* Journal of Indian Prosthodontic Society, 2013. **13**(4): p. 389-392.

99.   Benaglia, M., *Recoverable and recyclable catalysts*. 2009: John Wiley & Sons.

100.   Busca, G., *Heterogeneous Catalytic Materials: Solid State Chemistry, Surface Chemistry & Solid State Behaviour*. 1st ed. 2014.

101.   *Synthesis of Solid Catalysts.* Focus on Catalysts, 2009. **2009**(12): p. 8.

102.   Regalbuto, J., *Catalyst Preparation - Science and Engineering*. Taylor & Francis.

103.   G. Ertl, H.K., J. Weitkamp, *Preparation of Solid Catalysts.* 1999.

104.   R. Schlogl in G. Ertl, H.K., J.Weitkamp, *Handbook of Heterogeneous Catalysis*. Vol. 1. 1997, Weinheim: Wiley-VCH.

105.   *Foreword*, in *Studies in Surface Science and Catalysis*, M.D.S.H.P.A.J.J.A.M. E.M. Gaigneaux and P. Ruiz, Editors. 2010, Elsevier. p. xix-xxi.

106.   Danaci, S., et al., *Efficient CO2 methanation over Ni/Al2O3 coated structured catalysts.* Catalysis Today, 2016. **273**: p. 234-243.

107.   Fan, J., X. Liu, and F. Huang, *Mesoporous metal oxide catalysts: rational synthesis and fast exploration.* Chemistry Bulletin / Huaxue Tongbao, 2013. **76**(8): p. 675-683.

108.   Jackson, S.D. and J.S. Hargreaves, *Metal oxide catalysis*. Vol. 1. Wiley Online Library.

109.   Li, Y. and W. Shen, *Morphology-dependent nanocatalysis on metal oxides.* Science China Chemistry, 2012. **55**(12): p. 2485-2496.

110.   Lee, D.-H., et al., *Inkjet printed high-mobility indium zinc tin oxide thin film transistors.* Journal of Materials Chemistry, 2009. **19**(20): p. 3135-3137.

111.   Kuscer, D., et al., *Formulation of an Aqueous Titania Suspension and its Patterning with Ink-Jet Printing Technology.* Journal of the American Ceramic Society, 2012. **95**(2): p. 487-493.

112.   Duraisamy, N., et al., *Fabrication of TiO2 thin film memristor device using electrohydrodynamic inkjet printing.* Thin Solid Films, 2012. **520**(15): p. 5070-5074.

113.   Millet, P., *Fundamentals of Water Electrolysis*, in *Hydrogen Production*. 2015, Wiley-VCH Verlag GmbH & Co. KGaA. p. 33-62.

114.   Yang, Z., et al., *Designing 3D graphene networks via a 3D-printed Ni template.* RSC Advances, 2015. **5**(37): p. 29397-29400.

115.   Zhu, C., et al., *Highly compressible 3D periodic graphene aerogel microlattices.* Nature Communications, 2015. **6**: p. 6962.

116.   Lonkar SP, A.A., *Applications of Graphene in Catalysis.* J Thermodyn Catal, 2014. **5**(132).

117.   Wei, X., et al., *3D Printable Graphene Composite.* Scientific Reports, 2015. **5**: p. 11181.

118.   Dimension, N., *Nano Dimension Announces New Collaboration with Tel Aviv University, Enabling 3D Printing of Sensors Using Nickel Nano- Particles*, N. Dimension, Editor. 2016, Nano Dimension.

119.   Lau, M., et al., *Near-field-enhanced, off-resonant laser sintering of semiconductor particles for additive manufacturing of dispersed Au–ZnO-micro/nano hybrid structures.* Applied Physics A, 2014. **114**(4): p. 1023-1030.

120.   Dhas, V., et al., *Enhanced conversion efficiency in dye-sensitized solar cells based on ZnO bifunctional nanoflowers loaded with gold nanoparticles.* Applied Physics Letters, 2008. **93**(24): p. 243108.

121.   Wang, X., et al., *i3DP, a robust 3D printing approach enabling genetic post-printing surface modification.* Chemical Communications, 2013. **49**(86): p. 10064-10066.

122.   Lee, K.G., et al., *3D printed modules for integrated microfluidic devices.* RSC Advances, 2014. **4**(62): p. 32876-32880.

123.   MakerBot. *Thingiverse*. Available from: https://www.thingiverse.com/.

124.   Kundu, A., et al., *Process intensification by micro-channel reactor for steam reforming of methanol.* Chemical Engineering Journal, 2008. **135**(1–2): p. 113-119.

125.   Hu, J., et al., *Conversion of Biomass Syngas to DME Using a Microchannel Reactor.* Industrial & Engineering Chemistry Research, 2005. **44**(6): p. 1722-1727.

126. Grundemann, L. and S. Scholl, *Ecological and Economic Assessment of Micro-/Milli-Continuous Campaign Manufacturing: The Case of Writing Ink.* Processes, 2014. **2**(1): p. 238-264.

127. Karakaya, M. and A. Avci, *Simulation of on-Board Fuel Conversion in Catalytic Microchannel Reactor-Heat Exchanger Systems.* Topics in Catalysis, 2009. **52**(13-20): p. 2112-2116.

128. Parra, A.A.M., et al., *Stability Analysis of Reactive Multiphase Slug Flows in Microchannels.* Processes, 2014. **2**(2): p. 371-391.

129. Phan, X.K., et al., *Preparation and performance of Cu-based monoliths for methanol synthesis.* Applied Catalysis A: General, 2011. **405**(1–2): p. 1-7.

130. Garimella, S. and B.M. Fronk, *Single- and Multi-Constituent Condensation of Fluids and Mixtures with Varying Properties in Micro-Channels.* Experimental Heat Transfer, 2013. **26**(2-3): p. 129-168.

131. Chen, Y., et al., *Optimal surface fractal dimension for heat and fluid flow in microchannels.* Applied Physics Letters, 2010. **97**(8): p. 084101.

132. Salimpour, M.R., M. Sharifhasan, and E. Shirani, *Constructal optimization of the geometry of an array of micro-channels.* International Communications in Heat and Mass Transfer, 2011. **38**(1): p. 93-99.

133. Bello-Ochende, T., L. Liebenberg, and J.P. Meyer, *Constructal cooling channels for micro-channel heat sinks.* International Journal of Heat and Mass Transfer, 2007. **50**(21–22): p. 4141-4150.

134. Garza-Garcia, L.D., et al., *Continuous flow micro-bioreactors for the production of biopharmaceuticals: the effect of geometry, surface texture, and flow rate.* Lab on a Chip, 2014. **14**(7): p. 1320-1329.

135. Hossain, S., M.A. Ansari, and K.-Y. Kim, *Evaluation of the mixing performance of three passive micromixers.* Chemical Engineering Journal, 2009. **150**(2–3): p. 492-501.

136. Tsai, R.-T. and C.-Y. Wu, *An efficient micromixer based on multidirectional vortices due to baffles and channel curvature.* Biomicrofluidics, 2011. **5**(1): p. 014103.

137. Wu, C.-Y. and R.-T. Tsai, *Fluid mixing via multidirectional vortices in converging–diverging meandering microchannels with semi-elliptical side walls.* Chemical Engineering Journal, 2013. **217**: p. 320-328.

138. Jeon, W. and C.B. Shin, *Design and simulation of passive mixing in microfluidic systems with geometric variations.* Chemical Engineering Journal, 2009. **152**(2–3): p. 575-582.

139. Myrstad, R., et al., *Fischer–Tropsch synthesis in a microstructured reactor.* Catalysis Today, 2009. **147, Supplement**: p. S301-S304.

140. Bakhtiary-Davijany, H., et al., *Performance of a multi-slit packed bed microstructured reactor in the synthesis of methanol: Comparison with a laboratory fixed-bed reactor.* Chemical Engineering Science, 2011. **66**(24): p. 6350-6357.

141. Agarwal, A., T.M. Bandhauer, and S. Garimella, *Measurement and modeling of condensation heat transfer in non-circular microchannels.* International Journal of Refrigeration, 2010. **33**(6): p. 1169-1179.

142. Hsieh, S.-S., J.-W. Lin, and J.-H. Chen, *Mixing efficiency of Y-type micromixers with different angles.* International Journal of Heat and Fluid Flow, 2013. **44**: p. 130-139.

143. Coleman, J.W. and S. Garimella, *Characterization of two-phase flow patterns in small diameter round and rectangular tubes.* International Journal of Heat and Mass Transfer, 1999. **42**(15): p. 2869-2881.

144. Ansari, M.A. and K.-Y. Kim, *Shape optimization of a micromixer with staggered herringbone groove.* Chemical Engineering Science, 2007. **62**(23): p. 6687-6695.

145. Kim, S.-M. and I. Mudawar, *Analytical heat diffusion models for heat sinks with circular micro-channels.* International Journal of Heat and Mass Transfer, 2010. **53**(21–22): p. 4552-4566.

146. Quan, X., L. Dong, and P. Cheng, *Determination of annular condensation heat transfer coefficient of steam in microchannels with trapezoidal cross sections.* International Journal of Heat and Mass Transfer, 2010. **53**(19–20): p. 3670-3676.

147. Kim, B.S., et al., *Optimization of microscale vortex generators in a microchannel using advanced response surface method.* International Journal of Heat and Mass Transfer, 2011. **54**(1–3): p. 118-125.

148. Hsiao, K.-Y., C.-Y. Wu, and Y.-T. Huang, *Fluid mixing in a microchannel with longitudinal vortex generators.* Chemical Engineering Journal, 2014. **235**: p. 27-36.

149. Aubin, J., D.F. Fletcher, and C. Xuereb, *Design of micromixers using CFD modelling.* Chemical Engineering Science, 2005. **60**(8–9): p. 2503-2516.

150. Salman, B.H., et al., *Characteristics of heat transfer and fluid flow in microtube and microchannel using conventional fluids and nanofluids: A review.* Renewable and Sustainable Energy Reviews, 2013. **28**: p. 848-880.

151. Zhao, S., et al., *Three-dimensional simulation of mixing performance inside droplets in micro-channels by Lattice Boltzmann method.* Chemical Engineering Journal, 2012. **207–208**: p. 267-277.

152. Nema, G., S. Garimella, and B.M. Fronk, *Flow regime transitions during condensation in microchannels.* International Journal of Refrigeration, 2014. **40**: p. 227-240.

153. Reddy Cherlo, S.K. and S. Pushpavanam, *Effect of depth on onset of engulfment in rectangular micro-channels.* Chemical Engineering Science, 2010. **65**(24): p. 6486-6490.

154. Fani, A. *T-shaped micro-mixer: engulfment regime*. 2015; Available from: http://www.andreafani.com/?p=2709.

155. Chuan, L., et al., *Fluid flow and heat transfer in microchannel heat sink based on porous fin design concept.* International Communications in Heat and Mass Transfer, 2015. **65**: p. 52-57.

156. Taylor, M.G., et al., *Catalyst Design Based on Morphology- and Environment-Dependent Adsorption on Metal Nanoparticles.* ACS Catalysis, 2015. **5**(11): p. 6296-6301.

157. Wachs, I.E., *Characterization of Catalytic Materials*. 2010, Momentum Press: New York.

158. Amin, M.H., et al., *Highly stable ytterbium promoted Ni/γ-Al2O3 catalysts for carbon dioxide reforming of methane.* Applied Catalysis B: Environmental, 2012. **119–120**: p. 217-226.

159. *Catalytic Coating & Materials*. 2005; Available from: https://www.dieselnet.com/tech/cat_mat.php#intro.

160. Bravo, J., et al., *Wall coating of a CuO/ZnO/Al2O3 methanol steam reforming catalyst for micro-channel reformers.* Chemical Engineering Journal, 2004. **101**(1–3): p. 113-121.

161. Hwang, S.-M., O.J. Kwon, and J.J. Kim, *Method of catalyst coating in micro-reactors for methanol steam reforming.* Applied Catalysis A: General, 2007. **316**(1): p. 83-89.

162. Kwon, O.J., et al., *A silicon-based miniaturized reformer for high power electric devices.* Chemical Engineering Journal, 2007. **133**(1–3): p. 157-163.

163. Leu, C.-H., et al., *Influence of CuO/ZnO/Al2O3 wash-coating slurries on the steam reforming reaction of methanol.* International Journal of Hydrogen Energy, 2011. **36**(19): p. 12231-12237.

164. Samei, E., M. Taghizadeh, and M. Bahmani, *Enhancement of stability and activity of Cu/ZnO/Al2O3 catalysts by colloidal silica and metal oxides additives for methanol synthesis from a CO2-rich feed.* Fuel Processing Technology, 2012. **96**(0): p. 128-133.

165. Meshkini, F., M. Taghizadeh, and M. Bahmani, *Investigating the effect of metal oxide additives on the properties of Cu/ZnO/Al2O3 catalysts in methanol synthesis from syngas using factorial experimental design.* Fuel, 2010. **89**(1): p. 170-175.

166. Peela, N.R. and D. Kunzru, *Oxidative steam reforming of ethanol over Rh based catalysts in a micro-channel reactor.* International Journal of Hydrogen Energy, 2011. **36**(5): p. 3384-3396.

167. Jones, T.C., *Dip coating.* Metal Finishing, 2010. **108**(11–12): p. 130-132.

168. Binda, M. *Organic Electronics: Principles, devices and applications*. 2011 09/12/15]; Available from: https://www.google.com.au/url?sa=t&rct=j&q=&esrc=s&source=web&cd=1&cad=rja&uact= 8&ved=0ahUKEwjA9Ya80c3JAhXFjJQKHT1TCKEQFggbMAA&url=http%3A%2F%2Fwww.resea rchgate.net%2Ffile.PostFileLoader.html%3Fid%3D550c9ed2d4c118d5298b467a%26assetKey %3DAS%253A273739944529946%25401442276098099&usg=AFQjCNEpxCBPyV_yKx_Qbvhs FB2yIf_mhA.

169. Bartlett, A.P., et al., *Modified Spin-coating Technique to Achieve Directional Colloidal Crystallization.* Langmuir, 2012. **28**(6): p. 3067-3070.

170. Zhou, X.L., et al., *Deposition behavior of mixed binary metallic powders in cold spraying process.* Applied Surface Science, 2011. **257**(24): p. 10628-10633.

171. Sigma-Aldrich. *Physical Vapor Deposition (PVD)*. 2015; Available from: http://www.sigmaaldrich.com/materials-science/material-science-products.html?TablePage=108832720.

172. Dobkin, D., Zuraw, M.K, *Principles of Chemical Vapor Deposition*. 2003, Netherlands: Springer Netherlands. 273.

173. Melián-Cabrera, I., M. López Granados, and J.L.G. Fierro, *Reverse Topotactic Transformation of a Cu–Zn–Al Catalyst during Wet Pd Impregnation: Relevance for the Performance in Methanol Synthesis from CO2/H2 Mixtures.* Journal of Catalysis, 2002. **210**(2): p. 273-284.

174. Figueiredo, R.T., et al., *Effect of alkali cations on the CuZnOAl2O3 low temperature water gas-shift catalyst.* Catalysis Today, 2011. **172**(1): p. 166-170.

175. Laura Prati, A.V., *The Art of Manufacturing Gold Catalysts.* Catalysts, 2012. **2**: p. 24-37.

176. Company, T.C. *Anodic oxidation – Aluminum finishing by Coatinc*. 2015; Available from: http://www.coatinc.com/en/processes/anodic-oxidation.html.

177. Hamouda, F., et al., *Large area nanopatterning by combined anodic aluminum oxide and soft UV–NIL technologies for applications in biology.* Microelectronic Engineering, 2011. **88**(8): p. 2444-2446.

178. Rodriguez, C. and G. Tremiliosi-Filho, *Electrochemical Deposition*, in *Encyclopedia of Tribology*, Q.J. Wang and Y.-W. Chung, Editors. 2013, Springer US. p. 918-922.

179. Fry, A., *Fundamentals of electrochemical deposition.* Choice, 2007. **44**(6): p. 1013-1014.

180. Fukuhara, C., Y. Kamata, and A. Igarashi, *Catalytic performance of plate-type Pd/Zn-based catalysts for steam reforming of methanol, prepared by electroless plating.* Applied Catalysis A: General, 2007. **330**(0): p. 108-116.

181. Fukuhara, C. and H. Ohkura, *Physicochemical properties of a plate-type copper-based catalyst, prepared on an aluminum plate by electroless plating, for steam reforming of methanol and CO shift reaction.* Applied Catalysis A: General, 2008. **344**(1–2): p. 158-164.

182. Columbia, U.o.B. *Sol-Gel Deposition*. 2006 [cited 2015 23/06]; Available from: https://www.google.com.au/url?sa=t&rct=j&q=&esrc=s&source=web&cd=9&cad=rja&uact= 8&ved=0CE0QFjAI&url=http%3A%2F%2Fcme.nuk.edu.tw%2Fdownload.php%3Ffilename%3 D413_d5d4d48c.pdf%26dir%3Dpersonal_subject%2F%26title%3D%25E6%2587%2589%25E7 %2594%25A8%25E8%2586%25A0%25E9%25AB%2594%25E5%258C%2596%25E5%25AD%2 5B8_Lecture%2B08-%25E6%2587%2589%25E7%2594%25A8%25E8%2586%25A0%25E9%25AB%2594%25E5%25 8C%2596%25E5%25AD%25B8_08_Introduction%2Bto%2BSol-Gel&ei=RpWIVc6FFNHo8AWxmYXYAQ&usg=AFQjCNFlZOuE_8UTMO_fGd-skMG1rrUVFA&sig2=COGhSfi_dASo_fp8JcpUZw&bvm=bv.96339352,d.dGc.

183. WestYorkSteel. *17-4PH Stainless Steel*. 2012; Available from: http://www.westyorkssteel.com/stainless-steel/precipitation-hardening/17-4ph/.

184. AK_Steel. *17-4 PH Stainless Steel Data Sheet*. 2007; Available from: http://www.aksteel.com/pdf/markets_products/stainless/precipitation/17-4_ph_data_sheet.pdf.

185. SandMeyer_Steel_Company, *Specification Sheet: Alloy 17-4PH*, SandMeyer_Steel_Company, Editor.

186. Sun, X., et al., *Core/Shell Au/CuPt Nanoparticles and Their Dual Electrocatalysis for Both Reduction and Oxidation Reactions.* Journal of the American Chemical Society, 2014. **136**(15): p. 5745-5749.

187. Kiyonaga, T., T. Kawahara, and H. Tada, *Low-Temperature Photocleaning of Sulfur-Poisoned Au Nanoparticles on Titanium Dioxide Film.* Electrochemical and Solid-State Letters, 2006. **9**(3): p. E9-E12.

188. Kidambi, S., et al., *Selective Hydrogenation by Pd Nanoparticles Embedded in Polyelectrolyte Multilayers.* Journal of the American Chemical Society, 2004. **126**(9): p. 2658-2659.

189. Paredis, K., et al., *Evolution of the Structure and Chemical State of Pd Nanoparticles during the in Situ Catalytic Reduction of NO with H2.* Journal of the American Chemical Society, 2011. **133**(34): p. 13455-13464.

190. Reimann, S., et al., *Asymmetric C☐C Bond-Formation Reaction with Pd: How to Favor Heterogeneous or Homogeneous Catalysis?* Chemistry – A European Journal, 2010. **16**(31): p. 9658-9668.

191. Xiao, J., et al., *Effect of TiO2, ZrO2, and TiO2–ZrO2 on the performance of CuO–ZnO catalyst for CO2 hydrogenation to methanol.* Applied Surface Science, 2015. **338**: p. 146-153.

192. Brites, F.F., V.S. Santana, and N.R.C. Fernandes-Machado, *Effect of Support on the Photocatalytic Degradation of Textile Effluents Using Nb2O5 and ZnO: Photocatalytic Degradation of Textile Dye.* Topics in Catalysis, 2011. **54**(1): p. 264-269.

193. Mo, X., et al., *Effect of component interaction on the activity of Co/CuZnO for CO hydrogenation.* Journal of Catalysis, 2012. **285**(1): p. 208-215.

194. Courson, C., et al., *Grafted NiO on natural olivine for dry reforming of methane.* Science and Technology of Advanced Materials, 2002. **3**(3): p. 271.

195. Braga, T.P., et al., *Cu, Fe, or Ni doped molybdenum oxide supported on Al2O3 for the oxidative dehydrogenation of ethylbenzene.* Chinese Journal of Catalysis, 2015. **36**(5): p. 712-720.

196. Grunwaldt, J.-D., L. Basini, and B.S. Clausen, *In Situ EXAFS Study of Rh/Al2O3 Catalysts for Catalytic Partial Oxidation of Methane.* Journal of Catalysis, 2001. **200**(2): p. 321-329.

197. Wang, Y., et al., *The Extractive Desulfurization of Fuels Using Ionic Liquids Based on FeCl3.* Petroleum Science and Technology, 2010. **28**(12): p. 1203-1210.

198. Peng, X.D., et al., *Single-Step Syngas-to-Dimethyl Ether Processes for Optimal Productivity, Minimal Emissions, and Natural Gas-Derived Syngas.* Industrial & Engineering Chemistry Research, 1999. **38**(11): p. 4381-4388.

199. Krylov, O.V., *Catalytic conversion of natural gas (Summary of the proceedings of "Natural gas conversion VII," an international symposium held in Dalian, China, on June 6–10, 2004).* Kinetics and Catalysis, 2005. **46**(1): p. 159-164.

200. Mark, M.F. and W.F. Maier, *CO2-Reforming of Methane on Supported Rh and Ir Catalysts.* Journal of Catalysis, 1996. **164**(1): p. 122-130.

201. Bradford, M.C.J. and M.A. Vannice, *CO2Reforming of CH4over Supported Pt Catalysts.* Journal of Catalysis, 1998. **173**(1): p. 157-171.

202. Zhang, Z. and X.E. Verykios, *Mechanistic aspects of carbon dioxide reforming of methane to synthesis gas over Ni catalysts.* Catalysis Letters, 1996. **38**(3): p. 175-179.

203. Silverwood, I.P., et al., *Application of inelastic neutron scattering to studies of CO2 reforming of methane over alumina-supported nickel and gold-doped nickel catalysts.* Physical Chemistry Chemical Physics, 2012. **14**(43): p. 15214-15225.

204. Srisombat, L., et al., *Simple preparation Au/Pd core/shell nanoparticles for 4-nitrophenol reduction.* Colloids and Surfaces A: Physicochemical and Engineering Aspects, 2017. **512**: p. 17-25.

205. CHALLA, S.S.R.K., *Fluidic channel coated with metal catalysts and devices and methods relating thereto*. 2014, Google Patents.
206. Wang, X., et al., *Anchoring of silver nanoparticles on graphitic carbon nitride sheets for the synergistic catalytic reduction of 4-nitrophenol.* Chemosphere, 2017. **172**(Supplement C): p. 147-154.
207. Dong, W., et al., *Fabrication of highly dispersed Pd nanoparticles supported on reduced graphene oxide for catalytic reduction of 4-nitrophenol.* Catalysis Communications, 2017. **90**(Supplement C): p. 70-74.
208. Nair, G.S., et al., *Glycerol utilization: solvent-free acetalisation over niobia catalysts.* Catalysis Science & Technology, 2012. **2**(6): p. 1173-1179.
209. Vicente, G., et al., *Acetalisation of bio-glycerol with acetone to produce solketal over sulfonic mesostructured silicas.* Green Chemistry, 2010. **12**(5): p. 899-907.
210. Millipore, M. *106798 | 4-Nitrophenol*. Available from: http://www.merckmillipore.com/AU/en/product/4-Nitrophenol,MDA_CHEM-106798#anchor_Description.
211. Park, H., et al., *Hydrogenation of 4-nitrophenol to 4-aminophenol at room temperature: Boosting palladium nanocrystals efficiency by coupling with copper via liquid phase pulsed laser ablation.* Applied Surface Science, 2017. **401**: p. 314-322.
212. Ma, A., et al., *Interfacial nanodroplets guided construction of hierarchical Au, Au-Pt, and Au-Pd particles as excellent catalysts.* Scientific Reports, 2014. **4**: p. 4849.
213. Kumar, A., et al., *Investigation into the Interaction between Surface-Bound Alkylamines and Gold Nanoparticles.* Langmuir, 2003. **19**(15): p. 6277-6282.
214. Esteban, J., M. Ladero, and F. García-Ochoa, *Kinetic modelling of the solventless synthesis of solketal with a sulphonic ion exchange resin.* Chemical Engineering Journal, 2015. **269**: p. 194-202.
215. Ferreira, P., et al., *Valorisation of glycerol by condensation with acetone over silica-included heteropolyacids.* Applied Catalysis B: Environmental, 2010. **98**(1–2): p. 94-99.

APPENDIX

A. The calculations for the external standards associated with glycerol acetalisation were performed using Excel spreadsheets as follows: first all peak areas corresponding to solketal, glycerol & acetal were recorded for each molarity, (0.1, 0.075, 0.05 and 0.025 M), as shown in **Error! Reference source not found.** and later revised data in **Error! Reference source not found.**.

Table 33 Peak areas for glycerol acetalisation

Peak Area (Intensity x Time)				
Compound	0.025 M	0.05 M	0.075 M	0.1 M
Solketal	233514	595807	737406	1114181
Acetal	5903	9609	14363	18910
Glycerol	63270	182897	252314	356190

Table 34 Revised peak areas for glycerol acetalisation

Peak Area (Intensity x Time)				
Compound	0.025 M	0.05 M	0.075 M	0.1 M
Solketal	247712.7	537683.6	962373.2	1154573
Acetal	0	8584.6	15362.4	18194.4
Glycerol	82014.9	181816.2	346604.1	419691.2

From the above peak areas and concentrations, the solketal peak areas were plotted against the solketal molarities. As shown in **Error! Reference source not found.** and **Error! Reference source not found.**, the plot of solketal peak area and molarity showed a linear relationship and the correlation coefficient R^2 was found to be ~0.97 for both external standard sets.
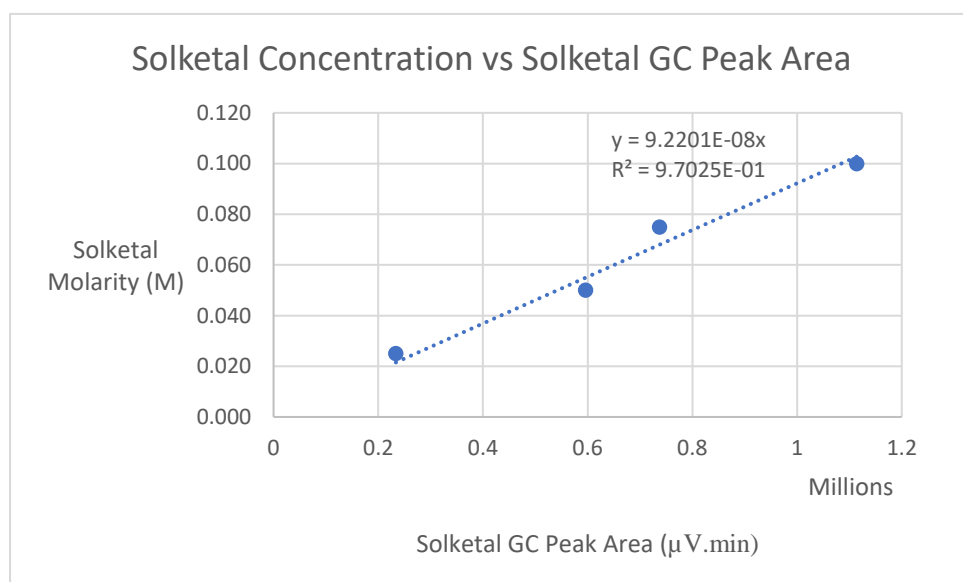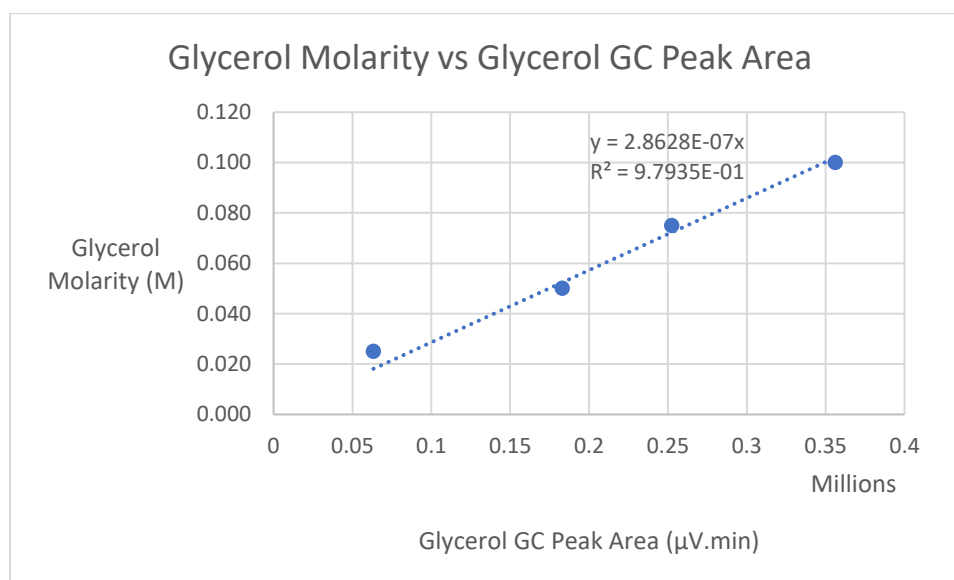

Figure 143 Original Solketal External Standard, R2 = 0.97025, Solketal Molarity = 9.2201 x 10-7 x (Solketal GC Peak Area).
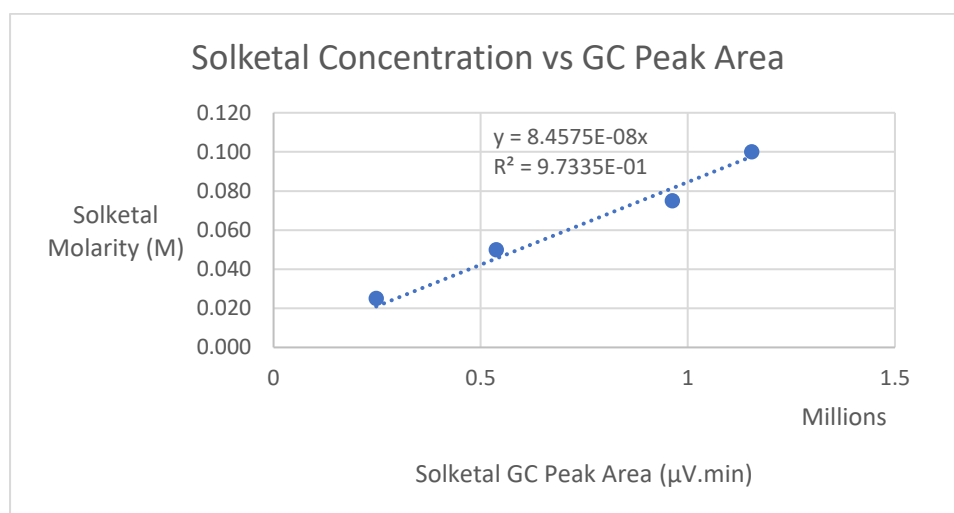
Figure 144 Final Solketal External Standard, R^2 = 0.97335, Solketal Molarity = 8.4575 x 10^{-8} x (Solketal GC Peak Area).

In a similar fashion, the glycerol peak areas were plotted against the glycerol molarities. As shown in **Error! Reference source not found.** and **Error! Reference source not found.**, the plot of glycerol peak area and molarity showed a linear relationship and the correlation coefficient R^2 was found to be greater than 0.95 for both external standard sets.

Figure 145 Original glycerol external standard, R^2 = 0.97935, glycerol molarity = 2.8628 x 10^{-6} x (Glycerol GC peak area).
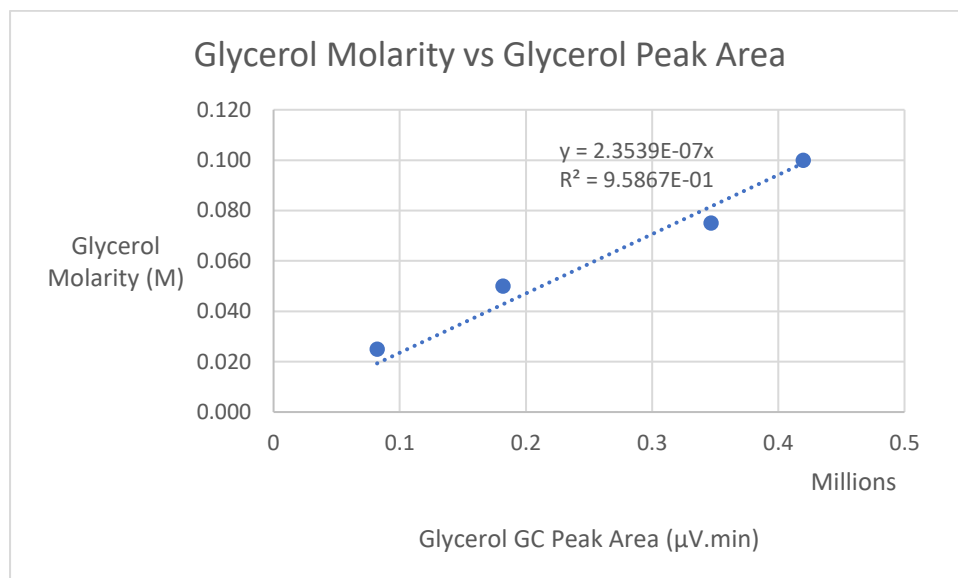
Figure 146 Revised glycerol external standard, R^2 = 0.95867, glycerol molarity = 2.3539 x 10^{-7} x (Glycerol GC peak area)

The conversion of glycerol was calculated as follows: after GC-FID was performed for a reaction, the peak areas were recorded for glycerol, solketal and acetal. Glycerol and solketal molarities were calculated using the formulae taken from the external standards plot of concentration vs. molarity as detailed in the captions of **Error! Reference source not found.** and **Error! Reference source not found..** For calculation purposes, the peak areas of solketal and acetal were combined and assumed to collectively represent the solketal peak area. The corresponding number of moles for solketal and glycerol were determined based on the known sample volume of 10mL and the n = CV formula. It follows that the amount of solketal moles produced per hour was calculated by this formula: $n_{Solketal}$/h = Solketal Moles/2.

Given that 1mmol glycerol was used and it converts in a 1:1 ratio to solketal, the mole total should always be close to 1 mmol. To correct for any errors due to loss of materials, **Error! Reference source not found.** and **Error! Reference source not found.** were applied with the underlying assumption that any loss of liquids occurs homogeneously.

$$Corrected\ solketal\ moles = \frac{Solketal\ moles}{(Solketal+glycerol)\ Moles} \times Expected\ mole\ total$$

Eq. 18 Solketal mass balance correction for glycerol acetalisation

$$Corrected\ glycerol\ moles = \frac{Glycerol\ moles}{(Solketal+glycerol)\ Moles} \times Expected\ mole\ total$$

Eq. 19 Glycerol mass balance correction for glycerol acetalisation

Finally, the amount of glycerol converted and left after the reaction was determined using the updated mole values in **Error! Reference source not found.** and **Error! Reference source not found.**.

$$Glycerol\ conversion\ (\%) = \frac{Solketal\ moles}{(Solketal+glycerol)\ Moles} * 100 \qquad \text{Eq. 20 Glycerol conversion}$$

$$Glycerol\ remaining\ (\%) = \frac{Glycerol\ moles}{(Solketal+glycerol)\ Moles} * 100 \qquad \text{Eq. 21 Glycerol remaining}$$

B. The GC-MS spectra gave qualitative information indicating that [FeCl$_3$-S-Dried], [FeCl$_3$-S-400°C/3h], [FeCl$_3$-T-Dried] & [FeCl$_3$-T-400°C/3h] were all acetalizing glycerol to solketal but not with 100% conversion in any case. Analysis of the mass spectra observed within the chromatograms focused around the peaks correlating to molar masses of 92 (glycerol), 117 (acetal) and 132 (solketal). Given that the mass-spectra was chosen to focus on the acetal and solketal concentrations, glycerol peaks are not visible in Figure 147 through Figure 150, nonetheless glycerol was present in other spectra of less interest.
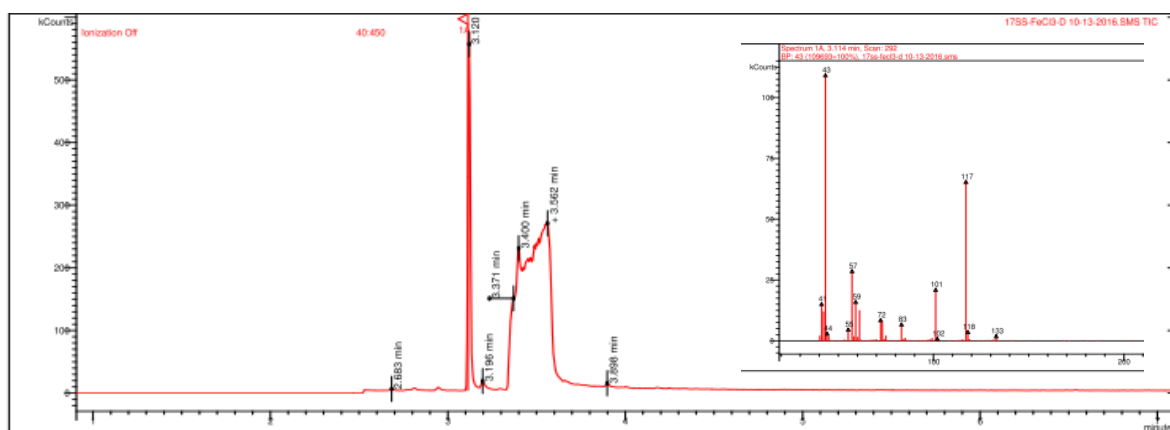

Figure 147 GC-MS of reaction solution after glycerol acetalisation for 17-4 PH coated by FeCl$_3$ and allowed to dry.
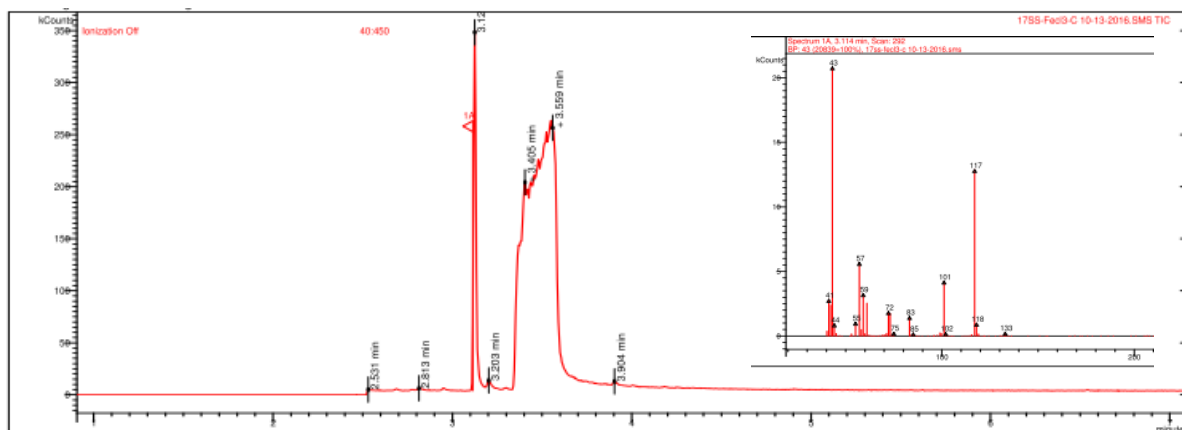
Figure 148 GC-MS of reaction solution after glycerol acetalisation for 17-4 PH coated by FeCl₃ calcined at 400ºC/3h.
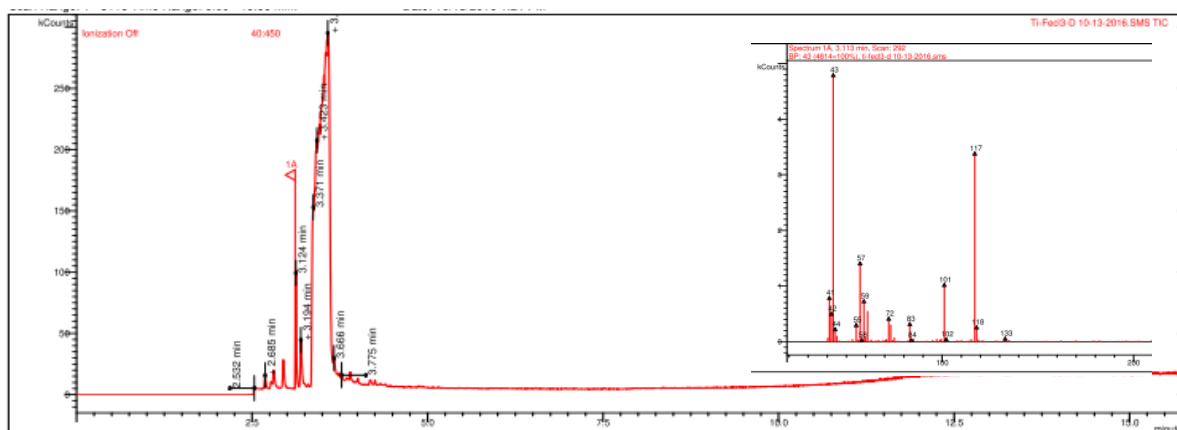

Figure 149 GC-MS of reaction solution after glycerol acetalisation for Ti6Al4V coated by FeCl₃ and allowed to dry.

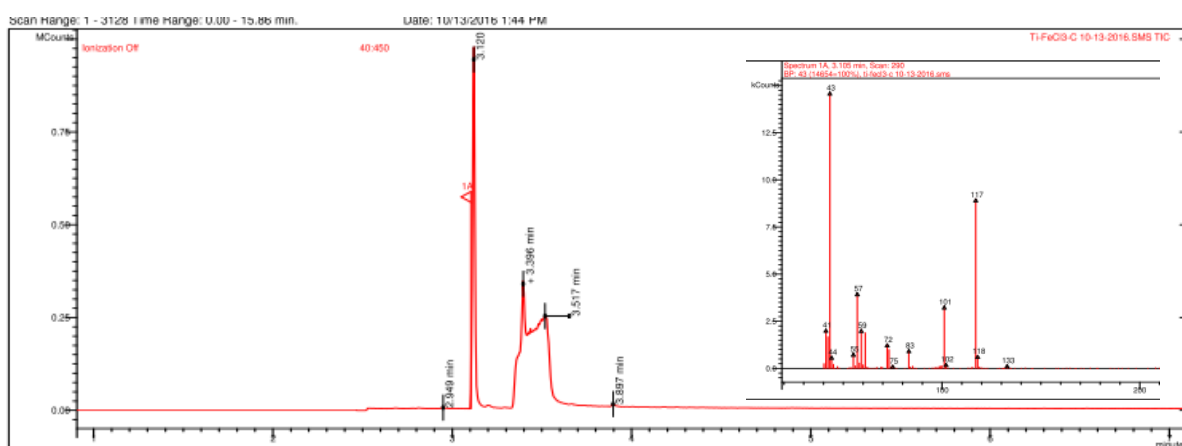*Figure 150 GC-MS of reaction solution after glycerol acetalisation for Ti6Al4V coated by FeCl₃ calcined at 400ºC/3h.*

C. The catalyst outcomes from metallic Nickel on 17-4 PH Steel, [A-c], was negligible conversion of CH_4 or CO_2, see the GC-FID data in Error! Reference source not found.. The intense peaks are the CH_4 and the small, broad peaks are due to the CO_2. The shortest, thin peaks which occur prior to the CH_4 peaks are the H_2 peaks. The position CO would occur in has negligible peak area that indicates a small amount of CO is present. All 4 of these peaks are labelled below, red for CH_4, Orange for CO_2, Yellow for H_2 and Blue for CO. This colour key applies to all future GC-FID data. Generally, this reaction is carried out under packed bed conditions, and the amount of Ni in a typical catalyst bed occupies 15 – 30 % of the volume the reactants pass through. In this case, the amount of Ni present is too small for the catalyst to perform comparably to a packed bed setup due to the far smaller Ni loadings afforded by this wall-coating method.
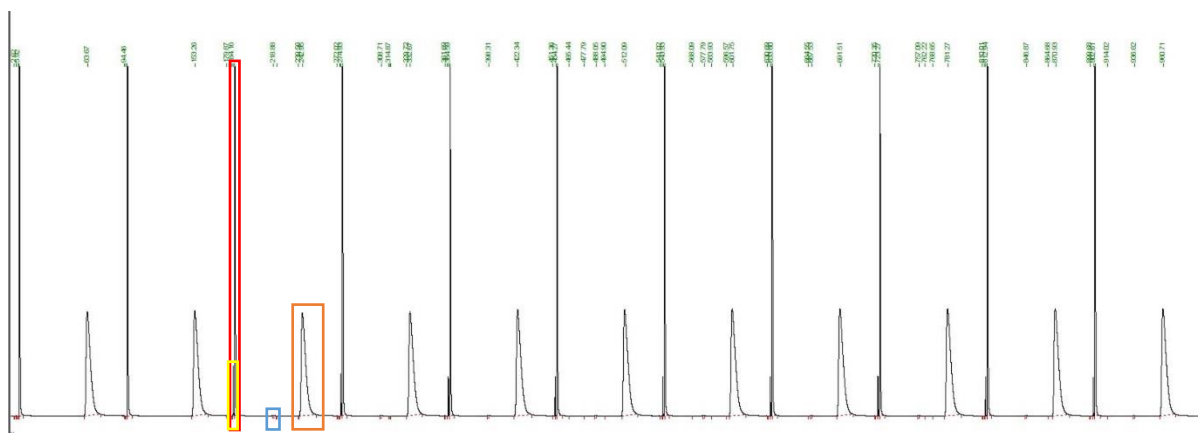

Figure 151 Online GC-FID data for Ni on 17-4 PH steel

This GC-FID data was not converted to a conversion vs. time graph because the peaks indicate that the conversion of CO_2 and CH_4 to H_2 and CO was not very high.

D. **Error! Reference source not found.** and Error! Reference source not found. indicates that some acetal and solketal are produced by both dried and 400°C/3h calcined $FeCl_3$ on TI6Al4V reactionware, as with the planar substrates, and likewise, there remains some unreacted glycerol after the 2h reaction period.
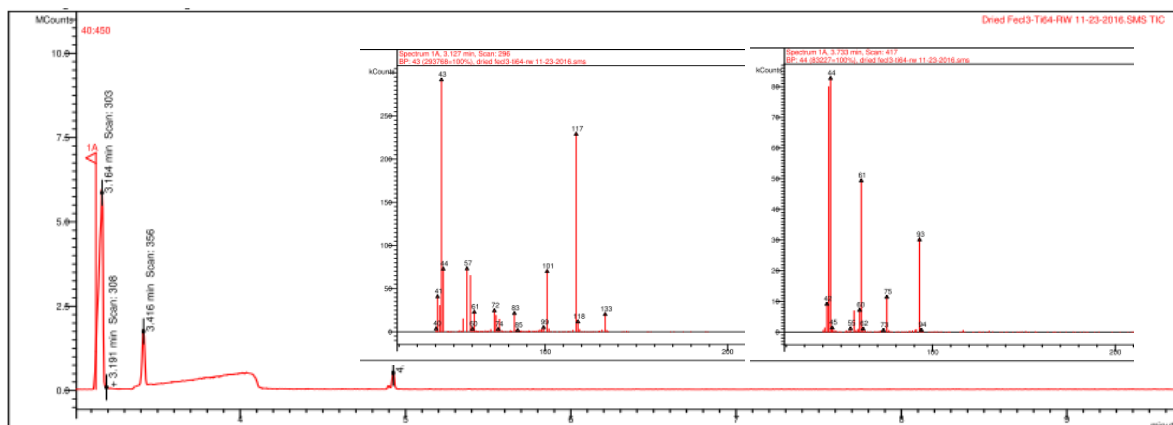
Figure 152 GC-MS of reaction solution after glycerol acetalisation in Ti6Al4V reactionware coated by FeCl₃ allowed to dry. Background figure: GC-MS chromatogram, Inner left figure: mass spectra for flag '1A', Inner right figure: mass spectra taken from the shallow slope terminating after 4 minutes.
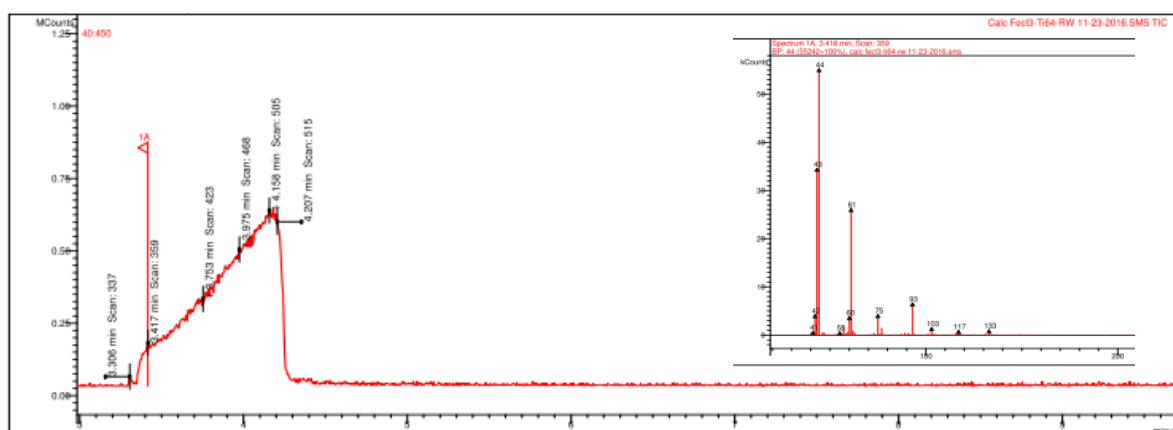

Figure 153 GC-MS of reaction solution after glycerol acetalisation in Ti6Al4V reactionware coated by FeCl₃ calcined at 400°C/3h.

2 Ti6Al4V plates and 2 Ti6Al4V reactionware vessels were coated in FeCl₃ and 1 of each were calcined at 250°C/4h instead of 400°C/3h. All 4 substrates were applied to glycerol acetalisation and produced the GC-MS chromatograms and highlighted mass spectra in **Error! Reference source not found.** and **Error! Reference source not found.** which also indicate that solketal and acetal are produced by these catalysts**.**
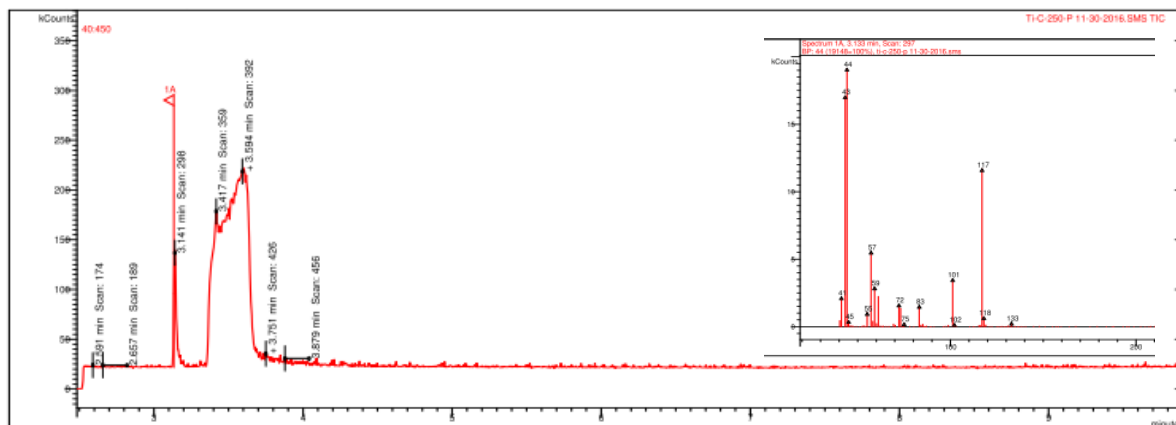
Figure 154 GC-MS of reaction solution after glycerol acetalisation for Ti6Al4V coated by FeCl₃ calcined at 250ºC/4h.
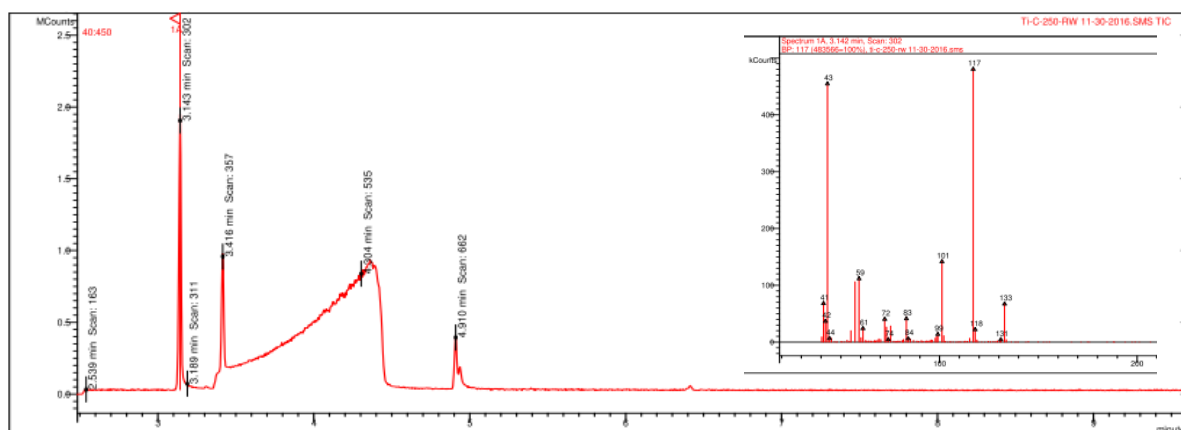

Figure 155 GC-MS of reaction solution after glycerol acetalisation for Ti6Al4V reactionware coated by FeCl₃ calcined at 250ºC/4h.